
Universidad del País Vasco
Euskal Herriko Unibertsitatea

# Development of new methods in Biomedical Engineering for brain connectivity biomarkers in epilepsy and other pathological conditions

**Thesis**
for obtaining the PhD degree in Biomedical Research program of Cell Biology and Histology Department, University of Basque Country

May 2018

**Asier Erramuzpe Aliaga**

**PhD Supervisor**
Jesus M. Cortes Diaz

*For their endless support, care and love, this thesis is dedicated to Isa, my parents Jose Luis and Elena and my sister Amaia, major contributors of my happiness.*

*Maite zaituztet*

**Acknowledgments**

This book represents the work done during my training stage to achieve scientific maturity and with these lines I would like to express my gratitude with those that helped me and made this path easier.

Jesús, we met in 2011 in Granada, thanks for inviting me to join you in Bilbao. I started dubiously my training period and thanks to your guidance, strong commitment and the trust you placed in me we made this possible. Your passion for Science has been a great inspiration but I also take with me the personal affection.

I want to thank all the present and former members of the Computational Neuroimaging Lab at Biocruces Health Research Institute and the institution itself; Sebastiano Stramaglia (for his valuable help during his stay), Paolo Bonifazi, Iñigo Gabilondo, Javier Rasero, Iñaki Escudero, Beatriz Mateos and specially Ibai Díez, whose help was crucial to write this book. Collaborators from Achucarro (Juan Manuel, Amanda), Madrid (Guillermo, Jesús, Rafael), Osatek (Alberto), Bordeaux (Ernesto), Leuven (Stephan) and Ghent (Daniele) and supervisors of my research stay in Freiburg, Marco and Elias, I could learn something from everyone of them. I am very grateful to other collaborators from Biocruces HRI external to this book's scope (Iñaki, Rafa, Lola and others) for allowing me to work with you.

I am also thankful to those who supported me economically: UGR, Euskampus, the Basque Health Department for several research stays and trainings (Freiburg, Vienna's BrainHack and Seattle's NeuroHackWeek), Ariel Rokem (Seattle), Jesús trough several project's budget and most importantly, the Basque Education Department for my predoctoral grant.

A short remark to the Open Source community and projects, without them, most of this work would have been impossible.

Finally, I can not forget many supportive individuals that made my day-to-day easier; Iker, Estibaliz and many others alongside my friends from Iruñea, València and Barakaldo.

Mila esker bihotz-bihotzez

# Contents

# Chapter 1

# Introduction

## 1.1 A little bit of history

Humankind has developed during its existence a deep understanding of the functioning of the human body and the diseases that affect it. From ancient times, using healing plants, to modern Medicine techniques, capable of organ transplants or eradication of virulent infectious diseases as smallpox.

In this development of knowledge, it could be said that Medicine has come a long way alone until the 19th century, when the advent of Chemistry and Biology led to important advances in anesthetics, antiseptics, virology and bacteriology.

Later on, Physics would barg in with important advances in techniques that evolved in modern technologies such radiology and electrophysiology. From the mid-20th century onwards, Engineering and Computer Science have been a determining factor in the advancement of Medicine, with the development of new algorithms and improvement of technology.

Taking a look at our recent history, it can be asserted that collaboration between disciplines, i.e. multidisciplinary Science, is the key to advancing human knowledge, not only in Medicine but in all disciplines. Close cooperation between experts in areas that are in principle divergent is necessary, and therefore the training of people

who can act as a link between them is vital.

The aim of this thesis is to humbly explore the application of diverse methodologies and theories coming from Computer Sciences, Mathematics and Physics in the field of neurosciences, with an special focus on neurodegenerative diseases.

Neuroscience, to the same extent as other fields, has developed disruptive advances since the first signs of practice in ancient Egypt (from the late Middle Kingdom onwards, in preparation for mummification, the brain was regularly removed). Circa 1000, Al-Zahrawi, born in Medina Azahara and living in Islamic Iberia, evaluated neurological patients and performed surgical treatments of head injuries, skull fractures, spinal injuries, hydrocephalus, subdural effusions and headache [4]. In the Renaissance, the multidisciplinary Leonardo Da Vinci made some contributions, beautifully picturing sketches of brain physiology, figure 1.1.

Seizing this Science-Art binomial, it is opportune to cite the case of calcareous concretions, calcifications, having been described in the brain, originated by some cases of cancer, subdural haematomas and, according to some, epilepsy. It is possible that the discovery of one of these mineral structures in the skull of a patient suffering from dementia created the legend of the "Stone of Madness" in Middle Age. The idea was common at the time and exploited by charlatans to perform trepanations and scam. Great artists like Jan Sanders van Hemessen, Pieter Bruegel, Pieter Huys and Jheronimus van Aken (better known as Hieronymus Bosch), all Dutch school painters, have shaped this event creating different versions of the "Cutting the Stone" or "The Extraction of the Stone of Madness", figure 1.2.

Back to pure neuroscience, the field has suffered a revolution in the last two centuries. Notable modern contributions, among others, are Santiago Ramón y Cajal's neuroanatomy descriptions (his book "Advice for a Young Investigator" was of great help and inspiration to write this thesis), the development of neuroradiology (X-rays, PET, CT, MR) and the creation of new disciplines such Computational Neuroscience.

The combination of new technologies for brain data acquisition


Figure 1.1: **Sketches of Leonardo Da Vinci of brain anatomy a, b, c, d:** Leonardo's annotations on brain physiology

Figure 1.2: **The Extraction of the Stone of Madness** The Extraction of the Stone of Madness is a painting by Hieronymus Bosch, displayed in the Museo del Prado in Madrid

(Electrophysiology and MRI) and techniques from graph theory and networks has been deeply explored in this work. A general introduction to these techniques can be found in the next pages among and overview an summary of the structure of the thesis.

## 1.2 Computational Brain

Despite rapid scientific progress, much about how the brain networks are altered across different diseases is not yet known. A much deeper knowledge of the brain is necessary to design new and effective treatments. To provide an understanding on the alterations in brain function occurring in neurodegenerative diseases and also healthy subjects, we need to look for techniques that allow us to trace this changes, both between subject and the subject with itself in different occurrences (longitudinal studies). Brain's structure, function or in the mixture between structure and function information can be analyzed using different data acquisition techniques and then converting this data to graphs to study their connectivity and dynamics.

In this thesis, different methods have been developed and applied to both healthy and unhealthy individuals e.g. epilepsy patients and Alzheimer Disease (AD) patients. In the following pages will be described different data acquisition techniques and its applications.

## 1.3 Brain data acquisition

Different techniques can be used to acquire data to study the brain. These techniques can be classified in different levels based on their spatial resolution [189]:

- **Microscale**: the ones corresponding to single neuron and synaptic connectivity measures.
- **Mesoscale**: measuring neuronal groups or populations with a spatial resolution of hundreds of micrometers.

- **Macroscale**: representing a very large number of neuronal populations forming distinct brain regions that are interconnected by inter-regional pathways.

This work will use both electrophysiology signal acquisition (either deep electrodes or electrocorticography in mesoscale and macroscale) and neuroimaging techniques for Magnetic Resonance Imaging (MRI) data (macroscale acquisitions).

### 1.3.1 Electrophysiology data

- **Electroencephalography**: Electroencephalography (EEG) is an electrophysiological monitoring method to record electrical activity of the brain. It is typically noninvasive, with the electrodes placed along the scalp. This technique is not going to be used in this Thesis due to its very low signal-to-noise ratio.

- **Electrocorticography**: Electrocorticography (ECoG), or intracranial electroencephalography (iEEG), is a type of electrophysiological monitoring that uses electrodes placed directly on the exposed surface of the brain to record electrical activity from the cerebral cortex. Because a craniotomy (a surgical incision into the skull) is required to implant the electrode grid, ECoG is an invasive procedure.

- **Deep electrodes physiology**: As ECoG, deep electrodes physiology is also an invasive type of EEG. Also known as invasive electroencephalography (iEEG), can be defined as EEG recording using invasive intracranial electrodes placed surgically. But in contrast to ECoG, the electrodes are not placed in the cortex, but inserted on the deep structures of the brain.

### 1.3.2 MRI data

MRI has demonstrated its ability to unveil non-invasively functional and structural properties of the brain in healthy populations, a know-

ledge that has been extremely useful to characterize the abnormal structural-functional brain patterns in several neurological disorders.

For many chapters of this thesis, we will make use of 3 types of MRI: structural, diffusion and functional scans. These scans are 3-dimensional images, composed by voxels, a value on a regular grid in three-dimensional space (the equivalent to a pixel in 3-dimensional images). The typical voxel size of these images is between 1mm - 5mm in each view (sagittal, coronal and axial).

- **MRI Structural data**: Also known as T1 or T2, this kind of image is a high-resolution image that is best suited to qualitatively and quantitatively describe the shape, size, and integrity of gray and white matter structures in the brain. In this work, it is mostly used to coregister and to provide a proxy for anatomical reference for other image modalities with lower spatial resolution.

- **MRI Diffusion data**: Diffusion MRI (DWI) measures the magnitude and direction (diffusion) of the motion of water molecules in each voxel. It is based on the principle that water molecules diffusion is a 3-dimensional process where molecules move differently in each of the directions. The diffusion of the water molecules in the white matter of the brain is much more restricted that the ones in the grey matter and this restriction of the diffusion happens on the direction of the axons. Although the spatial resolution of the DWI does not allow for detection of axons, it does detect diffusion on large population of axons called bundles (thousands of coherently organized axons, in macroscale) in each voxel.

  Once this direction and the strength of the tensor is known, it is possible to build pathways following these directions of diffusion in a process called tractography. It is important to emphasize that we are not obtaining the routes of individual axons, rather extracting the macroscopic structural connectivity of the brain.

- **MRI Functional data**:

Functional Magnetic Resonance Imaging (fMRI) is a noninvasive way to measure hemodynamic response within the brain. It is based on the principle that increased neural activity (increased firing of neurons) causes more energy demand, through a process called hemodynamic response, where blood provides oxygen to the fired neurons at a greater rate in comparison to inactive neurons. This causes a change of the relative levels of oxyhemoglobin and deoxyhemoglobin (oxygenated or deoxygenated blood) and this leads to magnetic signal variation which can be detected using an MRI scanner.

## 1.4 Brain networks

To study neurological dysfunction, it is of great interest to treat the brain as a network. Networks have shown an incredible potential to study complex biological systems, including the brain, and are beginning to reveal fundamental principles of brain architecture and function. The mathematical language that describes and quantifies networks is called graph theory.

The best way of characterizing brain data as a graph is to take regions of interest (ROIs) or electrode contacts as vertices of the graph. Once the vertices are selected the next step is to define the connectivity between these vertices.

There are three main types of connectivity [189, 30]:

- **Structural connectivity**: encodes anatomical connections between brain regions [188], typically white matter tracts computed from DTI [56].

- **Functional connectivity**: defines the activation profiles and dependencies among distinct neuronal populations [83]. If two regions have a similar functional activation profile they will have a strong connectivity index between these regions. Functional connectivity applies both to dynamics obtained from fMRI and electrophysiology (EEG, ECoG and/or iEEG).

- **Effective connectivity**: identifies causal interactions underlying temporally ordered activation or information flow [85]. Differently to structural or functional connectivity, where the information between edges is undirected, effective connectivity unveils the direction of the information between edges. That is, directed edges represent the fact that one vertex exerts some influence on its neighbor but not the other way around.

## 1.5 Thesis overview

In this thesis brain network analysis was used to unveil functional and structural patterns in both pathological and healthy brains. The Chapters 2, 3 and 4 explore in a different manner various aspects related with the epilepsy using all the possible data acquisition techniques described in the previous pages whilst Chapters 5 and 6 analyze AD and healthy aging.

More precisely, in Chapter 2 we present a longitudinal FC analysis on the same mouse brain across different days. The general goal of this work is to unveil whether FC can account for differences in brain states, across the entire transition from a healthy brain to an epileptic one after an initial episode of status epilepticus. To this aim, a setup based on a classical animal model of mesial temporal lobe epilepsy (MTLE) is used, achieved by intra-hippocampal injection of kainic acid (these experiments were led by Prof. Juan Manuel Encinas at Achucarro Basque Center for Neuroscience).

In Chapter 3 we used Information Theory based measures for triplets to analyze complex dynamics of the brain within an electrode area in the cortex. This technique will be used to study the information flow between electrodes in epilepsy with a known post-surgical outcome. Our approach relies on the measure of interaction information (II). The sign of II provides information as to the extent to which the interaction of variables in triplets is redundant (R) or synergetic (S). Here, based on this approach, we calculated the R and S status for triplets of electrophysiological data recorded from drug-resistant patients with MTLE in order to study the spatial or-

ganization and dynamics of R and S close to the epileptogenic zone (the area responsible for seizure origination and propagation).

Chapter 4 describes a multimodal approach to unveil epileptic networks. Extending the analyses based on electrocorticography in previous chapters, here there will be used deep electrodes among DWI and fMRI, having a unique data set from three different sources. Functional and structural networks will be explored at both link and module level, obtaining promising results in the understanding of epilepsy.

Next, in Chapter 5 Principal Component Analysis is used to extract more information from the Resting State Networks (RSNs emerge from the correlation in signal fluctuations across brain regions during resting state, a condition defined by the absence of goal-directed behavior or salient stimuli) of the brain and compute new information flow measures using many brain components. We used this method to find differences in the communication of Resting State Networks in Alzheimer's disease and we demonstrate that the differences are not always shown in the 1st principal component (the one corresponding with the average activity, usually used for information flow analyses).

Finally, in Chapter 6 it will be described the functional and structural reorganization of the brain aging in healthy subjects. Here, we collected brain images from healthy participants (N=155) ranging from 10 to 80 years to build functional (resting-state) and structural (tractography) connectivity matrices. We then calculated the brain-connectome age (BCA) as the maximum likelihood age-estimator, and compared BCA to the chronological age (ChA).

In Chapter 7 is provided a general conclusion of the chapters and thesis.

# Chapter 2

# Longitudinal variations of brain functional connectivity

In the previous chapter we made an introduction to brain networks. This chapter is the first of a series of three were we explore epilepsy disease, using different data types. In this chapter we used a mouse model of MTLE that allowed us to explore the longitudinal deterioration of the epileptic brain.

## 2.1 Introduction

These experiments where guided by Prof. Juan Manuel Encinas at Achucarro Basque Center for Neuroscience. Functional Connectivity (FC) quantifies the statistical similarities between brain areas [83]. FC measures the influences between areas originated by different causes, such as two areas having a shared structural connectivity (wiring connections) or being driven by a common input. As such, studies based on FC are highly valuable for addressing disruptions of brain functioning in neurological disorders such as epilepsy, a major neurological disorder characterized by chronic unprovoked seizures. Indeed, FC studies in epilepsy are abundant [28, 208, 24, 43, 214, 21], but these studies typically perform group comparison between health and disease; differently, we present here a longitudinal FC analysis

on the same mouse brain across different days.

Our general goal here is to unveil whether FC can account for differences in brain states, across the entire transition from a healthy brain to an epileptic one after an initial episode of status epilepticus. To the best of our knowledge, variations in FC across this transition have not addressed before. Our hypothesis is that FC can indeed differentiate those states.

To this aim, we introduce a setup based on a classical animal model of mesial temporal lobe epilepsy (MTLE), achieved by intrahippocampal injection of kainic acid (KA) [182, 19]. After an initial provoked seizure, the latent period emerges and eventually, brain's mouse resembles the main characteristics of human MTLE (see for instance [185] and references therein). Using this setup we show herein that indeed FC can differentiate those states when applied to longitudinal data.

## 2.2 Methods

### 2.2.1 Experimental Protocol and Mouse Recordings

An adult mouse was subjected to an intrahippocampal injection of the glutamate agonist kainic acid, KA (1nmol of KA in 50 nL), an experimental model that reliably reproduces the physiopathological features observed in human MTLE [33, 185]. Changes in FC patterns were analyzed from intracraneal electroencephalographic data (EEG) across longitudinal sessions, from 0 days post KA injection (0 dpi) to 21 dpi. Implanted electrodes were intracraneal E363/8 platinum/iridium (Teflon insulated), 0.005mm of diameter and 2mm of length, mounted in a plastic pedestal, which was secured to the skull with dental cement.

The experimental setup is shown in figure 2.1. Four electrodes were implanted bilaterally in the hippocampus and the motor cortex; we labeled these electrodes as left cortex (LC), right cortex (RC), left hippocampus (LH) and right hippocampus (RH). The KA injection

was applied at the RH electrode (indicated by a red arrow in panel a).

Recording sessions had a duration of 4 hours and were performed every day during first week and every other day for the following weeks with a Nicolet video-electroencephalogram (vEEG) system (Nic View 5.71, CareFusion, San Diego, CA, USA). Recordings were first preprocessed with a 60 Hz notch filter and then passed through a 0.5-250 Hz bandwidth filter. Next, data was converted to ASCII using an EEG Converter for further analysis (EegSoft, Inc.). All postprocessing analysis was performed in Matlab (MathWorks Inc., Natick, MA).

### 2.2.2 Identification of Interictal States

Epileptic seizures and artifact-free epochs of interictal states were visually classified; seizures were identified according to repetitive-spikes and slow-wave discharges lasting 10 sec or more and synchronized with the behavioral stage of 4-5 generalized seizures (monitored by video recording) according to the Racine scale [153]. Interictal discharges were measured as fast and high amplitude spike events lasting up to 200 msec.

### 2.2.3 Functional Connectivity

For calculation of FC, we used 8 different non-overlapping windows of 1250 time points each to average the different measures across the following days: 0,1,2,7,14 and 21 dpi (or equivalently we averaged over 8 intervals of 5 seconds each at 250 Hz of sampling rate). All the results of FC reported in this manuscript are corresponding to averaging over 8 different windows, which ensured an appropriate sample dealing with the variability in the FC estimation, as the coefficient variation (the ratio between the standard deviation and the mean) was about 0.1 or smaller.

FC was addressed calculating the linear correlations (C) and partial correlations (PC) between the time-series electrodes data. The C matrix was evaluated in terms of the Pearson's Correlation, using

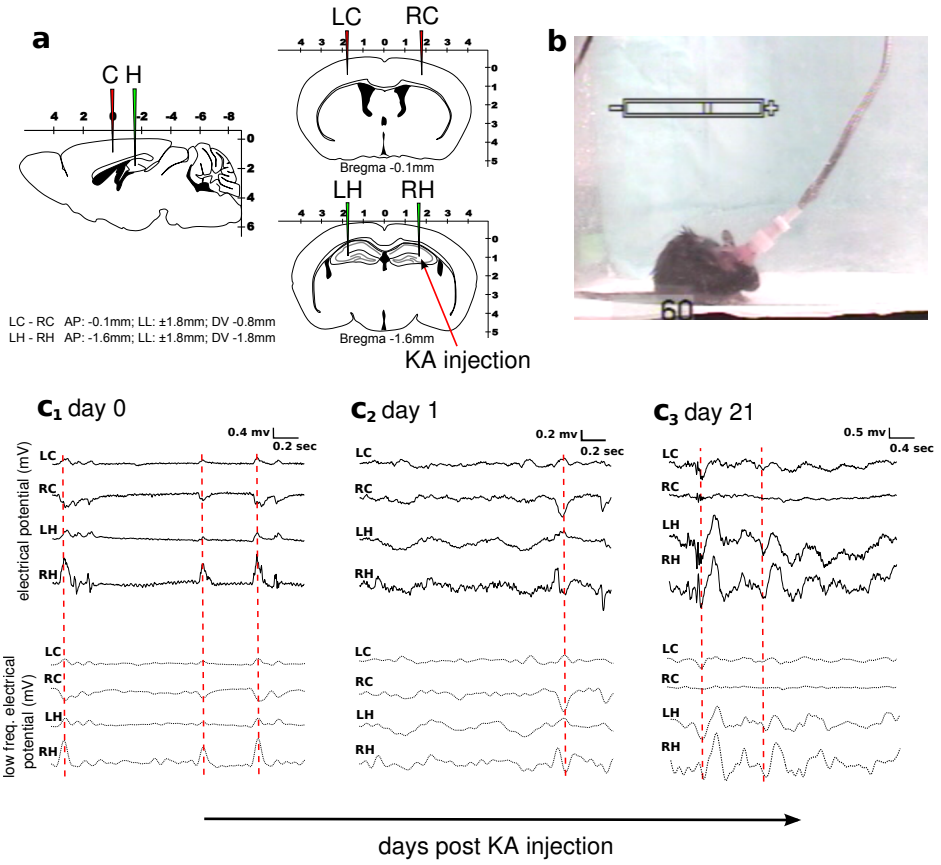


Figure 2.1: **Intracraneal EEG recordings from MTLE mice. a:** Experimental setup. The intracraneal placement of site recordings consisted on two electrodes placed bilaterally in the cortex (LC and RC, red) and two in the hippocampus (LH and RH, green). **b:** EEG recording was coupled to videographic recordings for visual confirmation of the seizure events. **c1-c3:** Examples extracted from the EEG recordings at the day of the injection (c1), the next day (c2) and after 21 days (c3). Overall changes in the electrical potential are shown in the upper row and after filtering for low frequency (1-14 Hz) in the lower row. The red dotted line marks high statistical similarities between electrodes, what provides high values of FC. Notice that RH is the site of the KA injection, and shows a higher epileptogenic activity that can be easily detected by looking at the amplitude of the time series associated to the RH electrode.

the *corr* function in Matlab (MathWorks Inc., Natick, MA). PC is an extension of C to calculate direct interactions between electrode pairs, as PC removes for a given pair the correlation contribution coming from other distinct pairs [128]. In particular, each element of the PC matrix is defined (assuming C to be a non-singular matrix) as $\mathrm{PC}_{ij} = -\frac{P_{ij}}{\sqrt{P_{ii}P_{jj}}}$, where $P \equiv \mathrm{C}^{-1}$ is the inverse correlation matrix (ie. the so-called precision matrix). Here, PC was calculated using the *partialcorr* function incorporated in Matlab (MathWorks Inc., Natick, MA).

### 2.2.4 Network Connectivity Index

The Network Connectivity Index (NCI), c.f. figures 2.2c-d, is an index accounting for all 4 electrode interactions. To calculate it, we summed all the absolute values of all matrix elements in either C or PC divided by $N(N-1)$, a normalization factor equal to the total number of pairs minus the principal diagonal elements; thus, the NCI ignores all diagonal elements $\mathrm{C}_{ii}$ and $\mathrm{PC}_{ii}$ as they are equal to one in both C and PC matrices.

For each of the 8 non-overlapping windows we calculated one value of NCI. Statistical significance differences between the NCI at dpi0 (control) respect to other conditions (1,2,7,14 and 21 dpi) were addressed by performing a t-test of the hypothesis that the data in the two conditions have a different mean. Here, the t-test was performed using the *ttest* function incorporated in Matlab (MathWorks Inc., Natick, MA).

### 2.2.5 Low and High Frequency Regimes

A zero-phase digital filter was applied to the electrophysiological signals at different frequency bands, using the *filtfilt* function existing in Matlab (MathWorks Inc., Natick, MA). In particular, we focused on low frequency bands (merging theta and delta bands, i.e., 1-14 Hz) and high frequency bands (gamma rhythms at 25-70 Hz). This selection of frequency bands was performed to show differences in the

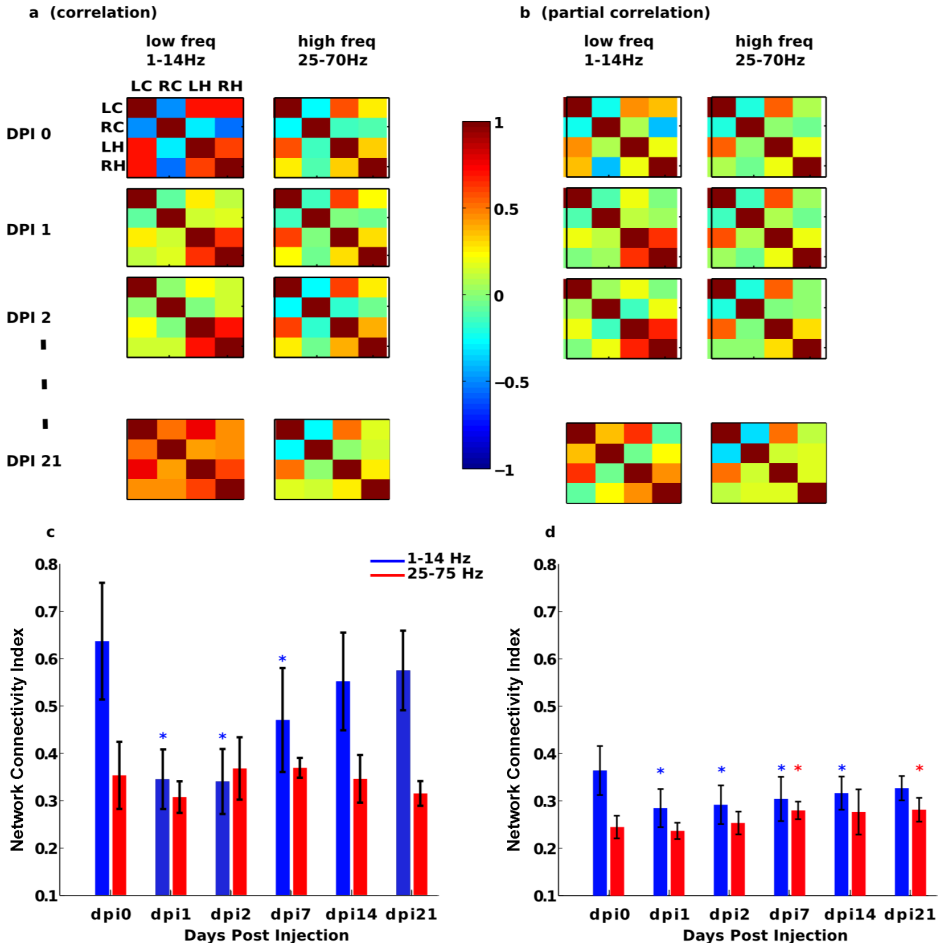


Figure 2.2: **Longitudinal variations of FC across different days and different frequency bands. a,b:** C and PC matrices across different days post KA injection and different frequency bands: low freq (1-14Hz) and high freq (25-70Hz). **c,d:** For the matrices plotted in panels a and b, we calculated the network connectivity index (for definition see methods) and represented across different days and frequency bands. Asterisks mean, for each condition respect to dpi0 (control), statistical significance differences with pvalue smaller than 0.05. While PC is not able to distinguish across days, C does it clearly in the lower frequency band (blue line), showing a strong decrement at dpi1 and afterwards, FC started to increase until dpi21.

dynamics between two highly different regimes: low vs high frequency.

## 2.3 Results

The setup represented in figure 2.1 provided unique data to test our hypothesis that the FC analysis, when applied to longitudinal data, can differentiate between brain states. Taking as an input the recordings belonging to the 4 electrodes LC, RC, LH and RH, we calculated FC matrices based on C and PC on 8 different time-windows (Methods). Figures 2.2a-b correspond to average matrices across the 8 segments. The C analysis (figure 2.2a) showed a strong non-linear behavior at low frequencies (left column of matrices), as FC values strongly decreased at 1 dpi and after this point the FC values started to increase up to 21 dpi. This tendency, which did not exist in the high-frequency regime (right column of matrices in figure 2.2a), confirmed that FC significantly varied across brain states, as data come from a well-validated model of mouse epilepsy.

Next, we quantified connectivity patterns by calculating the NCI (figures 2.2c-d) which, by summing the absolute values of all C and PC values (methods), provides information of the overall network connectivity. We analyzed NCI across brain regions and days post KA injection (figure 2.2a) and found that hippocampal electrodes LH and RH remained strongly correlated across days in comparison to cortical electrodes in the cortex. In particular, LC and RC started highly anticorrelated at 0dpi, but their mutual correlation was drastically decreased at 1 dpi to eventually start to increase again up to a highly correlated state at 21 dpi (figure 2.2a).

The PC analysis at the low frequency regime was also able to differentiate between hippocampal electrodes LH and RH, as the FC value between these two electrodes was high across days. Furthermore, the PC analysis showed small variations across days, and this occurred for both high and low frequency regimes. This has a particular interest, as PC removes interactions in a given pair coming from common neighbors, the so-called indirect effects. Thus, the indirect effects captured by C but not by PC were dominant at low

frequencies.

## 2.4 Discussion

Can FC differentiate between brain states when applied to longitudinal data? To answer this question, we have made use of an animal model of MTLE to address the variations in FC across the transition from an initial episode of status epilepticus to seizure chronification. We addressed FC by calculating C and PC. C (but not PC) revealed interactions through common neighbors (*i.e., network effects*) at low-frequency bands. More precisely, the network index for C showed a strong drop-off in the overall brain connectivity at 1 dpi but it smoothly increased for several days afterwards. This tendency might be correlated with the latency period, namely, the time interval between the original brain insult and the clinical presentation of the first spontaneous seizure. During this latency period, the transition from a healthy brain into an epileptic one, or epileptogenesis, occurs due to changes in the molecular, cellular, and network properties of the brain in response to the initial precipitating event. What we particularly show here is that the NCI for C works as a readout of the changes in brain functioning that take place during the latency period. In the near future, we aim to correlate the FC results with studies at the molecular and cellular level, what might an integrative approach to better understand the process of epileptogenesis to eventually open new venues for more efficient therapeutic strategies.

We are emphasizing the advantages of using animal models for studying epilepsy. Thus, rather than performing group comparison (health vs. epilepsy) as it is normally done when studying disease, our setup allowed us for addressing longitudinal variations in FC on the same animal from the initial episode of status epilepticus to chronic epilepsy. Although the results analyzed here correspond to a very limited sample (n=1), we firmly believe that the same analysis can be applied to larger samples, allowing for studying longitudinal group FC patterns rather than individual results.

# Chapter 3

# Redundant and synergetic circuits in functional connectivity matrices

In Chapter 2 we performed an analysis over mouse electrophysiology data. In this chapter we will use Information Theory based measures for triplets to analyse complex dynamics of the brain within an electrode area in the cortex. This technique will be used to study the information flow between electrodes in epilepsy with a known postsurgical outcome.

Neural systems are comprised of interacting units, and relevant information regarding their function or malfunction can be inferred by analyzing the statistical dependencies between the activity of each unit. Whilst correlations and mutual information are commonly used to characterize these dependencies, our objective here is to extend interactions to triplets of variables to better detect and characterize dynamic information transfer.

Our approach relies on the measure of interaction information (II). The sign of II provides information as to the extent to which the interaction of variables in triplets is redundant (R) or synergetic (S). Three variables are said to be redundant when a third variable, say Z, added to a pair of variables (X,Y), diminishes the information shared between X and Y. Similarly, the interaction in the triplet is

said to be synergetic when conditioning on Z enhances the information shared between X and Y with respect to the unconditioned state. Here, based on this approach, we calculated the R and S status for triplets of electrophysiological data recorded from drug-resistant patients with mesial temporal lobe epilepsy in order to study the spatial organization and dynamics of R and S close to the epileptogenic zone (the area responsible for seizure origination and propagation).

## 3.1 Introduction

The use of information theory to deal with data has become an important means to evaluate the interaction between groups of correlated variables in neuroscience, revealing functional relationships and the underlying circuits capable of processing specific information [32, 145, 152, 49]. In addition to information storage/coding/decoding, information theory can address whether interactions between related variables are mutually redundant or synergetic [179, 22].

In general, synergy (S) occurs if the understanding of one variable helps predict the behaviour of another variable with more precision than the sum of the information provided individually by the two variables. By contrast, redundancy (R) corresponds to situations where the same information is offered by the variables (see also the interpretation of S and R based on causality inference in [194]).

When interaction information (II) [134] is applied to sets of three variables, its sign indicates whether the relationship within the triplet can be considered as R or S. Thus, unlike mutual information, II can be either positive or negative, whereby a positive II identifies R and a negative II S. As an example of the mechanisms that produce both R and S, common-cause structures (such a common-input) lead to R, while S could be produced by combining one XOR gate with two independent random inputs (for instance) [125, 211].

The presence of S is well-known in sociological modelling, where the term *suppressors* was applied to those variables that increase the predictive validity of other variables after their inclusion in a linear regression equation [47]. Similarly, the interaction between triplets of

variables in gene regulatory networks was approached to study how a specific gene modulates the interaction between two other genes [11, 209]. Moreover, when applied to electrophysiological recordings from neural networks in culture, a series expansion approach takes into account terms that are coincident with the II [23]. Here, we use II to study triplet interactions in epilepsy but rather than focusing on the pathology, we aim to highlight here the methodological aspects. In particular, by applying II to human electrocorticography data, we reveal certain aspects of the interactions (not captured by looking solely to pairs of variables) that underpin the epileptogenic zone, the brain network that triggers epileptic seizures.

## 3.2 Methods

### 3.2.1 Surgery and postsurgical outcome

The selection of the area for resection was made according to current standard practices that are applied to surgery for epilepsy, which involves resecting the cortical area that displays the most excitatory activity electrophysiologically as a proxy of the epileptogenic zone [167].

The clinical outcome was assessed using the Engel Epilepsy Surgery Outcome Scale [74], ranging from I (seizure-free after surgery) to IV (no improvement after surgery). The electrocorticography data studied here correspond to n=3 Engel I patients that had no further seizures after surgery and n=1 Engel III patient for comparison.

### 3.2.2 Human electrocorticography data

The data analyzed here through the novel II approach has been published previously [144] and correspond to data recorded from drug-resistant patients with temporal lobe epilepsy who underwent surgery at the Epilepsy Unit at La Princesa Hospital (Madrid, Spain). After receiving the approval of the Ethics Committee at La Princesa Hospital, patients provided their informed consent to be evaluated

intraoperatively with a $4 \times 5$ subdural electrode grid (interelectrode distance, 1 cm), having been administered low doses of sevoflurane (0.5%) and remifentanil (0.1 mg/kg/min). While recording, the anaesthesia was stabilized within a bispectral index in the range of 55-60 (adimensional index) [168]. The grid was placed over the lateral temporal cortex, with its border parallel to the sylvian fissure and covering gyri T1-T3, and its position was recorded with a video camera or photographed. The reference electrode was placed on the contralateral ear and in some cases it was moved to the nearby scalp in order to verify there was no contamination of the recording, consistent with previous studies [142]. A presurgical evaluation was carried out according to the protocol used at La Princesa Hospital, as reported previously [147].

From the perspective of signal processing, it is important to emphasize the importance of electrocorticography studies as opposed to those based on scalp electroencephalography. In the former signal quality is much better, with a signal to noise ratio about 21 to 115 times greater, which makes these two modalities quite distinct [197].

### 3.2.3 Data processing

All of the analyses carried out here were performed retrospectively and thus, tailored lobectomies were not based on the results discussed here. An intraoperative electrocorticography session was recorded for 15-20 min using a 32-channel amplifier (Easy EEG II, Cadwell, USA), preprocessing with a filter with a 0.5-400 Hz bandwidth and with a 50 Hz notch filter, and finally downsampling at 200 Hz. Artefact-free epochs of inter-ictal activity lasting up to 5 min were selected by visual inspection. All post-processing analysis was performed in Matlab (MathWorks Inc., Natick, MA).

### 3.2.4 Frequency-band analysis

Electrophysiological signals were filtered within different frequency bands using a zero-phase digital filter (figure 3.5). In particular, we used the *filtfilt.m* function from Matlab (MathWorks Inc., Natick,

MA) to filter the following standard bands for brain electrophysiology: delta (1-4 Hz), theta (4-7 Hz), alpha (7-14 Hz), beta (14-26 Hz), and gamma (26-100 Hz).

### 3.2.5 Shannon entropy

The Shannon entropy of a random variable $X$ (i.e.: its average uncertainty) is defined as

$$H(X) = -\sum_{x} \text{prob}(x)\text{log prob}(x), \tag{3.1}$$

where prob($x$) represents the probability distribution of the state $x$ of variable $X$ [98, 51]. In this manuscript, variable X is defined by the electrical potential captured by electrode X. The joint entropy is just a generalization to any dimension, i.e., in 2D it becomes $H(X,Y) = -\sum_x \sum_y \text{prob}(x,y)\text{log prob}(x,y)$ and in 3D, we have $H(X,Y,Z) = -\sum_x \sum_y \sum_z \text{prob}(x,y,z)\text{log prob}(x,y,z)$. For a base 2 logarithm (as used here), the entropy is expressed in bits.

### 3.2.6 Interaction information

II is measured based on the Shannon entropy, allowing us to analyze the interactions between triplets [134]. For any triplet $(X,Y,Z)$, II is defined as

$$\text{II}(X,Y,Z) \equiv I(X,Y) - I(X,Y|Z) \tag{3.2}$$

where $I(X,Y)$ is the mutual information between $X$ and $Y$, which can be defined in terms of the marginal and joint entropies, ie.,

$$I(X,Y) = H(X) + H(Y) - H(X,Y), \tag{3.3}$$

and $I(X,Y|Z)$ is the conditional mutual information between $X$ and $Y$ conditioned to $Z$. Analogously, $I(X,Y|Z)$ can be written as a function of the marginal and joint entropies, i.e.,

$$I(X,Y|Z) \;=\; H(X,Z) - H(Z) + H(Y,Z) - H(X,Y,Z), \quad (3.4)$$

for further details see [51]. Thus, using the definition given by Eq. (3.2), and Eqs. (3.3) and (3.4), one can express II as a function of the Shannon entropies, i.e.,

$$\begin{aligned} \mathrm{II}(X,Y,Z) \;\equiv\; & H(X,Y,Z) + H(X) + H(Y) + H(Z) \\ & -H(X,Y) - H(X,Z) - H(Y,Z). \end{aligned} \quad (3.5)$$

From this equation, one can derive simple but important properties of II (for details see Appendix).

Note that our definition of II uses an opposite sign to the original form in [134]. Also, it is important to emphasize that when II is equal to zero, II is ill-posed as two different situations can correspond to $\mathrm{II} = 0$, namely that the three variables are either statistically independent of each other or that $I(X,Y) \approx I(X,Y|Z)$. Therefore, we will only report situations satisfying that $\mathrm{II} \neq 0$, i.e., values of $\mathrm{II} \approx 0$ will be ignored.

### 3.2.7 Calculation of the interaction information assuming Gaussian data

We calculated the II under a Gaussian approximation for which the Shannon entropy can be analytically calculated, i.e.: where the differential entropy for the multivariate Gaussian distribution has an analytical derivation (see details in [51]). To calculate the conditional mutual information, Eq. (3.4), we made use of [12], where for multivariate Gaussian random variables it was shown that:

$$I_{\text{gaussian}}\,(X;Y|Z) = \frac{1}{2}\ln\frac{|\Sigma(X|Z)|}{|\Sigma(X|Y\oplus Z)|}, \quad (3.6)$$

where $|\cdot|$ denotes the determinant, and the partial covariance matrix is defined by

$$\Sigma(X|Z) = \Sigma(X) - \Sigma(X,Z)\Sigma(Z)^{-1}\Sigma(X,Z)^{\top}, \quad (3.7)$$

in terms of the covariance matrix $\Sigma(X)$ and the cross covariance matrix $\Sigma(X, Z)$; the definition of $\Sigma(X|Y \oplus Z)$ is analogous, where $Y \oplus Z$ means appending the two variables.

To calculate II, Eq. (3.2), we also need to calculate the mutual information term; obtained using the same Eq. (3.6) but in absence of $Z$.

### 3.2.8 Calculation of the interaction information assuming non-Gaussian data

In the most general situation of data not following a Gaussian distribution, and in order to calculate the mutual information and the conditional mutual information (cf. rhs in Eq. (3.2), we first binned the data to 4 states and then evaluated equations (3.3) and (3.4) using the Mutual Information Toolbox [148], a C++ implementation of several Information Theory based functions plugged in Matlab (MathWorks Inc., Natick, MA). In particular, we made use of the functions *mutualinfo.m* and *condmutualinfo.m* incorporated in [148]. To calculate probabilities, also 6 and 10 bins were used and the results were no different.

### 3.2.9 Redundancy and synergy

Directly from the definition of II, Eq. (3.2), a positive sign of II means that $I(X, Y) > I(X, Y|Z)$, and together with the circulation property (establishing that II is invariant to any possible permutation in $(X, Y, Z)$; for further details see Appendix) this implies that the interaction in the triplet is redundant. Similarly, a negative sign of II corresponds to a synergetic interaction.

This is in agreement with the results based on the partial information decomposition reported in [212], where a similar interpretation of the sign of II was provided: a positive one for R and a negative one for S, taking into account the fact that the right hand side of Eq. (3.2) has the opposite sign to the II reported in [212] (see also a further discussion in [14]).

### 3.2.10 Statistical significance

All values reported in this manuscript were statistical significant. Statistical significance was approached by building the null-distribution of no interaction after a shuffling procedure of N=50000 repetitions in the time series used for calculation. Significant values (after Bonferroni correction) were obtained with a p-value of 0.05 for both the S and R tails of the distribution (negative and positive values), as II is not normally distributed, i.e., the tail of the II distribution has a different length on the positive and negative sides.

### 3.2.11 Averaging of the interaction information

For each of the 20 grid electrodes, we used different non-overlapping windows, ranging from 9 to 29 windows, each containing 2,000 time points (10 seconds at a sampling rate of 200 Hz). The values of II reported here correspond to the average II over all the different windows, producing an appropriate sample (figure 3.1).

### 3.2.12 Network measures for plotting interaction information in 2D

To obtain 2D plots of II, whereby each default value depends on a triplet of variables, we represented the II variation across two variables while keeping a third variable fixed.

In order to study the network of interactions rather than looking to individual values, we considered each variable to be a node within a network and after applied different network measures using the Brain Connectivity Toolbox [170, 169]. In particular, the fixed electrode was chosen as the one with maximum betweenness centrality (accounting for the fraction of all the shortest paths in the network that contain a given node, and thus, nodes with high betweenness participate in many of the shortest paths), that with maximum degree (the hub, obtained simply by summing the weighted links connected to a given node), and the one with a maximum clustering coefficient (calculated

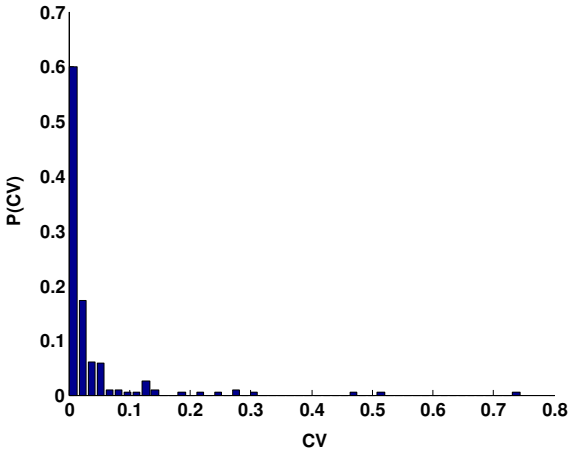


Figure 3.1: **Sampling validation of the interaction information.** The figure shows the coefficient of variation of the II (standard deviation of the estimation divided by its mean) resulting from averaging over 9 different windows and consisting of 2000 points each. One can see how the standard deviation is well-sampled and significantly smaller than the average.

as the fraction of triangles around a node, and thus providing relevant information of the clustering strength in a node neighbourhood).

### 3.2.13 Local synchronization index, individual redundancy and individual synergy

In the light of previous studies based on the local synchronization index (LSI) in electrocorticography data [144], we were interested in indexes that can work for individual electrodes. As reported in [144], the LSI measures the average synchronization of each electrode with their first neighbours, including those in the diagonals. In particular, LSI is calculated by averaging the absolute value of the Pearson correlation between a given node and its nearest neighbours, i.e., 3 neighbours at corner's grid, 5 neighbours at side's grid and 8 neighbours elsewhere.

In an analogous manner, the individual R was calculated for a given electrode $\bar{Z}$, summing all the values of positive $II(X, Y, \bar{Z})$ for

all $X$ and $Y$ variables. Likewise, the individual S was obtained by summing for all $X$ and $Y$ the negative values of $II(X, Y, \bar{Z})$ and finally taking the absolute value of this sum. For these two measures, the individual R and S values, we only summed on triplets such that the three variables were distinct to one another.

## 3.3 Results

II depends on triplets of variables and its positivity or negativity identifies rather the interaction in the triplet is (respectively) redundant or synergetic. First, we inspected the patterns of II by projecting it to the 2D plots, fixing one of the electrodes and plotting II by varying the other two variables (see Methods).

We first fixed the electrodes with maximum and minimum entropy, two good references for studying II as II(X,X,X) coincides with the entropy (see Appendix). We also fixed several electrodes that at the network level play an important role such as the one with maximum betweenness, the one with maximum degree of connectivity (i.e.: the hub) and the one with a maximum clustering coefficient (see Methods for further details on these measures). As it is shown in figure 3.2, the 2D plots drastically depend on what the electrode was fixed, indicating a clear 3D structure of II, i.e., a very distinct II patterns appears in the neighbourhood of the different electrodes.

Next, we assessed whether the R and S patterns were in any way related with the epileptogenic zone (the area responsible for seizure propagation). This could be addressed as some of the patients had an Engel I outcome (Methods) and did not experience further seizures after surgery. Given the resection area (an area known for all patients) and using the recordings before surgery, it is possible to guarantee that the resection area contained at least part of the epileptogenic zone. In addition to the resection area (the gray grid in figure 3.3), we also calculated the spatial distribution of S (red grid in figure 3.3), R (blue grid), Shannon entropy (green grid) and LSI (the magenta grid), an index that was proven to match the putative epileptogenic zone [144]. Accordingly, while R and LSI had the same spatial grid

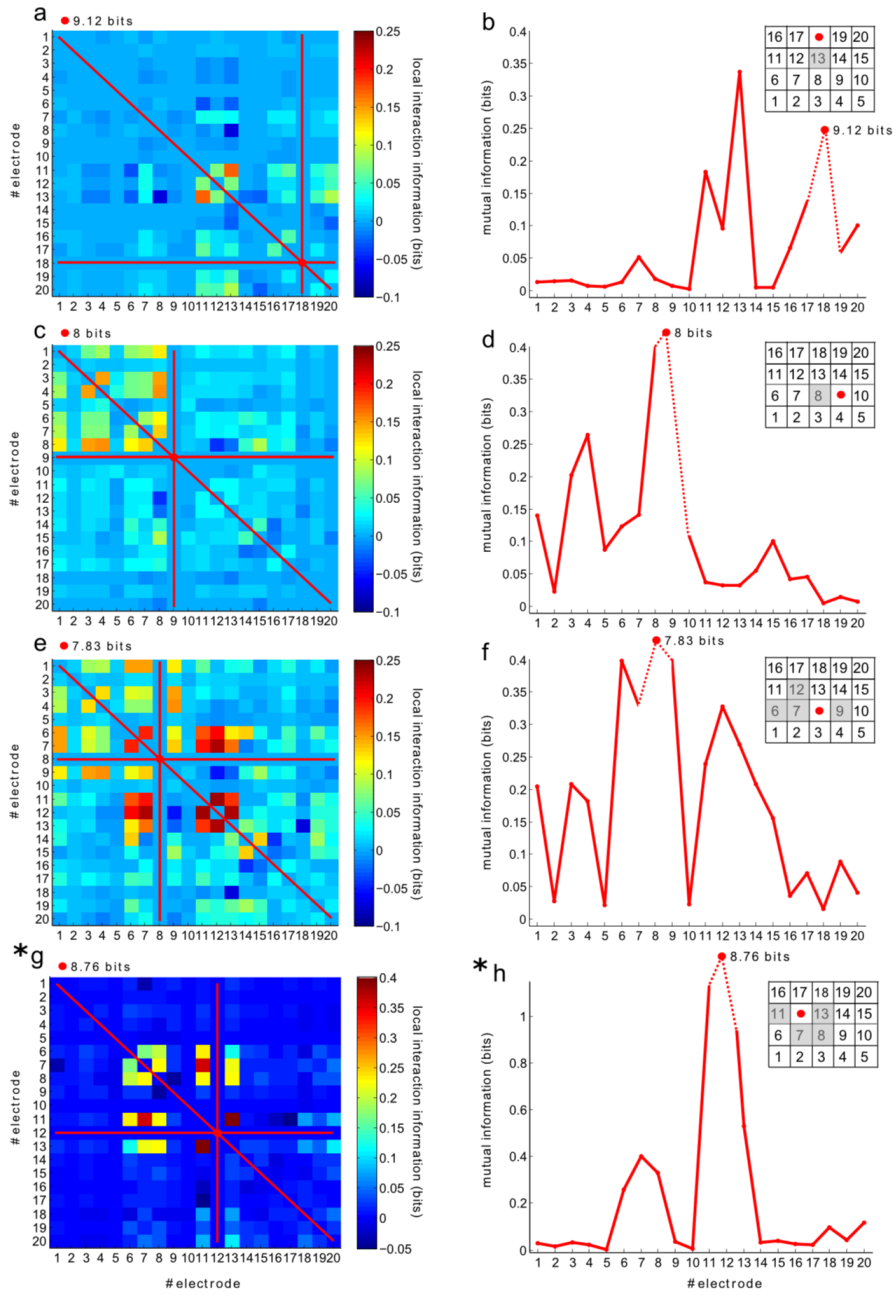


Figure 3.2: **Structure of the interaction information in epilepsy based on human electrocorticography data.**

Figure 3.2: **Structure of the interaction information in epilepsy based on human electrocorticography data.** Positive values of II indicate R, whereas negative values indicate S. The 2D plots of II were obtained by varying two variables but keeping one of them fixed. In particular, we fixed the electrode with **a:** maximum entropy (that for this particular case was coincident with the electrode with maximum betweenness) **c:** minimum entropy **e:** maximum degree (the hub, for this particular case was coincident with the electrode with maximum clustering coefficient). **g:** electrode number 12, as a representative belonging to the resection area. **a,c,e,g:** red lines correspond to the mutual information between the electrode that was kept fixed and the rest of electrodes in the grid. Indeed, as shown in Appendix, II is coincident with the mutual information when two variables are equivalent in the triplet. The solid red circle is the Shannon entropy value of the electrode that was fixed (coincident with II(X,X,X)). **b,d,f,h:** Same red lines as in panels a, c, e, g. Dashed lines have been introduced to show when the Shannon entropy value is much bigger than the values of mutual information. Electrocorticography grids are also plotted to show that similar values of mutual information were clustered within a geometrical similar region of the grid (in gray we plot the values of mutual information larger than 0.3 bits). Note that while II can be either positive or negative, the mutual information is strictly positive (when it is zero, statistical independence is indicated). **g,h:** (*) Different scale.

distribution, the organization of S surrounded them, an observation that was even clearer when II was calculated under the assumption of non-Gaussian data (figure 3.4). The pattern described by the Shannon entropy was more dispersed, and thus, less related to the epileptic zone.

Next, we asked whether the relationship between S/R and LSI (a proxy of the epileptogenic zone) preserved across different brain rhythms. Figure 3.5 shows 2D plots of II across different frequency bands, keeping fixed one of the electrodes corresponding to the resection area. From top to bottom in figure 3.5, the lower the panel, the fastest the rhythm was. Thus, straightforward from figure 3.5, II increased for faster rhythms – beta (14-26 Hz) and gamma (26-100 Hz) bands, the two lowest panels – in comparison to slower ones.

Regarding R and S across frequency bands (figure 3.6), R had a stronger contribution to high-frequency beta and gamma bands (in orange and brown), while both bands showed a similar spatial

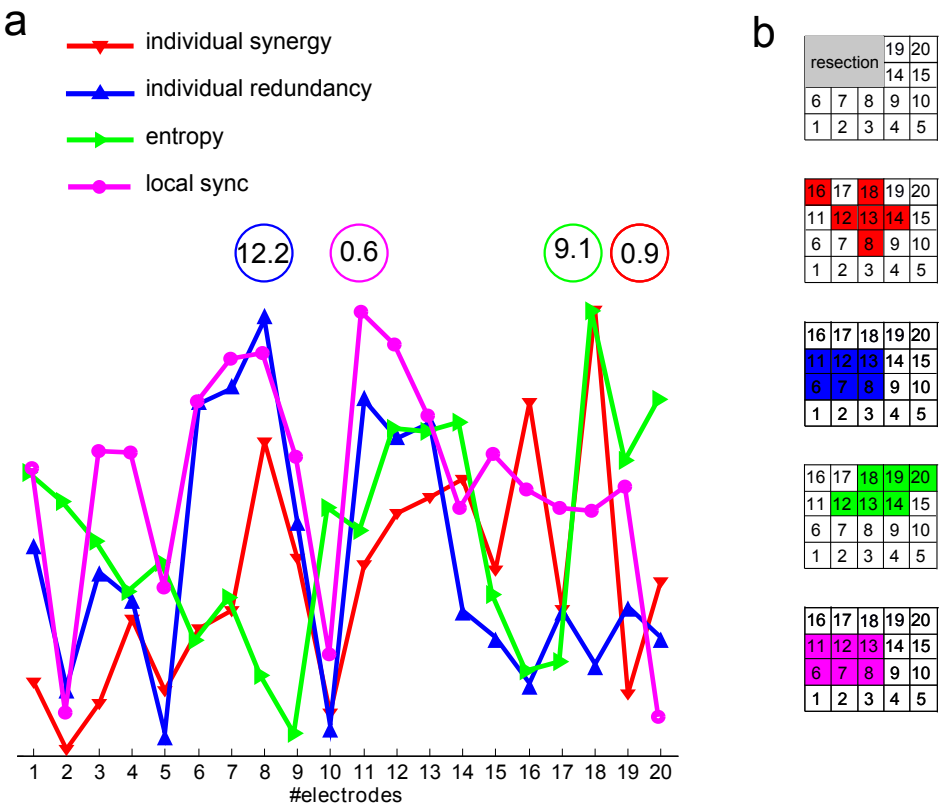


Figure 3.3: **Synergetic and redundant interactions in epilepsy from human electrocorticography data. a:** Varying $\bar{Z}$ (as explained in the methods), we can sum all the negative values of $II(X, Y, \bar{Z})$ to obtain the individual S (red) and similarly, the positive values of $II(X, Y, \bar{Z})$ to achieve the individual R (blue). In green, we plot the Shannon entropy for each electrode (i.e.: $II(X, X, X)$, see Appendix for further details) and in magenta, the LSI as measured in [144], summing the absolute value of the correlations between each electrode and its neighbouring electrodes in the grid. Note that for illustrative purposes the four measures are represented in an arbitrary scale. We plotted the maximum values for each measure in coloured circles. **b:** The six maximum electrode values for each of the measures plotted in panel a. In addition, we also plotted the resection area in gray, in this case from a patient in which the seizures disappeared after surgery.

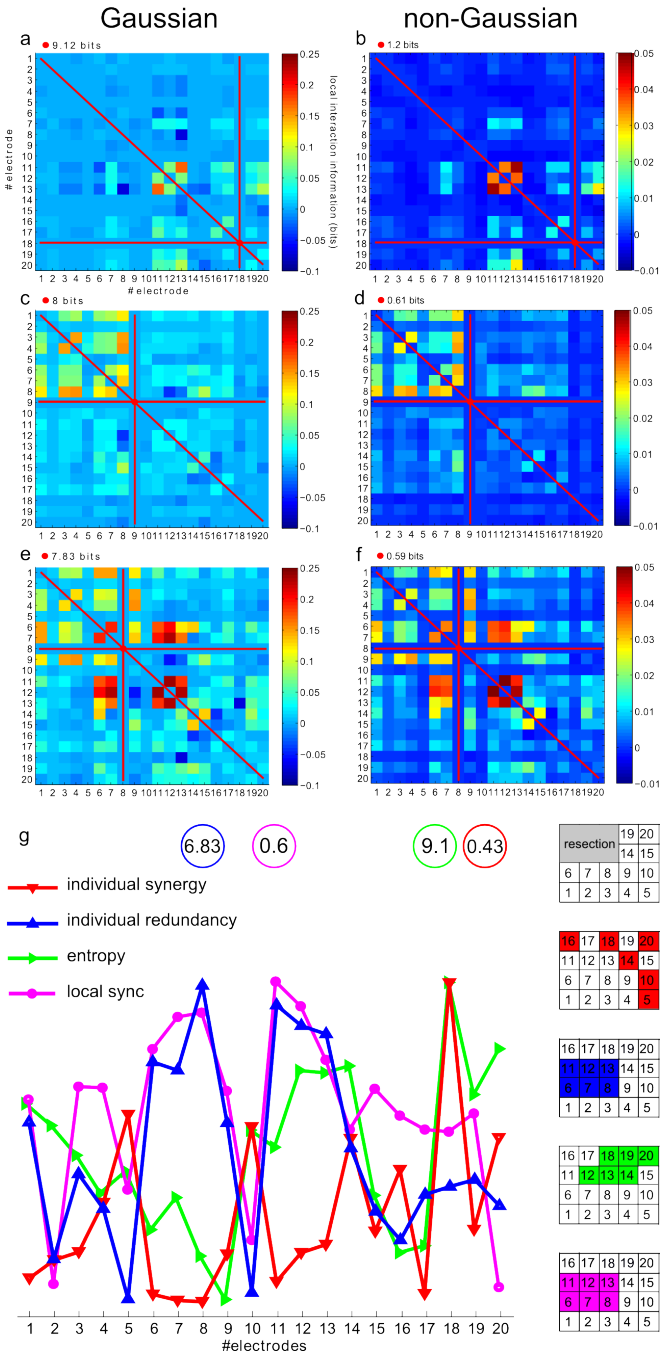


Figure 3.4: **Comparison between the Gaussian and the non-Gaussian assumptions.**

Figure 3.4: **Comparison between the Gaussian and the non-Gaussian assumptions.** Panels a, c and e have been plotted again from figure 3.2 for ready comparison. The interaction information obtained when keeping the electrode fixed with: **a,b:** maximum entropy; **c,d:** minimum entropy **e,f:** maximum degree (the hub that in this particular situation is coincident with the electrode with the highest clustering coefficient). **b, d, f:** The scenario for non-Gaussian data does not change qualitatively with respect to the Gaussian assumption. **g:** As in figure 3.3 but assuming a non-Gaussian distribution. Note that the same pattern is observed for R whilst some differences are found for S. Now, the statement of R and LSI having a similar spatial grid, and S surrounding R, is more clear than for the Gaussian case.

distribution, coincident with the LSI that is known to match the epileptogenic zone. By contrast, the low delta and theta bands had a stronger contribution to S (dark and light blues). Importantly, the spatial distribution of S differed considerably from that of R, and while the activation of R matched the epileptogenic zone (i.e., LSI) at high frequencies, S surrounded it and contributed more at low frequency bands.

In terms of the robustness of our conclusions across subjects, figures 3.2-3.6 are data from one of the patients with Engel I, but similar results were observed for the other patients with the same Engel I outcome. Indeed, figure 3.7 shows the total amount of R inside the resection area and the total S outside the resection area. For Engel I patients, where the resection area was accurate and patients suffered no further crises, the patterns identified were robust, unlike those from the Engel III patient. This is better captured when the ratio of these quantities is considered, with R within the resection area and S organized across areas surrounding it (see figure 3.7). In addition, the total R of the Engel III patient is much higher than that of the other three Engel I patients.

## 3.4 Discussion

Studying the interactions among variables in triplets, such as that captured by II, goes beyond bivariate and multivariate studies of

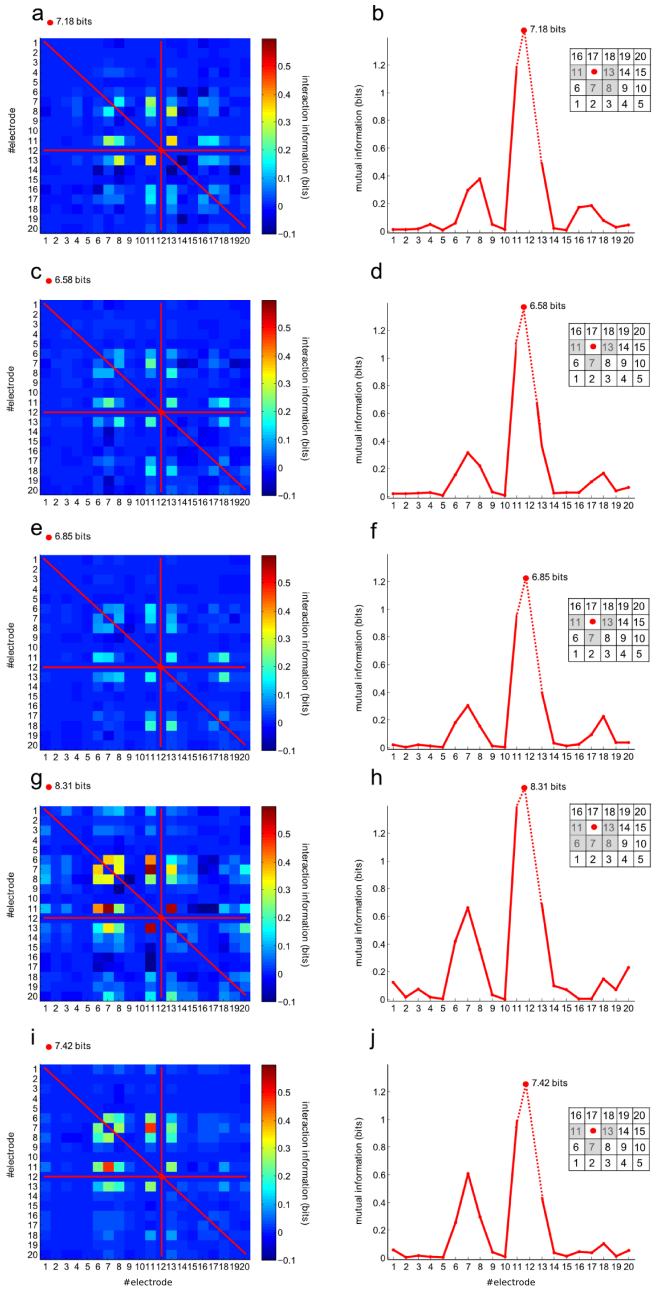


Figure 3.5: **Structure of the interaction information in epilepsy at different frequency-bands obtained from human electrocorticography data.**

Figure 3.5: **Structure of the interaction information in epilepsy at different frequency-bands obtained from human electrocorticography data.** As in figure 3.2, we plot II keeping one electrode belonging to the resection area fixed across the different frequency bands: **a,b** delta (1-4 Hz) **c,d** theta (4-7 Hz) **e,f** alpha (7-14 Hz) **g,h** beta (14-26 Hz) and **i,j** gamma (26-100 Hz). One can see how the values of II are higher at $\beta$ and $\gamma$ bands. **b,d,f,h,j:** Similar to figure 3.2, we plot in gray the values of mutual information larger than 0.3 bits.

interacting variables. Although this method has previously been applied to other fields, to the best of our knowledge we are unaware of similar studies in epilepsy. We have continued earlier studies that took advantage of Granger causality [91] to assess the effects of S and R on epileptic data [130, 214, 194], and we calculated the II in electrocorticography data from epileptic patients who underwent surgery. In particular, we paid special attention to the data from patients that achieved the best possible outcome following surgery and who experienced no further seizures (Engel I patients). Indeed, by taking the resection area in these patients as a reference, we addressed the patterns of II near to the epileptogenic zone, the area essential for seizures to propagate.

We calculated the II in two situations, assuming that the data adopts either a Gaussian or a non-Gaussian distribution. While the former permits an analytical derivation of the II, the non-Gaussian distribution is more general and it is not easy to choose the most appropriate method to estimate probabilities. We are aware that we have applied the simplest method to generate histograms (binning and counting frequencies), as the number of data points was considered to be sufficiently large to guarantee an appropriate sample [29]. Nevertheless, other methods could also be used to estimate probability density, such as kernel estimators, the nearest neighbour method, orthogonal series estimators, etc. (see [27] for further details).

Nevertheless, by assuming Gaussian and non-Gaussian distributions we obtained qualitatively similar results. That is, although data are non-Gaussian across segments, electrodes and patients (figure 3.8, in addition of obtaining p values of zero after a Kolmogorov-

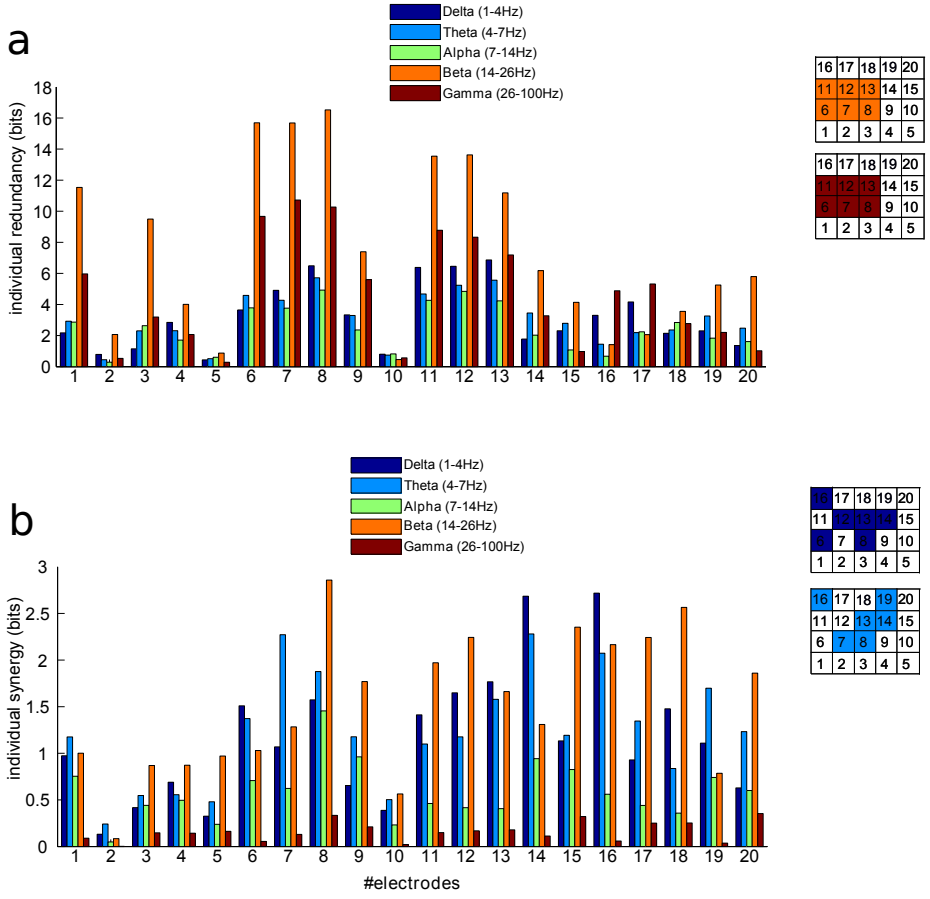


Figure 3.6: **Redundancy and synergy across frequency bands. a:** R receives a larger contribution from the high-frequency beta and gamma bands (orange and brown), with both bands showing a similar spatial grid map overlapping with the epileptogenic zone (cf. figure 3.3). **b:** The low delta and theta made a stronger contribution to S (dark and light blue). Importantly, the spatial distribution of S is quite different from that of R: whilst the activation of R overlaps the epileptogenic zone and it is represented by high frequencies, S tends to surround this region and it operates in low frequency bands.

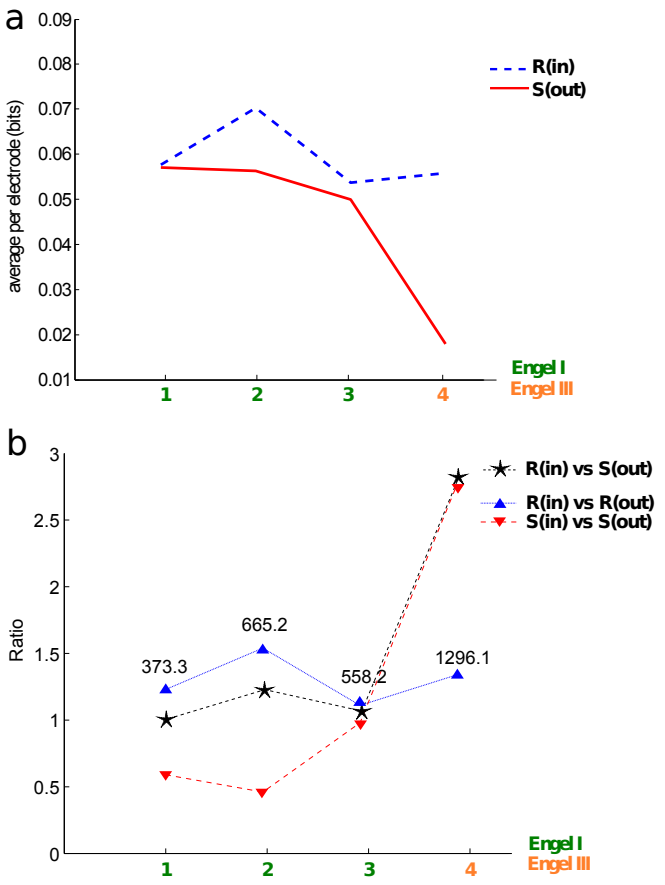


Figure 3.7: **Validation across patients. a:** We plotted the average values of R for each electrode inside the resection area (blue dashed line) and S outside the resection area (red solid line) – the total amount of R inside and S outside divided by the number electrodes in the resection area –. This was done for 3 patients with Engel I (where the resection area matched or exceeded the epileptogenic zone) and for 1 patient with Engel III (to illustrate at least one case where the resection area did not match the epileptogenic zone). The Engel I and III patterns were quite different. **b:** The ratio between R inside the resection area –R(in)– divided by that of S outside that area –S(out)–, and both the ratios of S inside –S(in)– divided by S(out) or R(in) divided by R(out). There are clearly important differences between Engel I and Engel III patients, corroborating the dynamic pattern found: R within the epileptogenic zone and S organized in the surrounding region. The total R for each patient is also represented (i.e., numbers 373.3, 665.2, 558.2 and 1296.1) whereby the Engel III value is much larger than that for the Engel I cases.

Smirnov for normality test), the Gaussian assumption captures the non-Gaussian character of II quite well. Indeed, although some differences were found with respect to S, the same pattern was observed for R. Importantly, the non-Gaussian assumption was consistent with the Gaussian one in situating S outside the R area.

It is important to emphasize that our aim was to provide a more complete characterization of the informational pattern in the neighbourhood of the epileptogenic zone. Accordingly, the LSI has already been shown to satisfactorily localize the epileptogenic zone [144]. What we found here was that R matched the LSI while S was evident in its surroundings for patients with Engel I. This pattern was particularly clear for II when assuming a non-Gaussian distribution, which is in accordance with the organization of local intracortical interactions that, under the influence of local inhibitory circuits, are responsible for controlling runway excitation [142]. The matching between LSI and R was less clear for a patient with Engel III (figure 3.9).

Finally, we studied II (including S and R) in relation to interictal activity. However, recent results suggest it might be of interest to carry out further studies into the application of II to pre- and postictal activity [207], thereby assessing how the structure of R and S changes with ongoing seizure dynamics.

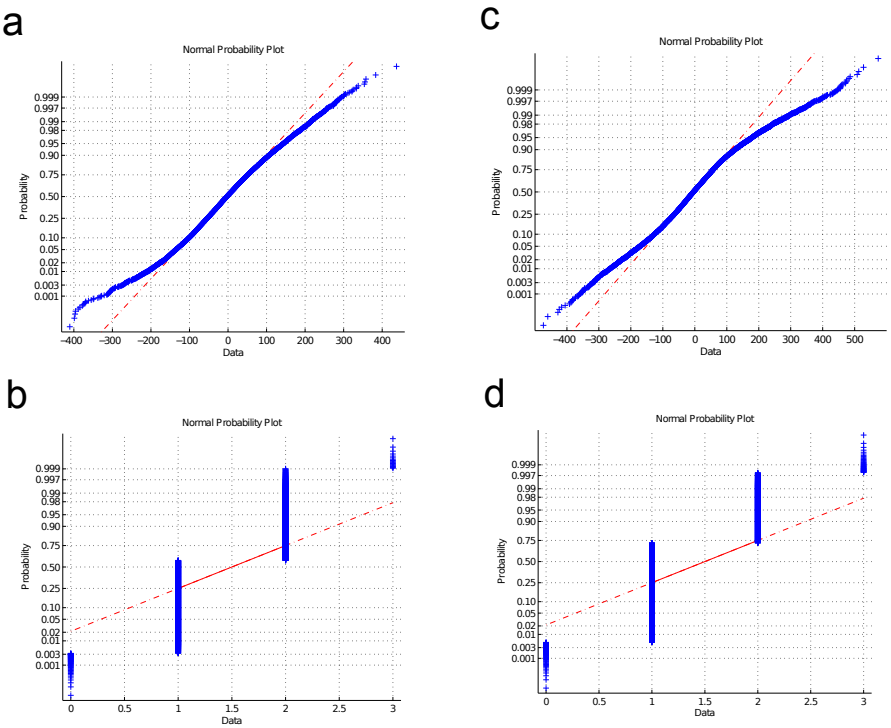


Figure 3.8: **Evidence of non-Gaussianity in the data.** Normal probability plots indicate strong data deviation from Gaussianity (the more the data do not follow the straight line, the more non-Gaussian is). **a:** data corresponding to one subject, one electrode and one of the segments used to average and calculate II (and therefore, R and S). **b:** Same data that in a, but binned to 4 states. Non-gaussianity also applied to binned data. **c,d:** Similar to panels a and b, for the same subject but different electrode. The same results are valid across subjects.

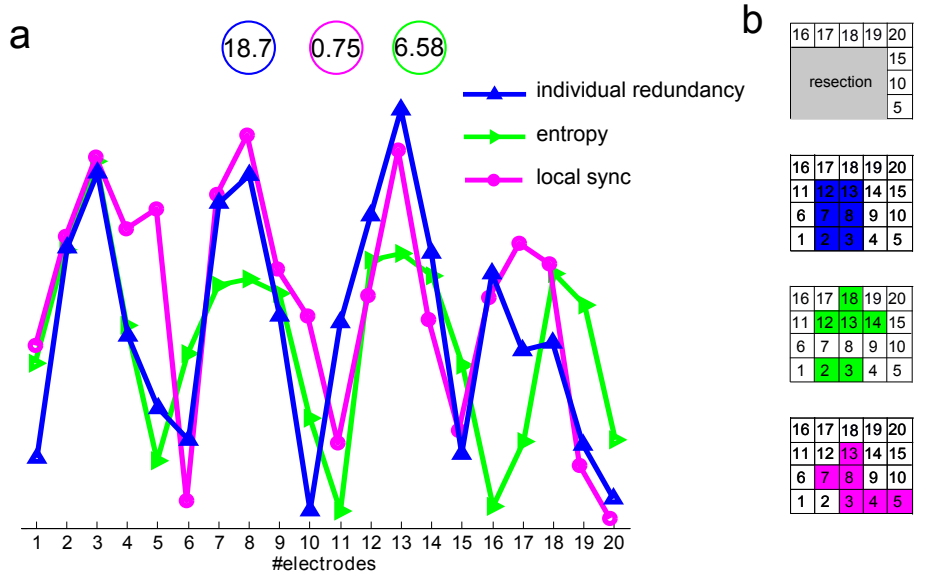


Figure 3.9: **Redundant interactions in epilepsy from human electrocorticography data for a patient with Engel III.** Similar to figure 3.3 but for a patient with Engel III, i.e., with patient's seizures not disappearing after surgery. Observe that the three electrodes 3, 8 and 13 have maximum LSI (local sync, an index which was proven to match the epileptogenic zone in [144]) and also have maximum R.

## 3.5 Appendix: Properties satisfied by the interaction information

Directly from equation (3.5), one can derive important properties which are particularly relevant to the present work:

- *Circulation*: II is invariant to any possible permutation in $(X, Y, Z)$ and thus, the evaluation of II gives the same result for each of the following six situations $(X, Y, Z)$, $(X, Z, Y)$, $(Y, X, Z)$, $(Y, Z, X)$, $(Z, X, Y)$, $(Z, Y, X)$. The proof is straightforward just using the Eq. (3.5).

- *Mutual information limit*: in the case of triplets with only 2 distinct variables, i.e.: $(X, Y, X)$, $(X, X, Y)$, $(Y, X, X)$, $II = I(X, Y)$ is satisfied, thus, II is equal to the mutual information between the two distinct variables. The proof of this is straightforward as, by definition, the entropy satisfies that $H(X, Y, Y) = H(X, Y)$ and that $H(Y, Y) = H(Y)$. Thus, the definition of the mutual information given in Eq. (3.3) provides the proof.

- *Shannon entropy limit*: in the case of triplets with three equal variables, the equality of II$= H(X)$ holds, i.e.: II is equal to the Shannon entropy of the variable. The proof of this is straightforward and is similar to the one derived for the mutual information limit.

# Chapter 4

# Multimodal connectivity analysis: Preliminary results with limited subjects number

In previous chapters we addressed the study of epilepsy using solely electrophysiology data (ECoG). In this chapter, we will also add the processing of structural and functional MRI data among deep electrodes electrophysiology. Thus, providing a different scope of analysis and exploring these different brain networks.

Here, we collected brain images and electrophysiology from epilepsy participants (N=5) to build functional (resting-state and deep electrodes) and structural (tractography) connectivity matrices, three datasets combined as connectivity descriptors.

We then explored the data using two approaches: modular (looking for similar structures across modalities) and single link (focused in link-to-link similarities inside the networks). The methodology developed for this chapter is completely exploratory, since to our knowledge, this multimodal exploration has no precedents.

## 4.1 Introduction

Epilepsy is a disease that has been deeply studied and the most common and harmless (non-invasive) method of exploring a patient has been scalp electrophysiology (EEG). As explained in previous chapters, patients not responding to drug treatmeant are susceptible of being screened for a resection. Usually, this presurgical evaluation consist in placing intracraneal electrodes close to the suspected area of epileptogenic activity (foci).

Although is not common in clinical practice, some studies in the literature have studied (i)EEG-fMRI combination (both simultaneous and non-simultaneously). Here, in addition to intracraneal electrodes, patients are explored with a fMRI scan at rest [203, 60, 206].

Previous publications have addressed the study of epilepsy by means of separate or combined analyses of FC (BOLD signal or electrophysiology), but none of them has proposed to use DWI combined with deep electrodes. In this work, we use a non-simultaneous iEEG - fMRI dataset, plus valuable DWI data, being able to explore brain's structure. To the extent of our knowledge, this is a unique dataset and there are no previous publications with this kind of triple multimodal data.

Two key motivations guide the present work: Firstly, to discover if there is any matching between the triplet FC-SC-EL i.e. fMRI-tractography-electrophysiology. Secondly, to explore the organization patterns of the different connectivity matrices, looking for modules that could match the epileptogenic area.

## 4.2 Methods

### 4.2.1 Participants

Participants were recruited from Ruber International Hospital (Madrid, Spain). This project was conducted by PI Paolo Bonifazi. All patients (N=5) were drug-resistant patients who underwent surgery. After receiving the approval of the Ethics Committee at Ruber In-

ternational Hospital, patients provided their informed consent to be evaluated intraoperatively with a deep electrodes. A presurgical evaluation was carried out according to the protocol used at Ruber International Hospital and all the data was anonymized.

### 4.2.2 Electrophysiology acquisition

All of the analyses carried out here were performed retrospectively and thus, tailored lobectomies were not based on the results discussed here.

An intraoperative deep-electrophysiology session was recorded for 8-24 hours using different deep-electrodes setup, depending on the subject's suspicious areas of being epileptogenic focus, preprocessing with a 50 Hz notch filter. As the suspected epileptogenic foci was located in different areas for each of the explored patients, localization of deep electrodes was distinct, being for each patient, differing for each patient in the amount of electrodes and contacts. Twelve artifact-free epochs of inter-ictal activity lasting up to 1 min were selected per subject by visual inspection and exported to raw text files using Neuroworks (Natus Medical Inc.). All post-processing analysis was performed using Python's NumPy library [205].

As explained in Chapter 2 for electrocorticography, from the perspective of signal processing, it is important to emphasize the importance of deep-electrophysiology studies in contrats to those based on scalp electroencephalography. In the former, signal quality is much better, with a signal to noise ratio about 21 to 115 times greater, which makes these two modalities quite distinct [197]. In addition to this, electrocorticography is not possible to identify with sufficient spatial depth the deep epileptogenic zones, while deep electrodes can.

### 4.2.3 Electrophysiology preprocessing

*Frequency-band analysis*

Electrophysiological signals were filtered within different frequency bands using a zero-phase digital filter. In particular, we used the NumPy's *filtfilt* function to filter the following standard bands for

brain electrophysiology: delta (0.5-3 Hz), theta (3-7 Hz), alpha (7-13 Hz), beta (13-30 Hz), gamma (30-70 Hz) and gamma-high (70-250 Hz).

*Active State analysis*

The so called Active State (AS) is a transformation of the electrophysiology signal into a binary one, accounting for periods where the signal has prolongated peaks. Thus, when building the correlation matrix, we are just relating states of high activation in populations of neurons. The AS connectivity matrices were also computed for all filtered bands.

### 4.2.4 Image acquisition

Magnetic resonance imaging (MRI) scanning was performed on a Siemens 3T Magnetom Trio MRI scanner with a 12-channel matrix head coil.

*Anatomical data:* A high resolution T1 image was acquired with a 3D magnetization prepared rapid acquisition gradient echo (MPRAGE): repetition time [TR] = 2300 ms, echo time [TE] = 2.98 ms, voxel size = 1 1 1.1 $mm^3$, slice thickness = 1.1 mm, field of view [FOV] = 256 240$mm^2$, 160 contiguous sagittal slices covering the entire brain and brainstem.

*Diffusion Tensor Imaging:* A DTI SE-EPI (diffusion weighted single shot spin-echo echo-planar imaging) sequence was acquired with the following parameters: [TR] = 8000 ms, [TE] = 91 ms, voxel size = 2.2 2.2 2.2 $mm^3$, slice thickness = 2.2 mm, [FOV] = 212 212 $mm^2$, 60 contiguous sagittal slices covering the entire brain and brainstem. A diffusion gradient was applied along 64 non-collinear directions with a b value of 1000 s/$mm^2$. Additionally, one set of images was acquired without diffusion weighting (b= 0 s/$mm^2$).

*Resting state functional data* was acquired over a 10 minute session using the following parameters: 200 whole-brain gradient echo echo-planar images with [TR/TE] = 3000/30 ms, [FOV] = 230 230$mm^2$, voxel size = 2.5 2.5 3.1$mm^3$, 80 80 matrix, slice thickness = 2.8 mm, 50 sagittal slices, interleaved in descending order.

### 4.2.5 Image preprocessing

The preprocessing protocol and pipeline for all modalities is publicly available at `https://github.com/compneurobilbao/ruber`. All the data was converted to BIDS format

*Quality checking of the data:* Quality checking of the fMRI and T1 data was performed using MRIQC [75]. Due to problems with movement artifacts, 1 patient was discarded, thus having 4 subjects in total for the analysis.

*Functional MRI:* Functional data were preprocessed using FMRIPREP [76], a Nipype [89] based tool using ANTS, FSL and Nilearn. For more details of the pipeline see `https://fmriprep.readthedocs.io/en/latest/workflows.html`.

Finally, FC matrices were calculated using Nilearn [1] by obtaining the pairwise Pearson correlation coefficient between the resting fMRI time series after being removed effects of framewise displacement, white matter and global signal and rotation effects. Exclusion criteria was based on not having more than 20% of the time points with a frame wise displacement greater than 0.5, and those over the threshold were scrubbed. Then, we separated the full FC data in FC raw, FC positive values and FC negative values.

*Diffusion Tensor Imaging:* DWI preprocessing was performed using a slightly modified pipeline of Pypes [176]. Eddy current and head motion correction algorithms. First, an eddy current correction was applied to overcome the artifacts produced by variation in the direction of the gradient fields of the MR scanner, together with the artifacts produced by head motion. A deterministic tractography algorithm was used to build the connectome. Finally, we created two SC matrices with the following criteria: SC raw, accounting the total number of streamlines between region pairs, and SC binary, just accounting if such a link exists or not between region pairs.

### 4.2.6 ROI selection

For each patient, using a T1 with implanted electrodes (1x1x1 mm voxel-size), all contacts were positioned and tagged manually. The

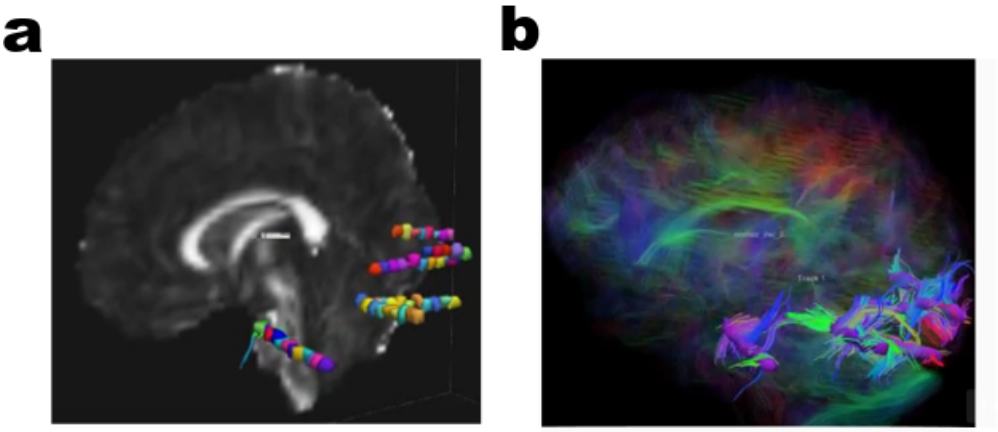


Figure 4.1: **ROI generation procedure a:** A ROI of 3mm radious is created for each contact. ROIs were after superposed over a structural image. Notice several intracraneal electrodes located in the occipital area. ROIs are not isometric, due to transformation deformations when going to DWI space from T1. **b:** Same subject, with the tractography reconstructed and highlighted the streamlines crossing specific ROIs. These streamlines were accounted for structural connectivity.

procedure to be as precise as possible consisted in selecting the voxels with the deepest and outer electrodes and interpolating the position of the rest accordingly. Then, taking the position of each contact as its center, 3mm radius spheres were created as ROIs for each contact (1mm and 2mm spheres were also tested, resulting in poor connectivity results, as they were not big enough).

Following this procedure we built matrices ranging from 24x24 to 64x64 (depending on the number of electrodes and contacts per subject) we built SC (by counting the number of white matter streamlines crossing all region pairs), FC (accounting for correlation between BOLD signal from region pairs), DC (Distance Connectivity, based on euclidean distance between contacts) and EL matrices (electrophysiology, with band filtering and both AS and raw and calculating the correlation between the signals belonging to region pairs). All matrices are symmetric, where connectivity from i to j is equal to that from j to i.

### 4.2.7 Module-wise and link-wise analysis

Two main approaches were carried in this study, the module-wise analysis looking for the organizational patterns of the matrices (trying to match epileptogenic area) and the link-wise analysis to explore relationships between different acquisition types.

In short, we have 20 connectivity matrices per subject: FC, FCPOS and FCNEG (respectively, separating positive and negative values in the correlation matrix), SC and SCbin (tractography), DC (distance between contacts) and, finally, 14 different matrices of EL (electrophysiology; previously described 7 frequency bands and 2 types, raw and Active State). Although most of these matrices were quickly discarded, as they were not adding information compared to others or just not showing relation to the rest, we tested all of them and made a complete analysis for all the cases.

## 4.3 Results

### 4.3.1 Link-wise and node-wise analysis

The aim of this analysis was to prove a match between different modalities of acquisition. We calculated the correlation between matrices (link by link) for each subject, resulting in a 20x20 matrix per subject, where each index accounted for each connectivity type and averaged over all subjects, resulting in figure 4.2.

#### Resection area matching

Once detected strong similarities between EL and FC, we decided to give a close look into the electrodes marked as candidates for resection from the MDs and compare them to the areas that are not candidate for resection, figure 4.3.

Figure 4.4 shows the specific single link relations between EL (beta) and FC.

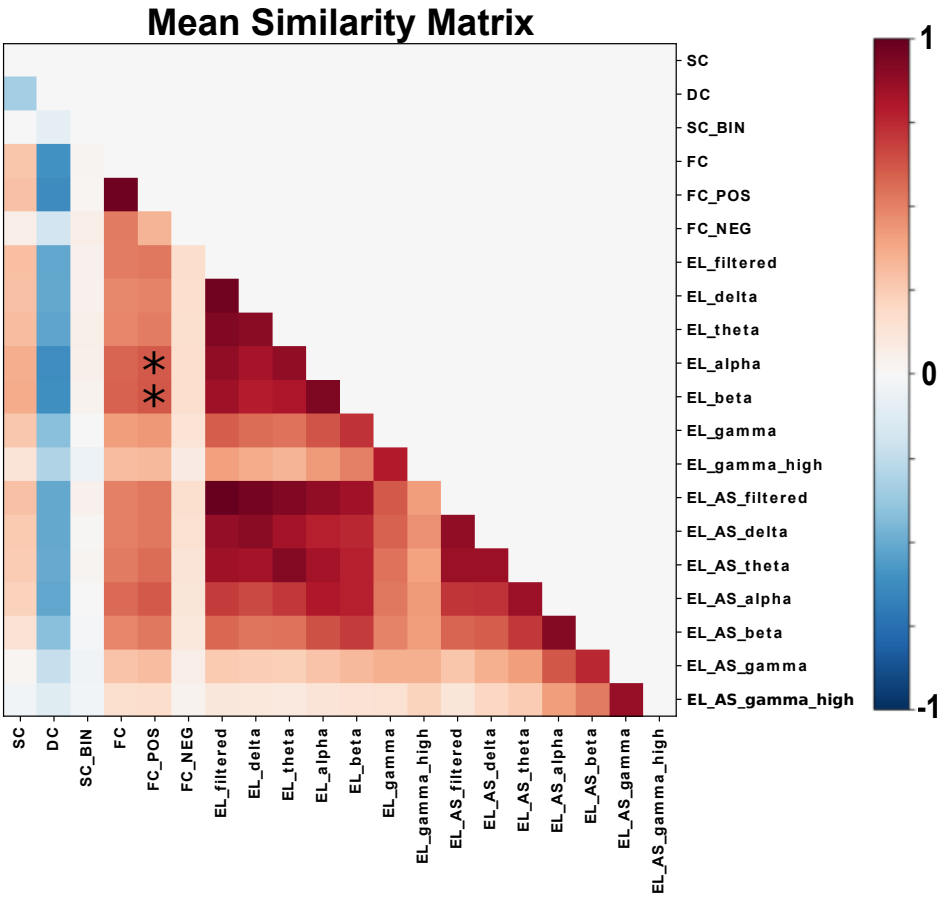


Figure 4.2: **Mean connectivity similarities over subjects** Here we show the mean correlation values between pairs of links. Distance Connectivity (DC), was the only metric negatively correlated with the rest, thus, explaining that the higher the distance between links, the smaller the correlation between them. Active State (AS) and electrophysiology raw signals did not show big differences, possibly due to short time windows. Interestingly, fMRI functional connectivity (FC and FCPOS) and electrophysiology in alpha and beta bands showed a mean relation of 0.62 between them (marked with an asterisk).

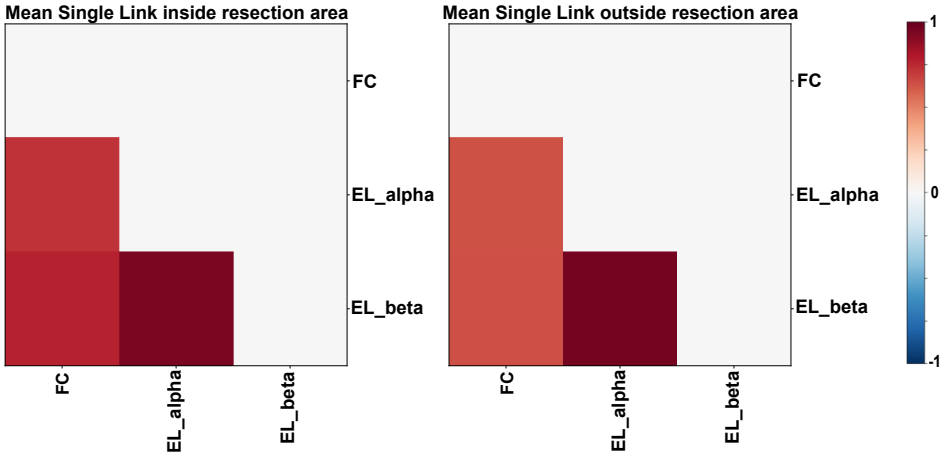


Figure 4.3: **Mean connectivity similarities inside-outside resection areas** Mean values (across all patients) over single link connectivity of FC and beta and alpha bands of electrophysiology. In average, r=0.77 inside and r=0.64 outside for beta band, showing stronger correlation between EL and FC in the candidates areas for resection. It was also higher for all individual patients.

### 4.3.2 Module-wise analysis

We performed a module-wise analysis over pairs of matrices, in a similar way as described in [69]; establishing a distance measure between links, reordering them according to a hierarchical tree in several partitions and then ordering a target matrix with the same order, to evaluate if the structures reordered in the source matrix were reproduced in the target.

The measure used to check the similarity between the new ordered partitions was the cross-modularity (also from [69]). This index was defined as the geometric mean between the modularity of the source partition (i.e., number of links inside a module of the partition divided by the number of links outside the module. Thus, robust modules having higher output), the modularity of the target partition, and the mean Sorensen similarity between modules existing in the two source and target partitions.

As the number of possible combinations is large, we are not show-

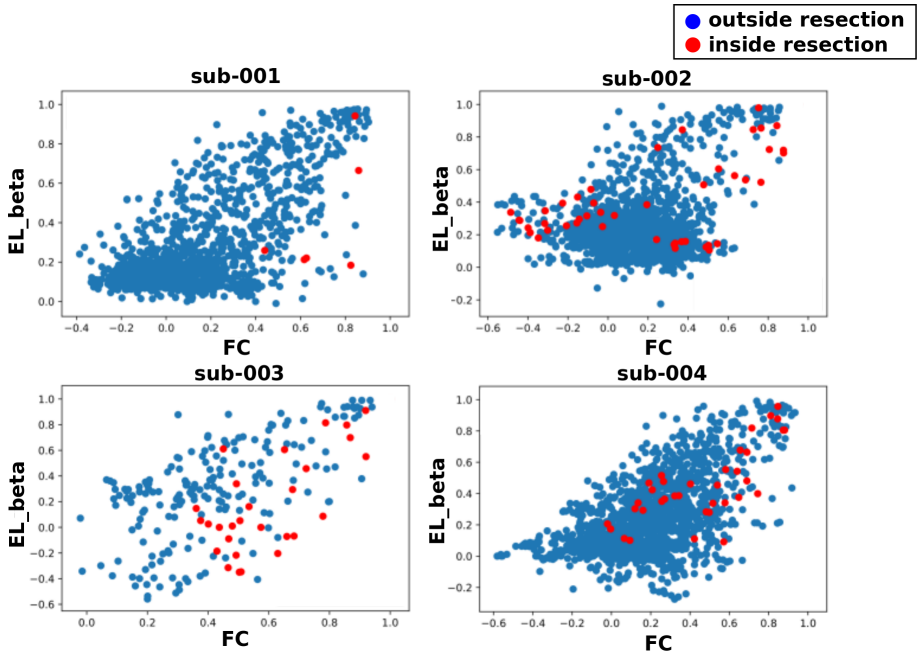


Figure 4.4: **Specific link values inside and outside resection for each subject and FC and EL (beta)** Distinguishable distributions arise across some of the subjects

ing all of them, but the ones with higher cross-modularity value cases in figure 4.5.

Taking into account these results and having the link-wise analysis results as prior, we selected the FC and EL modules in their maximum cross-modularity values with EL and FC respectively (one driving the order of the other). We found that when FC was the driver, having more and smaller modules, we encountered at least one module matching with the expected resection area in at least 60% of the contacts for 3 of the patients, an example of this in figure 4.6. Similarly, when EL (either alpha or beta filtered bands) was the driver, now existing bigger but less modules, also one module showed at least 50% of the expected contacts to be removed in surgery. SC or DC driving the ordering did not show relevant modules at all grouping candidate contacts.

## 4.4 Discussion

Firstly, we looked to link-wise relations of different (up to 20) connectivity matrices (figure 4.2). We could quickly discard several matrices that had no shared information at all or were redundant. In one side, EL raw and EL Active State matrices resulted in a very similar connectivity information, in agreement with the observation that the most active states can reproduce the point process anaylsis [198]. Moreover, we also found that the connectivity matrices such as SC or the gamma and gammahigh filtered bands, resulted in no relevant shared information with other connectivity matrices at all. We also found that the Distance Connectivity (DC) matrix was related with negative correlation values, thus showing that functional and structural connectivities are inversely correlated with the distance.

The link-wise analysis also remarked strong similarity between fMRI and electrophysiology dynamics. Particularly, FC (and FC-POS) and EL (alpha-beta bands) connectivity matrices had a high correspondence. Having the information of presurgical exploration provided by the medical doctors with regard to suspicious epileptogenic area, we could show the response of both acquisitions inside

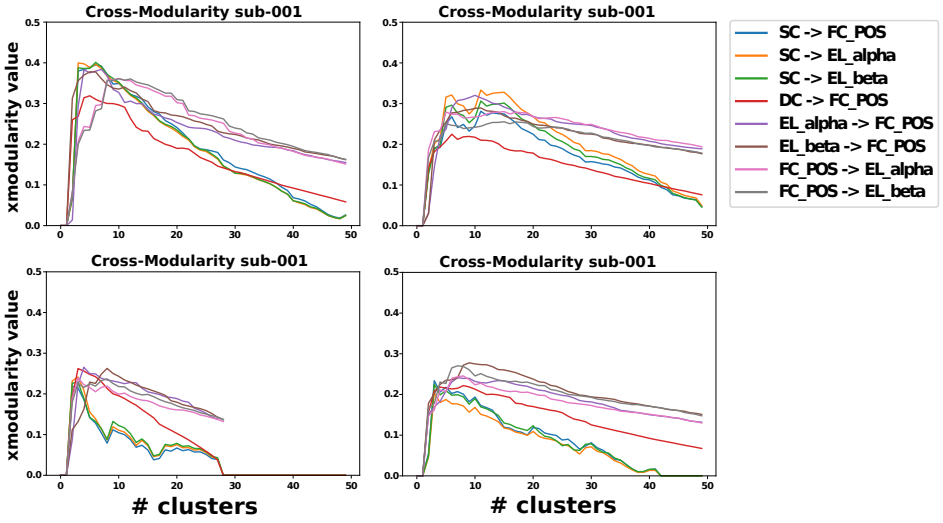


Figure 4.5: **Cross-modularity values between sources and targets reordered matrices** Overall, 3 cases can be distinguished: **SC driving:** SC driving the ordering of both FC and EL connectivities is an example of high modularity with few and big modules with a fast decay in cross-modularity values as the number of modules increases. **EL and FCPOS driving each other:** Also having high cross-modularity values, reflecting that one could be driver of the other, but achieving the maximum values later than the SC driver case. Also, this maximum similarity value, is in common with the number of electrodes implanted in each patient. The decay of similarity values is not as pronounced as the previous case, i.e., the FC-EL similarity is maintained across different partitions. **DC driving FCPOS:** This is an special case of distance connectivity matrix having high similarity values when driving FCPOS matrix, with a fast decay, only being mainteined in maximum values when number of modules is equal to number of electrodes.

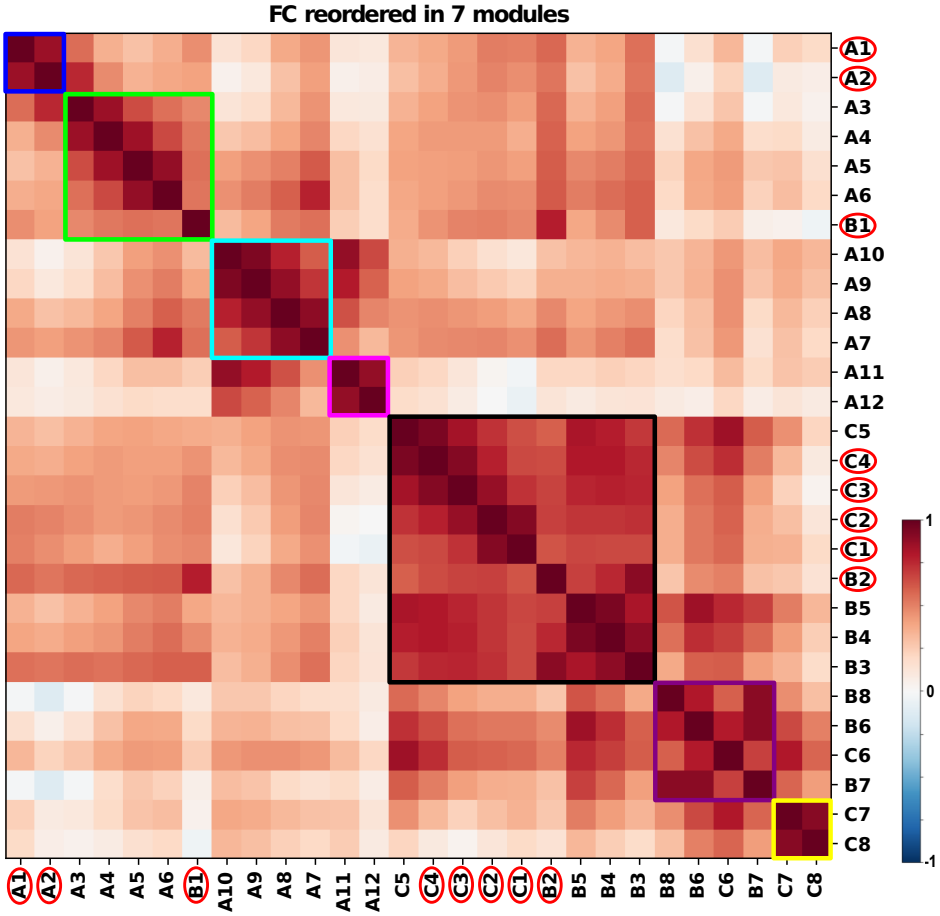


Figure 4.6: **Modularity analysis in a given subject maximizing the number of electrodes selected for resection in modules** The figure shows the reordering of the FC correlation matrix into 7 modules. The module highlighted in black has 5 out of 8 electrodes marked for resection (circled in red). Another 2 electrodes form their own module, in blue. Notice that all FC correlation values are high between electrodes.

and outside the expected resection areas. Our analysis showed that contacts inside expected resection area were more related in the FC-EL binomial (figure 4.3), this accounts for brain-areas that are more active in both fMRI and electrophysiology inside epileptogenic areas, what might be related to epileptogenic areas consuming more oxigen in comparison to the rest [200, 60].

Secondly, we performed a modular approach to understand the organization in different modules containing the electrodes. As explained in Methods, we reordered a connectivity matrix (target) in the same way as the one previously ordered (source) after calculating a distance over every pair of links in the matrix and measuring the similarities between the two resulting matrices using the cross-modularity. Results were diverse (figure 4.5); SC as driver (source) showed a high cross-modularity for low number of modules, then having a big and fast decay as possible indication of similar structure of big modules, but increasing the number of modules the matrix becomes very different to EL and FC. In the other hand, both FC and EL obtained high values of matching, but showing two interesting patterns. The first one is related to the maximum value of cross-similarity, coincident with the number of electrodes implanted, in agreement with EL data, as close contacts have similar electophysiological patterns, but FC is not related to this activity. Furthermore, the second pattern is that the decay of similarity when having more modules is much slower as compared to the case of SC driving, showing that the similarity of EL and FC is maintained across different partitions. To end up with the module-wise analysis, we looked to the maximum values of cross-modularity across subjects and looked for specific modules matching the possible resection area, finding modules containing at least 50% and 60% of the contacts.

To our knowledge, our multimodal approach to explore connectivity of epileptic patients have not been previously shown. Only very few studies have made use of connectivity metrics to study the effect of intracraneal electrophysiology and fMRI [200, 60], but this is the only one that adds the study of DWI. These preliminary findings remark the possibilities that fMRI can be used to detect areas of high

BOLD activity non-invasively (i.e., not using intracraneal electrodes, as fMRI can be a proxy) if MD's have priors or are suspicious of a given area of the brain.

## 4.5 Limitations of the study

We are aware that the present study has some limitations, even though there is also possible to solve some of them; the small sample make our conclusions to loose generality.

One of the main values of the project was to use DWI to explore both possible similarities between structural and functional connectivity and to measure the reorganization of the tracts after the resection of the epileptogenic area. We have found that neither single-link nor module analysis has obtained significant similarities between SC and any of the other connectivity matrices. This could be due to spacial proximity between contacts and electrodes and the fact that structural connectivity is not as dynamical as functional.

# Chapter 5

# Effective connectivity analysis in Resting State Networks

In this chapter we will use Principal Component Analysis to analyse more components of the brain within a given region and we will compute a new measure of information flow that uses these extra components. This technique will be used to study the information flow between Resting State Networks of the Brain in Alzheimer's Disease (AD).

## 5.1 Introduction

The overall brain dynamics generated at rest can be decomposed as a superposition of multiple activation patterns, the so-called Resting State Networks (RSNs). Becoming a fundamental characteristic of brain function, RSNs are a pivotal element for understanding the dynamics and organization of the brain basal activity in health and disease [157, 80, 154, 155, 156]. RSNs emerge from the correlation in signal fluctuations across brain regions during resting state, a condition defined by the absence of goal-directed behavior or salient stimuli. Despite the simplicity of the context in which these brain activity

patterns are generated, RSNs dynamics is rich and complex. Different RSNs have been associated to specific cognitive networks (figure 5.1) e.g. there are visual networks, sensory-motor networks, auditory networks, default mode networks, executive control networks, and some others (for further details see for instance [16] and references therein).

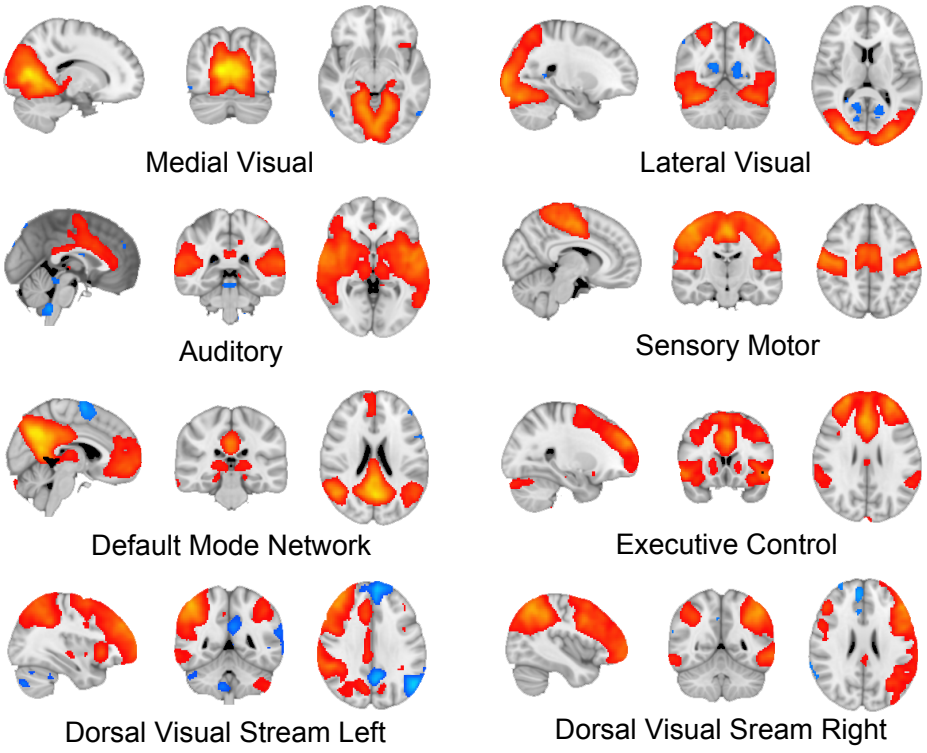


Figure 5.1: **Eight Resting State Networks associated with specific cognitive networks.**

Currently, it is well-established that a number of techniques, like Region-Of-Interest approach (ROI; seed-based), Independent Component Analysis (ICA) and Partial Least Squares (PLS), can decompose the resting state functional magnetic resonance images (rs-fMRI) to provide such RSNs [18, 17, 16, 135, 216]. Using these tech-

niques, altered functional connectivity in specific RSNs has been described in brain pathological conditions such as in patients with deficit of consciousness after traumatic brain injury [34, 141, 96, 128], schizophrenia [213, 103] and epilepsy [121]. In the particular case of Alzheimer's Disease (AD), the pathology we have addressed here, starting from the pioneer contribution showing alterations in fMRI [118], has been reported a decrease of functional connectivity in the Default Mode Network (DMN, a RSN related to memory function) and in the salience network at both early and advanced stages of the AD [92, 166, 26, 184].

Despite this emphasis on specific networks, it is important to realize that the RSNs functional-division into separate systems does not imply that the brain activity is composed of functional networks working in isolation [62]. Contrarily, the brain regions underlying the inter-RSNs relations have their independent organization and have a different function from the specific ones that each individual RSN has (for recent reviews see [79, 186]). These interactions between brain regions belonging to different RSNs have been described by means of whole-brain connectivity analysis techniques like graph analysis [188, 161, 191, 37], and more recently, where connectivity was also analyzed during different cognitive task conditions [136].

However, the analysis and interpretation of information flow (IF) between the RSNs remains an open question and has given rise to two contrasting theories attempting to interpret the resting brain activity. The functional integration theory (for review, see [216]) proposes that brain activity during resting-state requires the coordinated activity of all brain RSNs to support the reconstruction, analysis and simulation of experiences or possible scenarios to provide adaptive behavioral advantage. On the other hand, the functional segregation theory states that modality-specific mental activity (e.g. image- or language-based thoughts) is related to functional disconnection between the brain networks active during rest [65]. Therefore, resting activity would be maintained by functionally segregated inner-oriented and sensory-related cognition and the respective intrinsic and extrinsic brain networks they depend on.

The question of how different RSNs speak to each other is particularly relevant as the existence of disease-driven changes in functional connectivity between different brain networks has been reported [174, 180]. Importantly, as the disease progresses, responsible RSNs are in turn affected, and this gradual loss of functional connectivity within networks is accompanied by a loss of functional correlation between them [36]. This indicates that altered functional activity induced by a local dysfunction might influence the functioning of additional brain regions, leading to the spread of changes in brain activity beyond the network originally affected and in turn the whole-brain functional connectivity pattern [174].

Here we propose a new method to study RSNs inter communication. The method is based on the inference of IF in terms of Transfer Entropy (TE) to study Directed Functional Connectivity (DFC) between RSNs[1]. To show one potential application of this method, we apply it to a dataset of AD patients from the Alzheimer's Disease Neuroimaging Initiative (ADNI) and compared the results of inter-RSNs communication with a group of healthy subjects (remark that the method is general and can be applied to any other disease).

## 5.2 Methods

### 5.2.1 ADNI

Data used in the preparation of this work were obtained from the ADNI database (adni.loni.ucla.edu). The primary goal of ADNI has

[1]For brain connectivity studies, there exist different approaches for DFC [91, 181, 86, 149, 165, 12, 129, 85, 35, 84]: Dynamic Causal Modelling (DCM), addressing how the activity in one brain area is affected by the activity in another area using explicit models of effective connectivity (for details see [86, 149]). Alternatively, data-driven approaches for DFC work directly with the time-series, and not any further assumption have to be taken, neither about the hemodynamic response, nor about the biophysics from individual neuron to Blood Oxygen Level Dependent (BOLD) level. Two popular data-driven methods for calculating DFC are Granger causality (GC) [91] and transfer entropy (TE) [181]; for the Gaussian approximation the two methods are equivalent [12].

been to test whether serial MRI, PET, other biological markers, and clinical and neuropsychological assessment can be combined to measure the progression of Mild Cognitive Impairment (MCI) and early AD. Determination of sensitive and specific markers of very early AD progression is intended to aid researchers and clinicians to develop new treatments and monitor their effectiveness, as well as lessen the time and cost of clinical trials.

The Principal Investigator of this initiative is Michael W. Weiner, MD, VA Medical Center and University of California - San Francisco. The initial goal of ADNI was to recruit 800 subjects but ADNI has been followed by ADNI- GO and ADNI-2. To date, these three protocols have recruited over 1500 adults, ages 55 to 90, to participate in the research, consisting of cognitively normal older individuals, people with early or late MCI, and people with early AD. The follow up duration of each group is specified in the protocols for ADNI-1, ADNI-2 and ADNI-GO. Subjects originally recruited for ADNI-1 and ADNI-GO had the option to be followed in ADNI-2. For up-to-date information, see `www.adni-info.org`.

### 5.2.2 Subjects and data pre-processing

The analysis was performed on n = 10 healthy subjects as control (5 males, 5 females, 73.70 $\pm$ 1.16 years old) and n = 10 AD patients (5 males, 5 females, 73.40 $\pm$ 1.08 years old) and both data sets were downloaded from the ADNI database.

Notice that rather than increasing the population size to a very large number, we preferred to select two small populations but choosing them the most balanced as possible with regard to age and gender. Demographic data (including the ADNI identifier) are given in Tables 5.1.

Resting State Functional Magnetic Resonance and anatomical scans were acquired (for more information about scanning protocol refer to [70]).

Data were motion corrected and smoothed using a Gaussian Kernel of 6 mm FWHM. After intensity normalization, a low-pass filter was applied within the slow fluctuations range of (0.01-0.1 Hz)

Table 5.1: Demographic data

| **AD Patients** | | | **Healthy Subjects** | | |
|---|---|---|---|---|---|
| ADNI ID | sex | age | ADNI ID | sex | age |
| 002_S_5018 | M | 73 | 006_S_4485 | M | 73 |
| 006_S_4867 | M | 75 | 006_S_4150 | M | 75 |
| 018_S_4696 | F | 73 | 002_S_4262 | F | 73 |
| 018_S_5074 | F | 75 | 002_S_4270 | F | 75 |
| 100_S_5106 | M | 74 | 012_S_4026 | M | 74 |
| 130_S_4641 | F | 74 | 002_S_4264 | F | 74 |
| 130_S_4984 | F | 73 | 018_S_4349 | F | 73 |
| 130_S_5059 | M | 73 | 018_S_4400 | M | 72 |
| 136_S_4993 | F | 72 | 031_S_4032 | F | 72 |
| 006_S_4546 | M | 72 | 002_S_4225 | M | 72 |

that characterizes the resting state BOLD activity. Next, linear and quadratic trends were removed. Finally motion time courses, white matter signal, cerebrospinal fluid (CSF) signal and global signal were regressed out from the data.

### 5.2.3 ROIs definition from RSNs masks

The first step is to select the regions of interest to be studied. In this work we defined each ROI as the voxels belonging to each RSN, by using the masks reported in [16] and illustrated in figure 5.1. Notice that we are not dealing with the independent components per se, but with the multivariate activity of all the voxels time-series localized within the masks. Similar approaches, considering the RSNs masks rather the independent components per se, have been used before in previous work [198, 39, 94, 199]. Specifically, we have used the following eight RSNs: medial visual, lateral visual, auditory, sensory-motor, default mode, executive control, dorsal visual right, dorsal visual left (figure 5.1). Once we defined the ROIs we extracted all the rs-fMRI time-series belonging to all the voxels in each RSNs.

### 5.2.4 HRF blind deconvolution

As pointed out in Chapter 1, fMRI measures the hemodynamic response in the brain, an indirect measure of the neural activity, but for computing information flow between regions the neural information works better if we transform the hemodynamic signals to neural activity. While neural activity occurs in milliseconds, hemodynamic response is a slower mechanism and takes about 5 seconds to reach its maximum value followed by an undershoot at 15 seconds from the beginning. Figure 5.2 represents a typical hemodynamic response caused by neural activity. This hemodynamic response shape can slightly variate between individuals and brain regions. The response to a continuous neural activity is the sum of the hemodynamic signals translated in time (linear and time invariant system). Thus, computing the deconvolution we can extract the neural activity from fMRI signals removing the effect of the HRF.

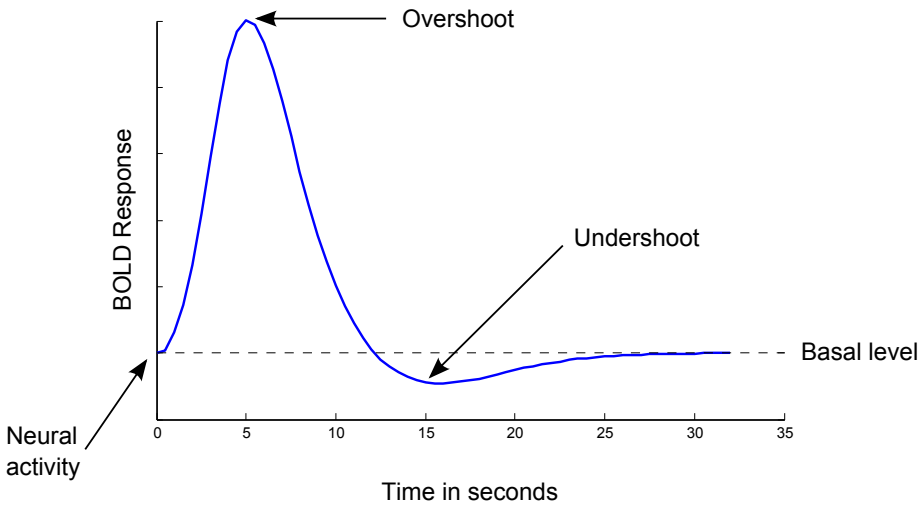


Figure 5.2: **Hemodynamic Response Function**

We individuated point processes corresponding to signal fluctuations with a given signature and extracted a voxel-specific HRF to be used for deconvolution, after following an alignment procedure.

The parameters for blind deconvolution were chosen with a physiological meaning, according to [215]: for a TR equal to 3s, the threshold was fixed to 1 SD (standard deviation) and the maximum time lag varying from 3 to 5 TR, but results did not change. Results in the manuscript have been done for maximum time lag equal to 5 TR. For further details on the complete HRF blind deconvolution method and the different parameters to be used, see [215]. All the time-series extracted from the RSNs regions were HRF blind deconvolution and the resulting time-series were used for the calculation of the IF.

### 5.2.5 Principal Component Analysis and multivariate Transfer Entropy

Let us consider two RSNs $A$ and $B$. We have used TE to estimate IF from $A$ to $B$ and vice-versa. The standard method to compute the IF between 2 ROIs is to compute the mean fMRI signal on each ROI and then compute TE using these two time-series. Computing the mean time-series of a region simplifies what this brain region is doing (a brain region is not involved only in one activity) and important information is missed about the activity.

For each ROI we have different number of time-series, each time-series describing the activity of an individual voxel within that ROI. Table 5.2 illustrates the number of voxels (time-series) for each ROI. Simplifying more than 5.000 different time-series that each ROI has in a single time-series (its average) can lead to a poor description of the ROI activity. Indeed, taking the mean signal of all these time-series accounts for about 12% of the explained variance of each of these regions (we are missing 88% of the explained variance).

Thus, to take one representative signal of the brain is not enough, but to use all the voxels time-series is computationally very expensive. We also must have in mind that usually neighbouring voxels have similar activity so is convenient to reduce the number of different activities within a region. To reduce the number of time-series, but at the same time, study the most representative activities of a given ROI, we can use Principal Component Analysis (PCA).

Table 5.2: Number of voxels in each RSN

| RSN | Number of Voxels |
|---|---|
| medial visual | 5649 |
| lateral visual | 8470 |
| auditory | 10894 |
| sensory-motor | 7668 |
| default mode | 8201 |
| executive control | 15209 |
| dorsal visual right | 12197 |
| dorsal visual left | 10524 |

PCA is a statistical procedure that uses an orthogonal transformation to convert a set of observations of possibly correlated variables into a set of values of linearly uncorrelated variables called principal components. These principal components maximize the variance explained in the data and often a small number of components can be used to reconstruct (or approximate) a given set of data.

To understand better what PCA does, let's simplify the problem, imaging that our region has only 2 voxels and a single time point (2-dimensions). Figure 5.3a represents an example data set where each circle represents the activity of voxel 1 and voxel 2 for a different subject. The colors represent 2 different groups, for example healthy subjects (blue) and disease (red).

PCA translates the data to a new coordinate system in which the biggest variance is captured by the first axis, the second highest variance in the second axis, similarly occurs for higher dimensions. Figure 5.3a shows two arrows identifying the new axis. The largest arrow corresponds to the axis of the first component and the other one to the second component. Figure 5.3a shows the data projected into the first component, while figure 5.3b shows the representation of the 2 components. We can see that the variance of the first component is higher, representing the 88.9% of the data variance, while the second component represents the 11.1%. In this example this first component is enough to see differences between the groups (first component $> 0$

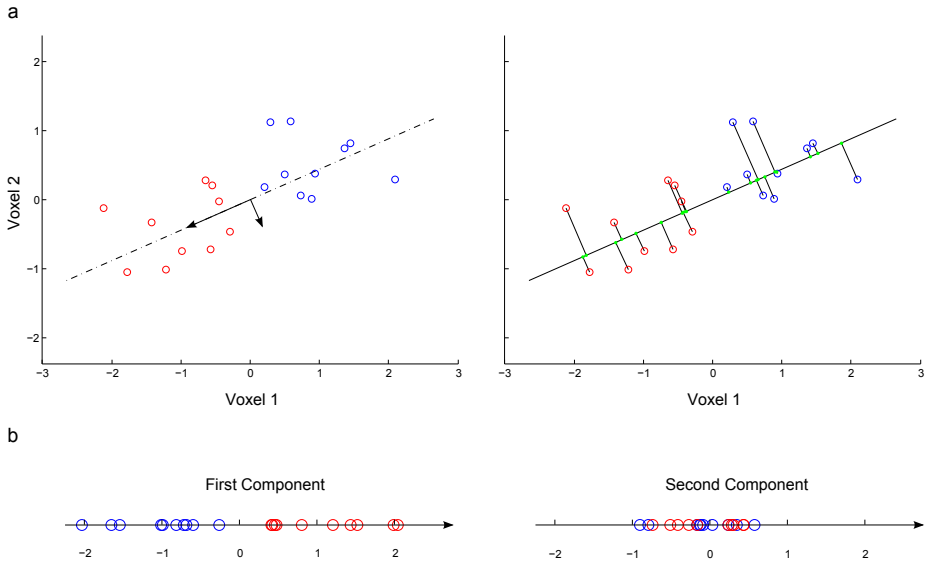


Figure 5.3: **PCA translates the data to a new coordinate system.** The left panel in a) shows the new coordinate system computed with PCA. This points are projected to the first component coordinate system as illustrated in the right panel of a). Finally the projected data into the first and second component is shown in b).

for disease and $< 0$ for healthy subjects). In such a way the data dimensionality is reduced and instead of using 2 time-series, just one represents the region with the 88.9% of the explained variance.

Finally, the data is projected into the new coordinate system wth the projection coefficients defininf the PCA decomposition. As illustrated in figure 5.4 when 2 voxels have the same activity or are highly correlated, just one component is enough to represent that activity, reducing the dimensionality of the data. In fMRI data, many neighbouring voxels are highly correlated so PCA performs well in reducing the dimensionality of a given region.

However, for more heterogeneous regions, not always the first component can discriminate between two groups. Figure 5.5 represents an example where the second component is the one that can account for differences between healthy and controls.

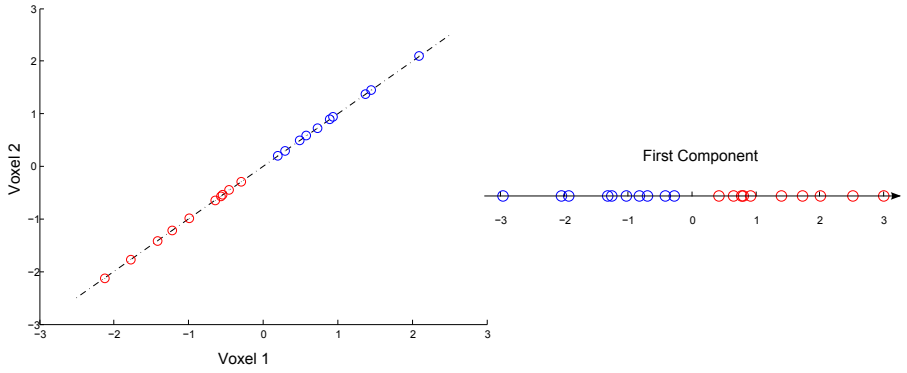


Figure 5.4: **Just one component is sufficient to represent highly correlated data.**

In a real case, regions of interest have more than 2 voxels and have more than one time point, but the aim to reduce the data dimensionality is the same as the simplified example illustrated before.

In the Alzheimer's dataset, after averaging between subjects, about 60% of total variability was captured by the first 10 components (k=10) (figure 5.6) and 99% of total variability was captured for k=72. No statistically significant differences were found in the amount of variability between control and AD, indicating that the data representation in the different principal components were disease independent. Therefore, the reader should not be confused and be aware that differences in IF are not related to these percentages.

## 5.3 Results

### 5.3.1 Information Flow between RSNs

Instead of using the standard procedure using the mean signal of each region, we decided to describe each ROI using more components for a given region. We computed the differences in the IF between RSNs for different number of components ranging from $k = 1$ to $k = 15$. Imagine, for instance, we want to compute IF from RSN $A$ to RNS

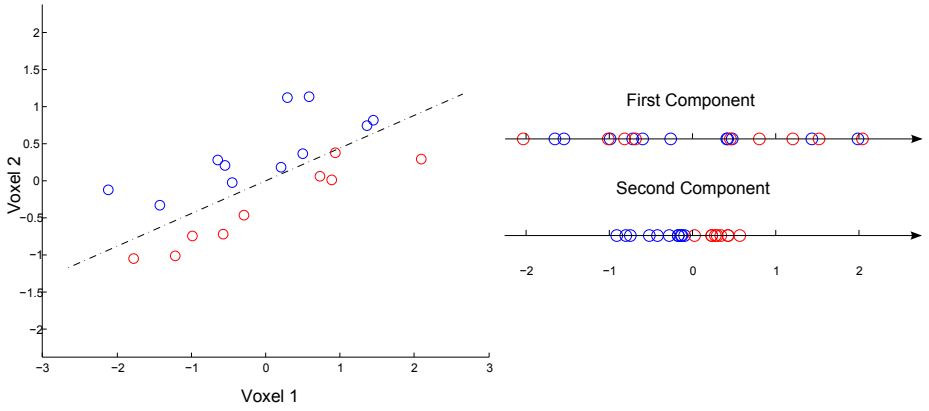


Figure 5.5: **Not always the components with highest variance are the ones that will show differences between groups.**

$B$ for $k = 5$ components. For both regions $A$ and $B$ we will extract 5 time-series using PCA and take the 5 time-series of the region $A$ and compute the multivariate transfer entropy to each of the 5 time-series describing region B. This method is univariate for the target and multivariate for the driver. This will lead to 5 transfer entropy values for each of the components in region $B$. Then we sum these TE values to account for all the contributions of these 5 components describing B which are statistically significant according to Bonferroni criterion($p < 0.05$). The complexity of the model is thus controlled by statistical testing, i.e. accepting only significant interactions (a similar strategy to control complexity is used in [131]).

To perform statistical significance between groups in figures 5.7-5.9, a non-parametric Wilcoxon rank sum test was used to validate the hypothesis that two data distributions have equal medians. This was implemented in Matlab, The Mathworks, Inc., with the function ranksum at $p = 0.05$ with Bonferroni correction.

The average IF between the different RSNs is represented in figure 5.7. Systematically, we recomputed IF with a different number of principal components (maintaining the same for all RSNs) from $k = 1$ up to $k = 15$. The case $k = 1$ is equivalent to calculating IF

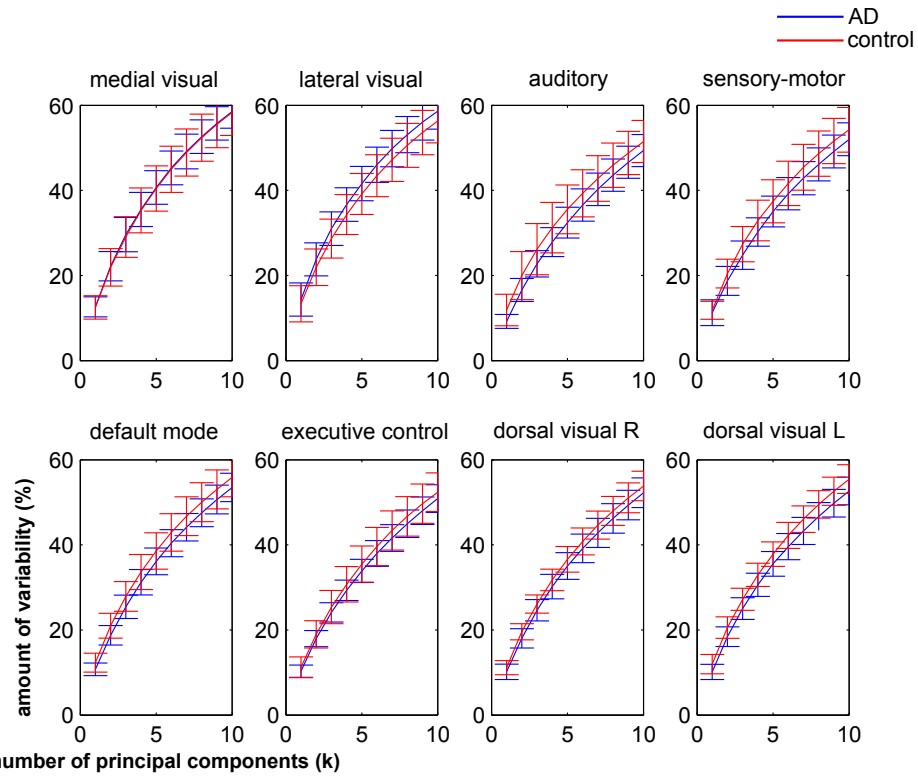


Figure 5.6: **Amount of data variability captured for different principal components, from k=1 to k=10**

between the average voxel activities for each RSN. The case $k > 1$ corresponds to a multivariate situation. For visualization purposes, figure 5.7 shows results up to $k = 11$ as for $k \geq 10$ the information was zero. Notice that having a zero IF is possible because, according to IF formula, the quantity IF is averaged over all the components. Thus, if adding a new component does not provide new independent information, the term in the denominator will eventually decrease the average IF. To represent figure 5.7, notice that as we were dealing with $n = 10$ healthy subjects and $n = 10$ AD patients, we first obtained for each subject a matrix of IFs in which the element (i, j) indicated IF from the ith RSN to the jth one. Next, we pooled

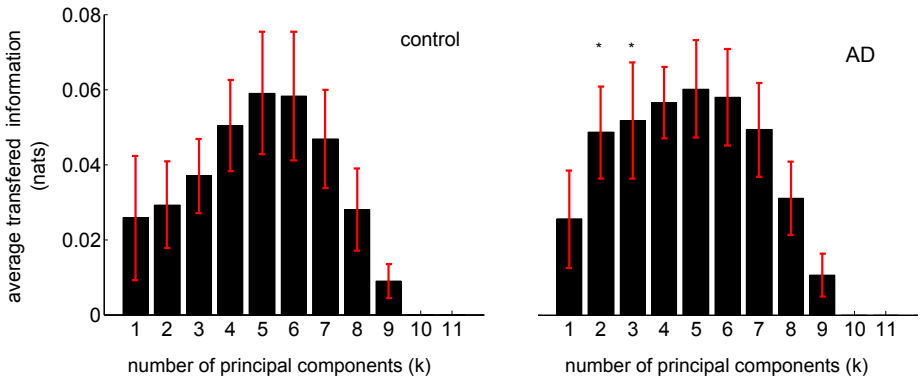


Figure 5.7: **Average transferred information between all RSNs as a function of the number of principal components**. Control (left) vs AD (right). The pattern of transferred information is the same for the two conditions; it increases from $k = 1$ up to the maximum at $k = 5$ to start to decrease up to zero information for $k \geq 10$. This means that the $k = 5$, multivariate, IF between the different RSNs is most informative than in any other dimension. Asterisks (*) represent statistical differences between control and Alzheimer, $p = 0.05$ (Bonferroni correction). Standard error (depicted in red) has been calculated across subjects for each group, control (n=10) vs Alzheimer ($n = 10$). Information has been calculated in nats (i.e. Shannon entropies have been calculated in natural logarithms); but to transform to information bits we have to multiply the value in nats by 1.44.

together all the matrices belonging to the same group (control and AD) and represented the average IF among all possible pairs; for 8 RSNs, the total number of pairs is 8 x ( $8 - 1$ ) = 56, which is equal to the number of pairs minus the elements in the principal diagonal. The profile of average information as a function of the number of principal components (used for calculation of the IF) is the same for control and AD: starting to increase from $k = 1$ up to the maximum at $k = 5$ to monotonically begin to decrease. Therefore we conclude that for dimensions bigger than $k = 5$, a higher dimension does not provide more IF. Statistically significant differences for the average IF between control and AD occurred for $k = 2$ and $k = 3$. Interestingly, the average inter-RSNs IF is higher in AD than in controls.

Figure 5.8 shows all possible values of IF between all RSNs. Here, the number of principal components was fixed to $k = 2$ (the one with biggest statistical difference in figure 5.7), but similar graphs were obtained for each value of k. Unlike correlations, TE measures directed functional connectivity and as such figure 5.8 represents for each condition control and AD the two directions in IF (ie., for two generic RSNs A and B, if in the top panel we represented IF from A to B, then in bottom panel we depicted IF from B to A). In other words, the average value among all the flows in figure 5.8 is the one plotted in figure 5.7. It is important to remark that all RSNs are communicating with each other, and, as it is shown figure 5.7, in average, the AD condition had higher information flowing between RSNs in comparison to control.

Next, we addressed IF arriving to and originating from each specific RSN. Figure 5.9 shows the outward information in blue and the inward information in red. The negativity in all the bars (obtained by subtracting the information in control minus the corresponding one in AD) confirmed that within all RSNs there existed an increase of the information for AD in both the outward and the inward directions.

### 5.3.2 Anatomical localization in brain differences: control vs AD

Finally, we performed a non-parametric two-sample unpaired t-test to localize the differences between AD and control for the $k = 2$ component in the brain. Using a General Linear Model we computed the contribution of each voxel of the brain to the $k = 2$ component, to obtain a subject-specific spatial map. Next, to search for the group differences (control vs AD) in the spatial maps we performed a permutation-based nonparametric inference as implemented in the function randomise in FSL, option Threshold-Free Cluster Enhancement (TFCE) with FWE-Corrected $p = 0.05$.

Results are shown in figure 5.10; the differences are plotted in two colours: blue for the activity existing in control but nonexistent in Alzheimer and in red, vice versa, activated areas belonging to

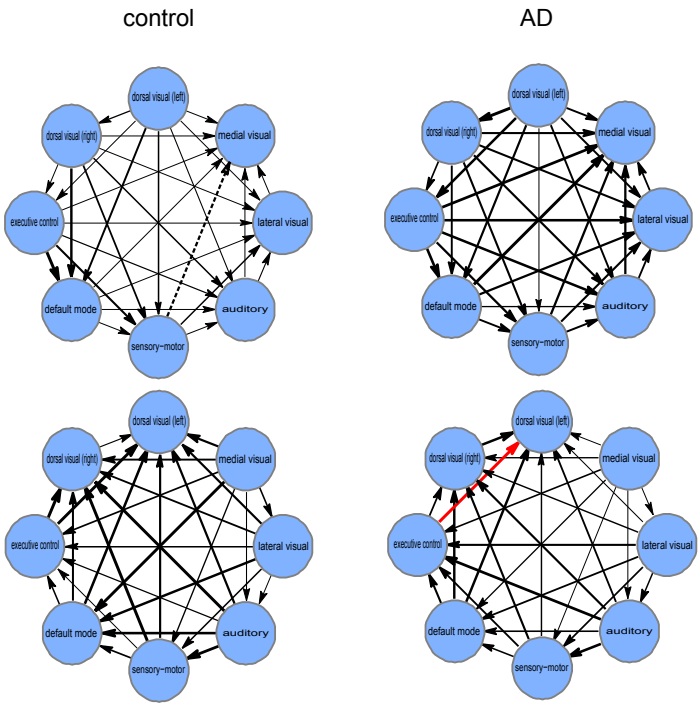


Figure 5.8: **Networks of IF between the different RSNs**. For $k = 2$ (where the biggest difference between control and AD in figure 5.7 occurs), we have represented the multivariate IF between the different RSNs. Note Control (left) vs AD (right) for the two directions of IF (top and bottom). IF values are proportional to arrow thickness. Values represented in figure 5.7 are the average among all the arrows represented in this figure taking into account the two flow directions (top and bottom). Only for visualization purposes, values of IF have been normalized to the common maximum (marked with the red arrow), corresponding to $TE = 0.078$ nats from the executive control network to the medial visual (left) in the AD condition. Dashed arrow from the sensory-motor network to the medial visual corresponds to the minimum value, which before normalization was $TE = 0.006$, and after normalization was fixed to zero.

Alzheimer but not to control.

To localize the spatial maps plotted in figure 5.10, we overlapped these maps with the Automated Anatomical Labeling (AAL) atlas [204] to get the anatomical regions underlying such differences.

Table 5.3: Localization of brain differences in AD vs control using the AAL parcellation

| RSN | Regions in AD but not in control (red in figure 5.10) | Regions in control but not in AD (blue in figure 5.10) |
|---|---|---|
| Medial Visual | Calcarine sulcus, Cuneus, Lingual Gyrus | Paracentral Lobule |
| Lateral Visual | Middle Occipital Gyrus | Superior Occipital Gyrus, Middle Occipital Gyrus |
| Auditory | Thalamus | Superior Temporal Gyrus |
| Sensory-Motor | Rolandic Operculum, Heschl's Gyrus, Superior Temporal Gyrus | Precentral |
| Default Mode | Medial Frontal Gyrus, Thalamus | Midcingulate Area, Cuneus, Angular Gyrus |
| Executive Control | Supramarginal Gyrus | Superior Frontal Gyrus, Middle Frontal Gyrus |
| Dorsal Visual Right | Inferior Parietal Lobule, Angular Gyrus | Inferior Frontal Gyrus, Pars Triangularis, Insula |
| Dorsal Visual Left | Angular Gyrus | –none upper 15% overlapping– |

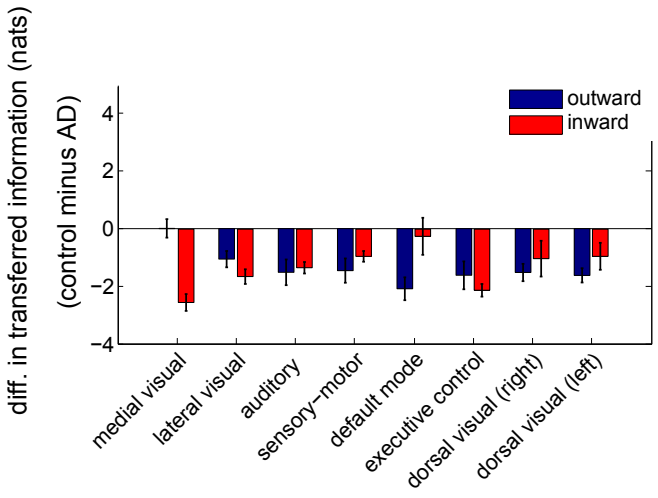


Figure 5.9: **Control minus AD differences in the total IF per RSN**. Note outward information (blue) and inward information (red) from/to each different RSN. Error bars have been calculated across subjects for each group. Notice that values in this figure are much higher than those in figure 5.7 due to two reasons. First, values in figure 5.7 correspond to the average value of IF, taking off principal diagonal elements. This implied dividing each IF value by a factor of 56. Second, to calculate both outward and inward information, we sum over columns and rows respectively. This means multiplying each IF value by a factor 6 (not including the self-node information, neither the element in the principal diagonal). Thus, values in this figure might be even up to 336 times bigger.

In particular, we calculated the overlapping percentage between all voxels in each spatial map and each of the 45 homologue brain areas existing in the AAL parcellation. Although the RSNs are widespread across the whole brain, our localization criteria only considered percentage of voxels in each spatial map to be bigger than 15% (with respect to the total spatial map size), results given in Table 5.3.

## 5.4 Discussion

RSNs are chiefly characterized by their universal emergence, meaning that, beyond individual subject differences, RSNs are ubiquitous in

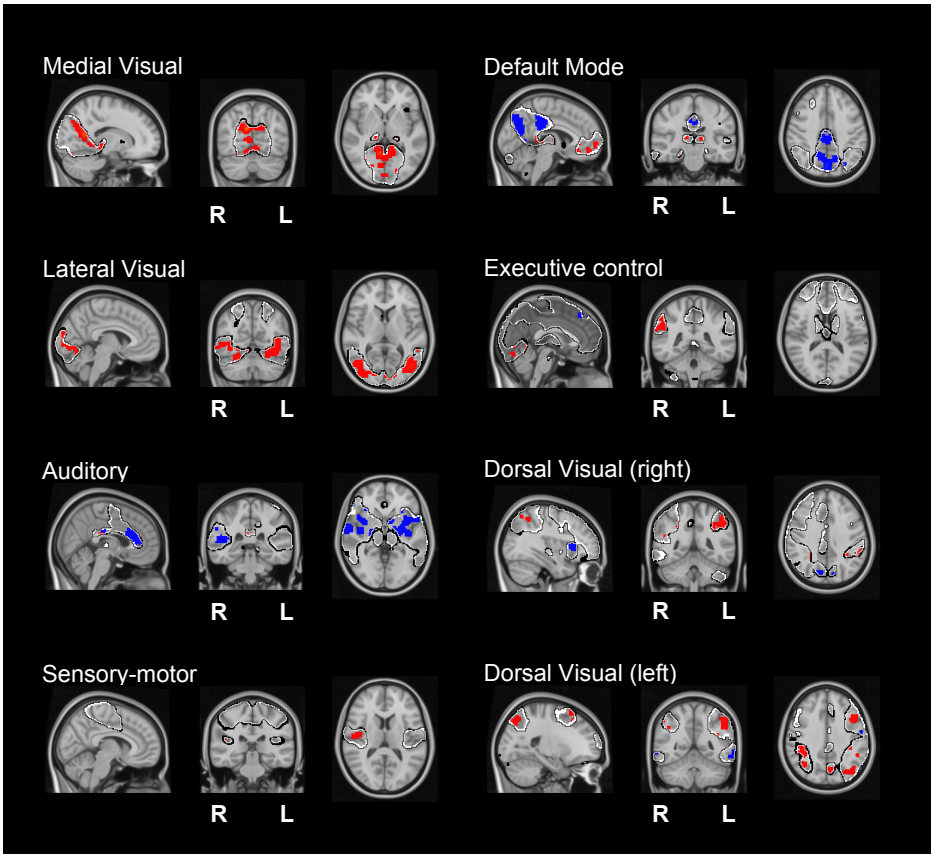


Figure 5.10: **Brain maps of statistical significance localizing the $k = 2$ component within each RSN**. After a two-sample unpaired t-test, we are representing two possible contrasts: in red, the figure shows the significant activity existing in AD but nonexistent in control. In blue, vice versa, differences which exist in control but not in AD.

healthy brains. Whilst the emergence of RSNs in healthy subjects is a well-known fact, how these RSNs speak to each other is not fully understood yet. In our approach, instead of applying ICA to each subject separately to get their specific RSNs, we used templates provided in [16] for all subjects. The use of the same templates for all the subjects is indeed assuming that the spatial structure of all RSNs

is universal. Our main hypothesis here is that the breakdown of this assumption might differentiate healthy subjects and AD patients, but the same method can be applied to any other disease. Searching for such differences might provide further insights about the alteration patterns of IF in the pathological brain. In other words, we were interested in providing an answer to the following question: what are the different features in healthy vs pathological brains under the hypothesis that the same templates characterize RSNs? To this end, we introduced a novel method that calculates IF between all the different RSNs.

We applied this methodology to AD datasets and compared these results to control. The interesting answer is that such assumption led –for the particular situation of AD– to differences in the information related to the second and third principal components and not to the first one (which is coincident with the average activity over all voxels per RSN). Thus, when we say that AD vs. control differences are associated to $k = 2$, we mean a multivariate driver having into account the two time-series $k = 1$ and $k = 2$. Therefore, as long as the average time-series of each ROI is concerned, no differences between the patterns of healthy and AD patients emerged. Performing a paired t-test to spatially localize the $k = 2$ component, we found the regions which were underlying those differences.

Some approaches have represented each ROI using more than one time-series, either using PCA [217] or cluster analysis [175]. The approach we are presenting here is rooted on principal component analysis and its novelty is based on two points: first, we preprocessed the time-series corresponding to each individual voxel by HRF blind deconvolution and second, instead of fixing the number of components according to a prescribed fraction of the data variance, as it is usually done, we have analyzed IF as the number of components increases, including more details of the ROIs dynamics.

Recently, the point process analysis described in [198] showed that the relevant information in resting-state fMRI can be obtained by looking into discrete events resulting in relatively large amplitude BOLD signal peaks. Following this idea, we have considered the

preprocessed resting fMRI time-series to be spontaneous event-related and individuated point processes corresponding to signal fluctuations with a given signature, extracting a voxel-specific HRF to be used for deconvolution.

We want to remark that the use the HRF deconvolution, apart from being conceptually mandatory in our opinion, is also crucial for our results. Indeed we repeated our analysis while omitting the deconvolution stage, and we found a clearly different pattern of IF between RSNs. In particular, IF differences were only significant for $k = 1$ and AD showed a decreased IF w.r.t. healthy subjects. We also verified that, in general, the use of HRF de-convolution increased the IF for all subjects in comparison to not using the de-convolution. Thus, if we had omitted the HRF deconvolution stage, we would not have observed the relevant role of the second and the third principal components in shaping the differences of IF in AD and controls.

Previous work has addressed DFC between the different RSNs; for instance, the authors in [66] ICA-extracted the time-courses of spatially independent components and found differences in DFC between schizophrenia and control conditions. It is worth mentioning that a method for effective connectivity inference, combining PCA and GC, was proposed in [217]. The main differences between our method (tailored to analyze the IF between RSNs) and the one developed in [217] are the blind deconvolution with HRF and the fact that we use the number of components as a parameter to be systematically increased (up to finding statistically significant different causalities), and both driver and target ROIs are described with the same number of components. In [217], instead, all voxels in the activated brain regions were taken as target and the PCA analysis was applied only to the driver region and not to the target one.

Following previous work extending the use of DFC to the multivariate situation [12, 67, 13, 120], we have applied here a multivariate DFC approach to the study of the interaction between RSNs. Specifically to AD, causal interactions among the different RSNs were addressed in [124] by a multivariate Granger causality. The authors found an increase in IF between RSNs in relation to the default mode

network and the executive control one, which is in agreement with the increase of IF reported here, possibly suggesting compensatory processes in the brain networks underlying AD. Similarly and more recent, an increase of connectivity in the default mode network was found by other authors in [119] in amnesic Mild Cognitive Impairment by using GC.

The main result of the present study is the finding that the AD condition had higher IF between RSNs in comparison to control. This is apparently in contradiction to a recent paper [117] where a Bayesian network approach reported a general decrease in connectivity strength for AD. Moreover, the authors in [117] found an increase in connectivity between the default mode network and the dorsal attention network when using the average voxels activity, which in our approach is equivalent to considering $k = 1$. Here, if we apply the HRF deconvolution preprocessing, we find no significant differences between controls and AD at $k = 1$; but, if no deconvolution is applied, $k = 1$ for AD shows a significantly decreased IF w.r.t. healthy subjects, in full agreement with [117]. Moreover, for $k = 1$ we find an increase of the interaction from the default mode network to the dorsal visual (left) network and this is also consistent with the findings in [117]. It follows that the results in the paper [117] are consistent with the application of our method when just one component is considered and the HRF deconvolution is omitted. Our findings suggest that in AD the second (and, to a lesser extent, the third) components of the signals within RSNs are responsible of the increased IF. Approximating each RSN by a single signal is not enough to put in evidence these phenomena.

The IF increase found in AD might have different causes; perhaps, due to a compensatory re-organization of brain circuits triggered by synaptic plasticity [2], or due to the fact that AD patients might fail in ignoring irrelevant inputs when integrating information to performing particular cognitive tasks [164], or due the reduction in inhibitory modulatory influence across the whole-brain network in AD [7, 20, 171], but the exact mechanism producing an increase of IF in AD needs further investigation.

The small population size included in this study only allows for a limited interpretation of the details of connectivity changes between networks. However, a conservative approach to this analysis indicates that the IF implicated in sensory processing networks and the DMN is relatively increased in AD compared to controls. Both reductions as well as increments in functional connectivity have been previously reported between brain regions in early AD. Interestingly, most of the regional connectivity increments have been described in the frontal regions, overlapping with regions belonging to the executive control network, DMN and frontal regions of the dorsal visual processing stream [174].

# Chapter 6

# Structure-function multi-scale connectomics

In this chapter, we study how physiological aging affects brain structure and function impacting its morphology, connectivity and performance. Here, we collected brain images from healthy participants (N=155) ranging from 10 to 80 years to build functional (resting-state) and structural (tractography) connectivity matrices, both datasets combined as connectivity descriptors. We then calculated the brain-connectome age (BCA) as the maximum likelihood age estimator, and compared BCA to the chronological age (ChA).

## 6.1 Introduction

Aging, a systemic time-dependent decline, involves changes at multiple scales from biological to psychological and social levels. Interestingly, individuals with the same chronological age (ChA) might exhibit different trajectories of age-related biological deterioration, as measured by biomarkers of functional performance, tissue integrity and metabolic health [104, 193]. This mismatch reflects two different concepts for aging. One is ChA, calculated as the time running since birth, whereas the other is the biological age, which, irrespective of birth year, is based on the level of biological maturation at a given

time. The mismatch between chronological and biological aging has gained major scientific interest in the past years due to its potential implication for health and disease of age-related molecular, genetic, cellular and organ-specific dynamics and their genetic, epigenetic, and environmental modulators [100]. Indeed, it is well established that aging is a major risk factor for most of the late-onset diseases such as cancer, cardiovascular disease, diabetes and neurodegenerative diseases [87].

In relation to brain biological aging, psychophysical, neuropsychological and physiological studies support that functional performance of the brain declines with age, with specific impact on cognition (long-term and working memory, executive functions, conceptual reasoning and processing speed) [90, 146], mood (anxiety and depression) [106], circadian behaviours (disruption of amplitude and period length) and sleep cycle (poor sleep quality and delayed sleep onset latency) [107].

These changes in brain performance occur in parallel with well-established age-related macrostructural and microstructural brain variations. At the microstructural level, age has been associated with alterations in synaptic structures (decreased synaptic density and synaptic terminals), aggregation of abnormal proteins outside and inside neurons such as plaques and tangles, reduced neurogenesis and synaptic plasticity, abnormal increase of astrocytes and oligodendrocytes, altered myelination and reduction of nerve growth factor concentration [111, 150, 151]. However, whether aging reduces the number of neurons is still under debate, as several post-mortem human and primate studies support that cortical cell number remains unchanged [139] and that rather neuronal shrinkage occurring along the lifespan (rather than cell loss) is the main process underlying brain atrophy.

At the macroscopic level, both global and regional atrophies are the most reported characteristics of the aging brain, supported by several post-mortem and MRI studies. Neuroimaging studies have shown that the overall brain volume varies with age in an inverted-U fashion, increasing volume in about 25% from childhood to adolescence, then remaining constant for about three decades to finally

decay down to childhood size at late ages [50]. This pattern of age-related brain atrophy along the lifespan has been associated with the deterioration of cognitive performance in the healthy population [163]. Of note, age-related grey and white matter brain atrophy is not homogeneous, with higher atrophy rates observed in white matter as compared to cortical grey matter [99, 162] and regionally, with more prominent atrophy in prefrontal and parietal cortices [160, 172, 196] and hippocampus[210]. In contrast, the volume of the cerebrospinal space (ventricles, fissures, and sulci) increases with age [162].

Beyond atrophy measured by structural imaging, modern techniques such as diffusion tensor imaging (DTI) have facilitated the in-vivo inspection of age-related microstructural changes of the brain [64, 133], in agreement with histological findings and revealing regional patterns and dynamics of structural connectivity (SC) degeneration, a phenomenon leading to cortical disconnection with loss of functional integration in some of the cognitive networks [90, 143]. Several DTI studies in normal aging support an association between white matter atrophy and a widespread degeneration of white matter fibres, with age-related changes predominantly affecting frontal tracts [143] and gradually extending to posterior tracts [63], a pattern that inverts the sequence of myelination during early brain development and that supports the "last-in-first-out principle for white matter deterioration along the lifespan.

The development of resting and task-based functional MRI (fMRI) has provided in-vivo functional correlates to the observed age-related atrophy and SC brain disconnection, showing consistently age-related regional changes in the patterns of brain activation, with decreased activity in the occipital lobe and increased activity in the frontal lobe across a variety of tasks [90]. Functional connectivity (FC) studies at rest have gone a step further and demonstrated that aging not only induces regional brain activity changes but also a decrease in functional connectivity of large-scale brain networks, specifically between anterior and posterior hubs, including superior and middle frontal gyrus, posterior cingulate, middle temporal gyrus, and the superior parietal region [10, 61].

The combination of SC and FC analyses by complex network approaches have led to the conceptualization of brain networks as a connectome [77, 190], and its correlates with age and disease has gained major attention in fundamental neuroscience [59]. Complex network approaches have highlighted the key role played by several network descriptors in aging and brain diseases, such as network hubness, node efficiency, network modularity and hierarchical organization. In relation to modularity, it has been shown that functional network modularity (segregation) decreases with age [42, 105, 187], a mechanism supporting the loss of functional specialization of certain key brain networks known to be involved in several cognitive domains affected by aging along the lifespan [41].

Moreover, combined SC and FC analyses have suggested that not only segregation (i.e., network modularity) decreases with age but integration (i.e., node efficiency) increases [93] in a counterbalanced manner that ensures network efficiency along the lifespan. Others, however, have suggested that small-worldness and network modularity remain stable along the lifespan, despite a considerable reduction in streamline number [123]. Analyses of longitudinal data, less abundant than cross-sectional data, have shown that the brain areas where age FC variations occur do not match with those areas associated to SC variations [78], highlighting that FC and SC are affected by age in a more independent manner than previously thought. However, only the age variations in FC and SC for the areas participating in the DMN match each other.

The combined FC and SC analyses also have revealed the key role that the deterioration of the cortical to subcortical connections is playing in the integration of several resting state networks for cognitive performance, such as those involving executive functions, processing speed and memory(Ystad et al., 2011). By calculating node-degree distributions, other studies have shown an age-related connectivity reduction of network hubs [25], supporting the hypothesis that the alteration of network hubs might trigger brain aging similar to what occurs in a plethora of other brain pathologies [59].

Very recently, new computational strategies for analysing the dy-

namics of brain atrophy (such as machine learning) have applied the concept of brain-predicted aging (by quantifying the mismatch between age-associated brain alterations and ChA) to several brain diseases, including traumatic brain injury [45], mild cognitive impairment and Alzheimers disease [88], HIV infection [46] and schizophrenia [178]. A critical issue in all these studies is the selection of an adequate approach to achieve the highest robustness and precision for the mismatch quantification between chronological and brain ages. Very strikingly, the combined rather than separate analysis of SC and FC has shown to provide a better estimation of ChA [218].

It is also of major importance to consider the possibility of some epigenetic and environmental factors as possible modulators of the chronological/biological age mismatch. Here, we address the effects of physical activity (PA), that has been shown to reduce disability [58], morbidity [101, 137] and mortality [112, 140, 173]. Moreover, studies with animal models have shown that PA has a beneficial effect on learning and memory by inducing neuroprotection, decreasing oxidative stress and increasing cerebral blood perfusion, which in turn influence angiogenesis, synaptogenesis and neurogenesis, showing correlations with memory improvement at the behavioral level [5].

Although previous publications have addressed the study of brain aging and the estimation of ChA by means of separate or combined analyses of SC and FC, none of them has proposed an optimal method that, applying complex network analysis of the structural-functional connectome, simultaneously identifies age-related brain changes and estimates brain age, considering the effect of a potential modulator of brain aging such as PA.

Two key hypotheses guide the present work; first, that the age estimation improves by combining FC and SC metrics, and second, that higher and lower levels of PA might be associated with younger and older biological age, respectively. To test these hypotheses, we built following previous work [45, 46, 44, 72, 82, 81, 88, 95, 108, 122, 126, 192] a data-driven approach to estimate ChA based on SC and FC biomarkers and investigated the extent to which the level of PA modulates the participants brain biological age. Lastly, we discuss the

general implications and applications of the described methodology to a broader umbrella of key biomedical problems.

## 6.2 Methods

### 6.2.1 Participants

Participants were recruited in the vicinity of Leuven and Hasselt (Belgium) from the general population by advertisements on websites, announcements at meetings and provision of flyers at visits of organizations and public gatherings (PI: Stephan Swinnen). A sample of N=155 healthy volunteers (81 females) ranging in age from 10 to 80 years (mean age 44.4 years, SD 22.1 years) participated in the study. All participants were right-handed, as verified by the Edinburgh Handedness Inventory. None of the participants had a history of ophthalmological, neurological, psychiatric or cardiovascular diseases potentially influencing imaging or clinical measures. Informed consent was obtained before testing. The study was approved by the local ethics committee for biomedical research, and was performed in accordance with the Declaration of Helsinki.

### 6.2.2 Physical activity score

Physical activity (PA) was assessed using the International Physical Activity Questionnaire [31] (IPAQ), which assesses PA undertaken across leisure time, domestic and gardening activities, and work-related and transport-related activities. The specific types of activity were classified into three categories: walking, moderate-intensity activities, and vigorous-intensity activities. Frequency (days per week) and duration (time per day) were collected separately for each specific activity category. The total score used to describe PA was computed as the weighted summation of the duration (in minutes) and frequency (days) for walking, moderate-intensity, and vigorous-intensity activity. Each type of activity was weighted by its energy requirements defined in Metabolic Equivalent of Task (MET): 3.3 METs for

walking, 4.0 METs for moderate physical activity, and 8.0 METs for vigorous physical activity [3].

Several studies have shown the IPAQ questionnaire to be an adequate proxy for long-term effects of PA. In particular, it was shown that the total IPAQ score correlated to objective measures of PA such as maximal treadmill time(Papathanasiou et al., 2010), maximal oxygen uptake[110, 127] , and data from accelerometer [57, 127], pedometer[68], and actometer [177] .

### 6.2.3 Imaging acquisition

Magnetic resonance imaging (MRI) scanning was performed on a Siemens 3T Magnetom Trio MRI scanner with a 12-channel matrix head coil.

*Anatomical data:* A high resolution T1 image was acquired with a 3D magnetization prepared rapid acquisition gradient echo (MPRAGE): repetition time [TR] = 2300 ms, echo time [TE] = 2.98 ms, voxel size = 1 1 1.1 $mm^3$, slice thickness = 1.1 mm, field of view [FOV] = 256 240$mm^2$, 160 contiguous sagittal slices covering the entire brain and brainstem.

*Diffusion Tensor Imaging:* A DTI SE-EPI (diffusion weighted single shot spin-echo echo-planar imaging) sequence was acquired with the following parameters: [TR] = 8000 ms, [TE] = 91 ms, voxel size = 2.2 2.2 2.2 $mm^3$, slice thickness = 2.2 mm, [FOV] = 212 212 $mm^2$, 60 contiguous sagittal slices covering the entire brain and brainstem. A diffusion gradient was applied along 64 non-collinear directions with a b value of 1000 s/$mm^2$. Additionally, one set of images was acquired without diffusion weighting (b= 0 s/$mm^2$).

*Resting state functional* data was acquired over a 10 minute session using the following parameters: 200 whole-brain gradient echo echo-planar images with [TR/TE] = 3000/30 ms, [FOV] = 230 230$mm^2$, voxel size = 2.5 2.5 3.1$mm^3$, 80 80 matrix, slice thickness = 2.8 mm, 50 sagittal slices, interleaved in descending order.

### 6.2.4 Imaging preprocessing

*Diffusion Tensor Imaging:* We applied DTI preprocessing similar to previous work [6, 8, 69, 71, 109, 132, 159, 158, 195] using FSL (FMRIB Software Library v5.0) and the Diffusion Toolkit. First, an eddy current correction was applied to overcome the artefacts produced by variation in the direction of the gradient fields of the MR scanner, together with the artefacts produced by head motion. To ensure that correlations with age were not due to differences in head motion (ie., to correct for the effect that older people move more), the average motion of each participant was used as a covariate of non-interest in the statistical analyses. In particular, the participants head motion was extracted from the transformation applied at the eddy current correction step, from every volume to the reference volume (the first volume, b=0). The motion information was also used to correct the gradient directions prior to the tensor estimation. Next, using the corrected data, a local fitting of the diffusion tensor was applied to compute the diffusion tensor model for each voxel. Next, a Fiber Assignment by Continuous Tracking (FACT) algorithm was applied [138]. We then computed the transformation from the Montreal Neurological Institute (MNI) space to the individual-participant diffusion space and projected a high-resolution functional partition to the latter, composed of 2514 regions and generated after applying spatially constrained clustering to the functional data [55].

Following this procedure we built 2514 x 2514 SC matrices, each per participant, by counting the number of white matter streamlines connecting all region pairs within the entire 2514 regions dataset. Thus, the element matrix (i,j) of SC is given by the streamlines number between regions i and j. SC is a symmetric matrix, where connectivity from i to j is equal to that from j to i. Exclusion criteria was based on not having the average head motion higher than the mean + 2 standard deviation. None of the participants were excluded based on this constraint.

*Functional MRI:* We applied resting fMRI preprocessing similar to the one explained in chapter 5. Further, to correlate with age, we also removed the effect of head motion by using the global frame

displacement as a non-interest covariate, as old participants moved more than the young, and this fact introduced trivial correlations with age.

Finally, FC matrices were calculated by obtaining the pairwise Pearson correlation coefficient between the resting fMRI time series. Exclusion criteria was based on not having more than 20% of the time points with a frame wise displacement greater than 0.5. Two participants were finally excluded.

### 6.2.5 Brain Hierarchical Atlas (BHA)

The aforementioned 2514 brain regions were grouped into modules using the Brain Hierarchical Atlas (BHA), recently developed [69] and applied by the authors in a traumatic brain injury study [71]. The BHA is available to download at `http://www.nitrc.org/projects/biocr_hcatlas/`. A new Python version, that was developed during Brainhack Global 2017 - Bilbao, can be download at `https://github.com/compneurobilbao/bha`.

The use of the BHA guarantees two conditions simultaneously: 1) That the dynamics of voxels belonging to the same module is very similar, and 2) that the voxels belonging to the same module are structurally wired by white matter streamlines; see in figure 6.1 the high correspondence between SC and FC modules. The BHA provides a multi-scale brain partition, where the highest dendrogram level M=1 corresponded to all 2514 regions belonging to a single module, coincident with the entire brain, whereas the lowest level M=2514 corresponded to 2514 separated modules, all of them composed of only one region.

It was also shown in [69] that the hierarchical brain partition with M = 20 modules was optimal based on the cross-modularity index X. This index was defined as the geometric mean between the modularity of the structural partition (Qs), the modularity of the functional partition (QF), and the mean Sorensen similarity between modules existing in the two structural and functional partitions (LSF).

### 6.2.6 Labeling of anatomical regions

The anatomical identification for each of the 2514 brain regions has been performed by using the Automated Anatomical Labeling [204] (AAL) brain atlas, and as a consequence, the anatomical labels used in this work follow the ones existing in the AAL atlas.

### 6.2.7 Removal of regions affected by the increment of ventricular space along lifespan

Ventricular space increases along the lifespan in a manner that, after transforming all images to a common space, some regions surrounding the ventricular space for the younger population are occupied by the ventricular space of older participants. In order to remove this effect, that can introduces a strong bias in the age estimation, we deleted these regions by (after projecting all images to the common space) searching for the participant with the highest ventricular volume, segmenting this space and treating it as mask to discard (for the connectivity analysis) all the regions within this space in all the participants. Figure 6.1a illustrates this procedure.

### 6.2.8 Structure-function correlo-dendrograms of brain aging

From both SC and FC matrices, we built the correlo-dendrogram (CDG) of brain aging by correlating chronological age with the values of internal (intra-module) and external (inter-module) connectivity for each dendrogram level M of the BHA. In particular, four different classes of module descriptors were built per participant: functional internal connectivity (FIC), functional external connectivity (FEC), structural internal connectivity (SIC), and structural external connectivity (SEC) (figure 6.2). Given a brain module composed by a set of R regions, its associated FIC (SIC) was calculated as the sum of the functional (structural) weights of all the links between the elements of R, whilst FEC (SEC) was defined as the sum of the functional (structural) weights of all the links connecting the elements of

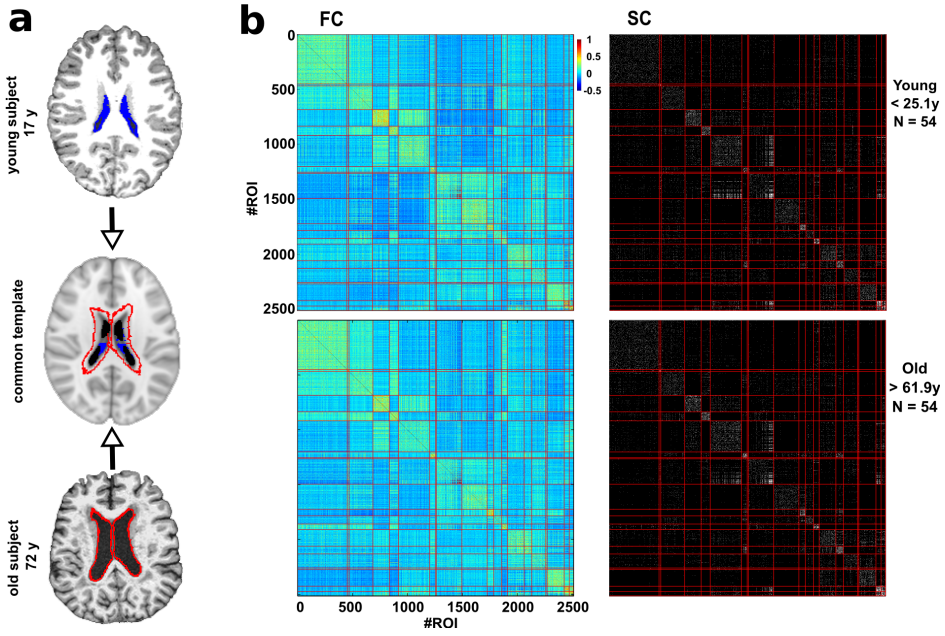


Figure 6.1: **Robustness of the Brain Hierarchical Atlas along lifespan a:** Common template normalization (middle) for young (top) and old brains (bottom). Ventricle 3D segmentation has been performed for a young (17 y, filled in blue) and old participant (72y, contours marked in red). Both segmentations are superimposed onto the common population template (middle row). For the connectivity analysis, regions located within the volume defined by the biggest ventricle size across all the participants have been ignored to correct for trivial age-effects in the results of age estimation (i.e., to correct for the effect that older people have bigger ventricle volume). **b:** Brain hierarchical atlas (BHA) parcellation for young (top) and old (bottom) populations shows the strong correspondence between functional modules (depicted as yellow squares in the matrix diagonal of the functional connectivity matrix, FC ) and structural modules (plotted in the SC matrix). FC and SC matrices are the result of averaging FC and SC individual matrices in two different populations, young (age<25.1 y, N=54 participants) and old (age>61.9 y, N=54 participants). Both connectivity FC and SC matrices have been reordered according to the BHA (here represented at the level of M=20 modules). FC is defined by the pairwise Pearson correlation between rs-fMRI time series whilst SC is defined by the streamline counting between region pairs (here binarized just for illustration purposes).

R to other regions in the brain. One of the properties of the BHA is that at each M level only one of the branches of the hierarchical tree divides in two, and therefore only 2 modules at each level are new with respect to the (M-1) upper levels (figure 6.2). Taking into consideration this point together with the fact that we started our analysis at the level of M=20 and arrived up to M=1000, we established the Bonferroni significance threshold equal to $0.05/[20 + 2 * (1000 - 20)]$ for the correlation between age and connectome metrics (FIC, SIC, FEC, SEC).

To localize age-affected brain areas at both functional and structural levels (rather than separate FC or SC analyses), and thus obtaining a major benefit from the combination of functional and structural data, we searched for brain regions such that the p-value was smaller than the square root of the product of the individual structural p-value multiplied by the individual functional one. Consequently, the value of the structure-function age correlation was calculated as the geometric mean of the two correlation values, one achieved by the functional descriptor and the other by the structural one. A Python pipeline implementing this strategy can be download at `https://github.com/compneurobilbao/aging` .

### 6.2.9 Maximum likelihood estimator (MLE)

Let us define for each participant $n$ the vector $x^n \equiv \left(1 x_1^n x_2^n \cdots x_{K-1}^n\right)^T$ of $K$ components, each one corresponding to a different connectivity descriptor (in principle any value of inter/intra module connectivity at any M level of the BHA calculated from either FC or SC), where $T$ denotes the transpose operator. The estimated age for the participant $n$ was calculated by a linear combination of the descriptors, ie.,

$$t_n = \omega_0 + \sum_{j=1}^{K-1} \omega_j x_j^n + \epsilon_n \tag{6.1}$$

where $\varepsilon_n$ is a zero mean Gaussian random variable with variance $\sigma^2$, and $\omega \equiv (\omega_0 \omega_1 \omega_2 \cdots \omega_{K-1})^T$ is the weight vector. For $P$ different

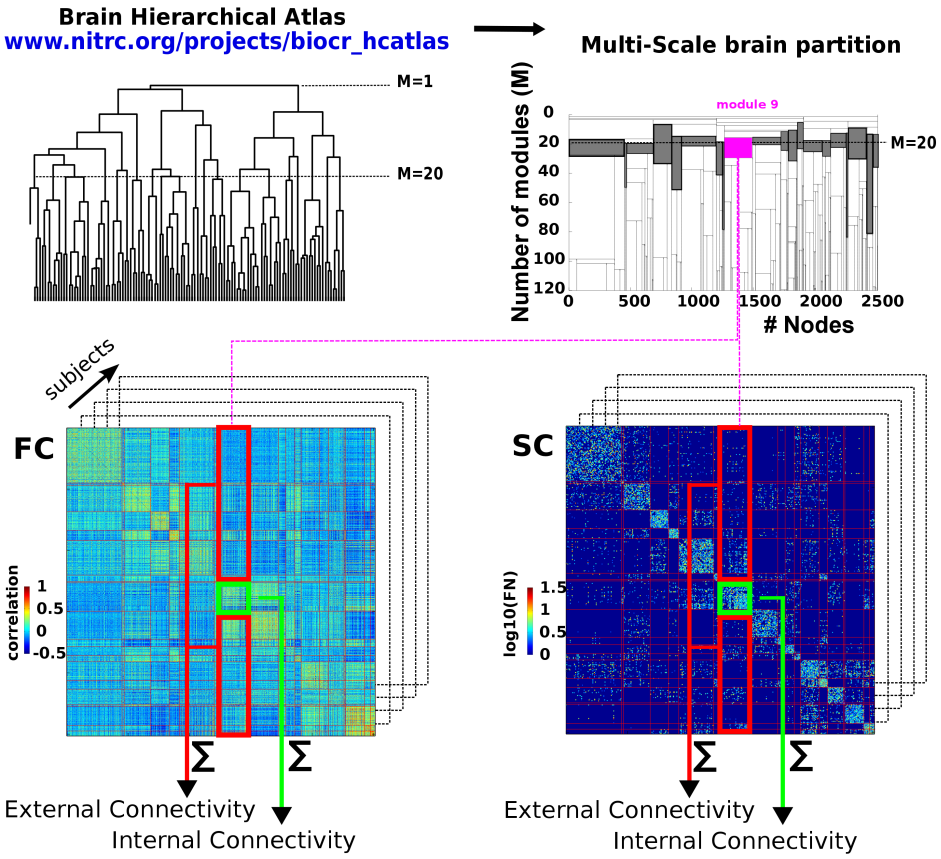


Figure 6.2: **Schematic representation of brain connectivity descriptors. Left-top:** First, we made use of BHA to define different modules resulting from a hierarchical agglomerative clustering. **Right-top:** The multiscale brain partition shows how modules divide when going down along the tree (here, we only considered the part of the tree that goes from 20 to 120 modules). The gray-colored modules represents the M=20 brain partition. **Bottom:** For the tree level of M=20 and for each participant, we calculated the structural/functional internal connectivity (green rectangle) and structural/functional external connectivity (red rectangle), by summing respectively the edge weights within and leaving out that module. The same procedure was applied for all the modules in all the 20<=M<=1000 levels of the tree.

participants, using Eq. 6.1, one can define the error function as

$$E(\omega) = \frac{1}{2}\sum_{n=1}^{P}\left\{t_n - \omega_0 - \sum_{j=1}^{K-1}\omega_j x_j^n\right\}^2 \tag{6.2}$$

which allows to calculate the weight vector that minimizes the error function, (i.e., which is solution of $\nabla_\omega E(\omega) = 0$, the first derivative with respect to $\omega$ equal to zero). Such a minimum defines precisely the Maximum Likelihood Estimator (MLE), which can be analytically solved [27, 48] and is given by:

$$w^{MLE} = \left(\varphi^T\varphi\right)^{-1}\varphi^T t \tag{6.3}$$

where the exponent $-1$ denotes the inverse of the matrix, $t{\equiv}\left(t_1 t_2 t_3 \cdots t_P\right)^T$ the vector of $P$ different estimations and $\varphi$ the so-called *design matrix*, ie.,

$$\varphi{\equiv}\begin{pmatrix} 1x_1^1 x_2^1 \cdots x_{K-1}^1 \\ 1x_1^2 x_2^2 \cdots x_{K-1}^2 \\ \vdots \\ 1x_1^P x_2^P \cdots x_{K-1}^P \end{pmatrix} \tag{6.4}$$

### 6.2.10 Adding non-linearities for age estimation

Although Eq. 6.1 accounts for a linear dependence on connectivity descriptors, the MLE strategy is more general and allows to incorporate non-linearities, such as quadratic or higher-order polynomial terms, or other functions such as, for instance, Gaussian, Exponential or Sigmoid, just by adding new columns accounting for such dependencies into the design matrix given by Eq. 6.4 (for further details see [27]). Figure 6.6 shows results after adding quadratic connectivity terms.

### 6.2.11 Mean absolute error (MAE) and brain connectome age (BCA)

As a metric for estimation quality, the mean absolute error (MAE) was calculated as

$$MAE\,(K) = \frac{1}{N_2}\sum_{n=1}^{N_2} |\,ChA_n - BCA_n\,(K)| \tag{6.5}$$

where || denotes absolute error and where we have defined the brain connectome age (BCA) for participant as

$$BCA_n\,(K) \equiv \omega_0^{MLE} + \sum_{j=1}^{K-1} \omega_j^{MLE} x_j^n \tag{6.6}$$

where $w^{MLE}$ is defined in Eqs. 6.3 and 6.4. When the entire dataset is used to calculate $w^{MLE}$, the estimation error decreases when the number of descriptors increase (the more descriptors, the better the estimation), but this strategy also provides a very high variance estimate, meaning that, when estimating the age using the $w^{MLE}$ solution in a different dataset can produce a very high error. Splitting the entire data in training and testing sets can solve this problem, a.k.a. overfitting [97]. Therefore, to calculate the MAE, for each experiment we performed data splitting, by randomly choosing 75% of the dataset (N1=115) for training (i.e., for calculating the $w^{MLE}$ solution) and the remaining 25% (N2=38) for testing (i.e., to calculate the MAE).

Remark that although in principle there were many potential descriptors (four classes –FIC, FEC, SIC and SEC– per module and number of modules M varying from 20 to 1000), finally only K of them were introduced into the MLE to estimate age. Therefore, and by construction, the MLE solution depends on K (see next subsection for the choice for the K descriptors).

### 6.2.12 Optimization of the maximum likelihood estimation (MLE)

In order to get the optimal model, ie. the K descriptors that better estimate age, we followed this procedure: 1. For K=1, we considered the descriptor that best correlated with ChA. 2. The K=2 descriptor was chosen among all the remaining ones by finding the descriptor such that after U=100 experiments of randomly choosing 75% of the dataset for training and 25% for testing, the mean MAE achieved by the two descriptors (the one found in stage 1 plus the new one) was minimal. 3. The K=3 descriptor was chosen among all the remaining ones by finding the descriptor such that after U=100 experiments of randomly choosing 75% of the dataset for training and 25% for testing, the mean MAE calculated with three descriptors (the previous two descriptors found in stage 2 plus the new one) was minimal. 4. Following this strategy, the curve MAE(K) has a minimum value as K increases, that defined the optimal model which has K descriptors. This age estimation strategy has been implemented using scikit-learn, `http://scikit-learn.org/stable/`. The entire code can be downloaded at `https://github.com/compneurobilbao/aging`.

## 6.3 Results

A population of N=155 healthy participants (81 female, 74 male) with age varying from 10 to 80 years (mean= 44, standard deviation=22) was used for the study. Together with physical activity scores, triple acquisitions including structural, diffusion tensor and resting functional imaging were acquired for each participant. We used the BHA Brain Hierarchical Atlas (BHA, see [69] and Methods) with 2514 regions and calculated for each participant the weighted SC and FC connectivity matrices, representing respectively the region-pairwise streamline number and the region-pairwise Pearson correlation of resting-state activity time series.

We first validated the use of BHA for the study of aging. figure 6.1 shows for two populations, one young (age<25.1 y, N=54 parti-

cipants) and other old (age>61.9 y, N=54 participants), indicating that BHA, although initially derived in a population of young adults, also preserves the correspondence between SC modules and FC modules independently on participant age. This issue was quantified by assessing cross-modularity (X), obtaining X = 0.312 for the young population and X = 0.309 for the old, and therefore showing that cross-modularity was 99% preserved along the lifespan.

Next, we calculated for all levels M of the BHA (with 20<=M<=1000), four different module descriptors (figure 6.2): 1) the functional internal connectivity (FIC), 2) the functional external connectivity (FEC), 3) the structural internal connectivity (SIC) and 4) the structural external connectivity (SEC), that we used for building the correlo-dendrograms (CDG) to find the highest correlation between module connectivity and ChA, whilst maximizing the spatial resolution.

Figure 6.3 shows the structure-function CDGs, calculated as the geometric mean between the correlation value obtained from the functional descriptor and the correlation value obtained from the structural one. This allowed building one CDG based on external structure-function connectivity (figure 6.3a, associated to connections with longer fiber length) and a different one based on internal structure-function connectivity (figure 6.3b, associated to connections with shorter fiber length). Brain maps from the external CDG (figure 6.3a) and the internal CDG (figure 6.3b) were built assigning to each brain region the maximum absolute value of structural-functional correlation across all BHA levels.

By looking to external connectivity patterns, maximum age correlations were found bilaterally in several cortical and subcortical AAL regions: the frontal superior and middle, cingulum middle, parahippocampus, calcarine, cuneus, lingual, occipital superior, middle and inferior, fusiform, precuneus, caudate, putamen, thalamus, temporal pole middle and temporal inferior.

By looking to internal connectivity patterns, maximum age correlations were found bilaterally in the insula, cingulum anterior, calcarine, cuneus, occipital superior, middle and inferior, fusiform, parietal

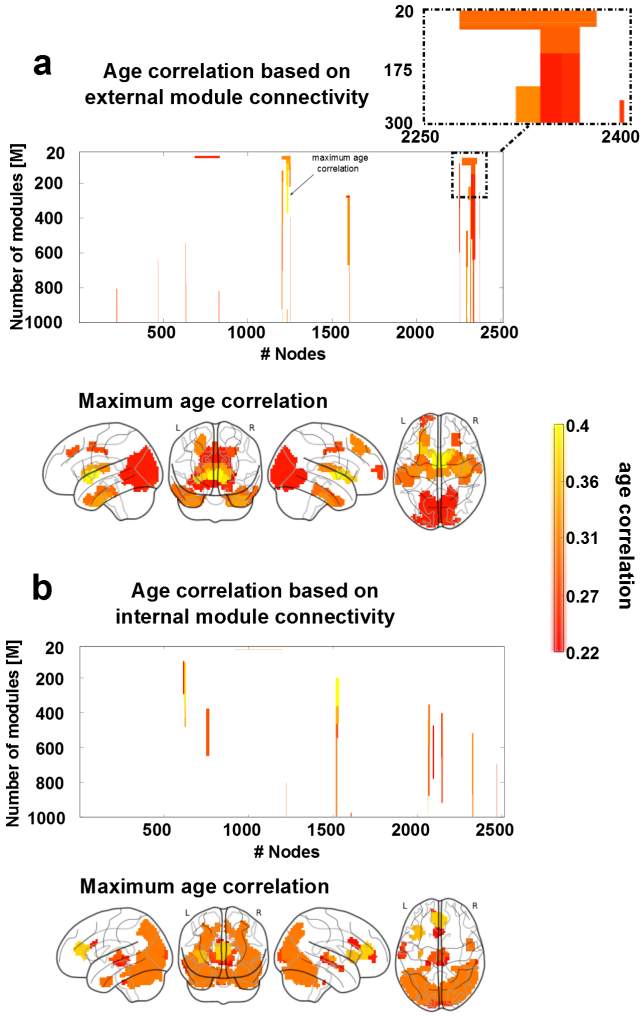


Figure 6.3: **Structure-function correlo-dendrogram (CDG) and structure-function brain maps of age correlation across the multi-scale brain partition.** To build structure-function age CDGs, we calculated for each module appearing in the BHA partition (20<=M<=1000) the correlation (and associated p-value) between age participant and FEC, FIC, SEC and SIC. **a:** Brain regions with external connectivity affected by age. 3D brains show per each of the 2514 regions, the value of maximum correlation achieved by that region among all values in the CDG (illustrated here with an arrow). A zoomed inset of the CDG is reported on the top right, showing how module division affects the correlation with age. **b:** Similar to panel a, but for age correlation with respect to internal connectivity.

superior, angular, precuneus, thalamus, temporal middle and inferior and cerebellum.

Since the structure-function CDG does not provide any information on the individual contribution that either the structural or the functional descriptor has on the correlation value, we separated all possible four cases of combined correlations (increased structural and functional; decreased structural and functional; increased structural and decreased functional; decreased structural and increased functional) and reported them separately in figure 6.4.

The external connectivity analysis identified brain regions with opposing tendencies by which the structural connectivity decreased with age whilst the functional connectivity increased (figure 6.4a, blue rectangle), a mechanism representing network homeostasis. These regions were found bilaterally in the frontal superior and middle, calcarine, cuneus, lingual, occipital superior, middle and inferior and precuneus. Regions for which both structural and functional connectivities decreased with age (figure 6.4a, green rectangle) were found bilaterally in the parahippocampus, fusiform, caudate, putamen, thalamus and temporal pole middle and inferior.

The internal connectivity analysis did not identify any brain region in which the structural connectivity decreased with age and the functional one increased (figure 6.4b, blue rectangle), indicating that network homeostasis only was appreciated when looking to external connectivity patterns. Regions where both structural and functional connectivity decreased with age (figure 6.4b, green rectangle) were found in the insula, cingulum anterior (the anterior part of the default mode network), calcarine, cuneus, occipital superior, middle and inferior, fusiform, parietal superior, angular, precuneus, temporal middle and inferior and the cerebellum.

To calculate the MLE we first pooled into a common list the four set of connectivity descriptors (FIC, FEC, SIC, SEC) and ordered them descendant in age correlation (that is, the first elements in the list were the descriptors that most correlated with age). By simply increasing the number of descriptors into the MLE, the correlation between ChA and BCA monotonously increased with age (figure

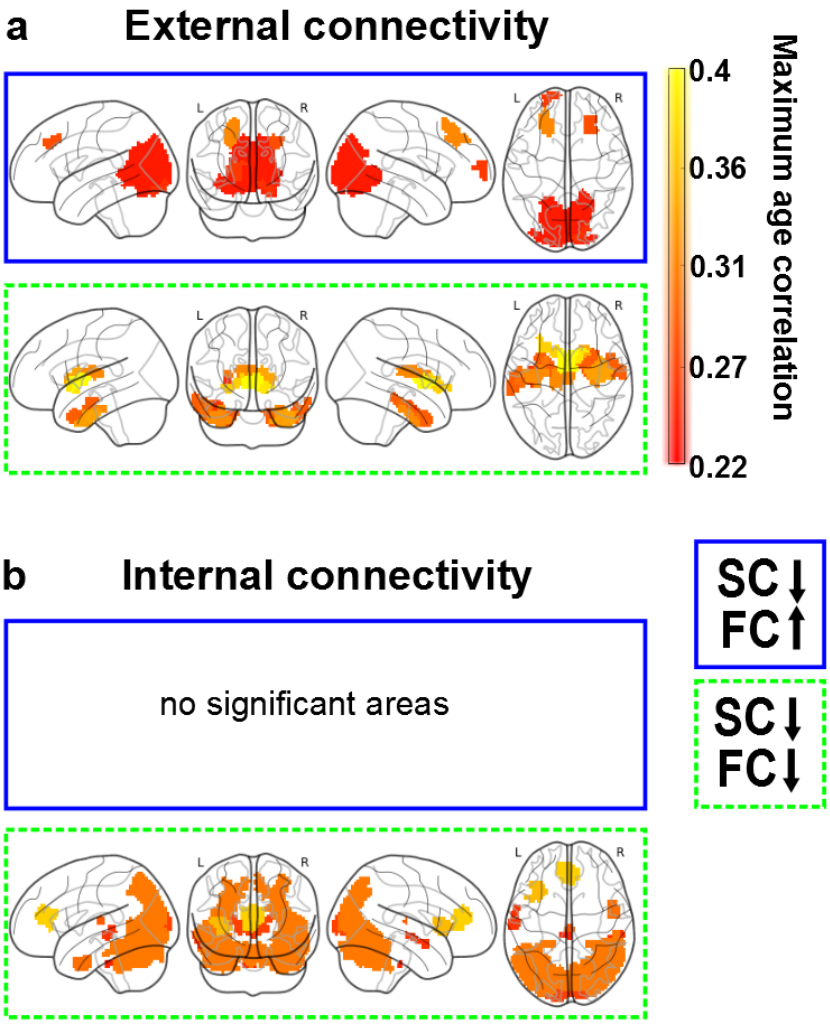


Figure 6.4: **Functional connectivity modulation along lifespan.** SC decreased with age, but FC might either increase (rectangle with solid blue line) or decrease (rectangle with dashed green line), and this occurred for both external connectivity descriptors (panel a) and internal connectivity descriptors (panel b). Notice that the situation of FC increasing and SC decreasing did not exist with regard to internal connectivity. As in figure 6.3), all the non-zero correlation values plotted here were statistically significant (after multiple-comparison correction).

6.5a), showing overfitting, that was solved by splitting the entire dataset in two pieces, 75% of the dataset used for training (to calculate the MLE solution) and the remaining 25% used for testing (to calculate the MAE). By adding one by one descriptor whilst following an optimization procedure (see Methods), the optimal age estimation occurred for K=38 descriptors, which provided a minimum mean MAE value (after U=100 repetition experiments) equal to 5.89 years (figure 6.5b). When calculating MLE using these K=38 best descriptors, the graphical representation of ChA as a function of BCA showed an excellent correspondence (figure 6.5c, correlation=0.95, p-value<10-20). Next, we obtained brain maps of the best K=38 descriptors (figure 6.5e). Because by construction of our model each of the 2514 regions might participate in four different classes of descriptors (FIC, FEC, SIC, SEC), we plotted each region according its Age Participation Index (API), an integer number between 0 and 4 and indicating with how many of the four classes a specific brain region contributed to the age estimator model.

Regions with API equal to 1 were found bilaterally in the frontal superior, insula, cingulum anterior and middle, hippocampus, parahippocampus, calcarine, cuneus, lingual, occipital superior, middle and inferior, fusiform, precuneus, thalamus, temporal middle and inferior and temporal pole middle. Regions with API equal to 2 were found bilaterally in the parahippocampus, fusiform, caudate, putamen, thalamus, temporal pole middle and temporal inferior. Finally, regions with API equal to 3, and therefore, the regions with a major correlate of physiological aging were found in the connectivity of basal ganglia (caudate, putamen, pallidum) and thalamus.

Next, we looked into the networks that, starting from regions with API=3, were connected to the rest of the brain. These regions were connected functionally and bilaterally to orbitofrontal (superior, middle and inferior), middle frontal, olfactory, gyrus rectus, cingulum (anterior, middle and posterior), calcarine, middle occipital, fusiform, precuneus, temporal middle and cerebellum. Structurally, these regions were inter-connected and also connect with the insula. Finally, regions with API=3 (including part of the caudate, putamen, pal-

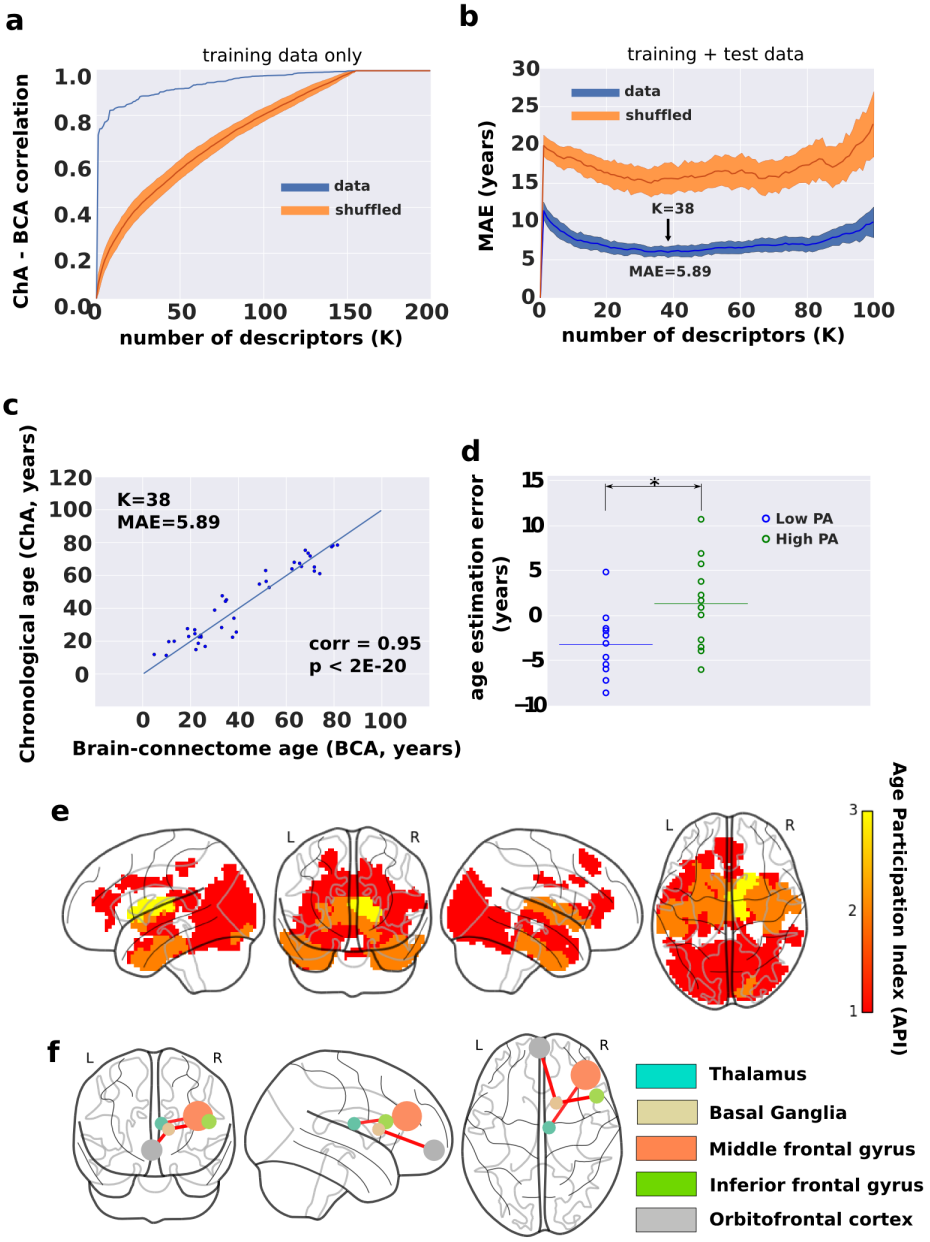


Figure 6.5: **Chronological age (ChA) vs Brain-connectome age (BCA) and its modulation by the amount of physical activity.**

Figure 6.5: **Chronological age (ChA) vs Brain-connectome age (BCA) and its modulation by the amount of physical activity.** **a:** Correlation between ChA and BCA as a function of the number of descriptors (K), using the entire dataset for training (methods). The larger number of descriptors, the higher the correlation. However, this strategy is well known to produce overfitting. In blue, we colored results from real data, and in orange, we plotted the results after shuffling the age vector a 100 times, providing the null-distribution (mean SD). **b:** Mean absolute error (MAE) as a function of K, using 75% of the dataset for training and 25% for testing. The minimum MAE, corresponding to 5.89 years provides optimal solution, achieved when K=38 different descriptors. Similar to panel a, blue and orange represent respectively real and shuffled data after 100 experiments. **c:** For a single estimate (chosen to have a similar MAE as the average one over the 100 experiments), we plot ChA (in years) as a function of the BCA (here, equal to the MLE solution with the best K=38 best connectivity descriptors), which provides a correlation value of 0.95 ($p<2E\text{-}20$). **d:** Age estimation error (ChA minus BCA) for two groups of participants, one performing high physical activity (PA), and a different one with low PA values. **e:** Brain maps of the K=38 best descriptors. Color bar indicates age participation index (API), accounting for how many times one brain region is significantly correlated with age in relation to any of the four following categories: SEC, SIC, FEC and FIC. Basal ganglia and thalamus are the brain structures whose connectivity participates most prominently in aging. **f:** Basal ganglia and thalamus connect according to a structure-function manner to the inferior and middle frontal gyri together with the orbitofrontal cortex, ie. the so called fronto-striato-thalamic (FST), is the major pathway participating in brain aging.

lidum and thalamus) were structurally-functionally connected to the orbitofrontal cortex and to the inferior and middle frontal gyri (figure 6.5f).

We finally asked whether PA can in any manner modulate BCA (ie., if PA can modify the brains structural-functional wiring in a manner that age estimation has a systematic bias). To provide an answer to that question, we compared the estimation error (defined as ChA minus BCA) in two groups, one group with high values of PA (90th percentile) and another one with low values of PA (10th percentile, figure 6.5d). By building the MLE with the best K=38 descriptors, we obtained a mean estimation error of -3.2 years (SD=-3.7) for the low PA group, and of 1.33 years (SD=4.94) for the group with high PA. The estimation error was significantly different in the

two groups (p-value=0.02 after a KolmogorovSmirnov test), and this occurred independently of ChA, as the correlation value between the estimation error and age was -0.05 (p-value=0.88) for the group with high PA and 0.39 (p-value=0.23) for the group of low PA.

## 6.4 Discussion

The chronological age (ChA) differs from the biological one. Whilst the former is defined as the time running since birth, the latter quantifies the maturity level that an individual (or an organ) has at the operational level. In relation with the brain, the discrepancy between the brain age and ChA might work as a biomarker for quantifying deterioration as a result of disease or improvement after some treatment or therapy, which has unlimited applications. Here, we asked whether the brain age could be determined exclusively based on structure-function connectivity metrics, and therefore, we did not take into consideration typical morphological descriptors (such as grey and white matter atrophy or ventricular volume) that have been widely shown to correlate with ChA. Our results demonstrate that the brain connectome age (BCA) is an accurate estimation of ChA, as it provides a mean absolute error of 5.89 years in a group of N=155 participants with age ranging from 10 to 80 years. Our results also reveal that the basal ganglia/thalamus and their connection with frontal areas is the key circuit accounting for the age estimation. Furthermore, we also report that the level of physical activity (PA) rejuvenates the brain connectome, implying that high-PA participants have an associated BCA that qualifies them as younger than low-PA participants.

Several studies have assessed discrepancies between brain morphological age and ChA for measuring brain functioning in pathological groups. In relation with mild cognitive impairment (MCI), it was shown that the brain age could become even 10 years higher than ChA [82]. In a different study, it was shown that the error in age estimation predicted the conversion from MCI to Alzheimers disease better than any other variable [88], as compared to imaging morphological variables (such as the volume of subcortical structures),

cognitive scales or protein biomarkers in cerebrospinal fluid. One-year bias was associated to 10% higher risk conversion. In relation to other pathologies, and also using morphological descriptors to estimate the brain age, the difference between brain age and ChA explained for instance brain deterioration from attenuated psychosis to chronic schizophrenia [108], brain deterioration in patients with human immunodeficiency virus [46], accelerated atrophy after traumatic brain injury [45] (suggesting that the chronic effects after the insult can resemble normal aging), but also brain rejuvenation after meditation [126]. Morphological age-related alterations have been reported in all body organs, such as liver, kidney, heart, lung, skin, but notably, what makes the brain distinct from other organs is precisely its complex wiring, where short-range connectivity operates at multiple scales in combination with long range circuitry, allowing the two main brain functional principles of segregation and integration [202] to work in harmony. Therefore, the BCA model presented here provides a new complementary and fundamental approach within the above framework, fully focused on the multi-scale organization of the brain circuitries and networks, enabling to correlate aging with lower and higher brain functions.

Only very few studies have made use of connectivity metrics for age estimation, but none so far have combined SC and FC metrics to perform the estimation. By combining morphological descriptors together with functional connectivity ones, Liem et al (2017) were able to improve age estimation up to 4.29 years [122]. In relation to connectivity metrics, a seminal study showed that resting FC descriptors estimated brain age [72], but rather than addressing physiological aging, the authors focused on neural development in the age range between 7 and 30 years. By using only structural networks, but not functional data, it was shown that a simple metrics such as the sum of all connectivity links (ie., streamline number) weighted by the age-link correlation, estimated ChA with high precision [95] in healthy participants aged 4 to 85 years.

By combining both SC and FC descriptors in the present study, we have achieved a high performance, quantified by an accuracy of

5.89 years. To the best of our knowledge, such an approach has never been reported before in the context of age-estimation. When repeating the entire procedure using only SC descriptors, the performance was worse (accuracy of 8.1 years). Analogously, when using only FC descriptors, the performance was also worse (accuracy of 8.45 years).

Our results not only reveal the relation between BCA and the aging process, but also highlight how the wiring and the dynamics of brain networks cannot be disentangled without losing the emergent synergetic picture for their operational complexity. Indeed, when looking solely at function, as it happens in task fMRI, a distinct scenario emerges, the so-called frontal super-activation, where younger people exhibit no or lateralized frontal activation when performing the task, while older people incorporate unilateral or bilateral frontal cortex activation [38]. Our BCA model, although obtained when the brain is at rest, extends task-related studies, revealing that the fronto-subcortical (striatum and thalamus) complex is the primary circuit critically accounting for the functional age-deterioration. Indeed, the key element is that the multi-scale modular BCA approach used in this work perfectly preserves the intrinsic link between structure and function. In fact, the resting activity is shaped by modular organization, where the structural and functional architecture clearly merge and match each other [69].

Several studies have shown that the connectivity profile of the basal ganglia (BG) and thalamus is affected by aging and correlates with age-related neuropsychological decay. For example, a reduction in thalamic volume along the lifespan has been associated with age-related sensorimotor performance deterioration [183]. In relation to BG, and far beyond its classical association to motor function[102], there is nowadays mounting evidence to associate the BG decline with executive function deficits along the lifespan, such as motor switching [53], inhibitory [52, 116] and cognitive control [90], but also motor learning [40], whereby older adults perform worse than young. The status of connectivity between the thalamus and BG, by means of the fronto-striato-thalamic (FST) circuit, has been associated with task-switching performance [54, 115, 113, 114], reflecting the capacity for

suppression of certain actions to flexibly adopt new different ones. However, what makes our approach particularly novel (and without any a priori assumption about the participation of these regions) is that it provides quantitative evidence that the FST circuit makes the major contribution for age estimation.

Different studies have argued that aging and age-associated cognitive impairment is dominantly mediated by the hippocampus and this is supported by the overwhelming amount of work done on this brain area in human and animal systems during the past decades (see [15, 73]. Therefore, these studies support the general idea that healthy ageing in somehow related (although less aggressive) to neurodegenerative ageing, where the disruption of the hippocampus circuit has been clearly established [9]. Although our analysis has shown that the hippocampus has an Age Participation Index of 1 (and therefore assumes some role in aging), however, we have demonstrated that the medial subcortical-cortical FST pathway is the major circuit-mediating aging (with an Age Participation Index three times higher than the one for the hippocampus). We infer from this result that future research on brain aging should make an increasing effort to study this circuit in much more detail, thus clearly differencing the two classes of ageing, healthy (FST-mediated) vs. neurodegenerative (hippocampus-mediated).

As far as we know, our study is the first one demonstrating that physical activity (PA) can rewire the human connectome to increase its resilience by slowing down brain aging. In relation to brain morphology, it has been shown [192] that none of the following activities have a strong implication in the estimation of brain age: walking/hiking, jogging, running, bicycling, aerobic exercise, lap swimming, tennis/squash/racquetball or low intensity exercise, but in addition, the same authors showed a small association between brain age and a variable named daily number of flights of stairs climbed. Here, by only looking to structure-function connectivity descriptors rather than morphological variations, we provided strong evidence for an association between PA and ChA estimation. Notably, and distinct from previous work [192], our methodology does not need

to disentangle which specific type of physical exercise significantly impacts brain aging, although it has the potentiality.

The originality of our approach is based on identifying, on a multi-scale level, brain modules whose connectivity correlate structurally and functionally with age. Next, the significant descriptors are pooled to create an optimized linear regression model capable to assess the biological brain age of a given connectome with minimal error. Such a methodology opens two important and different perspectives. First, it provides a quantitative approach to assess the impact of therapies on biological brain aging (ideally rejuvenating the brain connectome), diseases (accelerating the connectome aging) and other factors shaping lifestyle. Secondly, the same methodology can be used to correlate any graded variable to the brain connectome, and not only age as approached here, thus allowing for brain-connectome estimators of any other biomarker. In this framework, a biomarker might be any functional, structural or behavioural score obtained from participants such as, for instance, protein levels from cerebrospinal fluid or blood, or a clinical scale measuring disease severity.

## 6.5 Methodological considerations

We have approached age estimation with linear connectivity descriptors. However, aging has been shown to alter many of the cognitive functions in a quadratic manner, and more specifically, in an "U-inverted" fashion [90]. We repeated the same methodology while adding quadratic terms to the linear model defined by Eq. 6.1 quadratic terms. Results are given in figure 6.6. A striking difference is that the external connectivity patterns of the prefrontal and occipital cortices have a strong quadratic dependence on age (figure 6.6a), not observed when only linear terms were taken into the MLE (figure 6.3a), a fact which is in strong agreement with task-dependent functional imaging studies [90]. Similarly, when looking to internal connectivity patterns (figure 6.6b), quadratic dependencies reveal memory (hippocampus and temporal pole) together with limbic (amygdala) circuits strongly correlating with age, and this, again, was not observed when only

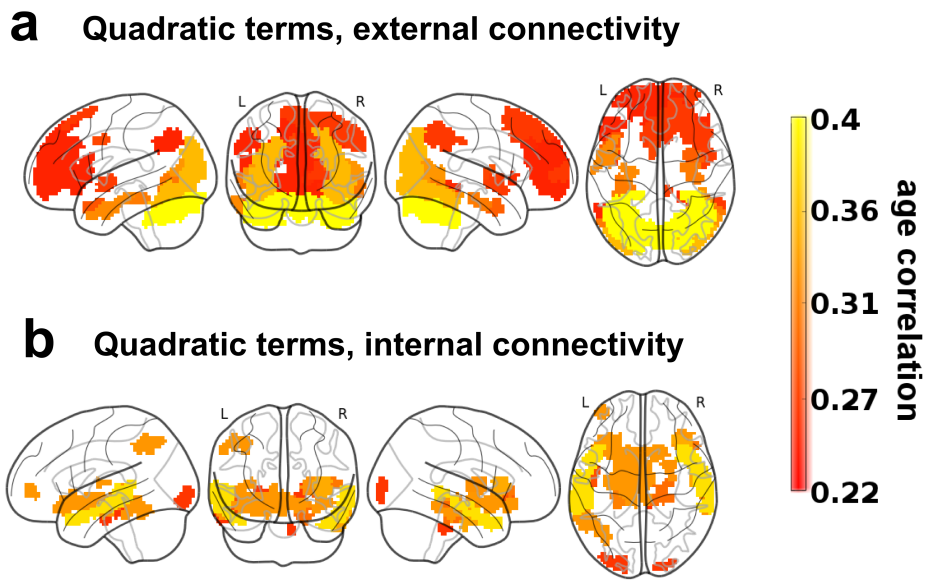


Figure 6.6: **Structure-function brain maps of quadratic terms most correlating with age.** **a:** External connectivity patterns (similar to figure 6.3a when only linear terms were considered for age estimation). **b:** External connectivity patterns (similar to figure 6.3b when only linear terms were considered for age estimation).

linear terms where considered (figure 6.3b).

However, after adding quadratic terms, the accuracy of the age estimation did not improve the results, as repeating exactly the same procedure with quadratic terms provided a very similar performance to the linear case (accuracy of 5.88).

We have built a MLE and estimated age from the entire dataset, but separating the data in small sets improved our results. When repeating the same procedure only to a young group (N1=50, 10.88<age<25), and after optimizing the BCA estimation, we achieved MAE=1.21 by using K=28 connectivity descriptors. Similarly, for a group of adults (N2=49, 25<age<60) and old participants (N3=56, 60<age<80.67) we achieved respectively MAE equal to 2.49 (K=30) and 1.57 (K=34), and therefore by stratifying the dataset along different groups of age,

the BCA estimated age more accurately.

Lastly, our method makes use of network node metrics to estimate brain age, but this method can also be extended to the link level, thus identifying specific pathways rather than brain regions, provided a large cohort is available to control for multiple comparisons (as a given connectome has N nodes and N2 links).

## 6.6 Summary

We have shown that the chronological age can be estimated with a much higher accuracy using structural-functional connectomics than separate structural or functional connectivity metrics. The strategy of assessing the mismatch between chronological and brain age is suggested to be useful for quantifying the brains deterioration or its reorganization after new treatments, implying a multitude of meaningful applications. In particular, we have shown that participants who exhibit higher levels of physical activity have a brain connectome age that appears younger than the chronological one, but also that low levels of physical activity increase the brain connectome age. Therefore, our results demonstrate that physical activity makes the brain more resilient by slowing brain aging. By using a blind approach in which no brain structures were a priori assumed to be affected by aging, our method has shown that the connectivity of the fronto-striato-thalamic circuit is critically important for brain aging, consistent with previous work associating this circuit to age-related deterioration of cognitive control of a multitude of actions.

# Chapter 7

# Conclusions

In this last chapter, I will summarize the main findings and conclusions of the previous chapters and give some final remarks over the thesis and the work done.

## 7.1 Summary of chapters

The three first chapters were a compound dedicated to epilepsy, were we analyzed extensively and using different types of data the majors of connectivity on this disease.

In Chapter 2, we used a mice model of MTLE that allowed us to explore the longitudinal deterioration of the epileptic brain. We observed variations in FC across the transition from an initial episode of status epilepticus to seizure chronification. More precisely, the network connectivity index showed a strong drop-off in the overall brain connectivity the first day, but it smoothly increased for several days afterwards.

In Chapter 3, by taking the resection area of patients as a reference, we addressed the patterns of II near to the epileptogenic zone, the area essential for seizures to initiate and propagate. In terms of spatial organization, our results show that R matched the epileptogenic zone while S was distributed more in the surrounding area. In relation to dynamics, R made the largest contribution to high fre-

quency bands (14-100Hz), whilst S was expressed more strongly at lower frequencies (1-7Hz)

In Chapter 4 we developed a multimodal approach to study epilepsy, adding to intracraneal EEG data both structural and functional MRI data. We then explored the data using two approaches: modular (looking for similar module structures across modalities) and single link (focused in link-to-link similarities inside the networks). We could identify notable similarities between fMRI and deep electrodes connectivity matrices and made an exploratory analysis over the suspected epileptogenic areas matching with positive fMRI activity.

In Chapter 5, we have seen that when comparing Alzheimer's Disease with a healthy population with regard to the information flow between the most fundamental resting state networks, the average activity (roughly coincident with the first principal component) within ROIs does not provide significant differences in information flow between disease and control. However, it is the second component and to a lesser extent the third, the ones that can differentiate the information flow between disease and control. In other words, differences are found when looking to information flow beyond average ROI activity, as curiously, it is usually done in neuroimaging. Finally, Alzheimer's Disease showed bigger information flow in comparison to control, meaning that, RSNs speak more each other in Alzheimer's Disease in comparison to control.

Finally, in Chapter 6 we studied aging in healthy population in a multiscale approach. Our results were two-fold. Firstly, we found that aging widely affects the structural-functional connectivity of multiple structures. And secondly, we found that the structure-function connectivity between basal ganglia and thalamus to frontal areas, a.k.a. the fronto-striatal-thalamic circuit, makes the major contribution to age estimation.

## 7.2 General conclusions

Having each chapter has its own conclusions, here, we briefly mention general aspects covering the entire scope of the thesis.

- A latency period was identified in a mice MLTE model. During this latency period, the transition from a healthy brain into an epileptic one, or epileptogenesis, occurs due to changes in the molecular, cellular, and network properties of the brain in response to the initial precipitating event. Studies at the molecular and cellular level, might add an integrative approach to better understand the process of epileptogenesis to eventually open new venues for more efficient therapeutic strategies.

- Applying Interaction Information to clinical data reveals new aspects of epileptogenic structure in terms of the nature (redundancy vs. synergy) and dynamics (fast vs. slow rhythms) of the interactions.

- Multimodal data approaches at electrode contact level can be of great importance to explain some connectivity patterns and to explore brain's reorganization after surgery.

- When comparing Alzheimer's Disease with a healthy population with regard to the information flow between the most fundamental resting state networks, the average activity within ROIs does not provide significant differences in information flow between disease and control. However, the second component can differentiate the information flow between disease and control.

- New connectivity circuits affecting healthy aging were found and, more importantly, the same multiscale methodology can be generally applied both to evaluate the impact of other factors and therapies on brain aging, and/or to identify the structural-functional connectivity patterns correlating to other biomarkers.

## 7.3 Reflection

This thesis reflects the application of methods from Computer Science, Mathematics and Physics to Medicine and the exploration of very diverse neural data (ranging from MR to electrophysiology in both human and mice). Although Computer Scientists are aware that day-to-day clinical practice is far away of using methodology presented in this thesis as a valid approach to identifying or solving diseases, we also believe that Computational Neuroscience has help to push forward the boundaries the human knowledge and the understanding of the brain.

If we want MDs to adopt methods to quantify possible diseases in the brain, Computational Neuroscience has to provide reliable and reproducible protocols. Despite the work presented in this book, the embrace of reproducible practices (towards excellence) has been a valuable lesson learned during this training period.

I truly believe that multidiscliplinar teams working in hospitals together are the key to open new challenges in Medicine that eventually will end up in the achievement of great goals. With this work, I humbly wanted to give an example of that interaction, showing the enormous potential of mixing disciplines.

# Euskaraz

# Kapitulua 8

# Sarrera

## 8.1 Ikuspegi historikoa

Gizadiaren historian, giza gorputzaren funtzionamendua eta harengan eragina duten gaixotasunen ulermen sakonaren garapena gertatu da. Historiaurretik, sendatzeko landareak erabiliz, medikuntza teknika modernoak agertu arte, organo transplante edo gaixotasun infekzioso birulentoak (baztanga, esaterako) desagerrarazteko gai izateraino.

Ezagutzaren garapen horretan, esan daiteke medikuntzak bide luzea egin duela bakarrik XIX. mendera arte, kimika eta biologiaren etorrerak anestesiaren, antiseptikoen, virologiaren eta bakterioaren aurrerapen garrantzitsuak ekarri zituenean.

Geroago, fisika modernoari esker aurrerapen garrantzitsuak egongo lirateke garatutako teknologietan, hala nola erradiografia eta elektrofisiologia. XX. mendearen erdialdetik aurrera, ingeniaritza eta informatika medikuntzaren aurrerapenean faktore erabakigarriak izan da, algoritmo berriak eta teknologiaren hobekuntza garatuz.

Gure historiari begiratuz gero, arloen arteko elkarlana, hau da, zientzia multidiziplinarrak, giza ezagutzak aurrera eramateko gakoa da; ez soilik medikuntzan, diziplina guztietan baizik. Hasiera batean urrun egon daitezkeen arloen adituen arteko lankidetza estua beharrezkoa da, eta horregatik, ezinbestekoa da haien arteko lotura izan

daitezkeen pertsonen formakuntza.

Tesi honen helburua da informatika, matematika eta fisika alorretatik datozen metodologiak eta teoriak neurozientzien alorrean aztertzea, gaixotasun neurodegeneratiboei arreta berezia emanez.

Neurozientziak, beste eremu batzuek bezala, aurrerapenak eragin ditu antzinako Egipton (momifikaziorako prestatzean garuna ateratzen zuteneko lehenbiziko seinaleak). KO 1000gn. urtean inguru, Al-Zahrawi, Medina Azaharan jaio zena eta Mairu Iberiar Penintsulan bizi zena, paziente neurologikoen ebaluazioa egin eta buruko lesioak, garezurreko hausturak, bizkarrezur-lesioak eta tratamendu kirurgikoak burutu zituen [4]. Errenazimenduan, Leonardo Da Vincik ekarpen anitz egin zituen neurozientziaren alorrean, garuneko fisiologiaren zirriborroak irudikatuz, 8.1 irudia.

Zientzia eta artearen binomio hau aintzat hartuta, hurrengo kasua aipatzea egokia da; burmuinean kaltifikazioak (harritxoak) antzeman dira, minbizi kasu batzuetan, hematoma subduralek edota epilepsiak eraginda. Posiblea da dementziak jota egondako gaixoren baten garezurrean egitura mineral horietako bat aurkitu izana Erdi Aroan eta "Eroaren-harria"kondaira sortu izana. Ideia ohikoa zen garai hartan eta iruzurtiek kondaira hauek baliatu zituzten trepanazioak egiteko. Jan Sanders van Hemessen, Pieter Bruegel, Pieter Huys eta Jheronimus van Aken (Hieronymus Bosch bezala ezaguna), Holandako eskolako pintoreak guztiak, "Eroaren-harria ateratzea"irudikatu zuten, 8.2 irudia.

Neurozientzietara bueltatuz, azken bi mendeetan iraultza jasan du diziplina honek. Ohiko ekarpen nabarmenak, besteak beste, Santiago Ramón y Cajal-en neuroanatomia deskribapenak (bere "Ikertzaile Gazteen Aholkularitza"liburua tesi hau idazteko laguntza eta inspirazio handikoa izan zen), neuroradiologia garatzea (X-izpiak , PET, CT, MR) eta Neurozientzia Komputazionalak diziplinaren sorrera.

Garunaren datuak eskuratzeko teknologien (elektrofisiologia eta erresonantzia magnetikoa) eta grafo teoriaren eta sareen tekniken arteko konbinazioa sakonki aztertu da lan honetan. Teknika hauen sarrera orokor bat eta tesiaren egituraren laburpen orokorra hurrengo orrietan aurki daiteke.


Irudia 8.1: **Leonardoren zirriborroak garunaren fisiologia deskribatuz a, b, c, d:** Leonardoren iruzkinak garun anatomian

Irudia 8.2: **Eroaren-harria ateratzea** Eroaren-harria ateratzea Hieronymus Boschen margolana, Madrilgo El Prado museoan ikus daitekeena

## 8.2 Burmuin Konputazionala

Ezagupen zientifikoen aurrerapenak azkarrak izan arren, garuneko sareak gaixotasun ezberdinetan nola aldatzen diren ez da oraindik sobera ezagutzen. Burmuinaren ezagutza sakonagoa behar da tratamendu berriak eta eraginkorrak diseinatzeko. Gaixotasun neurodegeneratiboetan eta pertsona osasuntsuenengan garuneko funtzioetan gertatzen diren aldaketak ulertzeko, aldaketa horiek jarraitzeko aukera ematen duten teknikak bilatu behar ditugu. Burmuinaren estruktura, funtzioa edo estruktura eta funtzioaren arteko nahasketak aztertu daitezke datuak eskuratzeko teknika ezberdinen bitartez, datu horiek grafo bilakatuz, konektibitatea eta dinamikak aztertzeko.

Tesi honetan, hainbat metodo garatu eta aplikatu dira bai gizabanako osasuntsuetan bai ez osasuntsuetan; adibidez, epilepsia pazienteak eta Alzheimer gaixotasuna (AD) pazienteak. Hurrengo orrialdeetan datuak eskuratzeko teknikak eta haien aplikazioak deskribatuko dira.

## 8.3 Burmuin datuak eskuratzen

Burmuina ikertzeko datuak eskuratzeko teknika desberdinak daude. Teknika hauek talde desberdinetan sailkatu daitezke erresoluzio espaziala kontuan hartuz [189]:

- **Mikroeskala**: Neurona eta konexio sinaptikoak neurtzeko eskala.
- **Mesoeskala**: Neurona taldeak neurtzen ditu, ehunka mikrometroko erresoluzio espaziala izanda.
- **Makroeskala**: Neurona talde handiak hartzen ditu barne. Neurona hauek burmuinaren area desberdinak sortzen dituzte interkonektatuta dauden bideen bidez.

Lan honetan Erresonantzia Magnetiko bidezko Irudigintza (MRI-*Magnetic Resonace Imaginig*) (makroeskalan hartukoak) eta elektro-

fisiologia (elektrodo sakonak edo garezur-barnekoak, mesoskalan zein makroeskalan hartukoak) datuekin lan egingo da.

### 8.3.1 Elektrofisiologia datuak

- **Elektroenzefalografia**: Elektroenzefalografia (EEG) garuneko jarduera elektrofisiologikoa erregistratzeko monitorizazio metodoa da. Normalean ez da inbaditzailea (ez du ebakuntzarik behar), buru-larruazalean kokatutako elektrodoekin egiten da. Teknika hau ez da tesi honetan erabiliko, duen seinale-zarata proportzio txikiagatik.

- **Elektrokortikografia**: Elektrokortikografia (ECoG), edo garezur barneko Elektroenzefalografia (iEEG), elektrofisiologia monitorizazio mota bat da, garuneko azalean (kortexean) zuzenean jarritako elektrodoek erregistratzen dutena. Kraneotomia (ebakuntza kirurgikoa garezurrean) egin beharra dagoenez elektrodoaren sareta ezartzeko, ECoG prozedura inbaditzailea da.

- **Elektrodo sakonak**: ECoG bezala, elektrodo sakonen fisiologia ere EEG mota inbaditzailea da, elektroenzefalografia inbaditzailea (iEEG) deitzen zaio. Baina ECoG-ekin alderatuta, elektrodoak ez dira kortexean jartzen, garunean dauden egitura sakonenetan sartuta baizik.

### 8.3.2 MRI datuak

MRI teknika, prozedura ez-inbaditzailea da eta biztanleria osasuntsuaren garunaren ezaugarri funtzionalak eta estrukturalak argitzeko trebetasuna duela erakutsi du. Beraz teknika honek oso erabilgarria den informazioa ematen du gaitz neurologiko desberdinetan agertzen diren aldaketa estruktural eta funtzionalak ikertzeko.

Tesi honetako atal gehienetan hiru irudi mota desberdin erabili dira: irudi estrukturala, difusio irudia eta irudi funtzionala. Irudi hauek hiru dimentsio dituzte eta *voxel*-ez osaturik daude, 3 dimentsioko sareta baten balioa (alegia, *pixel*-aren 3 dimentsioko balioki-

dea). Irudi hauen *voxel* tamaina 1 eta 5mm artekoa da normalean bista bakoitzean (sagitala, koronala zein axiala).

- **MRI datu estrukturalak**: T1 edo T2 izenez ezaguna, irudi mota hau bereizmen handiko irudia da, garunaren gai gris eta zuriaren egituren forma, neurria eta integritatea (lesiorik ez izatea) ikusteko kualitatiboki eta kuantitatiboki hobekien egokitzen dena. Lan honetan, gehienbat, estrukturen bereizmen hobeagoa lortzeko eta bestelako irudizko modalitateentzat erreferentzia anatomikoa izateko proxy bat bezala erabiliko da.

- **MRI difusio datuak**: Difusio MRIak (DWI), ur molekulen mugimendu termikoa (bai magnitudea eta bai norabidea) neurtzen du *voxel* bakoitzean.

  Ur molekulen hedapenean oinarritutako printzipioan oinarritzen da. Hau 3 dimentsioko prozesu bat da, non molekulak modu ezberdinean mugitzen diren norabide guztietan (libreki). Ur molekulen difusioa garuneko gai zurian askoz ere murriztuagoa dago materia grisean baino. Difusioaren murrizketa hau axonen norabidean gertatzen da. DWIak duen erresoluzio espazialak axonak detektatzeko aukera ematen ez badu ere, axonen bilkurak (zuntzak) ikusteko balio du (milaka axon, era koherente batean antolatuak, makroeskalan), voxel bakoitzeko axon populazioen norabidearen hedapena ematen du.

  Behin norabide hau eta tentsorearen indarra ezagutzean, bideak eraiki daitezke, traktografia izeneko prozesu batean zuntzen norabideak jarraituz. Garrantzitsua da azpimarratzea ez dugula axonen bideak lortzen, baizik eta garunaren egitura makroskopioaren konektibitatea ateratzen (zuntzak, milaka axon batera).

- **MRI datu funtzionalak**:

  Erresonantzia magnetiko bidezko irudigintza funtzionala (fMRI), teknika ez inbaditzailea da eta jarduera neuronalaren ondorioz agertzen den garunaren portaera hemodinamikoa neurtzen du. Jarduera neurologikoak gora egiten duenean, honek energi

eskaera bat eragiten du garunean eta odolak oxigeno gehiago askatzen du, prozesu honi erantzun hemodinamikoa deitzen zaio. Honek oxyhemoglobina eta deoxyemoglobina maila erlatiboak aldatzea eragiten du (odol oxigenatu edo deoxigenatua) eta seinale magnetikoaren aldaketa bat eragiten du, MRI eskanerra erabiliz antzeman ahal dena.

Jarduera neuronala milisegundoetan gertatzen den bitartean, erantzun hemodinamikoa mekanismo motelagoa da. Azken kasu honetan, 5 segundo behar ditu balio altuenera heltzeko eta hasieratik 15 segundo pasatuko dira balio txikienera heltzen denerarte. Erantzun hemodinamiko hau pertsonaren eta aztertutako burmuin zatiaren arabera aldatu ahal da.

## 8.4 Garun sareak

Konektibitatea aztertzeko garuna sare bat bezala erabiltzen da normalean. Sareek sistema biologiko konplexuak (garuna barne) aztertzeko potentzial izugarria dute eta hauek erabiliz, garunaren oinarrizko arkitektura eta funtzio nagusiak azaltzen hasi dira. Sareak deskribatzen eta kuantifikatzen dituen hizkuntza matematikoari Grafo teoria deritzogu.

Garuneko datuak grafiko gisa karakterizatzeko modurik onena interesdun eskualdeak (Region of Interest = ROI) edo elektrodoen kontaktuak, grafikoen erpinak izango balira bezala hartzea da. Erpin hauek definituta daudelarik, hurrengo urratsa erpin hauen arteko konektibitatea zehaztea izango litzake.

Hiru konektibitate modu nagusi daude [189, 30]:

- **Konektibitate estrukturala**: konexio anatomikoak kodetzen ditu garun leku desberdinen artean [188], normalean difusio irudietako gai zuriko zatietatik ateratako zuntzak [56].

- **Konektibitate funtzionala**: Neurona populazio ezberdinen arteko aktibazio eta menpekotasunak definitzen ditu [83]. Garuneko antzeko bi gunek aktibazio funtzionala badute, konekti-

bitate balio sendoa izango dute bi zonalde horien artean. Konektibitate funtzionalak bai fMRI-tik bai elektrofisiologiatik (EEG, ECoG edota iEEG) lortutako dinamikei eragiten die.

- **Konektibitate efektiboa**: Elkarreragin kausalak edo informazio fluxua identifikatzen ditu [85].

  Konektibitate estrukturala edo funtzionalarekin ez bezala, erpinen arteko informazioak norabide bikoitza dauka, konektibitate efektiboak erpinen arteko informazioa zuzentzen du. Hau da, zuzendutako ertzek adierazten dute dinamika bat bizilaguna den erpin batek eragina duela, baina ez alderantziz.

## 8.5 Tesiaren laburpena

Tesi honetan, garuneko sareen analisi funtzionalak eta estrukturalak erabili dira, garun patologiko eta osasuntsuetan patroi ezberdinak bilatzeko. 9., 10. eta 4. kapituloetan epilepsiarekin zerikusia duten hiru kasu desberdin analizatu dira. Aurreko orrietan deskribatutako datu eskuratze teknikak erabiliz, 5. eta 11. kapituluetan berriz AD eta zahartzea pertsona osasuntsuengan.

Zehazki, 9. kapituluan sagu baten garunean FC analisi longitudinal bat aurkezten dugu hainbat egunetan zehar. Lan honen helburu orokorra FCak garuneko dinamiken desberdintasunak azaltzea da, garun osasuntsu batetik epileptiko baterako trantsizioa ikustea krisi pasarte baten ondoren. Helburu horretarako, hipokanpusean azido kainikoa txertatuko zaio, animalia klasikoaren eredu batean oinarrituta. Hasierako krisi baten ondoren, latentzia aldia gertatzen da eta, azkenean, epilepsiak gora egiten du.

10. kapituloan Informazioaren Teorian oinarritutako neurriak erabiliko dira, garunaren dinamika konplexuak aztertzeko. Teknika hau elektrodoen arteko informazio-fluxua aztertzeko erabiliko da epilepsiadun pazienteengan, kirurgia ondorengo emaitza ezagunarekin. Gure ikuspegiak Interakzio Informazioaren (II) neurriari jarraitzen dio. II-aren zeinuak hirukotearen aldagaien arteko elkarrekintzak erredundanteak (R) edo sinergikoak (S) diren esaten digu. Hemen, ikuspegi

honetatik abiatuta, hirukoteen arteko R eta S egoerak kalkulatuko ditugu epilepsia mesio-temporalari droga-erresistentzia duten gaixoen datu elektrofisiologikoetan, espazio-antolamendua eta dinamikak aztertzeko eremu epileptogenotik hurbil (krisi epileptikoaren hedapenaren arduraduna).

Epilepsiarekin bukatzeko, 4. kapituloan, sekuentzia multimodal bat deskribatuko dugu, sare epileptikoak antzemateko. Elektrokortikografian egindako aurreko lanak zabalduz, lan honetan garun-barneko elektrodoak eta erresonantzia magnetikoko irudiak erabiliko ditugu (bai difusiozkoak, bai funtzionalak). Datu mota berezi hauek, hiru iturri ezberdinetatik jasoak, garunaren konektibitate funtzionala eta estrukturala aztertzeko aukera emango digute, erpinez-erpin eta moduloetan, epilepsia ulertzeko emaitza interesgarriak lortuz.

Hurrengoz, 5. kapituloan Osagai Nagusien Azterketa (PCA) erabiltzen da informazioa ateratzeko Atsedeneko Sareetatik (RSN) (RSNak atsedeneko, estimulu eza duten egoeren, fMRI korrelazioetatik irteten dira) eta informazio-fluxuen neurriak kalkulatzeko osagai ezberdinen bidez. Metodo hau erabiliz Alzheimer gaixotasuna duten eta osasuntsu dauden Atsedeneko Sareen arteko komunikazioan desberdintasunak daudela aurkitu ditugu eta desberdintasun hauek ez direla beti lehen osagai nagusian (normalean informazioaren fluxuen analisirako erabiltzen dena) agertzen frogatzen dugu .

Azkenik, 11. kapituloan, osasuntsu dauden pertsonen garunaren berrestrukturazio funtzional eta estrukturala azalduko dugu. Hemen,parte hartzaile osasuntsuen (N = 155) garuneko irudiak biltzen ditugu, 10-80 urte bitartekoak, funtzionala (atsedenerako egoera) eta estrukturala (traktografia) konektibitate matrizeak eraiki ahal izateko. Ondoren, garun-konektoma adina kalkulatu dugu (BCA) estimatzaile bat erabiliz, eta BCA alderatu dugu adin kronologikoarekin, benetako adinarekin (ChA). Zahartze osasuntsu prozesuak burmuineko egitura anitzekin erlazioa duela antzeman dugu konektibitate funtzionala eta estrukturalari erreparatuz; hala nola, ganglia basala eta talamoa, zirkuito fronto-striato-talamikoa osatzen dutenak. Orain artean, zahartze prozesua paziente gaixoengan aztertua izan denez, hipokanpoaren garrantzia gainentzen zen soilik. Gainera, metodolo-

gia bera aplikatu daiteke garuneko zahartzearen gaineko beste faktore eta terapia batzuen eragina ebaluatzeko, eta/edo ChA-n eragin dezaketen beste biomarkatzaileekin korrelazioak identifikatzeko.

12. kapituloan, kapitulo ezberdinen eta tesi osoaren ondorio nagusiak laburbiltzen dira.

# Kapitulua 9

# Garuneko konexio funtzionalen aldakuntza longitudinalak

Aurreko atalean garuneko sareen sarrera jorratu da. Kapitulu hau hiru saileko lehenengoa izango da epilepsia gaixotasuna aztertzeko, datu mota ezberdinak erabiliz. Kapitulu honetan MTLE sagu eredu bat erabili dugu, garun epileptikoaren garapena denboran zehar aztertzeko.

## 9.1 Sarrera

Konektibitate funtzionalak (KF) garuneko area ezberdinen arteko antzekotasun estatistikoak kuantifikatzen ditu [83]. KF-k area ezberdinen arteko kausa desberdinetatik sortutako eraginak neurtzen ditu, esate baterako bi konexio estruktural partekatua izatea (garuneko fibrak) edo sarrera komun batek bultzatutakoak. Hori dela eta, KF-ean oinarritutako ikasketak oso baliagarriak dira gaixotasun neurologikoetan garuneko funtzionamenduaren gora-beherak tratatzeko, esate baterako, epilepsia, krisi kronikoak jasaten dituen gaixotasun neurologiko nagusia. Izan ere, KF-arekin egindako ikerketak ugariak dira epilepsian [28, 208, 24, 43, 214, 21], baina ikerketek normalean

pertsona osasuntsuaren eta gaixoaren arteko taldeen konparazioa egiten dute; horrekin alderaturik, lan honetan saguaren garuneko analisi longitudinal bat aurkezten dugu.

Gure helburu orokorra KF-k garuneko funtzio desberdintasunak kontutan izanik, garun osasuntsu batetik epileptiko baterako trantsizio osoa irudikatzea da, egoera epileptiko baten hasierako pasarte baten ondoren. Guk dakigula, trantsizio honetan gertatzen diren KF-aren aldaketek ez dira inongo aurreko lanean argitaratu. Gure hipotesiak KF egoera horiek bereizten ditu.

Helburu horretarako, epilepsia temporal-mesial klasikoan (MTLE) oinarritutako sagua erabiliko dugu, kainic acid (KA) (azido kainikoa) [182, 19] injekzioaren bidez lortzen dena. Hasierako krisi bat gertatu ondoren, egoera latentea (edo ezkutukoa) deritzoguna gertatzen da eta, azkenik, saguaren garunean giza MTLE-ren ezaugarri nagusiak antzematen dira (adibidez, ikus [185] eta barneko erreferentziak). Konfigurazio hau erabiliz lan honetan erakusten dugu, hain zuzen ere, KF-k egoera horiek bereizteko gai dela datuak longitudinalki landuz gero.

## 9.2 Metodologia

### 9.2.1 Experimentuaren protokoloa eta sagu grabaketak

Experimentu hauek Juan Manuel Encinas doktoreak gidatuak izan ziren Achucarro Basque Center for Neuroscience-n. Sagu heldu batek azido kainiko (KA) injekzio intrahippocampal bat jaso zuen (KA 1nmol 50 nL-ko), giza MTLE-n [33, 185] antzematen funtzio fisiopatologikoak errepikatzen dituen eredu esperimental bat erreproduzitzen duena. KF-ean aldaketak detektatzearen bila, garun barneko elektroenzefalografia (EEG) ikuskatu zen saio longitudinaletan zehar, 0 eguneko KA injekzioa (0 dpi) eta 21 dpi artekoak. Jarritako elektrodoak E363 / 8 platinum / iridio intrakraneal (Teflon isolatuta), 0.005 mm-ko diametrokoak eta 2 mm-ko luzerakoak izan ziren, plastikozko horma batean muntatutakoak, gerora hortzetarako hormigoi

bereziarekin garezurrean txertatutakoa.

Konfigurazio esperimentala 9.1 irudian ikus daiteke. Lau elektrodo txertatu ziren hipokanpoan eta geruza motorrean (motor cortex); Elektrodo hauek ezkerreko kortex (LC), eskuineko kortex (RC), ezkerreko hipokanpo (LH) eta eskuineko hipokanpo (RH) gisa markatu ditugu. KA injekzioa RH elektrodoan aplikatu zen (panelean gezi gorri batek adierazten duena).

Grabaketa saioek 4 ordu iraun zuten eta aste bakoitzeko lehenengo egunean egin ziren hurrengo asteetan, Nicolet bideo elektroentzefalograma sistema erabiliz (vEEG, Nic View 5.71, CareFusion, San Diego, CA, AEB). Grabazioak 60Hz-ko notch iragazkiaren bidez garbitu ziren lehenengo eta gero (0.5-250)Hz-ko banda zabaleko iragazkia pasa zitzaien. Ondoren, datuak ASCII formatura bihurtu ziren EEG Converter erabiliz (EegSoft, Inc.). Matematika-prozesu analisi guztiak Matlab-en (MathWorks Inc., Natick, MA) egin dira.

### 9.2.2 Egoera interiktalen identifikazioa

Bistazko lana eginez, krisi epileptikoak eta artefakto gabeko grabaketa interiktalak identifikatu ziren; Krisiak punta errepikakorrei, aktibitate moteleko 10 segunduko deskargak eta sinkroniari antzemanda identifikatu ziren (bideo-grabaketa monitorizatua erabiliz) Racine eskalaren arabera [153]. Krisi arteko deskargak anplitudearen espektro altu eta baxuei erreparatuz (200 milisegundorainokoak) identifikatu ziren.

### 9.2.3 Konektibitate funtzionala

KF kalkulatzeko, 8 tarte ezberdinen bataz bestekoa erabili ditugu, 1250 puntukoak, hurrengo egunetan datu desberdinak neurtzeko: 0, 1, 2, 7, 14 eta 21 dpi (edo baliokidea dena, 8 tarteren bataz bestekoa; tarte bakoitza 5 segundokoa izanik 250 Hz-ko laginketa-tasa erabiliz). Lan honetako KF-aren emaitza guztiek 8 tarte desberdinen batez bestekoaz kalkulatuak izan dira. Horrek KF estimazioaren aldakortasunari buruzko lagin egokia bermatu du, koefizienteen aldakuntza (desbiderapen estandarraren eta batez bestekoaren arteko

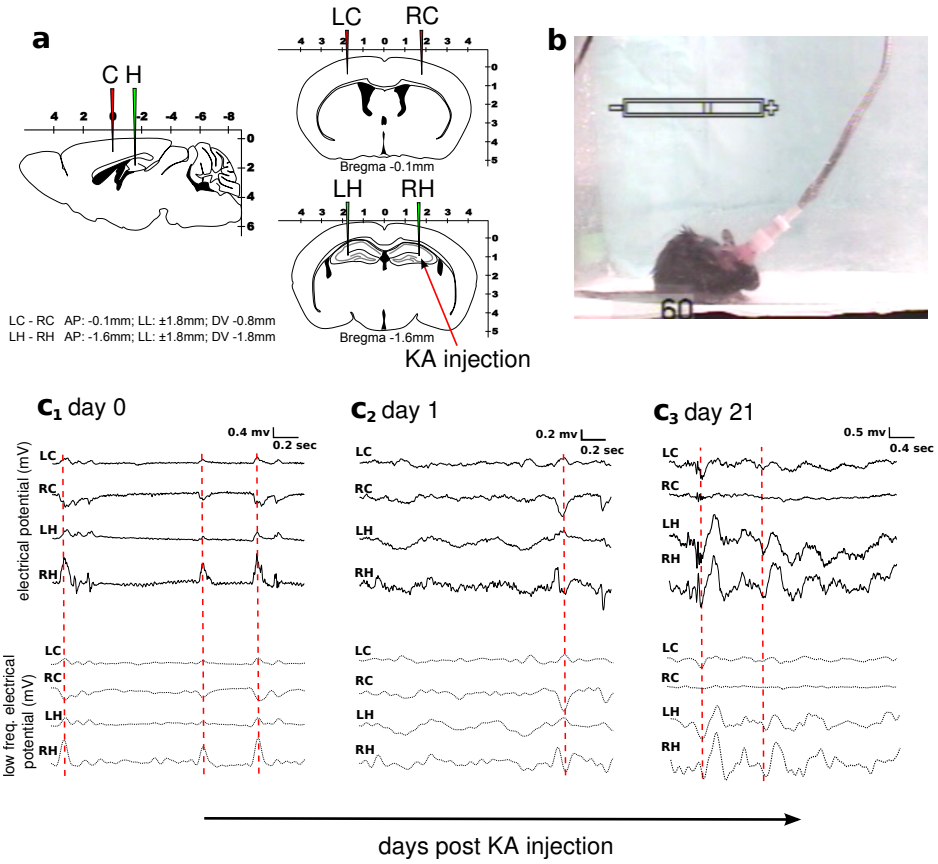


Irudia 9.1: **Garun barneko EEG grabaketak MTLE sagu batean. a:** Esperimentaziorako konfigurazioa. Garun barneko kokapena binakako taldeetan ezarri zen. Bi elektrodo kortexean (garun geruzan) kokatu ziren (LC eta RC, gorriz) eta beste biak hipokanpoan (LH eta RH, berdez). **b:** EEG grabaketa grabazio bideografikoekin batera egin zen krisien ikusizko konfirmazioa egiteko. **c1-c3:** EEG grabazioetatik ateratako adibideak injekzioaren egunean (c1), hurrengo egunean (c2) eta 21 egun (c3) ondoren. Potentzial elektrikoaren aldaketa orokorrak beheko errenkadan agertzen dira eta maiztasun baxuko frekuentziak (1-14 Hz) iragazi ondoren, beheko errenkadan . Linea eten gorriek elektrodoen artean antzekotasun estatistiko handia daukaten momentuak markatzen dituzte, KFren balio altuak ematen dituztenak. Kontuan izan RH KA injekzioaren gunea dela eta RH elektrodoarekin loturiko jarduera epileptogenikoa handiagoa dela, denbora-seriearen anplitudea handiagoa dela ikusiz erraz detektatu daiteke.

erlazioa) 0.1 ingurukoa izanik.

KF-ren balioak korrelazio linealak (C) eta korrelazio partzialak (PC) kalkulatuz lortu genuen, elektrodoen datuetatik. C matrizea Pearson-en Korrelazioa erabiliz ebaluatu zen, *corr* funtzioa erabiliz Matlab-en (MathWorks Inc., Natick, MA). PC-a C-ren hedapena da, elektrodo bikoteen arteko zuzeneko elkarrekintzak kalkulatzeko, beste bikote ezberdinetatik datozen korrelazioen ekarpena kentzen baitu PC-k [128]. Bereziki, PC matrizeen elementu bakoitza definitzen da (C matrize ez-singularra dela suposatuz) $\mathrm{PC}_{ij} = -\frac{P_{ij}}{\sqrt{P_{ii}P_{jj}}}$ bezala, non $P \equiv \mathrm{C}^{-1}$ alderantzizko korrelazio matrizea den (hau da, zehaztasun matrizea deitzen dena). Hemen, PC Matlab-en (MathWorks Inc., Natick, MA) *partialcorr* izeneko funtzioa erabiliz kalkulatua izan da.

### 9.2.4 Sare konektibitate indizea

Sare Konektibitate Indizea (NCI), c.f. 9.2 irudian ikus c-d, elektrodoen elkarrekintza guztien indizea da. Horretarako, C edo PC matrizeetan dauden elementu guztien balore absolutoak gahituko ditugu eta $N(N-1)$-rekin zatitu, bikote guztien kopuruari diagonalaren elementu nagusiak kenduz lortzen den normalizazio faktorea; Horrela, NCIk $\mathrm{C}_{ii}$ eta $\mathrm{PC}_{ii}$ diagonalaren elementu guztiak alde batera utziko ditu, C eta PC matrizeetan unitate bateko balioa izanen dutelarik.

Ateratako 8 tarte bakoitzean, NCI-ren balioa kalkulatu genuen. Esangura estatistikoaren arteko diferentziak dpi0 (kontrola) beste baldintza batzuei dagokienez (1, 2, 7, 14 eta 21 dpi) t-test bat burutuz egin zen, hipotesia bi baldintzetan bataz besteko ezberdina zela izanik. Horretarako, Matlab-en (MathWorks Inc., Natick, MA) t-test *ttest* funtzioa erabili zen.

### 9.2.5 Seinalearen maiztasun handiak eta baxuak

Seinale elektrofisiologikoari maiztasun banda desberdinetan zero-faseko iragazki digital bat pasa zaie, *filtfilt* funtzioa erabiliz Matlab-en (MathWorks Inc., Natick, MA). Arreta frekuentzia banda baxuetan (theta

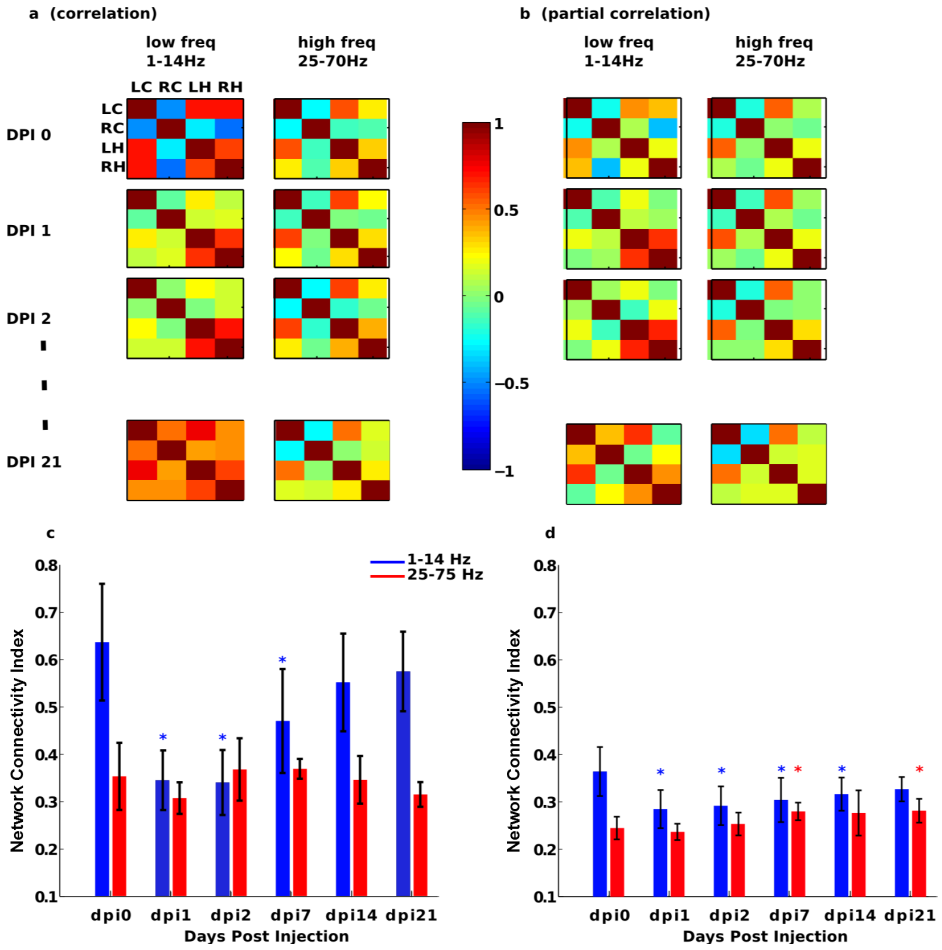


Irudia 9.2: **KF-ren aldakuntza longitudinalak hainbat egunetan zehar eta maiztasun-banda ezberdinetan. a,b:** C eta PC matrizeak hainbat egunetan zehar KA injekzioaren ondoren eta maiztasun banda desberdinetan: freq baxua (1-14Hz) eta freq altukoa (25-70 Hz). **c,d:** a eta b paneletako matrizekin, sare konektibitate indizea (definizioa Metodologian) kalkulatu dugu eta egun eta maiztasun banda ezberdinetan irudikatzen da. Asteriskoek esan nahi dute, baldintza bakoitzarentzat dpi0-rekiko (kontrola), estatistika esangura diferentziak 0,05 baino txikiagoa dutela p-baloreei erreparatuta. PC-k egun ezberdinak bereizteko gai ez den bitartean, C-k argi eta garbi erakusten du maiztasun-banda baxuann (lerro urdina), dpi1-ean jaitsiera indartsu bat erakutsiz eta gero, KF-k dpi21 arte igotzen jarraitzen duelarik.

eta delta bandak bateratzen ditugu, hau da, 1-14 Hz) eta maiztasun handiko bandetan (25-70 Hz bitarteko gamma erritmoak) jarri dugu. Maiztasun-banda hauen hautaketa bi egoera dinamiko ezberdinen arteko diferentziak antzemateko aukeratu ditugu.

## 9.3 Emaitzak

9.1 irudian agertzen den konfigurazioa erabiliz jasotako datuek gure hipotesia probatzeko erabili genituen, KF datu longitudinalekin aztertuta, garuneko egoeren artean bereiz dezakegula. 4 elektrodoetako (LC, RC, LH eta RH) datuez osatutako grabazioak kontuan hartuta, C eta PC-en oinarritutako 8 matrizeak kalkulatu ziren 8 tarte desberdinetan (ikus Metodologia). 9.2a-b irudiak batez besteko matrizeak dira. C-ren analisia (9.2a irudia) maiztasun baxuan portaera ez-lineal sendoa (ezkerreko zutabeko matrizeetan) erakusten du, KF-k 1 dpi-n balioa gutxitu eta puntu honetatik aurrera igoera azkarra duelako 21 dpi-ra iritsi arte. Joera hori, maiztasun handiko erregimenean ez da ikusten eskuineko zutabeko matrizeetan, 9.2a irudian, KF egoera desberdinetan nabarmen aldatu zela berretsiz, datuak epilepsiaren eredu baliozkotzat frogatuz.

Ondoren, konektibitate-ereduak kuantifikatu ziren NCI (9.2c-d irudia) kalkulatzeko. Horrek, C eta PC balio guztien (ikus Metodologia) balio absolutuak zenbatzen dituena, sareko konexio orokorraren informazioa ematen du. NCI aztertua izan zen garuneko zonalde ezberdinetan eta injekzioaren ondorengo egunetan (9.2a irudia), LH eta RH hipokanpo elektrodoak gogorki korrelatuak zeudela ikusiz, garuneko geruzan zeudenekin konparatuz. Bereziki, LC eta RC-k 0 dpi-n oso korrelazio altuan hasi ziren, baina haien arteko korrelazioa 1 dpi-n behin betiko murriztu egiten da, berriz, 21 dpi-raino oso egoera korrelatuan iristeko (9.2a irudia).

PC analisiak frekuentzia baxuko erregimenean ere elektrodo hipokanalen (LH eta RH) artean bereizteko gai izan zen, bi elektrodo horien arteko KF balio handia izan baitzen egun guztietan zehar. Dena den, PC azterketak aldakuntza txikiak izan zituen egunetan zehar, egoera hau maiztasun handiko eta ertaineko erregimenetan gertatu

zen. Honek interes berezia du, PC-k interakzioan bikote jakin batek sortu ditzakeen efektuak deuseztatzen dituelako (efektu ez-zuzenak, alegia). Horrela, maiztasun txikietan nagusiak ziren efektuak antzeman zituen C-k, baina ez PC-k .

## 9.4 Eztabaida eta ondorioak

KF datu longitudinaletan aplikatutta garuneko egoeren artean bereizten dezake? Galdera honi erantzuteko, MTLE animalia eredu bat erabili dugu KF-ren aldaketei analisia egiteko, egoera epileptiko baten hasierako egoeratik kronifikazioa gertatzen den arte aztertzeko. K eta C kalkulatuz egin genuen. C-k (baina ez PC-k) elkarrekintzak agerian utzi zituen (*sare efektuak*) maiztasun baxuko bandetan. Zehazkiago, C-ren sareko indizeak 1 dpi-n garunaren konektibitate orokorrean jaitsiera handia izan zuen baina handik egun batzuetara gora joan zen berriro. Joera hori latentzia-denborarekin (ezkutuko egoera) lotu daiteke, hau da, garunak epilepsiaren aurka jotzen duen lehen egoeraren iraupenaren denbora tartea, lehen krisia izan arte. Latentzia-aldi honetan, burmuin osasuntsu bat epileptiko bateko trantsizioa egiten du, burmuineko molekula, zelula eta sarearen propietateen aldaketak gertatzen dira. Hemen erakusten dugu bereziki, C-ren NCI-k latentzia aldian garatzen duen garunaren funtzionamendu aldaketak antzematen dituela. Etorkizun hurbilean, helburu dugu KF emaitzak maila molekularrekin eta zelularrekin egindako ikerketekin korrelatzeko. Horrela, epileptogenesiaren prozesua hobeto ulertzeko joera izanik, estrategia terapeutikoen eraginkortasunerako gune berriak ireki ahal izateko.

Epilepsia ikasteko animalien ereduak erabiltzearen abantailak azpimarratzen ari gara. Horrela talde alderaketa (osasuna vs. epilepsia) egin beharrean, gaixotasuna aztertzean normalean egiten den bezala, gure konfigurazioak KF-ren aldakuntza aztertzeko aukera eman zigun, lehen momentutik epilepsia kronikoa suertatu arte. Hala ere, aztertu ditugun emaitzek lagin oso mugatua (n = 1) izan dutenaren konsziente gara, analisi bera lagin handiagoei aplikatu ahal zaieelakoan gaude, KF eredu longitudinalak aztertzeko.

## 9.5 Ondorioak eta gerorako lana

Laburbilduz, garun barneko elektroenzefalogradia datu batzuetatik kalkulatutako KF-k burmuinaren funtzionamenduaren inguruko informazioa ematen du eta garun osasuntsu batetik epileptikorakoan gertatzen diren aldaketa molekularrak, zelularrak eta fisiologikoak ulertzeko erabilgarria da. Garrantzitsuki, lan honetan aurkezten den KF analisia esperimentazio luze baten grabazio longitudinaletan oinarritzen da, irakurketa iraunkor eta zehatza ahalbidetzen duena, KF-a esanguratsua eta sendoa dela kalkulatzeko. Azkenik, garrantzitsua da azpimarratzea gure analisiak zientzia esperimentalak, sagu gaixo modeloak, zientzia biologikoa eta zientzia konputazionala biltzen dituenak, beste gaitz batzuk aztertzeko eta balioztatzeko tresnak lortzeko bidea erraztu dezakeela.

# Kapitulua 10

# Erredundantzia eta sinergia zirkuitoak konektibitate funtzional matrizeetan

9. kapituluan saguen elektrofisiologiari buruzko datuak aztertu ditugu. Kapitulu honetan Informazioaren Teorian oinarritutako neurriak erabiliko dira, garunaren dinamika konplexuak aztertzeko. Teknika hau elektrodoen arteko informazio-fluxua aztertzeko erabiliko da epilepsiadun pazienteengan, kirurgia ondorengo emaitza ezagunarekin.

Neurona-sistemak unitate interaktiboek osatzen dute, eta haien funtzioari edo funtzionamenduari buruzko informazio garrantzitsua lor daiteke, unitate bakoitzaren aktibitatearen menpekotasun estatistikoak aztertuz. Korrelazioak eta elkarrekiko informazioa mendekotasun horiek karakterizatzeko erabili ohi diren bitartean, gure helburua hiruko elkarreraginak aztertzea da, informazioaren transferentzia dinamikoa hobeto hautemateko eta karakterizatzeko.

Gure ikuspegiak Interakzio Informazioaren (II) neurriari jarraitzen dio. II-aren zeinuak hirukotearen aldagaien arteko elkarrekintzak erredundanteak (R) edo sinergikoak (S) diren esaten digu.

Hiru aldagai erredundanteak direla esan ohi da hirugarren aldagaia, Z esatearren, aldagai pare bati (X, Y) gehitzean, X-k eta Y-k partekatutako informazioa murrizten duenean. Halaber, elkarrekintza sinergikoa baldin bada X-k eta Y-k partekatutako informa-

zioa hobetzen du Z-k. Hemen, ikuspegi honetatik abiatuta, hirukoteen arteko R eta S egoerak kalkulatuko ditugu epilepsia mesiotemporalari droga-erresistentzia duten gaixoen datu elektrofisiologikoetan, espazio-antolamendua eta dinamikak aztertzeko eremu epileptogenotik hurbil (krisi epileptikoaren hedapenaren arduraduna).

## 10.1 Sarrera

Informazioaren Teoria erabiltzea bide garrantzitsua bihurtu da neurozientziako datuen aldagai korrelatuen arteko elkarrekintza ebaluatzeko, harreman funtzionalak eta informazio espezifikoa tratatzen duten gordetako sareak azaleratuz [32, 145, 152, 49].

Informazioaren biltegiratze/kodeketa/deskodetzeaz gain, Informazioaren Teoriak aldagai erlazionatuen arteko elkarrekikotasun erlazioak erredundanteak edo sinergikoak diren argitu dezake.

Oro har, sinergia (S) gertatzen da aldagai bateko ulermena beste aldagai baten portaera aurreikusten laguntzen badu, bi aldagaiek emandako informazioaren batura baino zehatzago. Aitzitik, erredundantzia (R) gertatzen denean aldagaiek eskaintzen duten informazioa berdina da hirugarren bat gehituta ere (ikus S-ren eta R-ren interpretazioa kausalitate inferentzian oinarrituta [194]).

Interakzio Informazioa (II) [134] hiru aldagaiez osatutako multzoei aplikatzen zaionean, bere ikurrak (positiboa edo negatiboa) adierazten du R edo S gisa har daitekeen ala ez. Horrela, Elkarrekiko Informazioa (Mutual Information, MU) ez bezala, II positiboa edo negatiboa izan daiteke, horrela, II positiboa identifikatzen du R-k eta negatiboa S-k. R eta S suertarazten dituzten mekanismoen adibide gisa, kausa komunak duten egiturak (berdinak diren sarrerak) R sortzen dute, eta S sor daiteke XOR ate bat konbinatuz ausazko bi sarrera independenteekin (adibidez) [125, 211].

S-ren presentzia ezaguna da modelizazio soziologikoan, non *ezabatzaile* terminoa beste aldagai batzuen baliozkotasun prediktiboa handitzen zuten aldagaiei aplikatzen zitzaien, erregresio linealeko ekuazio batean sartzearen ondorioz [47].

Era berean, hirukoen arteko elkarrekintza aztertua izan da gene

zehatz batek beste bi geneen arteko elkarrekintza modulatzen duen aztertzeko [11, 209]. Gainera, sare neural haztegiei elektrofisiologia aplikatzen zaienean, serie hedapenaren ikuspuntuak kontuan hartzen ditu II-arekin bat diren terminoak [23]. Hemen, II erabiliko dugu hirukoteen arteko elkarrekintzak aztertzeko epilepsian, baina patologian oinarritu ordez, alderdi metodologikoak azpimarratu nahi ditugu. Bereziki, giza elektrokortikografia datuei II aplikatuz, elkarrekintzaren zenbait alderdi (aldagai bikoteei begira ikusten ez direnak) azpimarratzen ditugu; sare epileptogenoaren eremua adibidez, krisi epileptikoak eragiten duen garuneko sarea.

## 10.2 Metodologia

### 10.2.1 Kirurgia eta kirurgia osteko emaitza

Ebakuntza eremuaren hautapena epilepsia kirurgikoari aplikatzen zaizkion ohiko praktika arauen arabera egin zen, eremu epileptogenikoaren proxy gisa jarduera elektrofisiologikorik fuerteena baliatuz [167].

Emaitza klinikoa Engel Epilepsia Kirurgia Emaitza Eskalaren bidez ebaluatu zen [74], I.tik (krisiez libre kirurgia ondoren) IV.era arte (kirurgia ondoren hobekuntzarik ez). Hemen aztertzen diren elektrokortikografia datuak kirurgia ondoren krisi gehio izan ez duten Engel I (n=3) pazienteen eta Engel III (n=1) pazienteenak izango dira, konparaketa egin ahal izateko.

### 10.2.2 Giza electrokortikografia datuak

II kalkuluaren bidez aztertu diren datuak aldez aurretik argitaratuak izan dira "La Princesa"Ospitaleko Epilepsia Unitatean (Madril, Espainia) [144]. Datuak gingil (lobulu) temporaleko epilepsia izan eta kirurgia pasa duten pazienteenak dira. "La Princesa"Ospitaleko Etika Batzordearen onespena jaso ondoren, gaixoek beren baimena eman zuten $4 \times 5$ elektrodo sare subdural batek datuak jaso zitzan (zentimetro bateko distantzia elektrodoen artean), sevofluranoaren dosi baxuak (%0,5 ) eta remifentanil (0,1 mg/kg/min) jaso ondoren.

Grabatzen ari zen bitartean, anestesia egonkortu zen bispectral indize baten barruan 55-60 bitartekoan (indize adimentsionala) [168]. Elektrodo sarea aldi baterako cortexaren gainean jarri zen, Silvioren artekarekiko paralelo eta T1-T3 geruza estaltzen, bere posizioa bideokamerarekin eta argazkiekin grabatu zen. Erreferentziazko elektrodoa belarrian jarri zen eta, kasu batzuetan, inguruko buru-azalera mugitu zen, grabaketan kutsadurarik ez zegoela egiaztatzeko, aurreko lanekin bat etorriz [142]. Ebakuntza aurreko ebaluaketa egin zen La Princesa Hospitalean erabilitako protokoloaren arabera, aldez aurretik jakinarazi bezala [147].

Seinalearen prozesamenduaren ikuspuntutik, garrantzitsua da elektrokortikografia lanen garrantzia azpimarratzea, buru-azaleko electroencefalografian oinarritutakoak ez bezala. Seinaleen kalitatean askoz hobea da, 21 eta 115 aldiz handiagoa den zarata-seinale erlazio batekin, bi modalitate hauek oso ezberdinak direla erakutsiz [197].

### 10.2.3 Datuen prozesamendua

Lan honetan egindako azterketa guztiak ebakuntza ondorengoak izan dira, lobektomiak ez ziren egin hemen eztabaidatutako emaitzetan oinarrituta. Elektrokortikografia saio intraoperatibo bat 15-20 minutuz grabatu zen 32 kanal anplifikadorea erabiliz (Easy EEG II, Cadwell, AEB), 0.5-400 Hz banda-paseko iragazki eta 50 Hz notch iragazkia erabiliz eta, azkenik, 200 Hz-ra lagin murrizketa. Gehienez 5 minutu irauten duten artefakto gabeko bloke inter-intalak ikusizko ikuskapenez hautatuak izan ziren. Analisi guztiak Matlab-en (MathWorks Inc., Natick, MA) egin dira.

### 10.2.4 Frekuentzia-banda analisia

Seinale elektrofisiologikoak maiztasun banda ezberdinetan iragazi ziren zero-faseko iragazki digital bidez (10.5 irudia). Matlab (MathWorks Inc., Natick, MA) *filtfilt.m* funtzioa erabili zen, elektrofisiologiako banda estandarrak iragazteko: delta (1-4 Hz), theta (4-7 Hz) , alfa (7-14 Hz), beta (14-26 Hz) eta gamma (26-100 Hz)

### 10.2.5 Shannon-en entropia

Ausazko $X$ aldagai baten Shannon-en entropia (hau da, batez besteko ziurgabetasuna) definitzen da

$$H(X) = -\sum_x \text{prob}(x)\text{log prob}(x), \tag{10.1}$$

non prob($x$)-k $X$ aldagaiaren $x$ egoeraren probabilitate banaketa adierazten du [98, 51]. Lan honetan, X aldagaiak X elektrodoak hartutako potentzial elektrikoek (seinaleek) definitzen dute. Entropia bateratua (Joint Entropy) dimentsio orokor bat besterik ez da, hau da, 2 dimentsiontan $H(X,Y) = -\sum_x \sum_y \text{prob}(x,y)\text{log prob}(x,y)$ bilakatzen da eta 3 dimentsiotan, honakoa dugu:

$H(X,Y,Z) = -\sum_x \sum_y \sum_z \text{prob}(x,y,z)\text{log prob}(x,y,z)$. 2 basedun logaritmoarentzako (guk erabili dugun modukoa), entropia bitetan adierazten da.

### 10.2.6 Interakzio Informazioa

Interakzio Informazioa (II) Shannon-en entropian oinarrituta neurtzen da, hirukoen arteko elkarrekintzak aztertzeko aukera ematen du [134]. Edozein $(X,Y,Z)$ hirukoterako, II definitzen da

$$\text{II}(X,Y,Z) \equiv I(X,Y) - I(X,Y|Z) \tag{10.2}$$

non $I(X,Y)$ $X$ eta $Y$-ren arteko Elkarrekintza Informazioa da (Mutual Information, (I)), entropia marjinal eta bateratuen arabera definitu daitekeena,

$$I(X,Y) = H(X) + H(Y) - H(X,Y), \tag{10.3}$$

eta $I(X,Y|Z)$ baldintzapeko elkarrekintza informazioa da $X$ eta $Y$, $Z$-rekin baldintzatua. Analogoki, $I(X,Y|Z)$ entropia marjinal eta bateratuen arabera definitu daiteke, hau da,

$$I(X,Y|Z) = H(X,Z) - H(Z) + H(Y,Z) - H(X,Y,Z) \quad (10.4)$$

detaile gehiagorako, ikus [51]. Horrela, (10.2), (10.3) eta (10.4) ekuazioek emandako definizioak erabiliz, II Shannon-en entropien funtzio bezala idatzi daiteke.

$$\begin{aligned} \mathrm{II}(X,Y,Z) \equiv\ & H(X,Y,Z) + H(X) + H(Y) + H(Z) \\ & -H(X,Y) - H(X,Z) - H(Y,Z). \end{aligned} \quad (10.5)$$

Ekuazio horretatik, II propietate sinple eta garrantzitsuak lor daitezke (xehetasunak ikusi A eranskinean).

Kontuan hartu behar da gure II definizioak kontrako zeinua erabiltzen duela jatorrizko formakoarekin alderatuz [134]. Halaber, azpimarratu beharra dago II.a zero denean, bi egoera suertatu daitezkeela; hiru aldagaiak estatistikoki independenteak izatea edo $I(X,Y) \approx I(X,Y|Z)$ gertatzea. Hori dela eta, $\mathrm{II} \neq 0$ balioak bakarrik landuko ditugu, hau da, $\mathrm{II} \approx 0$ balioak ez dira kontuan hartuko.

### 10.2.7 Interakzio Informazioaren kalkuloa datuen gaussianitatea onartuz

Datuek Distribuzio Gaussianoa jarraitzen dutenaren ustean, Shannonen entropia analitikoki kalkulatua izan da, hau da, non entropia diferentzialak aldagai anitzeko Distribuzio Gausianoak deribazio analitiko bat daukan (ikus xehetasunak [51]). Baldintzapeko elkarrekintza informazioa kalkulatzeko, (10.4 ekuazioa), [12] erabili dugu, non aldagai anitzeko ausazko aldagai gaussianoek agerian dituzten

$$I_{\text{gaussian}}(X;Y|Z) = \frac{1}{2} \ln \frac{|\Sigma(X|Z)|}{|\Sigma(X|Y \oplus Z)|}, \quad (10.6)$$

non $|\cdot|$ determinatzailea da, eta kobariantza partzial matrizea da

$$\Sigma(X|Z) = \Sigma(X) - \Sigma(X,Z)\Sigma(Z)^{-1}\Sigma(X,Z)^{\top}, \tag{10.7}$$

kobariantza matrizean $\Sigma(X)$ eta zeharkako kobariantza matrizea $\Sigma(X,Z)$; $\Sigma(X|Y \oplus Z)$ -ren definizioa ere analogoa da, non $Y \oplus Z$ bi aldagai eranstea den.

II kalkulatzeko, (10.2) ek., beharrezkoa da elkarrekintza informazioa kalkulatzea; (10.6) ek. berbera erabiliz lortzen dena, baino $Z$ aldagairik gabe.

### 10.2.8 Interakzio Informazioaren kalkuloa datuen ez-gaussianitatea onartuz

Datuek Distribuzio Gausioanoa ez jarraitzearen egoeran, eta elkarrekintza informazioa eta baldintzazko elkarrekintza informazioa kalkulatzeko, (cf. rhs-en (10.2) ekuazioa), lehenik eta behin datuak 4 multzotan banatu ditugu. Ondoren, ekuazioak ebaluatu (10.3) eta (10.4) Mutual Information Toolbox [148] erabiliz, C++-en programatutako Informazio Teoriaren kalkuloak egiteko Matlab-erako tresna(MathWorks Inc., Natick, MA). Bereziki, *mutualinfo.m* eta *condmutualinfo.m* funtzioak [148] erabili ziren. Probabilitateak kalkulatzeko, 6 eta 10 multzo ere erabili ziren eta emaitzak ez ziren ezberdinak izan.

### 10.2.9 Erredundantzia eta sinergia

Zuzenean II-ren definiziotik, (10.2) ek., IIren seinale positiboa esan nahi du $I(X,Y) > I(X,Y|Z)$ eta zirkulazioaren propietatearekin (II berdina dela $(X,Y,Z)$-ren edozein permutazio posibleetan; xehetasun gehiago nahi izanez gero, ikusi A Eranskina), hau da, hirukotearen arteko elkarrekintzak erredundantea dela esan nahi du. Era berean, II-k ikur negatibo bat badu elkarrekintza sinergikoa da.

Hau informazio partzialaren deskonposizioan oinarritutako emaitzekin bat dator [212], non II-aren zeinuaren antzeko interpretazioa eman zen: R positiboa eta S negatiboa. Kontuan hartu beharrekoa

da (10.2) ekuazioaren zeinua [212]-en agertzen denaren zeinu kontrakoa duela (ikus [14]) eztabaida gehiago jakiteko).

### 10.2.10 Esangura estatistikoa

Lan honetan adierazitako balio guztiek esangura estatistikoa pasa zuten. Esangura estatistikoa N=50000 errepikapeneko prozedura baten ondoren kalkula daitekeen denborazko seriean oinarritutako distribuzio nuloaren bitartez kalkulatua izan zen. Balio esanguratsuak (Bonferroni zuzenketaren ondoren) 0.05 peko S eta R buztanak hartuz lortzen dira (balio negatiboak eta positiboak). IIk ez du Distribuzio Normal bat jarraitzen, hau da, II-ren buztanen luzera alde positibo eta negatiboan desberdina da.

### 10.2.11 Interakzio Informazioaren bataz bestekoa

Elektrodo bakoitzeko, leiho ez gainjartzaileak erabili ziren. 9 eta 29 leiho artean, bakoitzak 2,000 denbora-tartekoak (10 segundo, 200 Hz-ko frekuentzian). II balioak deskribatutatko leiho guztien arteko batez bestekoa eginez lortu zen, lagin egokia sortuz (10.1 irudia).

### 10.2.12 Interakzio Informazioa 2D-n adierazteko sare neurriak

II-ren 2D irudiak izateko, non balioak hirukoteetan oinarritzen diren, II-ren aldaketa bi aldagaietan adierazi dugu, hirugarrena finkatu ondoren.

Interakzioen sarea aztertzeko, banakako balioak bilatu ordez, aldagai bakoitza sare baten barruan nodoa balitz bezala hartu dugu eta sare-neurri desberdinen aplikazioa egin Brain Connectivity Toolboxekin [170, 169]. Espezifikoki, finkatutako elektrodoa aukeratu zen maximum betweenness centrality (nodo jakin batek duen sareen bide laburrenen zatien proportzioa adierazten du, eta, beraz, nodoek zentraltasun handia dute bide laburrenean gehienetan parte hartzen dutenak); maximum degree (nukleoa, nodo jakin bati konektatuta-

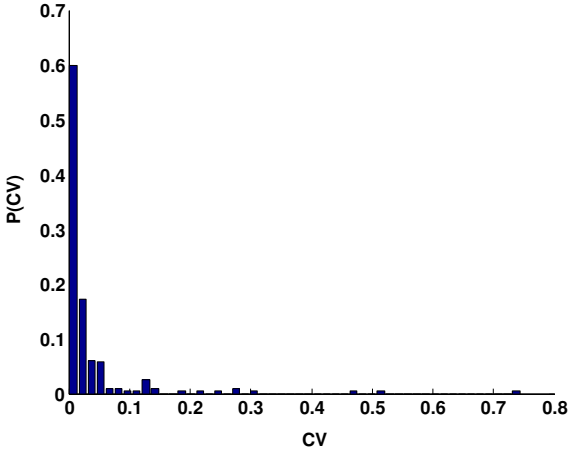


Irudia 10.1: **Interakzio Informazioaren laginketa balidazioa.** Irudiak II aldaketaren koefizientea erakusten du (estimazioaren desbiderapen estandarra bere bataz bestekoarekin zatitua) 9 leiho desberdinen batez bestekoa egin ondoren, 2000 puntu lehio bakoitzeko. Desbiderapen estandarra ondo lagindua dagoela ikusten da, batez bestekoa baino txikiagoa izanik.

ko lotura estandarrak bakarrik aintzat hartzen dituena), eta maximum clustering coefficient-ari begiratuz (nodo baten inguruan dauden triangeluak kontatuz kalkulatzen dena, horrela, kluster indarra nodo auzo batean irudikatuz).

### 10.2.13 Tokiko sinkronizazio indizea, banakako erredundantzia eta banakako sinergia

Aurreko lanen arabera, tokiko sinkronizazio indizearekin (TSI) aztertutako elektrokortikografia datuak [144], bakarkako elektrodoekin lan egiteko indizeak izan nahi genituzke. [144]-n azaldu zen bezala, TSI-k elektrodo bakoitzaren batez besteko sinkronizazioa neurtzen du lehen mailako elektrodo auzokideekin, baita diagonaletan ere. Bereziki, TSI-k kalkulatzen du Pearson korrelazio baten batez besteko balio absolutua nodo jakin batean eta inguru hurbilenean, hau da, 3 bizilagun izkinetan, 5 aldameneko elektrodoetan eta 8 sarearen beste edozein tokitan jarririk.

Modu berdintsuan, banakako R elektrodo jakin batentzat kalkulatu zen $\bar{Z}$, $II(X, Y, \bar{Z})$-en balore positibo guztiak batzen $X$ eta $Y$ aldagai guztientzako. Era berean, banakako S lortu zen $II(X, Y, \bar{Z})$-en balore negatibo guztiak batzen $X$ eta $Y$ aldagai guztientzako, azkenik, batuketa horren balio absolutua hartuz. Bi neurri hauei, banakako R eta S deitu diegu, hiru aldagaiak bata bestearekiko ezberdinak zirenean soilik batu ditugularik.

## 10.3 Emaitzak

II hiruko aldagaien araberakoa da eta positibo edo negatibo izateak hirukoatearen interakzioa erreduntantea edo sinergikoa den identifikatzen du. Lehenik eta behin, II ereduak ikuskatu genituen 2D grafikoetan proiektatuz, elektrodo jakin bat finkatuz eta II ikuskatuz beste bi aldagaiak aldatuz (ikus Metodoak).

Entropia maximo eta gutxieneko elektrodoak finkatu ditugu lehenik, II II(X,X,X) bezala aztertzeko erreferentzia onak, entropiarekin bat egiten dutenak (ikus A eranskina). Sare-mailan funtzionalitate berezia betetzen dituzten elektrodoak ere finkatu ditugu, maximum betweenness, maximum degree daukana(hau da, sarearen nukleorik garrantzitsuena) eta maximum clustering coefficient altuena dituztenak (ikus Metodoak informazio gehiago lortzeko).

10.2 irudian agertzen den bezala, 2D ikuskapenak finkatutako elektrodoaren araberakoak dira, II-aren 3D egitura argi bat adieraziz, hau da, elektrodo desberdinetan II eredu desberdinak agertzen dira.

Ondoren, R eta S ereduak zonalde epileptogenoarekin (propagazioarekin zerikusia duten eremuak) erlazionatuta zeudela ikusi genuen. Gaixo batzuek Engel I (Metodoak) emaitza izanik, krisiak ekidin eta ez zuten kirurgia egin ondoren krisialdirik izan. Ebakitako eremua (paziente guztientzat ezaguna den eremua) eta kirurgiaren aurreko grabazioak erabiliz, erresekzio eremuak zona epileptogenoaren zati bat gutxienez hartuko duela onartu daiteke. Erresekzio eremua gris zatia 10.3) irudian, S ( sareta gorria), R (sareta urdina), Shannon-en entropia (sareta berdea) eta TSI (sareta magenta) marraztu genituen, TSI izanik zona epileptogenikoa markatzen duen

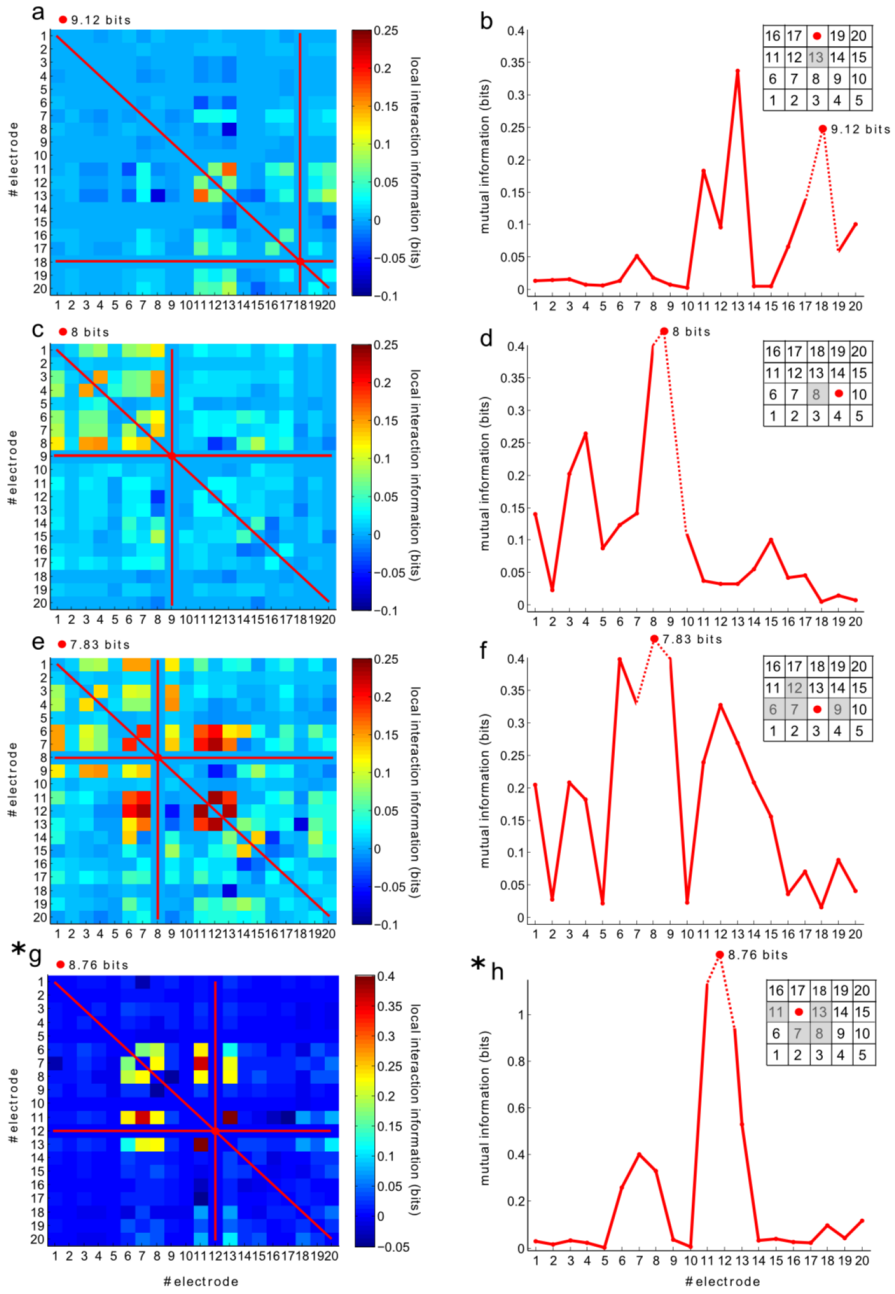


Irudia 10.2: **Interakzio Informazioaren egitura giza epilepsia elektrokortikografia datuetan oinarrituta.**

Irudia 10.2: **Interakzio Informazioaren egitura giza epilepsia elektrokortikografia datuetan oinarrituta.** II-ren balore positiboek R adierazten dute, balio negatiboek S adierazten duten bitartean. II. 2D irudikapenak aldagai bat finkaturik mantenduz lortu ziren, beste biak aldatuak izan zitezkelarik. Izan ere, elektrodoak hurrengo kalkuloekin finkatuak izan ziren: **a:** entropia maximoa (kasu partikular honetan maximum betweenness-arekin bat datorrena) **c:** gutxieneko entropia **e:** gehienezko maila (maximum degree) (nukleoa , kasu honetan bat dator maximum clustering coefficient-arekin). **g:** 12gn. elektrodoa, ebakuntzan kendutako eremuko ordezkari gisa. **a, c, e, g:** lerro gorriek finkatutako elektrodoaren eta gainerako elektrodoen artean dagoen elkarrekintza informazioari dagokiozte. Izan ere, A eranskinean ageri den bezala, II bat dator elkarrekintza informazioarekin, bi aldagai hirukotean balio berbera dutenean. Zirkulu gorri lodiak elektrodoaren entropia balioa markatzen du (II(X, X, X) denean). **b, d, f, h:** a, c, e, g paneletan bezala, lerro etenak Shannon entropiaren balioak elkarrekintza informazioaren balioak baino handiagoak direla erakusteko daude. Elektrokortikografia sareek ere erakusten dute elkarrekintza informazioaren antzeko balioek sarearen antzeko eskualde geometriko batean biltzen direla (grisean 0,3 bit baino gehiagoko balioak marraztuta). Kontuan izan, II positiboa edo negatiboa izan daitekeen bitartean, elkarrekintza informazioa positiboa dela beti (zero denean, independentzia estatistikoa onartzen da). **g, h:** (*) Eskala desberdina.

indizea [144]. Hori dela eta, R-K eta TSI-K distribuzio espazial bera izan zuten bitartean, S inguruan antzematen zen, hau argiagoa izanik nahiz eta II datu ez gaussianokin kalkulatu (10.4 irudia). Shannon-en entropia deskribatutako eremuak sakabanatuagoa zegoen eta, beraz, ez zuen epilepsia eremuarekin zerikusirik.

Ondoren, S/R eta LSI-ren (eremu epileptogenikoaren proxya) arteko harremana ikuskatu genuen garuneko erritmoetara begiratuz. 10.5 irudiak erakusten du II banda desberdinetan zehar, erresekzio eremuari dagozkion elektrodoren bat finkaturik dagoela. 10.5 irudiaren goialdetik beherainoko segidan, gero eta beherago panela, gero eta erritmo azkarragoa. Horrela, 10.5 iruditik abiatuta, II-k balio altuagoak ditu erritmo azkarretan – beta (14-26 Hz) eta gamma (26-100 Hz) beherago daunden bi panelak –, motelagoak direnekin alderatuz.

R eta S-ren frekuentzietan zehar ikusiz (10.6 irudia), R maiztasun handiko beta eta gamma bandetan (laranja eta marroia) ekarpen sendoagoa izan zuen, bi bandek antzeko patroi espaziala erakutsi zuten, TSI-arekin bat etorriz, aldi berean zonalde epileptogenikoarekin

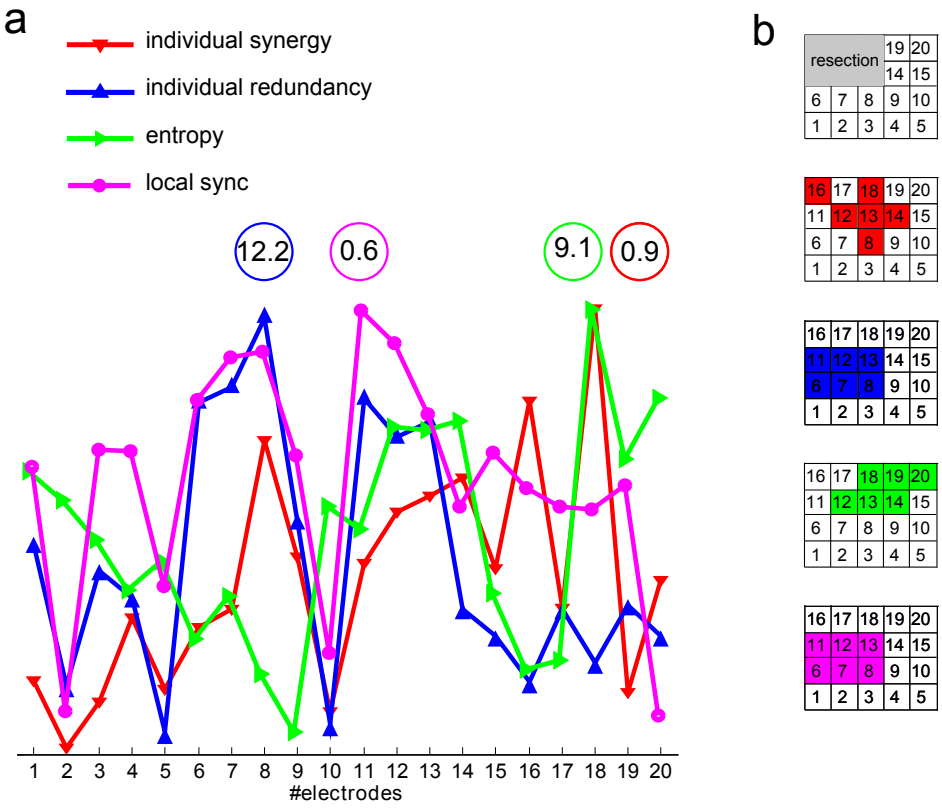


Irudia 10.3: **Erredundantzia eta sinergia interakzioak giza epilepsia elektrokortikografia datuetan oinarrituta. a:** $\bar{Z}$ aldaturik (Metodologian azaldu bezala), $II(X, Y, \bar{Z})$-ren balio negatibo guztiak batu ditzakegu banakako S (gorriz) lortzeko, modu berean, balio positiboak batu daitezke banakako R (urdinez) lortzeko. Berdez, Shannon-en entropia adierazi izan da, elektrodo bakoitzeko (hau da, $II(X, X, X)$, ikus A Apendizea detaile gehiagorako). Azkenik, magentaz TSI [144]-n bezala kalkulaturik, hurbileko elektrodoen harteko korrelazioen balioak batuz. Ikusi nola neurriak arbitrarioki irudikatzen direla, hobe ulertu ahal izateko. Balio maximoak kolorezko zirkulo batekin irudikatu dira. **b:** Elektrodo balio maximoak panelean marraztutako neurri bakoitzeko. Gainera, erresekzio eremua grisean marraztu dugu, kasu honetan kirurgia ondoren krisirik gabe geratu den paziente batena.

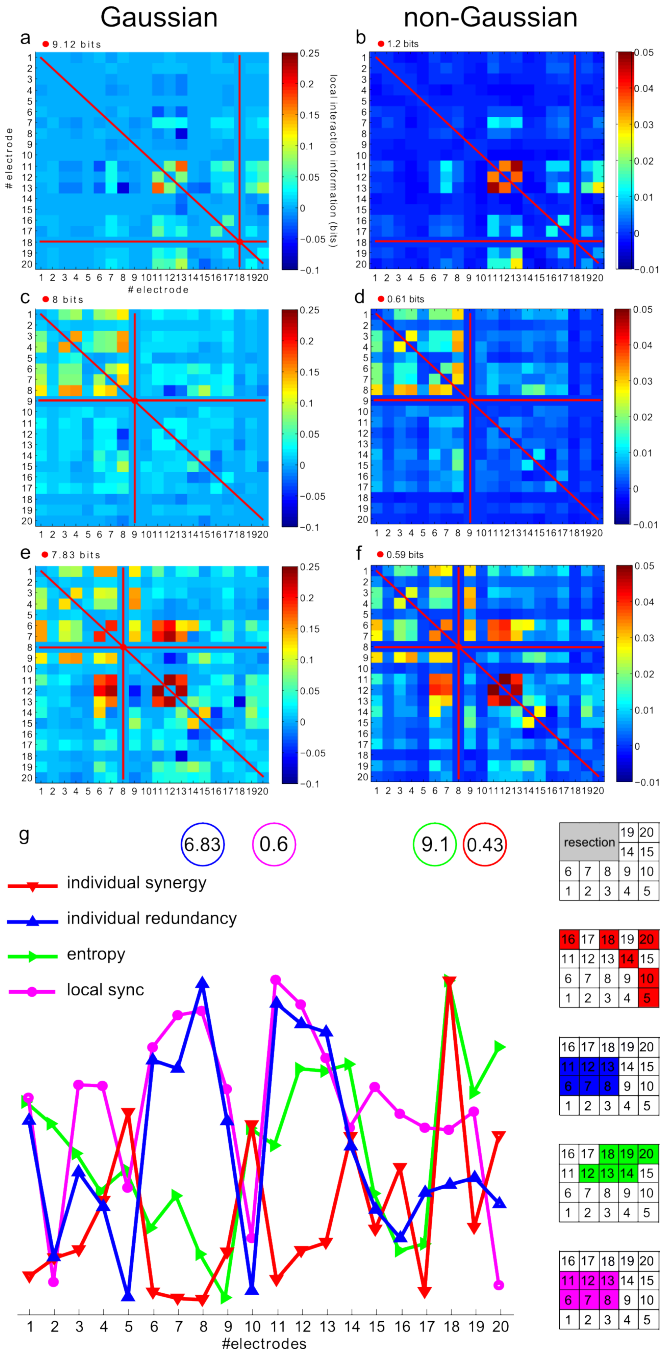


Irudia 10.4: **Data gaussiano eta ez-gaussianoaren arteko konparaketa.**

Irudia 10.4: **Data gaussiano eta ez-gaussianoaren arteko konparaketa.** a, c eta e panelak berriz irudikatu dira aurreko 10.2 iruditik konparaketa azkarra egitearren. Jasotako II balioak elektrodoak finkaturik ondoko neurriekin: **a,b:** entropia maximoa; **c,d:** entropia minimoa **e,f:** maximum degree (sarearen konexio nukleoa, kasu honetan clustering coefficient-arekin bat datorrena). **b, d, f:** Data ez-gaussianoa onartzen duen kasuak eta gaussianitatea onartzen duenak ez dira oso ezberdinak. **g:** 10.3 irudian bezala, baino ez-gaussianitatea onartzen. Ikus nola patroi berberak ikus daitezkeen R-rentzako, S-k ezberdintasun batzuk erakusten dituen bitartean. Hemen, R eta TSI patroi eta espazialitate berbera partekatzen dutela eta S hauen inguruan agertzen dela argiago ikus daiteke kasu gaussianoan baino.

bat datorrena. Aitzitik, delta eta theta bandek S-rengan (urdin iluna eta argia) ekarpen handiagoa izan zuten. Garrantzitsua da S-aren banaketa espaziala R-tik oso desberdina izan zela esatea, eta R-ren aktibazioa maiztasun handiko eremu epileptogenikoarekin (hau da, TSI) lotu zen bitartean, S inguruan eta maiztasun baxuko bandetan antzeman zela.

Esperimentuen inguruko ondorioen sendotasunari dagokionez, 10.2 - 10.6 irudietako zifrak Engel I duten pazienteetako baten datuak dira, baina emaitzak antzekoak izan dira beste Engel I pazienteengan. Izan ere, 10.7 irudiak erakusten du R erresekzioaren barrutian eta S erresekzioaren eremutik kanpo. Engel I gaixoen kasuan, erresekzio eremua zehatza izan zen eta pazienteek ez zuten beste krisirik jasan, identifikatutako ereduak sendoak ziren, Engel III gaixoarenak ez bezala. Kantitate hauen ratioa kontuan hartuta hobeto ulertzen da R eta S-k hartzen duten eremua eta antolakuntza (ikus 10.7 irudia). Gainera, Engel III pazientearen R-a beste hiru Engel I gaixoena baino askoz handiagoa da.

## 10.4 Eztabaida

Hirukote aldagaien arteko elkarrekintzak aztertzean, II-ak ematen dituenak, bi aldagaien edo multialdagaien arteko elkarrekintzak aztertzen dituzten lan akademikoak gainditzen dira. Metodo hau aldez aurretik beste eremu batzuetara aplikatua izan den arren, epilepsian

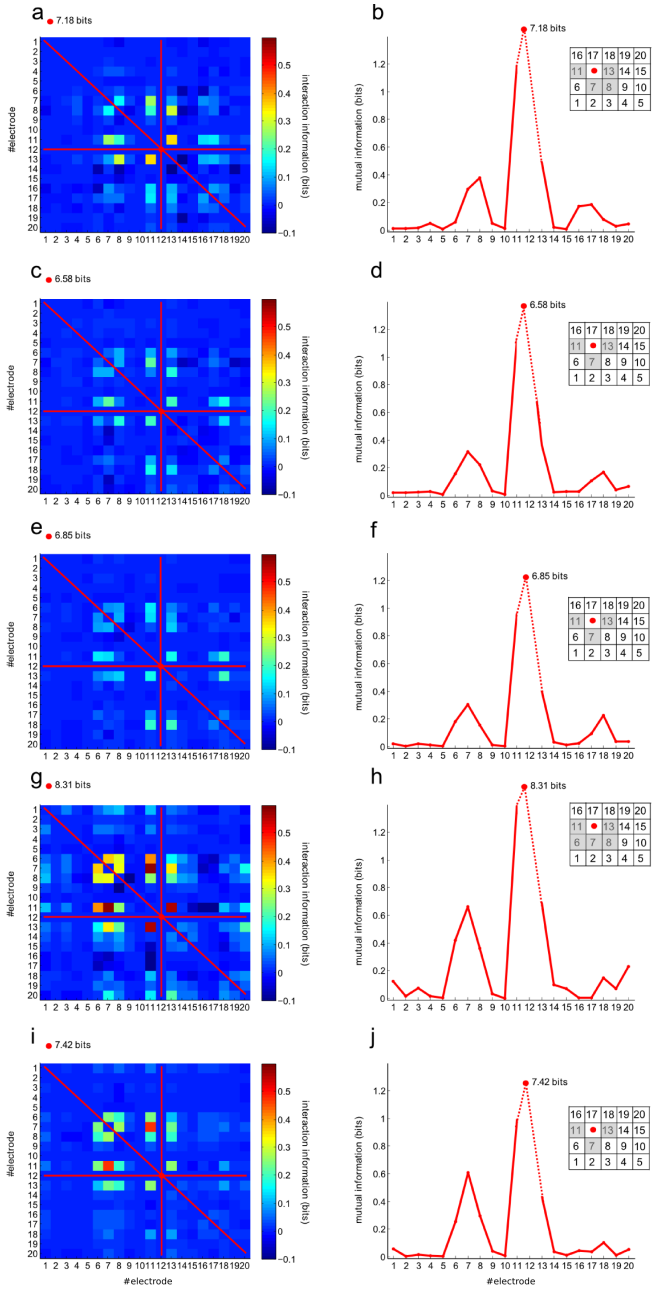


Irudia 10.5: **Interakzio Informazioaren egitura giza epilepsia elektrokortikografia datuetan oinarrituta frekuentzia banda ezberdinetan.**

Irudia 10.5: **Interakzio Informazioaren egitura giza epilepsia elektrokortikografia datuetan oinarrituta frekuentzia banda ezberdinetan.** 10.2 figuran bezala, II irudikatzen dugu elektroko finko bat jarriz, erresekzioaren eremukoa izanik beti ere, ondooko frekuentzia bandetan: **a,b** delta (1-4 Hz) **c,d** theta (4-7 Hz) **e,f** alpha (7-14 Hz) **g,h** beta (14-26 Hz) and **i,j** gamma (26-100 Hz). Ikus daiteke nola balioak altuagoak diren $\beta$ eta $\gamma$ bandetarako. **b,d,f,h,j:** 10.2 irudiaren antzera, grises marrazten dira 0.3 bit baino altuagoak diren elkarrekintza informazioaren balioak.

antzeko lanik ez dugu ezagutzen. Beste lanek proposatutakoa jarraitu dugu dena den, Granger kausalitatea aprobetxatu dugu [91], S eta R efektuak ebaluatzeko datu epileptikoetan [130, 214, 194] eta gaixo epileptikoetan elektrokortikografia datuetan II kalkulatu dugu. Kirurgiaren ondoren emaitzarik hoberena lortu zuten pazienteen datuei arreta berezia eman zaie, inolako krisirik ez zutenak (Engel I pazienteak). Izan ere, paziente hauen erresekzio eremua erreferentziatzat hartuta, eremu epileptogenoaren inguruko zonaldeetan aztertu dugu II, krisi epileptikoak hedatzeko funtsezko esparrua izanik.

II bi egoeratan kalkulatu dugu, datuek distribuzio gaussianoak eta ez-gaussianoak jarraitzen dituztela suposatuz. Lehenak II-aren deribazio analitikoa ahalbidetzen duen bitartean, distribuzio ez-gaussianoa orokorragoa da eta ez da erraza probabilitateak kalkulatzeko metodorik egokiena aukeratzen. Jakin badakigu histogramak sortzeko metodo errazena aukeratu genuela (salikatu eta maiztasunak kontatzearena), baina datu-puntu kopurua nahikoa handia izan zen lagin egokia bermatzeko [29]. Dena den, probabilitatearen dentsitatea kalkulatzeko beste metodo batzuk ere erabil daitezke, esate baterako, kernel estimatzaileak, hurbileko bizilagunaren metodoa, serie ortogonala eta abar (ikus [27]).

Hala ere, bi distribuzioak landuz gero, eta beti emaitzen arabera, lortu ziren ondorioak kualitatiboki ez ziren izan oso ezberdinak. Hau da, datuak segmentuen artean gaussianoak edo ez gaussianoak izan, elektrodoak eta paziente ezberdinak landuz ( 10.8 irudia, p-balioak zero izanik, Kolmogorov-Smirnov-en normaltasunaren proba egin ondoren), gaussianitate hipotesiak bere barne hartzen du ez-gaussianitate datuen funtsa. Izan ere, S-rekiko diferentzia batzuk aurkitu arren,

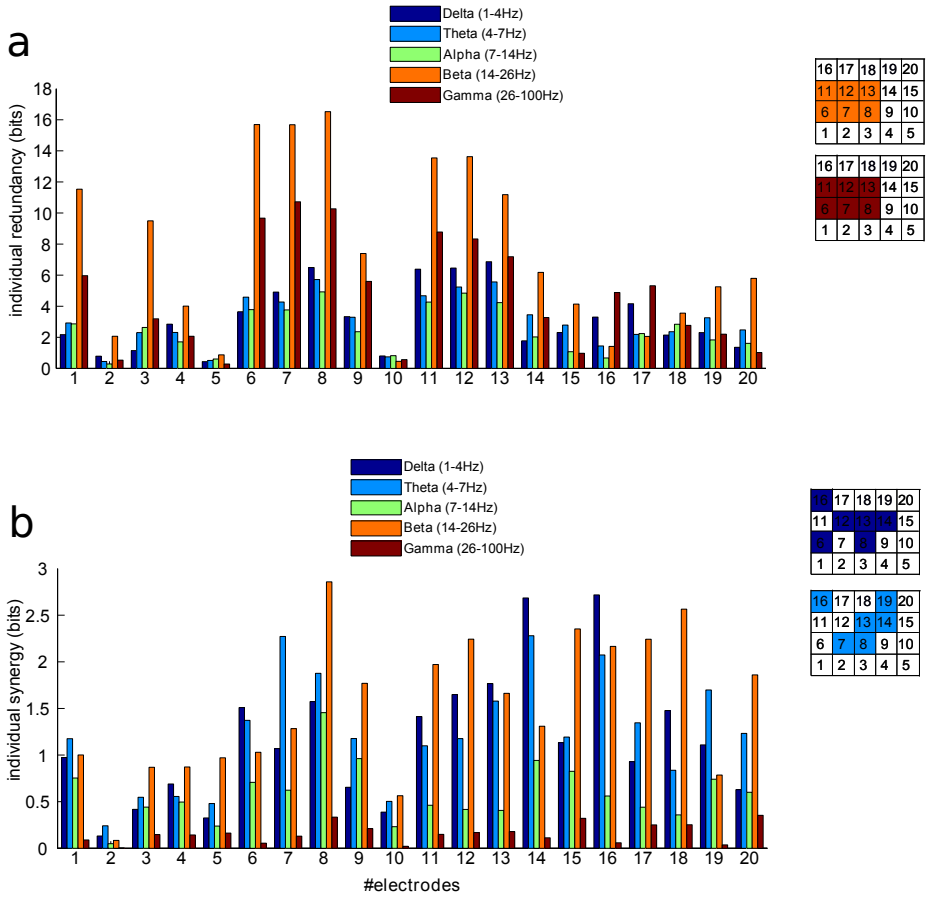


Irudia 10.6: **Erredundantzia eta sinergia frekuentzia bandetan. a:** R-k balio altuagoak jasotzen ditu maiztasun handiko bandetatik , beta eta gamma (laranja eta marroia), bi hauek distribuzio espazial antzekoa sortuz eta eremu epileptogenikoarekin bat eginez (10.3 irudia). **b:** Frekuentzia motelak, delta eta theta esaterako, kontribuzio handiagoa lortzen dute S-S-rendako (urdin iluna eta argia). Gainera, distribuzio espaziala nahiko ezberdina da R-rekin alderatuz, R-ren inguruan ematen baita, R-k zonalde epileptogenoa markatzen duen bitartean. R-ren aktibazioa maiztasun handiko eremu epileptogenikoarekin (hau da, TSI) lotu den bitartean, S inguruan eta maiztasun baxuko bandetan antzematen da

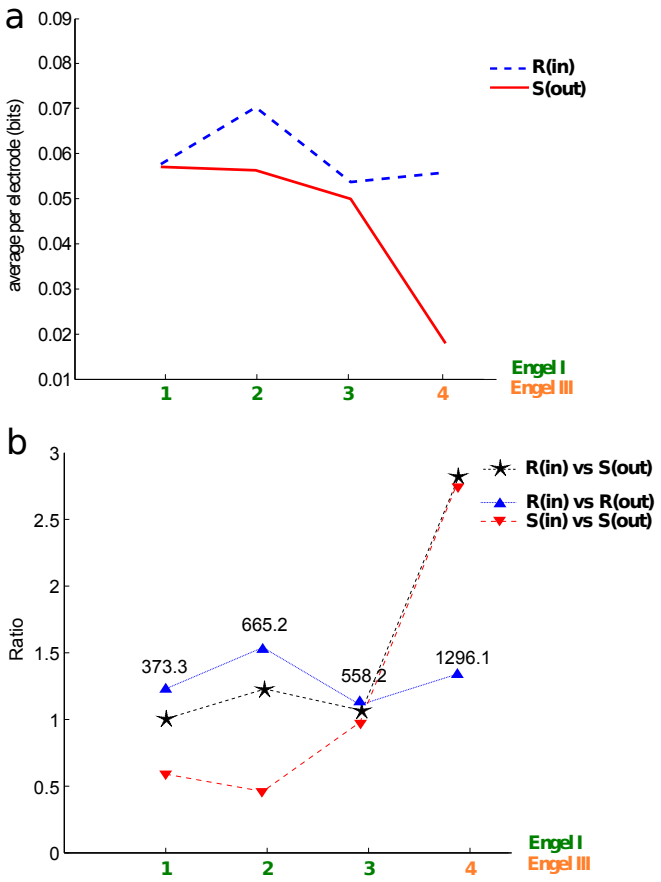


Irudia 10.7: **Pazienteen arteko balidazioa. a:** R-ren batez besteko balioak elektrodo bakoitzeko erresekzio eremuan (marra urdina) eta S erresekzio eremutik kanpo (linea gorriz). Erresekzio eremu barruko R guztia eta eremu kanpoko S guztiaren arteko erlazioa erakusten da. Hau Engel I zuten 3 gaixrekin eta Engel III zuen gaixo batekin kalkulatu zen (erresekzioa eta area epileptogenikoa bat ez zetozen kasu bat erakustearren). Engel I eta III-aren arteko emaitzak nahiko ezberdinak suertatu ziren. **b:** Erresekzio barruko R-a – R(in)– eta kanpoko S-aren –S(out)– arteko erlazioa eta baita barneko S-a –S(in)– S(out) eta R(in)-ekin zatituta. Engel I eta Engel III gaixoen arteko ezberdintasun garrantzitsuak daude, patroi dinamiko bat antzemanez: R zonalde epileptogenikoan eta S inguruetan . Paziente bakoitzeko R guztira ere irudikatzen da (hau da, 373,3, 665,2, 558,2 eta 1296,1 bit), non Engel III balioa Engel I kasuetakoan baino askoz handiagoa den.

eredu berdina izan da R-rentzat. Ikus daitekeenez, gaussianitatearen ustea ez-gaussianitatearekin bat dator eta koherentea da S R eremutik kanpo kokatzearekin.

Garrantzitsua da azpimarratzea geure xedea eremu epileptogenoaren inguruko ereduaren karakterizazioa osatzea izan dela. Horrela, TSI dagoeneko frogatua izan da zona epileptogenikoa antzemateko [144] eta lan honetan aurkitu duguna R TSI-rekin bat datorrela eta S inguruan agerikoa dela Engel I gaixoengan. Patroi hau argi ikusten da bereziki, ez-gaussianoa den distribuzioa onartuz, eta ondorio hau bat dator garun barneko interakzioen antolakuntzarekin, non tokian tokiko inhibizio zirkituen eraginaren menpe, kitzikapenak kontrolatzeko ardura duten [142]. TSI eta R arteko bateragarritasuna ez zen horren argia izan Engel III pazientearengan ( 10.9 irudia).

## 10.5 Ondorioak eta gerorako lana

Espazio-antolamenduari dagokionez, gure emaitzek erakusten dute R-k espazio epileptogenikoa batzen duela S inguruetan banatzen den bitartean. Dinamikari dagokionez, R-k maiztasun handiko bandetan (14-100Hz) ekarpen handiena egin du, eta S-k indizerik handiena maiztasun txikiagoko bandetan (1-7Hz) lortzen du. Horrela, interakzio informazioa datu klinikoei aplikatuz, interakzio epileptogenikoaren datu berriak agerian utzi ditugu egituretan (erredundantzia vs. sinergia) eta dinamiketan (erritmo bizkorrak vs. erritmo motelak).

Bukatzeko, eta ondorio bezala, nahiz eta II (S eta R) aktibitate interkritikoan aztertuak izan diren, emaitzek iradokitzen dute interesgarria izan daitekeela II krisi aurreko eta ondorengo datuetan analizatzea [207], horrela, R eta S egiturak aldatu egiten diren ikusiz.

## 10.6 Gehigarria: Elkarrekintza informazioak betetzen dituen propietateak

(10.5) ekuaziotik, zuzenean, propietate garrantzitsuak atera daitezke lan honekin erlazio zuzena dutenak:

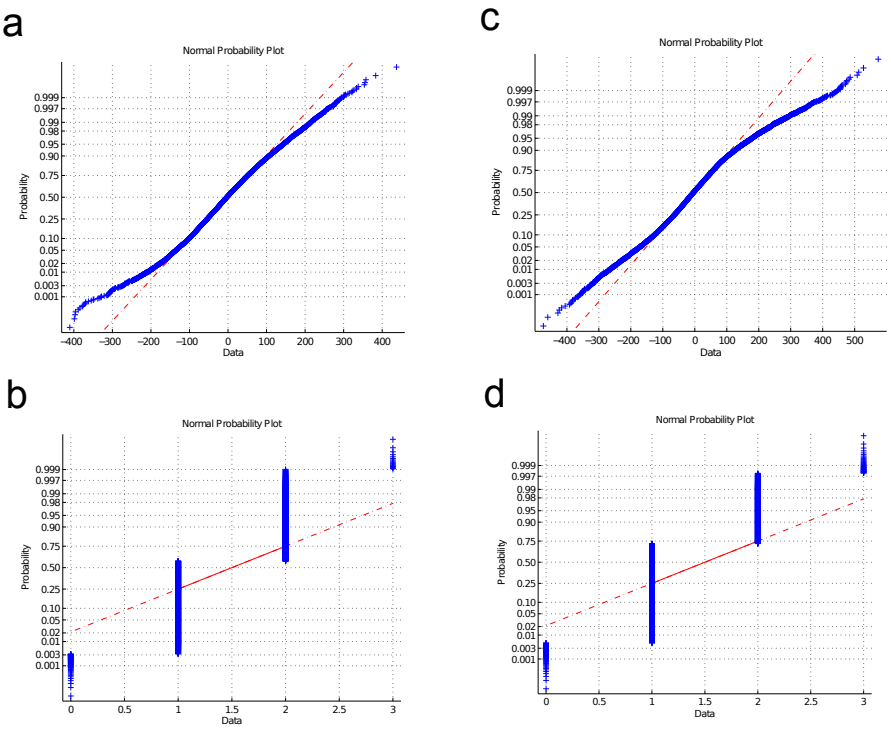


Irudia 10.8: **Ez-gaussianitate ebidentzia datuetan.** Probabilitate irudiek erakusten dute datuen jatorri ez-gaussianoa. **a:** gaixo baten datuak, elektrodo eta segmento bakarrarenak. II kalkulatzeko erabiliak (eta bide batez, R eta S). **b:** Datu berberak, baina 4 multzotan sailkaturik. Ez-gaussianitatea ere datu hauei egin zitzaien. **c,d:** Aurreko panelen antzera, Gaixo berbera, baino elektrodo ezberdina. Emaitza berberak jaso ziren gaixo ezberdinekin.

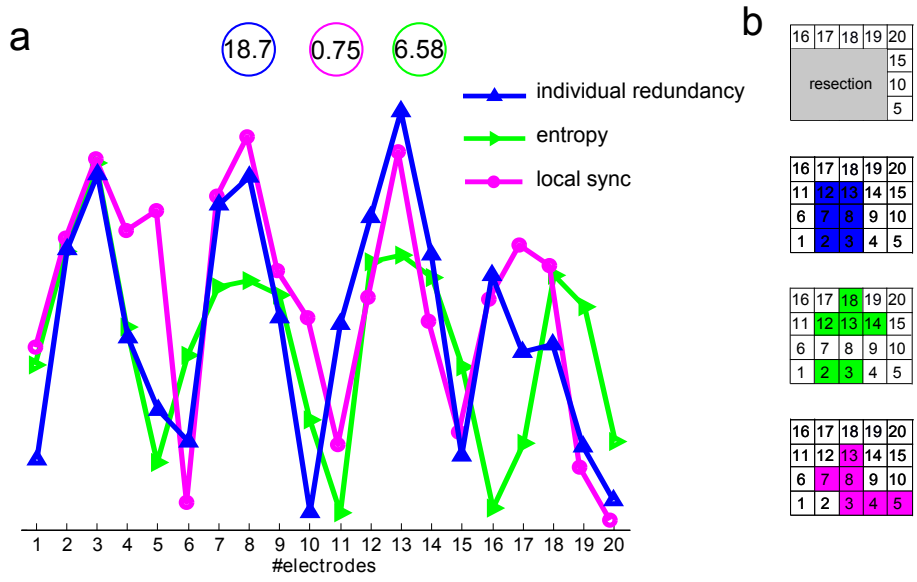


Irudia 10.9: **Erredundantzia interakzioak epilepsia elektrokortikografia datuetan oinarrituta Engel III-dun gaixo batengan.** 10.3 irudiaren antzera, baina Engel III duen gaixo batengan, hau da, ebakuntza ondoren krisiak desagertzen ez zaizkion gaixo baten datuetan oinarritutakoak. Ikus nola 3, 8 eta 13gn elektrodoek TSI balio maximoa duten ( TSI zonalde epileptogenoaren proxy balioztatu zen [144]) eta baita ere R balio maximoa.

- *Zirkulazioa*: II ez da aldatuko $(X, Y, Z)$ aldagaien ordena aldaturik ere eta horrela, II-ren kalkuloak emaitza bera emango du hurrengo kasu guztietan: $(X, Y, Z)$, $(X, Z, Y)$, $(Y, X, Z)$, $(Y, Z, X)$, $(Z, X, Y)$, $(Z, Y, X)$. Hau egiazta daiteke era zuzenean (10.5) formula erabiliz.

- *Elkarrekintza informazioaren limitea*: Bakarrik bi aldagai ezberdin duten hirukoteen kasuan, hau da: $(X, Y, X)$, $(X, X, Y)$, $(Y, X, X)$, $II = I(X, Y)$ betetzen da. Horrela II-k eta elkarrekintza informazioak (MI) balio bera dute, MI-ren aldagaiak berdinak ez badira. Honen egiaztapena definiziotik dator, entropia $H(X, Y, Y) = H(X, Y)$ eta $H(Y, Y) = H(Y)$ delako. Horrela, elkarrekintza informazioaren definizioak (10.3) ekuazioan probatutzat har dezakegu.

- *Shannon-en entropiaren limitea*: Hirukotearen hiru aldagaiak berdinak direnean, II= $H(X)$ betetzen da, hau da: II-k aldagaiaren Shannon-en entropiaren balioa hartzen du. Honen egiaztatzea aurreko puntuaren asoziazio berberetik uler daiteke eta era berean frogatzen da.

# Kapitulua 11

# Estruktura-funtzio multi-eskala konektomak (Laburpena)

Azken kapitulo honetan, osasuntsu dauden pertsonen garunaren berrestrukturazio funtzional eta estrukturala azalduko dugu. Hemen, parte-hartzaile osasuntsuen (N = 155) garuneko irudiak biltzen ditugu, 10-80 urte bitartekoak, funtzionala (atsedenerako egoera) eta estrukturala (traktografia) konektibitate matrizeak eraiki ahal izateko. Ondoren, garun-konektoma adina kalkulatu dugu (BCA) estimatzaile bat erabiliz, eta BCA alderatu dugu adin kronologikoarekin, benetako adinarekin (ChA). Zahartze osasuntsu prozesuak burmuineko egitura anitzekin erlazioa duela antzeman dugu konektibitate funtzionala eta estrukturalari erreparatuz; hala nola, ganglia basala eta talamoa, zirkuito fronto-striato-talamikoa osatzen dutenak. Orain artean, zahartze prozesua paziente gaixoengan aztertua izan denez, hipokanpoaren garrantzia gainentzen zen soilik. Gainera, metodologia bera aplikatu daiteke garuneko zahartzearen gaineko beste faktore eta terapia batzuen eragina ebaluatzeko, eta/edo ChA-n eragiten dezaketen beste biomarkatzaileekin korrelazioak identifikatzeko.

## 11.1 Sarrera

Zahartzea, denboraren menpe dagoen eta sistematikoa den gainbehera; biologikoki, maila psikologikoan eta sozialean eskala anitzetan aldaketak dakartzana. Interesgarria da adin kronologiko (ChA) bereko pertsonek, adinarekin erlazionaturik dagoen hondamen biologikoa erakus dezaketela, errendimendu kognitiboa ebaluatzean, gorputzeko ehun ezberdinen azterketan edo osasun metabolikoan oinarrituz [104, 193]. Ezberdintasun hauek bi zahartze prozesuak ulertzeko bi erakislatzen ditu. Bat ChA da, jaiotzetik abiatzen den denbora gisa kalkulatzen dena (hau da, jaiotzetik igarotako denbora, ez besterik) eta bestea adin biologikoa da, jaiotze-urtea edozein dela ere, momentu jakin batean heltze biologikoaren maila dena.

Zahartze kronologiko eta biologikoaren arteko ezberdintasunak azken urteetan interes zientifiko handia lortu du, zahartzaroarekin lotu daitezkeen molekulak, eragile genetikoak, organoaren dinamika zelularrak eta haren modulatzaile genetiko, epigenetiko eta ingurumenekoak duten inplikazioengatik [100]. Izan ere, zahartzeak arrisku faktore garrantzitsu bat da hasiera berantiarreko gaixotasun gehienetan, hala nola minbizia, gaixotasun kardiobaskularrak, diabetesa eta gaixotasun neurodegeneratiboak [87].

Kapitulo honetan, markatzaile estrukturalak eta funtzionalak erabiliko ditugu metodologia multi-eskala bat erabilita, garunaren zahartze prozesuan markatzaile hauek ematen duten konektibitateak adin kronologikoa nola baldintzatzen duen ikusteko.

Orain artean, konektibitate estrukturalak (SC) eta konektibitate funtzionalak (FC) demostratu dute adinarekin sare hauek segregazioa (modularitatea, sendotzea) galtzen dutela baina integrazioak (hau da, sarearen eraginkortasuna, efizientzia) gora egiten duela; konpensazio mekanismo bat balitz bezala [93], gure burmuinaren efizientzia bermatuz bizi osoan zehar. Dena den, FC eta SC analisi gehienek konektibitatearen hondatze hori gaixotasun ezberdinen menpean zeuden datuengan ikusi dira, Alzheimer, Dementzia edo Parkinsonak jota zeuden pazienteengan. Guk, lan hontan, sujetu osasuntsuengan egingo dugu analisi guztia.

Orain arteko lanetan, zahartzearen ikertzea bai SC baliatuz bai

FC erabiliz egin da, baina hau da lehen aldia (guk dakigularik) biak batera erabiliko direla. Lehen aldiz argitaratzen dugu ere optimoa den klasifikazio metodo baten erabilera adin kronologikoa modulatu dezakeen hirugarren faktore bat erabilpenarekin.

Lan hau bideratzen duten bi hipotesi nagusiak dira; lehena, adinaren estimazioa hobetu daitekeela FC eta SC metrikak erabiliz. Bigarrena, jarduera fisikoak eragina duela burmuineko markadoreetan, jarduera fisiko handiagoa egindako sujetuek garun gazteagoak izanen dituztela. Hipotesi hauek frogatzeko, aurreko lanetatik abiatuta [45, 46, 44, 72, 82, 81, 88, 95, 108, 122, 126, 192] datuek gidatutako estimatzaile bat eraiki dugu, FC eta SC biomarkatzaileetan oinarrituta.

## 11.2 Metodologia

### 11.2.1 Partehartzaileak

Partehartzaileak Leuven eta Hasselt (Belgika) udalerrietako biztanleen artean hautatuak izan ziren (IP: Stephan Swinnen). N=155 lagun osasuntsuko lagina lortu zen (81 emakumeak izanda) 10-80 bitarteko adinekin (44.4 urteko bataz bestekoa, desbiderapen estandarra 22.1 urtekoa). Ikerketa tokiko etika batzordeak onetsi zuen, Helsinkiko Adierazpenaren arabera.

### 11.2.2 Jarduera fisikoaren puntuazioa

Jarduera fisikoa (PA) Nazioarteko Jarduera Fisikoaren Galdesorta erabiliz ebaluatu zen [31] (IPAQ), aisialdi, etxeko eta lorezaintzako jardueretan burutzen den jarduera fisikoa ebaluatzen duena.

Hainbat ikerketek erakutsi dute IPAQ galdeketa egokia dela epe luzeko PA efektuak antzemateko [110, 127, 177, 57, 68].

### 11.2.3 Irudien eskuratzea eta tratamendua

Erresonantzia magnetikoaren irudi eskaneatzea Siemens 3T Magnetom Trio MRI eskaner baten bidez egin zen, 12 kanaldun bobina batekin. FC eta SC matrizeak lortzeko tratamendua aurreko kapituloetan aurkeztutakoaren antzekoa izan zen.

Horrela, 2514 x 2514 konektibitate matrizeak eraiki ziren sujetu bakoitzeko. FC zein SC matrizeak simetrikoak dira, non i-tik j-rako konektibitatea eta j-tik i artekoa berdina den.

### 11.2.4 Brain Hierarchical Atlas-a (BHA)

Erabilitako partizioa Brain Hierarchical Atlas (BHA) izan zen, orain gutxi sortutakoa [69]. Bertan, modularki banatzen eta egituratzen da burmuina gero eta modulo txikiagoetan, estruktura zein funtzio konektibitateei batera erreparatuz. Horrela, partizioak estrukturalki eta funtzionalki optimoak izatea lortzen da.

11.1 irudian, partizio honen aplikazioa ikus daiteke, SC eta FC matrizeetan. Bietan ikus daiteke behin partizioa aplikatuta, bien arteko korrelazioa altua dela, matrizeak oso berdintsuak direla.

### 11.2.5 Bentrikuluen haztearen eragina ezabatzen

Jakina da garuneko bentrikuluen tamaina adinarekin hazten dela. Faktore tribial honen ekarpenak ezabatzeko, gure analisitik bentrikulu handienen eragina ezabatu behar dugu. Horretarako, garun guztien bentrikuluen antzematea egin dugu, espazio komun batera erregistratu eta bertan, handienen mugak hartuz, bentrikuluak hartzen zituzten eskualdeak ezabatu ditugu. 11.1a irudiak erakusten du prozedura hau.

### 11.2.6 Estruktura-funtzio korrelo-dendrogramak

SC eta FC matrizeetatik abiatuta, burmuinaren adinaren korrelo-dendrogramak (CDG) eraiki ditugu, adina eta barne-kanpo moduluen arteko informazioa erabiliz. Lau deskriptore mota erabiliko ditugu;

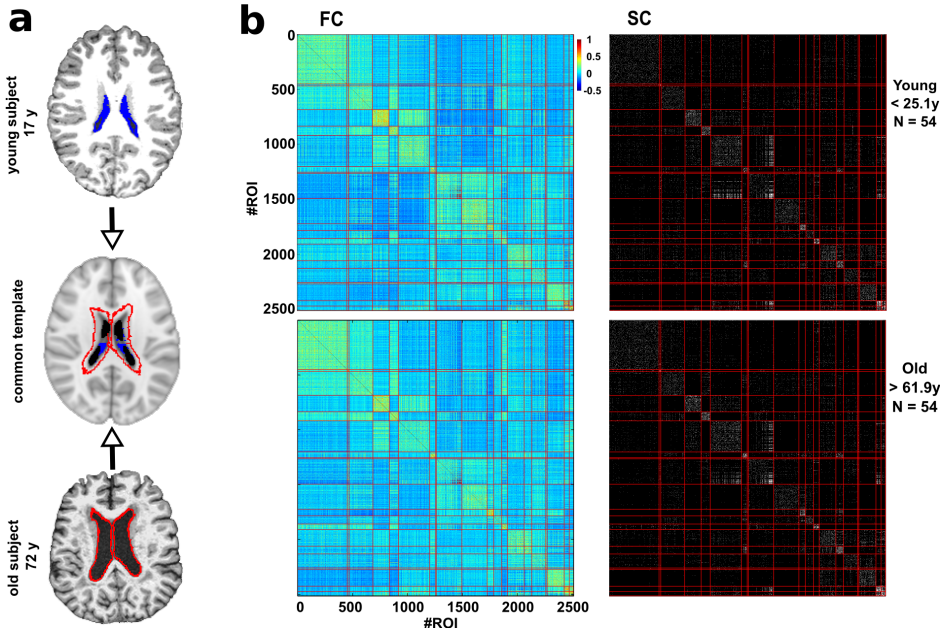


Irudia 11.1: **Brain Hierarchical Atlasa berdin mantentzen da adin ezberdinetan a:** Espazio komunean normalizazioa (erdiko burmuina). Adibide honetan, garun gazte bat (17 urtekoa, goiko irudian) eta zahar batena (72 urte, beheko irudian). Bentrikuluen 3D segmentazioa egin ondoren, haien mugak bateratzen dira eta handienek hartzen zituzten eskualdeak ezabatu. **b:** Brain Hierarchical Atlas (BHA) ordenatzea gazte (goian) eta zaharrentzako (behean), adin tarte ezberdinak izanagatik, oso antzekoak dira lau matrizeak.).

barne funtzional (FIC), kanpo funtzional (FEC), barne estruktural (SIC) eta kanpo estrukturalak (SEC) 11.2 irudian ikus daitekeen bezala.

Barne konektibitatea modulo barneko erpinen batuketa eginez lortzen da eta kanpo konektibitatea modulo kanpoko konektibitate balioak batuz. Ondoren, deskriptore hauek (N=155 izanik)adinarekin korrelatzen dira, Bonferroni korrekzioa egin ondoren, emaitzak baliogarriak izan daitezen.

FC eta SC deskriptoreen efektua batera antzemateko, deskriptore funtzional nahiz estrukturalen p-baloreak esanguratsuak behar dira erro karratuen biderketa egin ondoren, hau da, biak 0.05 azpitik egon behar dute Bonferroni korrekzioa pasa eta gero. Hala izanik, bien korrelazio baloreen bataz-besteko geometrikoa burutzen da. Prozedura osoa kode irekian aurki daiteke, `https://github.com/compneurobilbao/aging`.

### 11.2.7 Gehienezko Probabilitate Zenbateslea (MLE)

Partehartzail $n$ bakoitzeko $K$ konponentedun $x^n \equiv \left(1 x_1^n x_2^n \cdots x_{K-1}^n\right)^T$ bektorea definitzen dugu, bakoitza konektibitate deskriptore bat dagokiona, zeinean $T$ trasposatu operadorea den.

Adin estimatua, $n$, partehartzaile bakoitzarentzat konbinazio lineal baten bitartez kalkulatua izan zen. Hau da:

$$t_n = \omega_0 + \sum_{j=1}^{K-1} \omega_j x_j^n + \epsilon_n \tag{11.1}$$

non $\varepsilon_n$ ausazko zero baliodun aldagai Gaussianoa den $\sigma^2$, bariantzarekin eta $\omega \equiv \left(\omega_0 \omega_1 \omega_2 \cdots \omega_{K-1}\right)^T$ pisua daraman bektorea. $P$ partehartzaile ezberdinekin , 11.1 ekuazioa erabiliz, errore funtzioa horrela definitu daiteke:

$$E\left(\omega\right) = \frac{1}{2} \sum_{n=1}^{P} \left\{ t_n - \omega_0 - \sum_{j=1}^{K-1} \omega_j x_j^n \right\}^2 \tag{11.2}$$

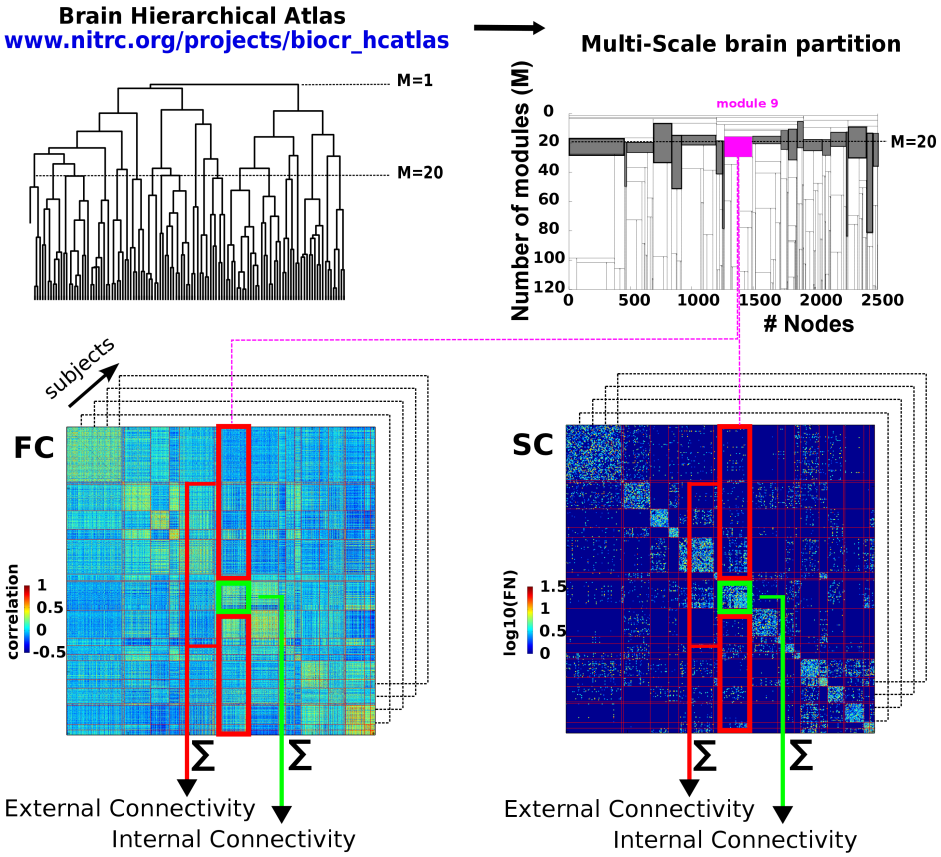


Irudia 11.2: **Deskriptoreen deskripzio eskematikoa Goi-ezker:** BHA atlasaren hierarkia zuhaitza, partizio optimoan moztuta (M=20) **Goi-eskuin:** Partizio multieskalak erakusten du nola moduloak maila ezberdinetan banatzen diren zuhaitzan behera egiten duten einean. Irudi honetan partizioa M=20-tik M=120-ra erakusten dugu. Grisez koloreztatuak dauden moduloak M=20 partizioarekin bat datozenak dira. **Behean:** M=20 partiziorako, partehartzaile bakoitzarentzat, bere barne (berdez) eta kanpo (gorriz) konektibitatea kalkulatzen dugu bai FC eta bai SC matrizeetan. Prozedura hau M=20 eta M=1000 partizioetan jarraitzen da.

errorea minimizatzen duen pisu-bektorea kalkulatzeko balio digu-na (erantzuna $\nabla_\omega E(\omega) = 0$ denean, lehen deribatua $\omega$-rekiko zero denean). Minimo horrek definitzen du beraz Gehienezko Probabilitate Zenbateslea (Maximum Likelihood Estimator - MLE), analitikoki ebatzia izan daitekeena [27, 48]:

$$w^{MLE} = \left(\varphi^T \varphi\right)^{-1} \varphi^T t \tag{11.3}$$

$-1$ adierazleak matrizearen alderantzizkoa delarik, $t \equiv (t_1 t_2 t_3 \cdots t_P)^T$ , $P$ bektorearen estimazioak eta $\varphi$ *diseinu matrizea*, hau da:

$$\varphi \equiv \begin{pmatrix} 1 x_1^1 x_2^1 \cdots x_{K-1}^1 \\ 1 x_1^2 x_2^2 \cdots x_{K-1}^2 \\ \vdots \\ 1 x_1^P x_2^P \cdots x_{K-1}^P \end{pmatrix} \tag{11.4}$$

### 11.2.8 Adin estimaziorako ez-linearitateak eransten

11.1 ekuazioak linealki dependienteak diren konektibitate deskriptoreak aintzat hartzen baditu ere, MLE estrategia orokorragoa da eta ez-linearitateak batzeko aukera ematen du (termino kuadratikoak, polinomialak edo beste funtzio batzuk, esaterako). 11.6 irudiak termino kuadratikoak erantsita lor daitezkeen emaitzak erakusten ditu

### 11.2.9 Bataz-besteko errore absolutoa (MAE) eta garun-konektoma adina (BCA)

Estimatzailearen kalitatea berresteko metrika bezala, bataz-besteko errore absolutoa (MAE) horrela kalkulatu zen:

$$MAE(K) = \frac{1}{N_2} \sum_{n=1}^{N_2} |ChA_n - BCA_n(K)| \tag{11.5}$$

||-k errore absolutoa esan nahi du eta garun-konektoma adina (BCA) horrela difinitu dugularik:

$$BCA_n\left(K\right) \equiv \omega_0^{MLE} + \sum_{j=1}^{K-1} \omega_j^{MLE} x_j^n \tag{11.6}$$

$w^{MLE}$ 11.3 eta 11.4 ekuazioetan difinitzen da database guztia erabili denenan $w^{MLE}$ kalkulatzeko. Estimazioaren erroreak behera egiten du deskriptoreak batzen dihoazen einean (deskriptore gehiago, estimazio hobea), baina estrategia honek bariantza handiegia suertarazten du, beste datu batzuetan $w^{MLE}$ emaitza erabiliz, erroreak gora egin dezakeelako. Arazo hau, datuak trebakuntza-test multzoetan banatuz ekidin daiteke [97]. Horrela, MAE kalkulatzeko, dautak banatu egin dira kalkulo bakoitzean ( %75 (N1=115) trebakuntzarako eta %25 (N2=38) testetarako erabiliz.

Gogorarazten dugu, nahiz eta hasiera batean lau deskriptore mota zeuden –FIC, FEC, SIC and SEC– modulo bakoitzeko – M=20 M=1000 bitartean–, azkenean K deskriptore erabiliko direla MLE adina estimatzeko. Beraz, MLE erantzunak dependentzia dauka K-rekiko (ikus hurrengo sekzioa K deskriptoreak nola hautatu diren ulertzeko).

### 11.2.10 MLE-ren optimizazioa

Modelo optimoa lortzeko, hau da, adina estimatzeko hobeak diren K deskribatzaileak hautatzeko, prozedura hau jarraitu dugu:

1. K=1 kasuarentzako, benetazko adinarekin hobeto korrelatzen duen deskriptorea erabili da. 2. K=2 deskriptorea, soberan zeuden guztien artean hautatzen da, 100 esperimentu egin ostean, bataz-besteko MAE txikiena hobesten duena K=1 deskriptorearekin batera. Hautatu gabe dauden deskriptore guztien artean, ausaz, bata bestearen atzetik frogatzen dira datuen %75 trebakuntzarako eta %25 testendako erabiliz. 3. K=3 eta hurrengokoek 2. pausuan jarraitu den estrategia bera luzatuz batzen dira, horrela, bataz-bestean batzen

diren deskriptoreen emaitzak beti optimoak izango dira. 4. Estrategia hau jarraituz, MAE(K) dinamikak behera egiten du minimo baten bila K-k gora egiten duen einean. Horrek definitzen du modelo optimoa, K deskriptorez osatua.

Optimizazio estrategia hau scikit-learn erabiliz programatu da, `http://scikit-learn.org/stable/`. Kodigo guztia librea da eta hurrengo estekan deskargatu daiteke `https://github.com/compneurobilbao/aging`.

## 11.3 Emaitzak

N=155 partehartzaileko popuplazio osasuntsu bat erabili da ikerketaratko, 10 eta 80 urte artekoa (bataz-besteko adina 44 urtekoa izanik, 22 urteko desbiderapenarekin). Aktibitate fisikoarekin batera, erresonantzia magnetikoko difusio, estruktura eta funtzional irudiak jaso ziren.

BHA (ikus [69] eta Metodologia) erabili dugu 2514 areako SC eta FC matrizeak kalkulatzeko, haien arteko konektibitatea, eta azterketa multi-eskala egiteko.

Lehenik eta behin, BHA-ren balidazioa egin dugu, adin populazio ezberdinek emaitza antzekoak ematen dituztela bermatuz, 11.1 irudian ikus daitekeen bezala. Bi populazio ageri dira, gazteak, 25 urtetik beherakoak eta zaharrak 61 urtetik gorakoak (biek 54 sujetu izanik). Irudian ikus daiteke ez dagoela matrizeen arteko ezberdintasunik.

Ondoren, partizio bakoitzeko modulo ezberdinen lau deskriptoreak kalkulatu genituen (barne funtzional (FIC), kanpo funtzional (FEC), barne estruktural (SIC) eta kanpo estrukturalak (SEC)) eta hauek adinarekin korrelazionatu korrelodendrogramak sortuz.

Kanpo konektibitate patroiak aztertuz, area dexente ikus daitezke markaturik, hala nola frontala (goi eta mediala), erdi-zingulua, parahipokanpoa, goi-okzipital area, fusiformea, prekuneo eta kaudatea, talamoa eta lobulu temporala (mediala eta behekoa).

Beste honetan ordea, beste egitura batzuk ikus daitezke: insula, zinguloa, kalkareo eta kuneusa, okzipital osoa, fusiformea, goiko

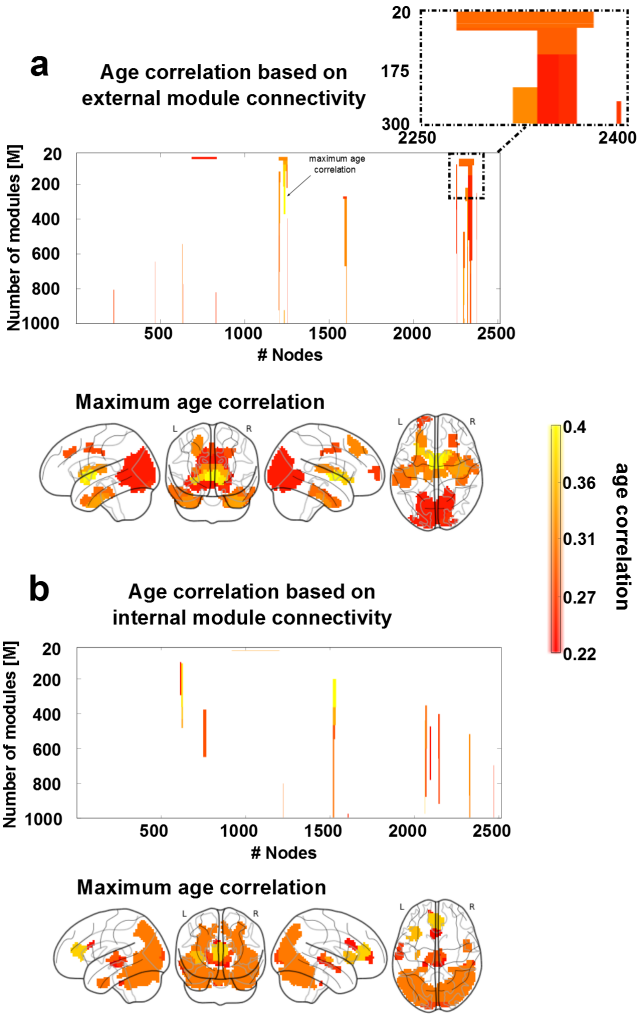


Irudia 11.3: **Estruktura-funtzio korrelodendrogramak (CDG) eta adin korrelazioaren estruktura-funtzio mapak multi-eskala partizioan.** Korrelodendrogramak eraikitzeko, partizio (20<=M<=1000) modulo bakoitzaren korrelazioa adin eta deskriptoreen (FEC, FIC, SEC eta SIC) artean kalkulatuz eraiki dira. **a:** Kanpo konektibitateak adinarekin duen erlazio. Mapek garunaren eskualde bakoitzean lortzen den korrelazio emaitza maximoa erakusten dute. **b:** a panelaren antzeko irudia, baino barne konektibitateari dagokiona

parietala, talamoa, tenporala (behe eta mediala) eta zerebeloa.

Estruktura-funtzio korrelodendrogramek ezin dute estrukturak zein funtzioak banaka egiten duten ekarpenei buruzko informazioa eman. Horretarako, deskriptoreak sailkatu behar dira, 11.4 irudian egin den bezala.

Kanpo konektibitate analisiak hainbat area erakusten ditu kontrako tendentzia daramatenak (SC-k behera eta FC-k gora), karratu urdinean adierazita, homeostasia adierazten duen mekanismoa erakutsiz. Karratu berdean, bi kasuetan gainbehera adirazten duten areak (gehienak barne burmuineko estrukturak). Barne konektibitatean aldiz, bakarrik bi kasuetan behera doazen deskriptoreak aurkitu dira.

MLE estimatzailea lortzeko, deskriptore hoberenak hartu ditugu eta estrategia optimo bat gauzatu dugu. 11.5a irudian ikus daitekeen bezala, deskriptoreak bata bestearen atzetik hartuz gero, overfitting-a gertatzen da (gehiegizko ikastea).

Lehen deskriptorearen gibeletik optimoa dena batuz (ikus Metodologia), estimatzaile optimoa K=38 deskriptore erabilitakoan gertatzen da. Bataz-besteko 5.89 urteko errorea ematen duena, 11.5b irudia.

K=38 deskriptore hoiek erabiliz lortzen dugun errepresentazio grafikoa 11.5c irudian agertzen da, 0.95-ekoa eta , p-balorea<10e-20-koa izanik.

Azkenik, deskriptore hoien kokapen espazialari erreparatu diogu, 11.5e irudian agertzen diren mapak lortuz. Gure modeloaren eraikuntzan lau deskriptore mota parte hartu dutenez, modulo bakoitza lau aldiz agertu daiteke. Adin Partehartze Indizieak (API), 0 eta 4 bitartean dagoenak, horren adierazle da.

API=3 dituzten estrukturak ganglia basala (kaudatea, putamena eta palliduma) eta talamoa dira. Hauek dira adin osasuntsuarekin estruktura-funtzionalki erlazio gehien duten areak.

## 11.4 Konsiderazio metodologikoak

Estimazioa termino linealak erabiliz egin dugu. Hala era, estudio askotan adinaren efektuak deskriptore kuadratiko bat bezala deskribatu

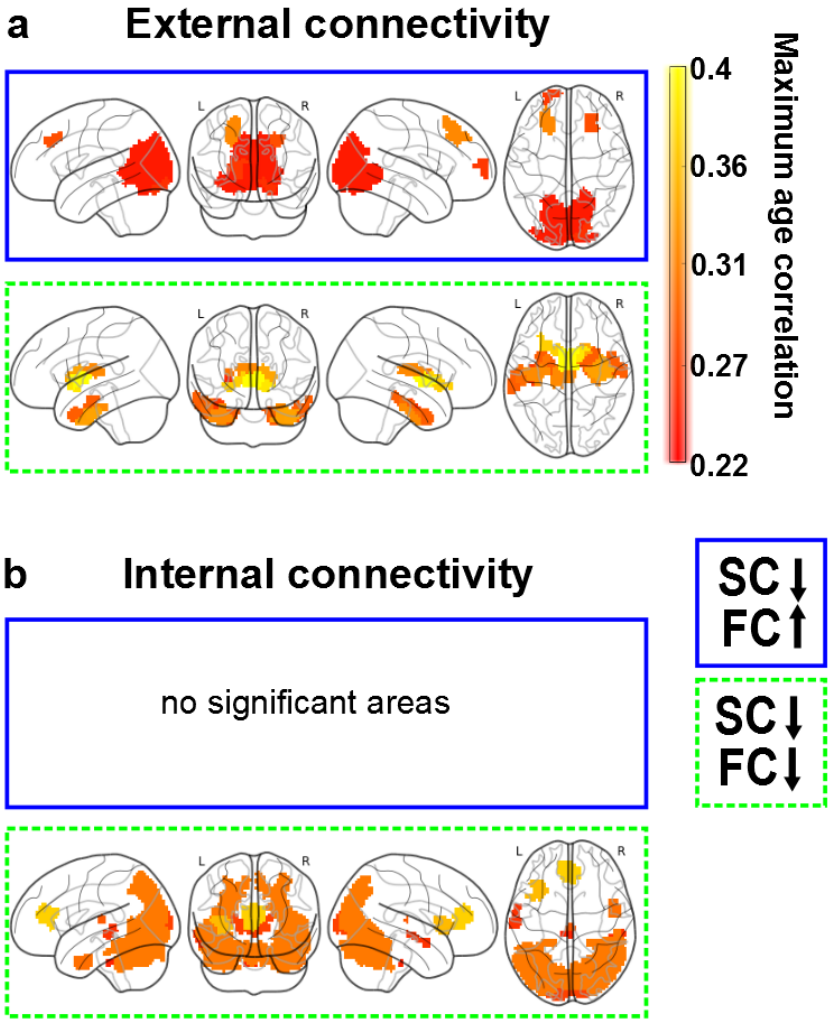


Irudia 11.4: **Konektibitate funtzionalaren modulazioa.** SC-k beherantz egin dezake adinarekin, baina FC-k konpentsazio efektua egin dezake (urdinez) edo behera joan ere (berdez). Gertakari hau kanpo deskriptoreekin (a panela) zein barne deskriptoreekin (b panela) gerta daiteke. Ikus SC-aren beheratze eta FC-aren goratze kasurik ez dagoela barne konektibitate kasurako.11.3) irudian bezala, zero ez diren balore guztiek p-balore esanguratsuak dituzte.

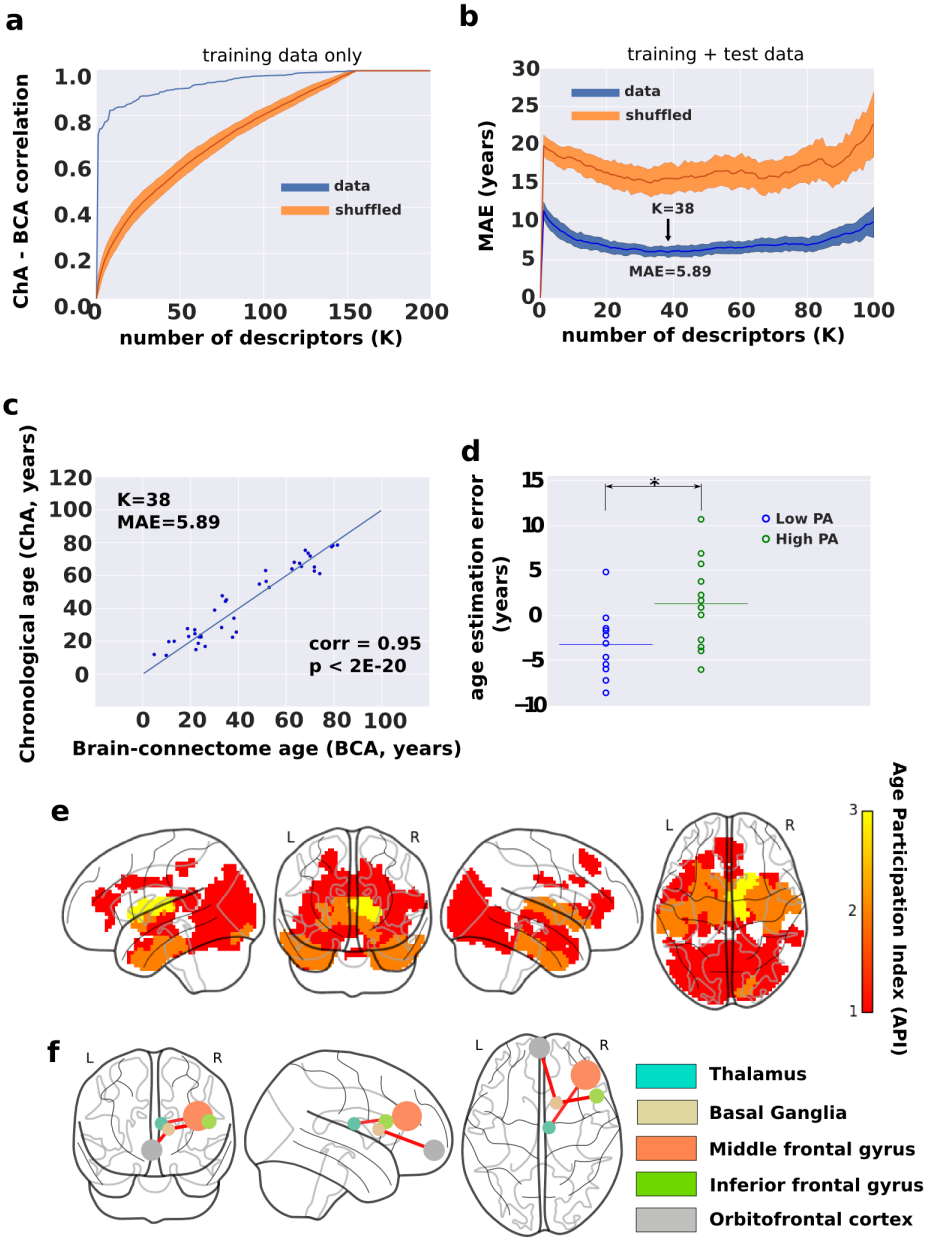


Irudia 11.5: **Adin kronologikoa (ChA) vs Garun-konektoma adina (BCA) eta jarduera fisikoarekiko modulazioa.**

Irudia 11.5: **Adin kronologikoa (ChA) vs Garun-konektoma adina (BCA) eta jarduera fisikoarekiko modulazioa.** **a:** ChA eta BCA arteko korrelazioa deskriptore kopuruaren arabera datu guztiak ikas-prozesuan erabilita. Deskriptore kopurua gora doan einean, korrelazioak ere gora egiten du, over-fitting-a eraginez. Hau ekiditeko datuak trebakuntza eta test multzoetan banatu behar dira. **b:** Bataz-besteko errore absolutoa (MAE) K-ren arabera, %75 trebatzeko eta %25 testa egiteko. Gutxieneko MAE-a 5.89 urtekoa izan zen K=38 deskriptore erabiliz. a) panelean bezala, urdinez kasu erreala eta laranjaz ausaz egindakoa. **c:** Ausazko estimazioa MLE estimatzailea erabiliz (bataz besteko erroretik hurbil egoteko aukeratua) K=38 deskriptore optimoak erabiliz. . **d:** Adin estimazio errorea (BCA-ri ChA kenduz) bi partehartzaile multzo ezberdinentzako: multzo batek jarduera fisiko asko egiten duena eta gutxi egiten dutenak. **e:** K=38 deskriptoreak burmuinean espazialki kokatzen duen mapa. Gure modeloaren eraikuntzan lau deskriptore mota parte hartu dutenez, modulo bakoitza lau aldiz agertu daiteke. Adin Partehartze Indizieak (API), 0 eta 4 bitartean dagoenak, horren adierazle da. Talamoa eta ganglia basala dira gehien agertzen diren estrukturak. **f:** Ganglia basala eta talamoaren konektibitate sareak. Estruktura eta funtzionalki fronto-striato-talamo egitura osatzen dute.

da (hau da, gaztetan funtzionalitateak gora egiten du eta zahartzaroan gainbehera dator) [90].

Metodologia bera errepikatu genuen termino kuadratikoak erabiliz modelo berri batekin, 11.1 ekuazioan termino kuadratikoak erantziz. 11.6 irudian ikus daitezke emaitzak.

Ezberdintasun nagusiak prefrontal eta okzipital konektibitateetan ikus daiteke. Area horietan termino kuadratikoek eragiten dutela aurreko lanetan ikusitakoarekin bat dator [90].

Estimatzaileari dagokionez, termino kuadratikoak batzerakoan, ez genuen emaitza hobeagorik lortu. Prozedura berdina jarraituz, 5.88 urteko errore tasa lortu genuen, termino linealak erabiliz jasotakoaren oso antzekoa.

## 11.5 Eztabaida eta laburpena

Biztanleria osasuntsuan zahartzea aztertu dugu eskala ezberdinetan (multieskala). Gure emaitzak ondokoak izan dira: Lehenik eta behin, zahartzeak konektibitate estrukturala eta funtzionala nabarmenki kal-

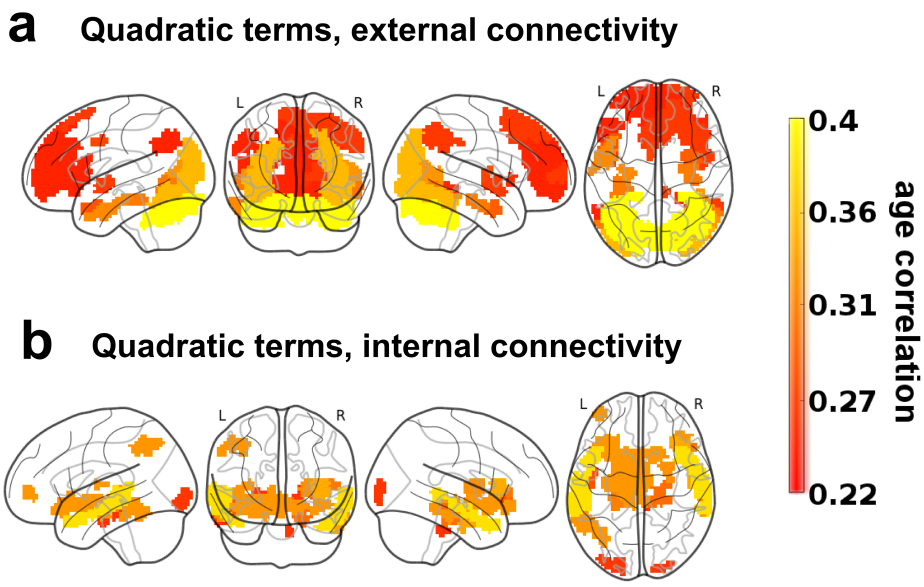


Irudia 11.6: **Estruktura-funtzio mapak termino kuadratikoak erabilita a:** Barne konektibitate patroiak . **b:** Kanpo konektibitate patroiak

tetzen ditu. Bigarrenik, ganglia eta talamoaren arteko estrukturafuntzio konektibitateak, zirkuitu fronto-striato-talamikoak alegia, ekarpen handiena egiten dio adinaren estimazioari.

Ganglia basala eta talamoarekin sare egituran loturik dagoen arearri (11.5f irudia), fronto-striato-talamo egitura deritzo. Fronto-striato-talamo egiturak adin osasuntsuan garrantzi nagusia duela ikusi dugu. Orain arteko ikerketetan, adinarekin erlazionatuak izan diren estrukturak hipokanpoaren higadurarekin bat zetozen [15, 73, 9], beti ere gaixoengan egindako ikerketak zirelarik.

Bestalde, gure emaitzek jarduera fisikoak burmuinaren osasunean (adin-osasunean, beti ere) eragina izan dezakeela erakutsi dute. Ez hori bakarrik, jarduera fisikoa adibide bat besterik ez izanik, beste edozein biomarkatzaile erabil daiteke gure estimatzailearekin batera, kanpoko faktore batek adin konektibitatean duen eragina aztertzeko.

# Kapitulua 12

# Ondorioak

Azken kapitulo honetan, kapitulo ezberdinen eta tesiaren ondorio nagusiak laburbilduko ditut.

## 12.1 Kapituloen laburpena

Lehen hiru kapituloak epilepsiari eskainitakoak izan dira, gaixotasun horri loturiko konektibitate eta datu mota ezberdinak aztertu ditugu.

9. kapituluan, MTLE sagu eredua erabili dugu, garun epileptikoaren hondatzea aztertzea baliotu digunak. FC-aren aldakuntzetan ikusi ditugu trantsizio guztia, hasierako krisi pasarte batetik kronifikaziora. Hain zuzen ere, lehen egunean garunaren konektibitate orokorrarak jaitsiera handia izan zuen, baina egun batzuk geroago handitu egin zen berriz.

10. kapituluan, pazienteen erresekzio eremua erreferentziatzat hartuz, eremu epileptogenoaren inguruko Informazio Interakzioa neurtu dugu. Eremu epileptogenoaren inguruko informazio patroien ereduaren karakterizazio osoa osatu dugu. Espazialitateari dagokionez, gure emaitzek erakusten dute erredundantziak (R) eremu epileptogenikoa bateratzen duela sinergia (S) inguruan banatzen den bitartean. Dinamikari dagokionez, R-ek maiztasun handiko bandan (14-100Hz) ekarpen handiena egin du, S maiztasun txikiagoetan nabarmentzen den bitartean (1-7Hz).

Epilepsiarekin amaitzeko, 4. kapituluan gaixotasuna aztertzeko ikuspegi multimodal bat deskribatu dugu, garun bareneko EEG, MRI estrukturala eta funtzionala bateratuz. Datuak bi ikuspegi erabiliz aztertu ditugu: modularrak (egitura antzeko egiturak bilatzeko) eta erpin bakarrekoak (sareen arteko loturen antzekotasunak antzemanez). fMRI eta elektrodoen konektibitate matrizeen arteko antzekotasun nabariak identifikatu genituen eta fMRI-aren dinamika positiboekin bat datozen eremu epileptogenikoen azterketa bat egin da.

5. kapituloan, Alzheimer gaixotasuna duten eta populazio osasuntsuaren arteko ezberdintasunak ikusi ditugu, garunaren informazio fluxuei erreparatuz.

Interesdun area (ROI) baten eta bestearen arteko informazio fluxuek ez dute ezberdintasunik (eta lehen Osagai Nagusiekin (PCA) oso antzekoak dira). Dena den, bigarren osagaiari erreparatuz gero, orduan bai ezberdintasun esanguratsuak aurkitu daitezkeela. Ondorio gisa, Alzheimer gaixoak kontrolarekin alderatuz informazioa fluxu handiagoa duela esan daiteke.

Bukatzeko, 11. kapituluan biztanleria osasuntsuan zahartzea aztertu dugu eskala ezberdinetan (multieskala). Gure emaitzak ondokoak izan ziren: Lehenik eta behin, zahartzeak konektibitate estrukturala eta funtzionala nabarmenki kaltetzen ditu. Bigarrenik, ganglia eta talamoaren arteko estruktura- funtzio konektibitateak, zirkuitu fronto-striato-talamikoak alegia, ekarpen handiena egiten dio adinaren estimazioari.

## 12.2 Ondorio nagusiak

Kapitulu bakoitzak bere ondorioak izanik, hemen, tesiaren ikuspegi osoa jorratzen duten ondorio orokorrak laburki aipatzen ditugu.

- Latentzia-aldia identifikatu zen sagu MLTE ereduan. Latentzia-aldi honetan, burmuin osasuntsu bat epileptikora edo epileptogenesiserako trantsizioa gertatzen da. Burmuineko molekula, zelula eta sarearen propietateen aldaketak gertatzen dira hasierako gertaeraren aurrean (krisia). Maila molekular eta zelularretan egindako ikerketek, prozesu epistemologikoa ulertzeko

ikuspegi integratzaile bat eman dezakete, estrategia terapeutiko eraginkorretan gune berriak irekitzeko.

- Elkarrekintza Informazioa datu klinikoei aplikatuz, egitura epileptogenikoaren modularitate berriak (erredundantzia vs. sinergia) eta interakzioen dinamikak (erritmo bizkorrak vs. erritmo motelak) agerian uzten dira.

- MRI datu multimodalak (garun barneko elektrodoekin batera) garrantzia handia izan dezakete konektibitate ereduak azaltzeko eta garunaren berrantolaketa aztertzeko kirurgiaren ondoren.

- Alzheimerra duten gaixoak biztanleria osasuntsuarekin alderatuz gero, Oinarrizko Sareen arteko informazioa fluxuari erreparatuz, ROI-en batez besteko jarduera ez da desberdintasun esanguratsurik aurkitzen gaixoen eta kontrolen artean. Hala ere, Bigarren Osagaiak (PCA) gaixoen eta kontrolen arteko informazio fluxua bereizten du.

- Zahartze osasuntsua eragiten duten konektibitate zirkuitu berriak aurkitu dira eta garrantzitsuagoa dena, metodologia bera aplikatu daiteke, bai zahartzearen gaineko beste faktoreen eta terapia batzuen eragina ebaluatzeko, bai eta beste biomarkatzaile batzuekin korrelazio ereduak identifikatzeko. .

## 12.3 Hausnarketa

Tesi honek informatikako, matematika eta fisikako metodoen aplikazioa islatzen du medikuntzan eta datu oso anitzak aztertzen ditu (MRI-tik elektrofisiologikoetara, giza eta sagu garunak barne). Informatikariek badakite egungo klinika praktikoak, tesi honetan aurkezten den metodologia erabiltzetik oso urrun daudela gaixotasunen identifikazioa edo ebaluazioa egiteko. Hala ere, neurozientzia konputazionalak giza ezagutza eta garunarengan dugun ulermenaren mugak gainditzen laguntzen duela uste dugu.

Medikuek garuneko gaixotasunak kuantifikatzeko metodo hauek aintzat hartzea nahi badugu, neurozientzia konputazionalak protokolo fidagarriak eta erreproduzibleak sortu behar ditu. Liburu honetan horrela lan egin den arren, praktika erreproduzibleak (bikaintasunerako bidean) jorratzea trebakuntza periodo honetan ikasgai baliotsua izan da.

Benetan sinesten dut ospitaleetan lan egiten duten talde multidisziplinarrek ospitaleetan erronka berriei hasiera emateko gakoa direla, azkenean emaitza handiak lortuko dituztenak. Lan honekin, apalki, elkarrekintza horren adibide bat eman nahi izan dut, diziplinen arteko kolaborazioen indarra erakutsiz.

# Bibliography


[1] Alexandre Abraham, Fabian Pedregosa, Michael Eickenberg, Philippe Gervais, Andreas Mueller, Jean Kossaifi, Alexandre Gramfort, Bertrand Thirion, and Gael Varoquaux. Machine learning for neuroimaging with scikit-learn. *Frontiers in Neuroinformatics*, 8, 2014.

[2] IM Adams. Structural plasticity of synapses in Alzheimer's disease. *Mol. Neurobiol*, 5:411–419, 1991.

[3] B. E. Ainsworth, W. L. Haskell, M. C. Whitt, M. L. Irwin, A. M. Swartz, S. J. Strath, W. L. O'Brien, D. R. Bassett, K. H. Schmitz, P. O. Emplaincourt, D. R. Jacobs, and A. S. Leon. Compendium of physical activities: An update of activity codes and MET intensities. *Medicine and Science in Sports and Exercise*, 32(9 Suppl):S498–504, September 2000.

[4] N. R. Al-Rodhan and J. L. Fox. Al-Zahrawi and Arabian neurosurgery, 936-1013 AD. *Surgical Neurology*, 26(1):92–95, July 1986.

[5] Karim A. Alkadhi. Exercise as a Positive Modulator of Brain Function. *Molecular Neurobiology*, May 2017.

[6] C. Alonso-Montes, I. Diez, L. Remaki, I. Escudero, B. Mateos, Y. Rosseel, D. Marinazzo, S. Stramaglia, and J.M. Cortes. Lagged and instantaneous dynamical influences related to brain structural connectivity. *Front Psychol*, 6:1024, 2015.

[7] H Amieva, LH Phillips, S Della Sala, and JD Henry. Inhibitory functioning in Alzheimer's disease. *Brain*, 127:949–964, 2004.

[8] T. A. Amor, R. Russo, I. Diez, P. Bharath, M. Zirovich, S. Stramaglia, J. M. Cortes, L. de Arcangelis, and D. R. Chialvo. Extreme brain events: Higher-order statistics of brain resting activity and its relation with structural connectivity. *EPL (Europhysics Letters)*, 111(6):68007, September 2015.

[9] Per Andersen, editor. *The Hippocampus Book*. Oxford University Press, Oxford ; New York, 2007. OCLC: ocm64444087.

[10] Jessica R. Andrews-Hanna, Abraham Z. Snyder, Justin L. Vincent, Cindy Lustig, Denise Head, Marcus E. Raichle, and Randy L. Buckner. Disruption of Large-Scale Brain Systems in Advanced Aging. *Neuron*, 56(5):924–935, December 2007.

[11] Alexey V. Antonov, Igor V. Tetko, Michael T. Mader, Jan Budczies, and Hans W. Mewes. Optimization models for cancer classification: Extracting gene interaction information from microarray expression data. *Bioinformatics*, 20(5):644–652, March 2004.

[12] L. Barnett, A.B. Barrett, and A.K. Seth. Granger causality and transfer entropy are equivalent for Gaussian variables. *Phys Rev Lett*, 103:238701, 2009.

[13] A.B. Barrett, L. Barnett, and A.K. Seth. Multivariate Granger causality and generalized variance. *Phys Rev E*, 81:041907, 2010.

[14] Adam B. Barrett. Exploration of synergistic and redundant information sharing in static and dynamical Gaussian systems. *Physical Review E*, 91(5):052802, May 2015.

[15] T. Bartsch and P. Wulff. The hippocampus in aging and disease: From plasticity to vulnerability. *Neuroscience*, 309:1–16, November 2015.

[16] C.F. Beckmann, M. DeLuca, J.T. Devlin, and S.M. Smith. Investigations into resting-state connectivity using independent component analysis. *Philos. Trans. R. Soc. Lond. B. Biol. Sci*, 360:1001–1013, 2005.

[17] C.F. Beckmann and S.M. Smith. Probabilistic independent component analysis for functional magnetic resonance imaging. *IEEE Trans Med Imaging*, pages 137–152, 2004.

[18] A.J. Bell and T.J. Sejnowski. An Information-Maximization Approach to Blind Separation and Blind Deconvolution. *Neural Comput*, 7:1129–1159, 1995.

[19] Y Ben-Ari. Limbic seizure and brain damage produced by kainic acid: Mechanisms and relevance to human temporal lobe epilepsy. *Neuroscience*, 14:375–403, 1985.

[20] P. Bentley, J. Driver, and R.J. Dolan. Cholinesterase inhibition modulates visual and attentional brain responses in Alzheimer's disease and health. *Brain*, 131:409–424, 2008.

[21] BC Bernhardt, S Hong, and A Bernasconiand N Bernasconi. Imaging structural and functional brain networks in temporal lobe epilepsy. *Front Hum Neurosci*, 7:624, 2013.

[22] LM Bettencourt, GJ Stephens, MI Ham, and GW Gross. Functional structure of cortical neuronal networks grown in vitro. *Phys Rev E*, 75:021915, 2007.

[23] Luís M. A. Bettencourt, Vadas Gintautas, and Michael I. Ham. Identification of Functional Information Subgraphs in Complex Networks. *Physical Review Letters*, 100(23):238701, June 2008.

[24] G Bettus, E Guedj, F Joyeux, S Confort-Gouny, E Soulier, V Laguitton, PJ Cozzone, P Chauvel, JP Ranjeva, F Bartolomei, and M Guye. Decreased basal fMRI functional connectivity in epileptogenic networks and contralateral compensatory mechanisms. *Hum Brain Mapp*, 30:1580–1591, 2008.

[25] Richard F. Betzel, Lisa Byrge, Ye He, Joaquín Goñi, Xi-Nian Zuo, and Olaf Sporns. Changes in structural and functional connectivity among resting-state networks across the human lifespan. *NeuroImage*, 102:345–357, November 2014.

[26] M.A. Binnewijzend, M.M. Schoonheim, E. Sanz-Arigita, A.M. Wink, W.M. van der Flier, N. Tolboom, S.M. Adriaanseand, J.S. Damoiseaux, P. Scheltensand, B.N. van Berckel, and F. Barkhof. Resting-state fMRI changes in Alzheimer's disease and mild cognitive impairment. *Neurobiol Aging*, 33:2018–2028, 2012.

[27] CM Bishop. *Pattern Recognition and Machine Learning*. Springer, 2006.

[28] H Blumenfeld, KA McNally, SD Vanderhill, AL Paige, R Chung, K Davisand AD Norden, R Stokking, C Studholme, EJ Novotny, IG Zubal, and SS Spencer. Positive and negative network correlations in temporal lobe epilepsy. *Cereb Cortex*, 14:892–902, 2004.

[29] J.A. Bonachela, H. Hinrichsen, and M.A. Muñoz. Entropy estimates of small data sets. *J Phys A: Math Theor*, 41:202001, 2008.

[30] P. Bonifazi, M. Goldin, M.A. Picardo, I. Jorquera, A. Cattani, G. Bianconi, A. Represa, Y. Ben-Ari, and R. Cossart. The human connectome: A structural description of the human brain. *Science*, 326:1419–1424, 2009.

[31] M. Booth. Assessment of physical activity: An international perspective. *Research Quarterly for Exercise and Sport*, 71(2 Suppl):S114–120, June 2000.

[32] A Borst and FE Theunissen. Information theory and neural coding. *Nat Neurosci*, 2:947–967, 1999.

[33] V Bouilleret, V Ridoux, A Depaulis, C Marescaux, A Nehli, and G Le Gal La Salle. Recurrent seizures and hippocampal sclerosis following intrahippocampal kainate injection in adult mice: Electroencephalography, histopathology and synaptic reorganization similar to mesial temporal lobe epilepsy. *Neuroscience*, 89:717–729, 1999.

[34] P. Boveroux, A. Vanhaudenhuyse, M.A. Brun, Q. Noirhomme, S. Lauwick, A. Luxen, C. Degueldre, A. Plenevau, C. Schnakers, C. Phillips, J.F. Brichant, V. Bonhomme, P. Maquet, M.D. Greicius, S. Laureys, and M. Boly. Breakdown of within- and between- network resting state functional magnetic resonance imaging connectivity. *Anesthesiology*, 113:1038–1053, 2010.

[35] S.L. Bressler and A.K. Seth. Wiener-granger causality: A well-established methodology. *Neuroimage*, 58:323–329, 2011.

[36] M.R. Brier, J.B. Thomasand, A.Z. Snyder, T.L. Benzinger, D. Zhang, M.E. Raichle, D.M. Holtzman, J.C. Morris, and B.M. Ances. Loss of intranetwork and internetwork resting state functional connections with Alzheimer's disease progression. *J Neurosci*, 32:8890–8898, 2012.

[37] E. Bullmore and O. Sporns. Complex brain networks: Graph theoretical analysis of structural and functional systems. *Nat Rev Neurosci*, 10:186–198, 2009.

[38] Roberto Cabeza, Nicole D. Anderson, Jill K. Locantore, and Anthony R. McIntosh. Aging gracefully: Compensatory brain activity in high-performing older adults. *NeuroImage*, 17(3):1394–1402, November 2002.

[39] R.L. Carhart-Harris, R. Leech, P.J. Hellyer, M. Shanahan, A. Feilding, E. Tagliazucchi, D.R. Chialvo, and D. Nutt. The entropic brain: A theory of conscious states informed by neuroimaging research with psychedelic drugs. *Frontiers in Human Neuroscience*, 8:20, 2014.

[40] Sima Chalavi, Hamed Zivari Adab, Lisa Pauwels, Iseult A. M. Beets, Peter van Ruitenbeek, Matthieu P. Boisgontier, Thiago Santos Monteiro, Celine Maes, Stefan Sunaert, and Stephan P. Swinnen. Anatomy of Subcortical Structures Predicts Age-Related Differences in Skill Acquisition. *Cerebral Cortex*, pages 1–15, May 2017.

[41] Micaela Y. Chan, Fahd H. Alhazmi, Denise C. Park, Neil K. Savalia, and Gagan S. Wig. Resting-state network topology differentiates task signals across the adult lifespan. *The Journal of Neuroscience*, pages 2406–16, February 2017.

[42] Micaela Y. Chan, Denise C. Park, Neil K. Savalia, Steven E. Petersen, and Gagan S. Wig. Decreased segregation of brain systems across the healthy adult lifespan. *Proceedings of the National Academy of Sciences*, 111(46):E4997–E5006, November 2014.

[43] M Chavez, M Valencia, V Navarro, V Latora, and J Martinerie. Functional Modularity of Background Activities in Normal and Epileptic Brain Networks. *Phys Rev Lett*, 104:118701, 2010.

[44] J. H. Cole, S. J. Ritchie, M. E. Bastin, M. C. Valdés Hernández, S. Muñoz Maniega, N. Royle, J. Corley, A. Pattie, S. E. Harris, Q. Zhang, N. R. Wray, P. Redmond, R. E. Marioni, J. M. Starr, S. R. Cox, J. M. Wardlaw, D. J. Sharp, and I. J. Deary. Brain age predicts mortality. *Molecular Psychiatry*, April 2017.

[45] James H. Cole, Robert Leech, David J. Sharp, and Alzheimer's Disease Neuroimaging Initiative. Prediction of brain age suggests accelerated atrophy after traumatic brain injury. *Annals of Neurology*, 77(4):571–581, April 2015.

[46] James H. Cole, Jonathan Underwood, Matthan W.A. Caan, Davide De Francesco, Rosan A. van Zoest, Robert Leech, Ferdinand W.N.M. Wit, Peter Portegies, Gert J. Geurtsen, Ben A. Schmand, Maarten F. Schim van der Loeff, Claudio Franceschi, Caroline A. Sabin, Charles B.L.M. Majoie,

Alan Winston, Peter Reiss, and David J. Sharp. Increased brain-predicted aging in treated HIV disease. *Neurology*, page 10.1212/WNL.0000000000003790, March 2017.

[47] AJ Conger. A Revised Definition for Suppressor Variables: A Guide To Their Identification and Interpretation. *Educational and Psychological Measurement*, 34:35–46, 1974.

[48] J. M. Cortes, A. Lopez, R. Molina, and A. K. Katsaggelos. Variational Bayesian localization of EEG sources with generalized Gaussian priors. *The European Physical Journal Plus*, 127(11), November 2012.

[49] Jesus M. Cortes, Daniele Marinazzo, and Miguel A. Muñoz. Editorial for the research topic: Information-based methods for neuroimaging: Analyzing structure, function and dynamics. *Frontiers in Neuroinformatics*, 8, 2014.

[50] Eric Courchesne, Heather J. Chisum, Jeanne Townsend, Angilene Cowles, James Covington, Brian Egaas, Mark Harwood, Stuart Hinds, and Gary A. Press. Normal Brain Development and Aging: Quantitative Analysis at in Vivo MR Imaging in Healthy Volunteers. *Radiology*, 216(3):672–682, September 2000.

[51] TM Cover and JA Thomas. *Elements of Information Theory*. John Wiley & Sons, Inc, 2006.

[52] James P. Coxon, Daniel J. Goble, Inge Leunissen, Annouchka Van Impe, Nicole Wenderoth, and Stephan P. Swinnen. Functional Brain Activation Associated with Inhibitory Control Deficits in Older Adults. *Cerebral Cortex (New York, N.Y.: 1991)*, 26(1):12–22, January 2016.

[53] James P. Coxon, Daniel J. Goble, Annouchka Van Impe, Jeroen De Vos, Nicole Wenderoth, and Stephan P. Swinnen. Reduced basal ganglia function when elderly switch between coordinated

movement patterns. *Cerebral Cortex (New York, N.Y.: 1991)*, 20(10):2368–2379, October 2010.

[54] James P. Coxon, Annouchka Van Impe, Nicole Wenderoth, and Stephan P. Swinnen. Aging and inhibitory control of action: Cortico-subthalamic connection strength predicts stopping performance. *The Journal of Neuroscience: The Official Journal of the Society for Neuroscience*, 32(24):8401–8412, June 2012.

[55] R. Cameron Craddock, G. Andrew James, Paul E. Holtzheimer, Xiaoping P. Hu, and Helen S. Mayberg. A whole brain fMRI atlas generated via spatially constrained spectral clustering. *Human Brain Mapping*, 33(8):1914–1928, August 2012.

[56] R.C. Craddock, S. Jbabdi, C.G. Yan, J.T. Vogelstein, F.X. Castellanos, A. Di Martino, C. Kelly, K. Heberlein, S. Colcombe, and M.P. Milham. Imaging human connectomes at the macroscale. *Nat. Methods*, 10:524–539, 2013.

[57] Cora L. Craig, Alison L. Marshall, Michael Sj??Str??M, Adrian E. Bauman, Michael L. Booth, Barbara E. Ainsworth, Michael Pratt, Ulf Ekelund, Agneta Yngve, James F. Sallis, and Pekka Oja. International Physical Activity Questionnaire: 12-Country Reliability and Validity:. *Medicine & Science in Sports & Exercise*, 35(8):1381–1395, August 2003.

[58] Eileen M. Crimmins. Lifespan and Healthspan: Past, Present, and Promise. *The Gerontologist*, 55(6):901–911, December 2015.

[59] N. A. Crossley, A. Mechelli, J. Scott, F. Carletti, P. T. Fox, P. McGuire, and E. T. Bullmore. The hubs of the human connectome are generally implicated in the anatomy of brain disorders. *Brain*, 137(8):2382–2395, August 2014.

[60] Cameron B. J. Cunningham, Bradley G. Goodyear, Radwa Badawy, Fateh Zaamout, Daniel J. Pittman, Craig A. Beers, and Paolo Federico. Intracranial EEG-fMRI analysis of focal

epileptiform discharges in humans. *Epilepsia*, 53(9):1636–1648, September 2012.

[61] J.S. Damoiseaux, C.F. Beckmann, E.J. S. Arigita, F. Barkhof, Ph. Scheltens, C.J. Stam, S.M. Smith, and S.A.R.B. Rombouts. Reduced resting-state brain activity in the "default network" in normal aging. *Cerebral Cortex*, 18(8):1856–1864, August 2008.

[62] J.S. Damoiseaux, S.A. Rombouts, F. Barkhof, P. Scheltens, C.J. Stam, S.M. Smith, and C.F. Beckmann. Consistent resting-state networks across healthy subjects. *Proc Natl Acad Sci USA*, 103:13848, 2006.

[63] Simon W. Davis, Nancy A. Dennis, Norbou G. Buchler, Leonard E. White, David J. Madden, and Roberto Cabeza. Assessing the effects of age on long white matter tracts using diffusion tensor tractography. *NeuroImage*, 46(2):530–541, June 2009.

[64] Marius de Groot, Lotte G. M. Cremers, M. Arfan Ikram, Albert Hofman, Gabriel P. Krestin, Aad van der Lugt, Wiro J. Niessen, and Meike W. Vernooij. White Matter Degeneration with Aging: Longitudinal Diffusion MR Imaging Analysis. *Radiology*, 279(2):532–541, May 2016.

[65] P. Delamillieure, G. Doucet, B. Mazoyer, M.R. Turbelin, N. Delcroix, E. Mellet, L. Zago, F. Crivello, L. Petit, N. Tzourio-Mazoyer, and M. Joliot. The resting state questionnaire: An introspective questionnaire for evaluation of inner experience during the conscious resting state. *Brain Res. Bull*, 81:565–573, 2010.

[66] O. Demirci, M.C. Stevens, N.C. Andreasen, A. Michael, J. Liu, T. White, G.D. Pearlson, V.P. Clark, and V.D. Calhoun. Investigation of relationships between fmri brain networks in the spectral domain using ICA and Granger causality reveals distinct differences between schizophrenia patients and healthy controls. *Neuroimage*, 46:419–431, 2009.

[67] O. Demirci, M.C. Stevens, N.C. Andreasen, A. Michael, J. Liu, T. White, G.D. Pearlson, V.P. Clark, and V.D. Calhoun. Multivariate Granger causality analysis of fMRI data. *Hum Brain Mapp*, 30:1361–1373, 2009.

[68] Han Bing Deng, Duncan J. Macfarlane, G. Neil Thomas, Xiang Qian Lao, Chao Qiang Jiang, Kar Keung Cheng, and Tai Hing Lam. Reliability and Validity of the IPAQ-Chinese: The Guangzhou Biobank Cohort Study. *Medicine & Science in Sports & Exercise*, 40(2):303–307, February 2008.

[69] I. Diez, P. Bonifazi, I. Escudero, B. Mateos, M.A. Muñoz MA, S. Stramaglia, and J.M Cortes. A novel brain partition highlights the modular skeleton shared by structure and function. *Sci Rep*, 5:10532, 2015.

[70] I. Diez, A. Erramuzpe, I. Escudero, B. Mateos, A. Cabrera, D. Marinazzo, E.J. Sanz-Arigita, S. Stramaglia, and J.M. Cortes. Information Flow Between Resting-State Networks. *Brain Connect*, 2015.

[71] Ibai Diez, David Drijkoningen, Sebastiano Stramaglia, Paolo Bonifazi, Daniele Marinazzo, Jolien Gooijers, Stephan P. Swinnen, and Jesus M. Cortes. Enhanced pre-frontal functional-structural networks to support postural control deficits after traumatic brain injury in a pediatric population. *Network Neuroscience*, pages 1–56, February 2017.

[72] N. U. F. Dosenbach, B. Nardos, A. L. Cohen, D. A. Fair, J. D. Power, J. A. Church, S. M. Nelson, G. S. Wig, A. C. Vogel, C. N. Lessov-Schlaggar, K. A. Barnes, J. W. Dubis, E. Feczko, R. S. Coalson, J. R. Pruett, D. M. Barch, S. E. Petersen, and B. L. Schlaggar. Prediction of Individual Brain Maturity Using fMRI. *Science*, 329(5997):1358–1361, September 2010.

[73] Ira Driscoll, Derek A. Hamilton, Helen Petropoulos, Ronald A. Yeo, William M. Brooks, Richard N. Baumgartner, and

Robert J. Sutherland. The aging hippocampus: Cognitive, biochemical and structural findings. *Cerebral Cortex (New York, N.Y.: 1991)*, 13(12):1344–1351, December 2003.

[74] J Engel, PC Van Ness, TB Rasmussen, and LM Ojemann. *Surgical Treatment of the Epilepsies*. Raven Press, New York, 1993.

[75] Oscar Esteban, Daniel Birman, Marie Schaer, Oluwasanmi O. Koyejo, Russell A. Poldrack, and Krzysztof J. Gorgolewski. MRIQC: Advancing the automatic prediction of image quality in MRI from unseen sites. *PLOS ONE*, 12(9):e0184661, 25-sep-2017.

[76] Oscar Esteban, Ross Blair, Christopher J. Markiewicz, Shoshana L. Berleant, Craig Moodie, Feilong Ma, Ayse Ilkay Isik, Asier Erramuzpe, James D. Kent, Mathias Goncalves, Elizabeth DuPre, Kevin R. Sitek, Russell A. Poldrack, and Krzysztof J. Gorgolewski. Poldracklab/fmriprep: 1.0.8. Technical report, Zenodo, February 2018.

[77] Sarah Feldt, Paolo Bonifazi, and Rosa Cossart. Dissecting functional connectivity of neuronal microcircuits: Experimental and theoretical insights. *Trends in Neurosciences*, 34(5):225–236, May 2011.

[78] Anders M. Fjell, Markus H. Sneve, Håkon Grydeland, Andreas B. Storsve, Inge K. Amlien, Anastasia Yendiki, and Kristine B. Walhovd. Relationship between structural and functional connectivity change across the adult lifespan: A longitudinal investigation: Connectivity Change Across the Adult Lifespan. *Human Brain Mapping*, 38(1):561–573, January 2017.

[79] A. Fornito, A. Zalesky, and M. Breakspear. Graph analysis of the human connectome: Promise, progress, and pitfalls. *Neuroimage*, 80:426–444, 2013.

[80] M.D. Fox, A.Z. Snyder, J.L. Vincent, M. Corbetta, D.C. Van Essen, and M.E.A.G. Raichle. The human brain is intrinsic-

ally organized into dynamic, anticorrelated functionalnetworks. *Proc Natl Acad Sci USA*, 102:9673–9678, 2005.

[81] Katja Franke, Michael Ristow, and Christian Gaser. Gender-specific impact of personal health parameters on individual brain aging in cognitively unimpaired elderly subjects. *Frontiers in Aging Neuroscience*, 6, 2014.

[82] Katja Franke, Gabriel Ziegler, Stefan Klöppel, Christian Gaser, and Alzheimer's Disease Neuroimaging Initiative. Estimating the age of healthy subjects from T1-weighted MRI scans using kernel methods: Exploring the influence of various parameters. *NeuroImage*, 50(3):883–892, April 2010.

[83] K.J. Friston. Functional and effective connectivity in neuroimaging: A synthesis. *Hum. Brain. Mapp*, 2:56–78, 1994.

[84] K.J. Friston. Causal modelling and brain connectivity in functional magnetic resonance imaging. *PLoS Biol*, 7:e33, 2009.

[85] K.J. Friston. Functional and effective connectivity: A review. *Brain Connect*, 1:13–36, 2011.

[86] K.J. Friston, L. Harrison, and W. Penny. Dynamic causal modelling. *Neuroimage*, 19:1273–1302, 2003.

[87] T. Fulop, A. Larbi, J. M. Witkowski, J. McElhaney, M. Loeb, A. Mitnitski, and G. Pawelec. Aging, frailty and age-related diseases. *Biogerontology*, 11(5):547–563, October 2010.

[88] Christian Gaser, Katja Franke, Stefan Klöppel, Nikolaos Koutsouleris, and Heinrich Sauer. BrainAGE in Mild Cognitive Impaired Patients: Predicting the Conversion to Alzheimer's Disease. *PLoS ONE*, 8(6), June 2013.

[89] Krzysztof J. Gorgolewski, Oscar Esteban, David Gage Ellis, Michael Philipp Notter, Erik Ziegler, Hans Johnson, Carlo Hamalainen, Benjamin Yvernault, Christopher Burns, Alexandre Manhães-Savio, Dorota Jarecka, Christopher J. Markiewicz,

Taylor Salo, Daniel Clark, Michael Waskom, Jason Wong, Marc Modat, Blake E Dewey, Michael G. Clark, Michael Dayan, Fred Loney, Cindee Madison, Alexandre Gramfort, Anisha Keshavan, Shoshana Berleant, Basile Pinsard, Mathias Goncalves, Dav Clark, Ben Cipollini, Gael Varoquaux, Demian Wassermann, Ariel Rokem, Yaroslav O. Halchenko, Jessica Forbes, Brendan Moloney, Ian B. Malone, Michael Hanke, David Mordom, Colin Buchanan, Wolfgang M. Pauli, Julia M. Huntenburg, Christian Horea, Yannick Schwartz, Rosalia Tungaraza, Shariq Iqbal, Jens Kleesiek, Sharad Sikka, Caroline Frohlich, James Kent, Martin Perez-Guevara, Aimi Watanabe, David Welch, Chad Cumba, Daniel Ginsburg, Arman Eshaghi, Erik Kastman, Salma Bougacha, Ross Blair, Benjamin Acland, Ashley Gillman, Alexander Schaefer, B. Nolan Nichols, Steven Giavasis, Drew Erickson, Carlos Correa, Ali Ghayoor, René Küttner, Christian Haselgrove, Dale Zhou, R. Cameron Craddock, Daniel Haehn, Leonie Lampe, Jarrod Millman, Jeff Lai, Mandy Renfro, Siqi Liu, Jörg Stadler, Tristan Glatard, Ari E. Kahn, Xiang-Zhen Kong, William Triplett, Anne Park, Conor McDermottroe, Michael Hallquist, Russell Poldrack, L. Nathan Perkins, Maxime Noel, Stephan Gerhard, John Salvatore, Fred Mertz, William Broderick, Souheil Inati, Oliver Hinds, Matthew Brett, Joke Durnez, Arielle Tambini, Simon Rothmei, Sami Kristian Andberg, Gavin Cooper, Ana Marina, Aaron Mattfeld, Sebastian Urchs, Paul Sharp, K Matsubara, Daniel Geisler, Brian Cheung, Andrew Floren, Thomas Nickson, Nicolas Pannetier, Alejandro Weinstein, Mathieu Dubois, Jaime Arias, Claire Tarbert, Kai Schlamp, Kesshi Jordan, Franz Liem, Victor Saase, Robbert Harms, Ranjeet Khanuja, Kornelius Podranski, Guillaume Flandin, Dimitri Papadopoulos Orfanos, Isaac Schwabacher, Daniel McNamee, Marcel Falkiewicz, John Pellman, Janosch Linkersdörfer, Jan Varada, Fernando Pérez-García, Andrew Davison, Dmitry Shachnev, and Satrajit Ghosh. Nipype: A flexible, lightweight and extensible neuroimaging data processing framework in Python.

0.13.1. Technical report, Zenodo, May 2017.

[90] Cheryl Grady. The cognitive neuroscience of ageing. *Nature Reviews Neuroscience*, 13(7):491–505, June 2012.

[91] C.W.J. Granger. Investigating causal relations by econometric models and cross-spectral methods. *Econometrica*, 37:424–438, 1969.

[92] M.D. Greicius, C. Srivastava, A.L. Reiss, and V. Menon. Default-mode network activity distinguishes Alzheimer's disease from healthy aging: Evidence from functional MRI. *Proc Natl Acad Sci USA*, 101:4637–4642, 2004.

[93] P. Hagmann, O. Sporns, N. Madan, L. Cammoun, R. Pienaar, V. J. Wedeen, R. Meuli, J.-P. Thiran, and P. E. Grant. White matter maturation reshapes structural connectivity in the late developing human brain. *Proceedings of the National Academy of Sciences*, 107(44):19067–19072, November 2010.

[94] A. Haimovici, E. Tagliazucchi, P. Balenzuela, and D.R. Chialvo. Brain Organization into Resting State Networks Emerges at Criticality on a Model of the Human Connectome. *Phys. Rev. Lett*, 110:178101, 2013.

[95] Cheol E. Han, Luis R. Peraza, John-Paul Taylor, and Marcus Kaiser. Predicting age across human lifespan based on structural connectivity from diffusion tensor imaging. *2014 IEEE Biomedical Circuits and Systems Conference (BioCAS) Proceedings*, pages 137–140, October 2014.

[96] L. Heine, A. Soddu, F. Gomez, A. Vanhaudenhuyse, L. Tshibanda, M. Thonnard, V. Charland-Verville, M. Kirsch, S. Laureys, and A. Demertzi. Resting state networks and consciousness: Alterations of multiple resting state network connectivity in physiological, pharmacological, and pathological consciousness States. *Front Psychol*, 3:295, 2012.

[97] Gareth James, Daniela Witten, Trevor Hastie, and Robert Tibshirani. *An Introduction to Statistical Learning: With Applications in R*. Springer, New York, 1st ed. 2013, corr. 6th printing 2016 edition edition, August 2013.

[98] E.T. Jaynes. Information Theory and Statistical Mechanics. *Phys Rev 106*, 106:620–630, 1957.

[99] T. L. Jernigan, S. L. Archibald, C. Fennema-Notestine, A. C. Gamst, J. C. Stout, J. Bonner, and J. R. Hesselink. Effects of age on tissues and regions of the cerebrum and cerebellum. *Neurobiology of Aging*, 22(4):581–594, 2001 Jul-Aug.

[100] Linpei Jia, Weiguang Zhang, and Xiangmei Chen. Common methods of biological age estimation. *Clinical Interventions in Aging*, 12:759–772, 2017.

[101] Alexandre Kalache, Isabella Aboderin, and Irene Hoskins. Compression of morbidity and active ageing: Key priorities for public health policy in the 21st century. *Bulletin of the World Health Organization*, 80(3):243–244, 2002.

[102] Eric R. Kandel, James H. Schwartz, Thomas M. Jessell, Steven A. Siegelbaum, and A. J. Hudspeth, editors. *Principles of Neural Science, Fifth Edition*. McGraw-Hill Education / Medical, New York, 5th edition edition, October 2012.

[103] H. Karbasforoushan and N.D. Woodward. Resting-state networks in schizophrenia. *Curr Top Med Chem*, 12:2404–2414, 2012.

[104] Sadiya S. Khan, Benjamin D. Singer, and Douglas E. Vaughan. Molecular and physiological manifestations and measurement of aging in humans. *Aging Cell*, May 2017.

[105] B R King, P van Ruitenbeek, I Leunissen, K Cuypers, K F Heise, T Santos Monteiro, L Hermans, O Levin, G Albouy,

D Mantini, and S P Swinnen. Age-Related Declines in Motor Performance are Associated With Decreased Segregation of Large-Scale Resting State Brain Networks. *Cerebral Cortex*, pages 1–13, November 2017.

[106] Bob G. Knight and Kelly Durbin. Aging and the effects of emotion on cognition: Implications for psychological interventions for depression and anxiety. *PsyCh Journal*, 4(1):11–19, March 2015.

[107] Anna A. Kondratova and Roman V. Kondratov. The circadian clock and pathology of the ageing brain. *Nature Reviews. Neuroscience*, 13(5):325–335, March 2012.

[108] Nikolaos Koutsouleris, Christos Davatzikos, Stefan Borgwardt, Christian Gaser, Ronald Bottlender, Thomas Frodl, Peter Falkai, Anita Riecher-Rössler, Hans-Jürgen Möller, Maximilian Reiser, Christos Pantelis, and Eva Meisenzahl. Accelerated brain aging in schizophrenia and beyond: A neuroanatomical marker of psychiatric disorders. *Schizophrenia Bulletin*, 40(5):1140–1153, September 2014.

[109] Julia M. Kroos, Isabella Marinelli, Ibai Diez, Jesus M. Cortes, Sebastiano Stramaglia, and Luca Gerardo-Giorda. Patient-specific computational modeling of cortical spreading depression via diffusion tensor imaging: Patient-specific computational modeling of cortical spreading depression via diffusion tensor imaging. *International Journal for Numerical Methods in Biomedical Engineering*, 33(11):e2874, November 2017.

[110] Nanna Kurtze, Vegar Rangul, and Bo-Egil Hustvedt. Reliability and validity of the international physical activity questionnaire in the Nord-Trøndelag health study (HUNT) population of men. *BMC Medical Research Methodology*, 8(1), December 2008.

[111] Molly R. LaPoint, Jasmeer P. Chhatwal, Jorge Sepulcre, Keith A. Johnson, Reisa A. Sperling, and Aaron P. Schultz.

The association between tau PET and retrospective cortical thinning in clinically normal elderly. *NeuroImage*, May 2017.

[112] Michael F. Leitzmann, Yikyung Park, Aaron Blair, Rachel Ballard-Barbash, Traci Mouw, Albert R. Hollenbeck, and Arthur Schatzkin. Physical activity recommendations and decreased risk of mortality. *Archives of Internal Medicine*, 167(22):2453–2460, December 2007.

[113] Inge Leunissen, James P. Coxon, Karen Caeyenberghs, Karla Michiels, Stefan Sunaert, and Stephan P. Swinnen. Subcortical volume analysis in traumatic brain injury: The importance of the fronto-striato-thalamic circuit in task switching. *Cortex; a Journal Devoted to the Study of the Nervous System and Behavior*, 51:67–81, February 2014.

[114] Inge Leunissen, James P. Coxon, Karen Caeyenberghs, Karla Michiels, Stefan Sunaert, and Stephan P. Swinnen. Task switching in traumatic brain injury relates to cortico-subcortical integrity. *Human Brain Mapping*, 35(5):2459–2469, May 2014.

[115] Inge Leunissen, James P. Coxon, Monique Geurts, Karen Caeyenberghs, Karla Michiels, Stefan Sunaert, and Stephan P. Swinnen. Disturbed cortico-subcortical interactions during motor task switching in traumatic brain injury. *Human Brain Mapping*, 34(6):1254–1271, June 2013.

[116] Inge Leunissen, James P. Coxon, and Stephan P. Swinnen. A proactive task set influences how response inhibition is implemented in the basal ganglia. *Human Brain Mapping*, 37(12):4706–4717, December 2016.

[117] R Li, X Wu, K Chen, AS Fleisher, EM Reiman, and L Yao. Alterations of directional connectivity among resting-state networks in Alzheimer disease. *AJNR Am J Neuroradiol*, 34:340–345, 2013.

[118] S.J. Li, Z. Li, G. Wu, M.J. Zhang, M. Franczak, and P.G. Antuono. Alzheimers disease: Evaluation of a functional MR imaging index as a marker. *Radiology*, 225:253–259, 2002.

[119] P Liang, Z Li, G Deshpande, Z Wang, X Hu, and K Li. Altered Causal Connectivity of Resting State Brain Networks in Amnesic MCI. *PLoS One*, 9:e88476, 2014.

[120] W Liao, J Ding, D Marinazzo, Q Xu, Z Wang, C Yuan, Z Zhang, G Lu, and H Chen. Small-world directed networks in the human brain: Multivariate granger causality analysis of resting-state fmri. *Neuroimage*, 14:2683–2694, 2011.

[121] W. Liao, Z. Zhang, Z. Pan, D. Mantini, J. Ding, X. Duan, C. Luo, G. Lu, and H. Chen. Altered functional connectivity and small-world in mesial temporal lobe epilepsy. *PLoS One*, 5:e8525, 2010.

[122] Franziskus Liem, Gaël Varoquaux, Jana Kynast, Frauke Beyer, Shahrzad Kharabian Masouleh, Julia M. Huntenburg, Leonie Lampe, Mehdi Rahim, Alexandre Abraham, R. Cameron Craddock, Steffi Riedel-Heller, Tobias Luck, Markus Loeffler, Matthias L. Schroeter, Anja Veronica Witte, Arno Villringer, and Daniel S. Margulies. Predicting brain-age from multimodal imaging data captures cognitive impairment. *NeuroImage*, 148:179–188, March 2017.

[123] S. Lim, C. E. Han, P. J. Uhlhaas, and M. Kaiser. Preferential Detachment During Human Brain Development: Age- and Sex-Specific Structural Connectivity in Diffusion Tensor Imaging (DTI) Data. *Cerebral Cortex*, 25(6):1477–1489, June 2015.

[124] Z Liu, Y Zhang, L Bai, H Yan, R Dai, C Zhong, H Wang, W Wei, T Xue, Y Feng, Y You, and J Tian. Investigation of the effective connectivity of resting state networks in alzheimer's disease: A functional mri study combining independent components analysis and multivariate granger causality analysis. *NMR Biomed*, 25:1311–1320, 2012.

[125] T Lizier, FM Atay, and J Jost. Information storage, loop motifs and clustered structure in complex networks. *Phys Rev E*, 86:026110, 2012.

[126] Eileen Luders, Nicolas Cherbuin, and Christian Gaser. Estimating brain age using high-resolution pattern recognition: Younger brains in long-term meditation practitioners. *NeuroImage*, 134:508–513, July 2016.

[127] Urs MäDer, Brian W. Martin, Yves Schutz, and Bernard Marti. Validity of Four Short Physical Activity Questionnaires in Middle-Aged Persons:. *Medicine & Science in Sports & Exercise*, 38(7):1255–1266, July 2006.

[128] V. Maki-Marttunen, I. Diez, J.M. Cortes, D.R. Chialvo, and M. Villarreal. Disruption of transfer entropy and inter-hemispheric brain functional connectivity in patients with disorder of consciousness. *Front Neuroinform*, 7:24, 2013.

[129] D. Marinazzo, W. Liao, H. Chen, and S. Stramaglia. Nonlinear connectivity by granger causality. *Neuroimage*, 58:330–338, 2011.

[130] D Marinazzo, W Liao, M Pellicoro, and S Stramaglia. Grouping time series by pairwise measures of redundancy. *Phys Lett*, 374:4040–4044, 2010.

[131] D. Marinazzo, M. Pellicoro, and S. Stramaglia. Kernel method for nonlinear granger causality. *Phys Rev Lett*, 100:144103, 2008.

[132] Daniele Marinazzo, Mario Pellicoro, Guorong Wu, Leonardo Angelini, Jesús M. Cortés, and Sebastiano Stramaglia. Information transfer and criticality in the Ising model on the human connectome. *PloS One*, 9(4):e93616, 2014.

[133] J. Mårtensson, J. Lätt, F. Åhs, M. Fredrikson, H. Söderlund, H. B. Schiöth, J. Kok, B. Kremer, Danielle van Westen, E.-M.

Larsson, and M. Nilsson. Diffusion tensor imaging and tractography of the white matter in normal aging: The rate-of-change differs between segments within tracts. *Magnetic Resonance Imaging*, March 2017.

[134] WJ McGill. Multivariate information transmission. *Psychometrika*, 19:97–116, 1954.

[135] A.R. McIntosh and N.J. Lobaugh. Partial least squares analysis of neuroimaging data: Applications and advances. *Neuroimage*, 23:S250–263, 2004.

[136] D.G. McLaren, R.A. Sperling, and A. Atri. Flexible modulation of network connectivity related to cognition in Alzheimer's disease. *Neuroimage*, 15:544–557, 2014.

[137] C. N. Merz, A. Rozanski, and J. S. Forrester. The secondary prevention of coronary artery disease. *The American Journal of Medicine*, 102(6):572–581, June 1997.

[138] S. Mori, B. J. Crain, V. P. Chacko, and P. C. van Zijl. Three-dimensional tracking of axonal projections in the brain by magnetic resonance imaging. *Annals of Neurology*, 45(2):265–269, February 1999.

[139] J. H. Morrison and P. R. Hof. Life and death of neurons in the aging brain. *Science (New York, N.Y.)*, 278(5337):412–419, October 1997.

[140] Huseyin Naci and John P. A. Ioannidis. Comparative effectiveness of exercise and drug interventions on mortality outcomes: Metaepidemiological study. *BMJ*, 347:f5577, October 2013.

[141] Q. Noirhomme, A. Soddu, R. Lehembre, A. Vanhaudenhuyse, P. Boveroux, M. Boly, and S. Laureys. Brain connectivity in pathological and pharmacological coma. *Front Syst Neurosci*, 4:160, 2010.

[142] GJ Ortega, L Menendez de la Prida, R Garcia de Sola, and J Pastor. Synchronization clusters of interictal activity in the lateral temporal cortex of epileptic patients: Intraoperative electrocorticographic analysis. *Epilepsia*, 49:269–280, 2008.

[143] M. O'Sullivan, D. K. Jones, P. E. Summers, R. G. Morris, S. C. Williams, and H. S. Markus. Evidence for cortical "disconnection" as a mechanism of age-related cognitive decline. *Neurology*, 57(4):632–638, August 2001.

[144] A Palmigiano, J Pastor, R Garcia de Sola, and GJ Ortega. Stability of Synchronization Clusters and Seizurability in Temporal Lobe Epilepsy. *PLoS One*, 7:e41799, 2012.

[145] S Panzeri, SR Schultz, A Treves, and ET Rolls. Correlations and the encoding of information in the nervous system. *Proc Biol Sci*, 266:1001–1012, 1999.

[146] D. C. Park, A. D. Smith, G. Lautenschlager, J. L. Earles, D. Frieske, M. Zwahr, and C. L. Gaines. Mediators of long-term memory performance across the life span. *Psychology and Aging*, 11(4):621–637, December 1996.

[147] J Pastor, V Hernando-Requejo, L Dominguez-Gadea, I de Llano, ML Meilan-Paz, JL Martinez-Chacon, and R Garcia de Sola. Impact of experience on improving the surgical outcome in temporal lobe epilepsy. *Revista Neurologia*, 41:709–716, 2005.

[148] H Peng, F Long, and C Ding. Feature Selection Based on Mutual Information:Criteria of Max-Dependency, Max-Relevance, and Min-Redundancy. *IEEE Trans Pattern Anal Mach Intell*, 27:1226–1238, 2005.

[149] W.D. Penny, K.E. Stephan, A. Mechelli, and K.J. Friston. Modelling functional integration: A comparison of structural equation and dynamic causal models. *Neuroimage*, 23:264–274, 2004.

[150] Alan Peters. Structural changes that occur during normal aging of primate cerebral hemispheres. *Neuroscience and Biobehavioral Reviews*, 26(7):733–741, November 2002.

[151] J. L. Price and J. C. Morris. Tangles and plaques in nondemented aging and "preclinical" Alzheimer's disease. *Annals of Neurology*, 45(3):358–368, March 1999.

[152] RQ Quiroga and S Panzeri. Extracting information from neuronal populations: Information theory and decoding approaches. *Nat Rev Neurosci*, 10:173–185, 2009.

[153] RJ Racine. Modification of seizure activity by electrical stimulation. II. Motor seizure. *Electroencephalogr Clin Neurophysiol*, 32:281–294, 1972.

[154] M. Raichle and M. Mintum. Brain work and brain imaging. *Annu. Rev. Neurosci*, 29:449–476, 2006.

[155] M. Raichle and A.Z. Snyder. A default mode of brain function: A brief history of an evolving idea. *Neuroimage*, 37:1083–1090, 2007.

[156] M.E. Raichle. A Paradigm Shift in Functional Brain Imaging. *J Neurosci*, 29:12729– 12734, 2009.

[157] M.E. Raichle, A.M. MacLeod, A.Z. Snyder, W.J. Powers, D.A. Gusnard, and G.L. Shulman. A default mode of brain function. *Proc. Natl. Acad. Sci. USA*, 98:676–682, 2001.

[158] Javier Rasero, Carmen Alonso-Montes, Ibai Diez, Laiene Olabarrieta-Landa, Lakhdar Remaki, Iñaki Escudero, Beatriz Mateos, Paolo Bonifazi, Manuel Fernandez, Juan Carlos Arango-Lasprilla, Sebastiano Stramaglia, Jesus M. Cortes, and the Alzheimer's Disease Neuroimaging Initiative. Group-Level Progressive Alterations in Brain Connectivity Patterns Revealed by Diffusion-Tensor Brain Networks across Severity Stages in Alzheimer's Disease. *Frontiers in Aging Neuroscience*, 9, July 2017.

[159] Javier Rasero, Mario Pellicoro, Leonardo Angelini, Jesus M. Cortes, Daniele Marinazzo, and Sebastiano Stramaglia. Consensus clustering approach to group brain connectivity matrices. *Network Neuroscience*, 1(3):242–253, October 2017.

[160] N. Raz, F. M. Gunning, D. Head, J. H. Dupuis, J. McQuain, S. D. Briggs, W. J. Loken, A. E. Thornton, and J. D. Acker. Selective aging of the human cerebral cortex observed in vivo: Differential vulnerability of the prefrontal gray matter. *Cerebral Cortex (New York, N.Y.: 1991)*, 7(3):268–282, 1997 Apr-May.

[161] J.C. Reijneveld, S.C. Ponten, H.W. Berendse, and C.J. Stam. The application of graph theoretical analysis to complex networks in the brain. *Clin Neurophysiol*, 118:2317– 2331, 2007.

[162] Susan M. Resnick, Dzung L. Pham, Michael A. Kraut, Alan B. Zonderman, and Christos Davatzikos. Longitudinal magnetic resonance imaging studies of older adults: A shrinking brain. *The Journal of Neuroscience: The Official Journal of the Society for Neuroscience*, 23(8):3295–3301, April 2003.

[163] Stuart J. Ritchie, David Alexander Dickie, Simon R. Cox, Maria Del C. Valdes Hernandez, Janie Corley, Natalie A. Royle, Alison Pattie, Benjamin S. Aribisala, Paul Redmond, Susana Muñoz Maniega, Adele M. Taylor, Ruth Sibbett, Alan J. Gow, John M. Starr, Mark E. Bastin, Joanna M. Wardlaw, and Ian J. Deary. Brain volumetric changes and cognitive ageing during the eighth decade of life. *Human Brain Mapping*, 36(12):4910–4925, December 2015.

[164] E Rodriguez, N George, JP Lachaux, J Martinerie, B Renault, and FJ Varela. Perception's shadow: Long-distance synchronization of human brain activity. *Nature*, 397:430–433, 1999.

[165] A. Roebroeck, E. Formisano, and R. Goebel. Mapping directed influence over the brain using Granger causality and fMRI. *Neuroimage*, 25:230–242, 2005.

[166] S.A. Rombouts, F.F. Barkhof, R. Goekoop, C.J. Stam, and P. Scheltens. Altered resting state networks in mild cognitive impairment and mild alzheimer's disease: An fmri study. *Hum Brain Mapp*, 26:231–239, 2005.

[167] F Rosenow and H Luders. Presurgical evaluation of epilepsy. *Brain*, 124:1683–1700, 2001.

[168] Carl Rosow and Paul J. Manberg. Bispectral index monitoring. *Anesthesiology Clinics of North America*, 19(4):947–966, December 2001.

[169] M Rubinov and O Sporns. Brain Connectivity Toolbox https://sites.google.com/site/bctnet/.

[170] M Rubinov and O Sporns. Complex network measures of brain connectivity: Uses and interpretations. *Neuroimage*, 52:1059–1069, 2010.

[171] R Rytsar, E Fornari, RS Frackowiak, JA Ghika, and MG Knyazeva. Inhibition in early Alzheimer's disease: An fMRI-based study of effective connectivity. *Neuroimage*, 57:1131–1139, 2011.

[172] David H. Salat, Randy L. Buckner, Abraham Z. Snyder, Douglas N. Greve, Rahul S. R. Desikan, Evelina Busa, John C. Morris, Anders M. Dale, and Bruce Fischl. Thinning of the cerebral cortex in aging. *Cerebral Cortex (New York, N.Y.: 1991)*, 14(7):721–730, July 2004.

[173] Guenther Samitz, Matthias Egger, and Marcel Zwahlen. Domains of physical activity and all-cause mortality: Systematic review and dose-response meta-analysis of cohort studies. *International Journal of Epidemiology*, 40(5):1382–1400, October 2011.

[174] E.J. Sanz-Arigita, M.M. Schoonheim, J.S. Damoiseaux, S.A. Rombouts, E. Maris, F. Barkhof, P. Scheltens, C.J., and Stam.

Loss of 'small-world' networks in Alzheimer's disease: Graph analysis of fMRI resting-state functional connectivity. *PLoS One*, 5:e13788, 2010.

[175] JR Sato, A Fujita, EF Cardoso, CE Thomaz, MJ Brammer, and E Amaro. Analyzing the connectivity between regions of interest: An approach based on cluster Granger causality for fMRI data analysis. *NeuroImage*, 52:1444–1455, 2010.

[176] Alexandre M. Savio, Michael Schutte, Manuel Graña, and Igor Yakushev. Pypes: Workflows for Processing Multimodal Neuroimaging Data. *Frontiers in Neuroinformatics*, 11, 2017.

[177] Korine Scheeres, Hans Knoop, Jos van der Meer, and Gijs Bleijenberg. Clinical assessment of the physical activity pattern of chronic fatigue syndrome patients: A validation of three methods. *Health and Quality of Life Outcomes*, 7(1):29, 2009.

[178] Hugo G. Schnack, Neeltje E. M. van Haren, Mireille Nieuwenhuis, Hilleke E. Hulshoff Pol, Wiepke Cahn, and René S. Kahn. Accelerated Brain Aging in Schizophrenia: A Longitudinal Pattern Recognition Study. *The American Journal of Psychiatry*, 173(6):607–616, June 2016.

[179] E Schneidman, W Bialek, and MJ Berry. Synergy, redundancy, and independence in population codes. *J Neurosci*, 23:11539–11553, 2003.

[180] M.M. Schoonheim, J.J. Geurts, D. Landi, L. Douw, M.L. van der Meer, H. Vrenken, C.H. Polman, F. Barkhof, and C.J. Stam. Functional connectivity changes in multiple sclerosis patients: A graph analytical study of MEG resting state data. *Hum Brain Mapp*, 34:52–61, 2013.

[181] T. Schreiber. Measuring Information Transfer. *Phys Rev Lett*, 85:461–464, 2000.

[182] R Schwarcz, R Zaczek, and JT Coyle. Microinjection of kainic acid into the rat hippocampus. *Eur J Pharmacol*, 50:209–220, 1978.

[183] Leen Serbruyns, Inge Leunissen, Toon Huysmans, Koen Cuypers, Raf L. Meesen, Peter van Ruitenbeek, Jan Sijbers, and Stephan P. Swinnen. Subcortical volumetric changes across the adult lifespan: Subregional thalamic atrophy accounts for age-related sensorimotor performance declines. *Cortex; a Journal Devoted to the Study of the Nervous System and Behavior*, 65:128–138, April 2015.

[184] Y.I. Sheline and M.E. Raichle. Resting state functional connectivity in preclinical Alzheimer's disease. *Biol Psychiatry*, 74:340–347, 2013.

[185] A Sierra, S Martin-Suárez, R Valcarcel-Martin, J Pascual-Brazo, SA Aelvoet, O Abiega, JJ Deudero, AL Brewster, I Bernales, AE Anderson, V Baekelandt, M Maletic-Savatic, and JM Encinas. Neuronal Hyperactivity Accelerates Depletion of Neural Stem Cells and Impairs Hippocampal Neurogenesis. *Cell Stem Cell*, 16:488, 2015.

[186] S.M. Smith, D. Vidaurre, C.F. Beckmann, M.F. Glasser, M. Jenkinson, K.L. Miller, T.E. Nichols, E.C. Robinson, G. Salimi-Khorshidi, M.W. Woolrich, D.M. Barch, K. Ugurbil, and D.C. Van Essen. Functional connectomics from resting-state fmri. *Trends Cogn Sci*, 17:666–682, 2013.

[187] Jie Song, Rasmus M. Birn, Mélanie Boly, Timothy B. Meier, Veena A. Nair, Mary E. Meyerand, and Vivek Prabhakaran. Age-Related Reorganizational Changes in Modularity and Functional Connectivity of Human Brain Networks. *Brain Connectivity*, 4(9):662–676, November 2014.

[188] O. Sporns, D.R. Chialvo, M. Kaiser, and C.C. Hilgetag. Organization, development and function of complex brain networks. *Trends. Cogn. Sci*, 8:418–425, 2004.

[189] O. Sporns, G. Tononi, and R. Kotter. The human connectome: A structural description of the human brain. *PLoS Comput. Biol*, 1:245–251, 2005.

[190] Olaf Sporns. *Networks of the Brain*. MIT Press, Cambridge, Mass, 2011. OCLC: ocn551342282.

[191] C.J. Stam and J.C. Reijneveld. Graph theoretical analysis of complex networks in the brain. *Nonlinear Biomed Phys*, 1:3, 2007.

[192] Jason Steffener, Christian Habeck, Deirdre O'Shea, Qolamreza Razlighi, Louis Bherer, and Yaakov Stern. Differences between chronological and brain age are related to education and self-reported physical activity. *Neurobiology of Aging*, 40:138–144, April 2016.

[193] Claire Joanne Steves, Timothy D. Spector, and Stephen H. D. Jackson. Ageing, genes, environment and epigenetics: What twin studies tell us now, and in the future. *Age and Ageing*, 41(5):581–586, September 2012.

[194] S Stramaglia, JM Cortes, and D Marinazzo. Synergy and redundancy in the Granger causal analysis of dynamical networks. *New J Phys*, 16:105003, 2014.

[195] S. Stramaglia, M. Pellicoro, L. Angelini, E. Amico, H. Aerts, J. M. Cortés, S. Laureys, and D. Marinazzo. Ising model with conserved magnetization on the human connectome: Implications on the relation structure-function in wakefulness and anesthesia. *Chaos: An Interdisciplinary Journal of Nonlinear Science*, 27(4):047407, April 2017.

[196] E V Sullivan and A Pfefferbaum. Neuroradiological characterization of normal adult ageing. *The British Journal of Radiology*, 80(special_issue_2):S99–S108, December 2007.

[197] M Kerna T Ball, I Mutschler, A Aertsen, and A Schulze-Bonhage. Signal quality of simultaneously recorded invasive and non-invasive EEG. *Neuroimage*, 46:708–716, 2009.

[198] E. Tagliazucchi, P. Balenzuela, D. Fraiman, and D.R. Chialvo. Criticality in large-scale brain fmri dynamics unveiled by a novel point process analysis. *Front Physiol*, 3:15, 2012.

[199] E. Tagliazucchi, R. Carhart-Harris, R. Leech, D. Nutt, and D.R. Chialvo. Enhanced repertoire of brain dynamical states during the psychedelic experience. *Hum Brain Mapp*, 35:5442–5456, 2014.

[200] V. Tavares, A. S. Ribeiro, C. Capela, L. Cerqueira, and H. A. Ferreira. Epileptogenic focus localization using complexity analysis of BOLD signals. In *2017 IEEE 5th Portuguese Meeting on Bioengineering (ENBENG)*, pages 1–4, February 2017.

[201] Peter N. Taylor, Nishant Sinha, Yujiang Wang, Sjoerd B. Vos, Jane de Tisi, Anna Miserocchi, Andrew W. McEvoy, Gavin P. Winston, and John S. Duncan. The impact of epilepsy surgery on the structural connectome and its relation to outcome. *NeuroImage: Clinical*, 18:202–214, January 2018.

[202] G. Tononi, O. Sporns, and G. M. Edelman. A measure for brain complexity: Relating functional segregation and integration in the nervous system. *Proceedings of the National Academy of Sciences*, 91(11):5033–5037, May 1994.

[203] Louise Tyvaert, Pierre LeVan, Francois Dubeau, and Jean Gotman. Noninvasive Dynamic Imaging of Seizures in Epileptic Patients. *Human brain mapping*, 30(12):3993–4011, December 2009.

[204] N. Tzourio-Mazoyer, B. Landeau, D. Papathanassiou, F. Crivello, O. Etard, N. Delcroix, B. Mazoyer, and M. Joliot. Automated Anatomical Labeling of activations in SPM using a

Macroscopic Anatomical Parcellation of the MNI MRI single-subject brain. *Neuroimage*, 15:273–289, 2002.

[205] S. van der Walt, S. C. Colbert, and G. Varoquaux. The NumPy Array: A Structure for Efficient Numerical Computation. *Computing in Science Engineering*, 13(2):22–30, March 2011.

[206] Louis André van Graan, Louis Lemieux, and Umair Javaid Chaudhary. Methods and utility of EEG-fMRI in epilepsy. *Quantitative Imaging in Medicine and Surgery*, 5(2):300–312, April 2015.

[207] Pieter van Mierlo, Margarita Papadopoulou, Evelien Carrette, Paul Boon, Stefaan Vandenberghe, Kristl Vonck, and Daniele Marinazzo. Functional brain connectivity from EEG in epilepsy: Seizure prediction and epileptogenic focus localization. *Progress in Neurobiology*, 121(Supplement C):19–35, October 2014.

[208] AB Waites, RS Briellmann MD2, MM Saling, DF Abbott, and GD Jackson. Functional connectivity networks are disrupted in left temporal lobe epilepsy. *Ann Neurol*, 59:335–343, 2006.

[209] K Wang, M Saito, BC Bisikirska, MJ Alvarez, WK Lim, P Rajbhandari, Q Shen, L Nemenman, I Basso, AA Margolin, U Klein, R Dalla-Favera, and A Califano. Genome-wide identification of post-translational modulators of transcription factor activity in human B cells. *Nat Biotechnol*, 27:829–839, 2009.

[210] M. J. West. Regionally specific loss of neurons in the aging human hippocampus. *Neurobiology of Aging*, 14(4):287–293, 1993 Jul-Aug.

[211] M Wibral, JT Lizier, S Voegler, V Priesemann, and R Galuske. Local active information storage as a tool to understand distributed neural information processing. *Front Neuroinform*, 8, 2014.

[212] P Williams and R Beer. Nonnegative decomposition of multivariate information. *arXiv*, page 1004.2515v1, 2010.

[213] N.D. Woodward, B. Rogers, and S. Heckers. Functional resting-state networks are differentially affected in schizophrenia. *Schizophr Res*, b130:86–93, 2011.

[214] GR Wu, F Chen, D Kang, X Zhang, D Marinazzo, and H Chen. Multiscale causal connectivity analysis by canonical correlation: Theory and application to epileptic brain. *IEEE Trans Biomed Eng*, 58:3088–3096, 2011.

[215] G.R. Wu, W. Liao, S. Stramaglia, J.R. Ding, H. Chen, and D. Marinazzo. A blind deconvolution approach to recover effective connectivity brain networks from resting state fmri data. *Med Image Anal*, 17:365–374, 2013.

[216] D. Zhang and M.E. Raichle. Disease and the brain's dark energy. *Nat Rev. Neurol*, 6:15–28, 2010.

[217] Z. Zhou, Y. Chen, M. Ding, P. Wright, Z. Lu, and Y Liu. Analyzing brain networks with PCA and conditional Granger causality. *Hum Brain Mapp*, 30:2197–2206, 2009.

[218] Joelle Zimmermann, Petra Ritter, Kelly Shen, Simon Rothmeier, Michael Schirner, and Anthony R. McIntosh. Structural architecture supports functional organization in the human aging brain at a regionwise and network level: Structure Supports Function in Aging. *Human Brain Mapping*, 37(7):2645–2661, July 2016.

# List of Figures

10.5 **Interakzio Informazioaren egitura giza epilepsia elektrokortikografia datuetan oinarrituta frekuentzia banda ezberdinetan.** 10.2 figuran bezala, II irudikatzen dugu elektroko finko bat jarriz, erresekzioaren eremukoa izanik beti ere, ondooko frekuentzia bandetan: **a,b** delta (1-4 Hz) **c,d** theta (4-7 Hz) **e,f** alpha (7-14 Hz) **g,h** beta (14-26 Hz) and **i,j** gamma (26-100 Hz). Ikus daiteke nola balioak altuagoak diren $\beta$ eta $\gamma$ bandetarako. **b,d,f,h,j:** 10.2 irudiaren antzera, grises marrazten dira 0.3 bit baino altuagoak diren elkarrekintza informazioaren balioak. . . . . 157

10.6 **Erredundantzia eta sinergia frekuentzia bandetan. a:** R-k balio altuagoak jasotzen ditu maiztasun handiko bandetatik , beta eta gamma (laranja eta marroia), bi hauek distribuzio espazial antzekoa sortuz eta eremu epileptogenikoarekin bat eginez (10.3 irudia). **b:** Frekuentzia motelak, delta eta theta esaterako, kontribuzio handiagoa lortzen dute S-S-rendako (urdin iluna eta argia). Gainera, distribuzio espaziala nahiko ezberdina da R-rekin alderatuz, R-ren inguruan ematen baita, R-k zonalde epileptogenoa markatzen duen bitartean. R-ren aktibazioa maiztasun handiko eremu epileptogenikoarekin (hau da, TSI) lotu den bitartean, S inguruan eta maiztasun baxuko bandetan antzematen da . . . . . 158

# List of publications

## First author contributions as a result of this Thesis

- **A Erramuzpe***, P Bonifazi*, I Diez, M Boisgontier, L Pauwels, S Stramaglia, S Swinnen** and JM Cortes**. Single-subject age prediction from structure-function brain networks and its modulation by physical activity **Under review**, 2017 (*Equal first author contribution) (**Equal last author contribution). Preliminary version: `https://www.biorxiv.org/content/early/2017/09/04/183939`

- **A Erramuzpe**, GJ Ortega, J Pastor, RG de Sola, D Marinazzo, S Stramaglia and JM Cortes. Identification of redundant and synergetic circuits in triplets of electrophysiological data. **Journal of Neural Engineering** 12: 066007, 2015

- **A Erramuzpe***, I Diez*, I Escudero, B Mateos, D Marinazzo, A Cabrera, E Sanz-Arigita, S Stramaglia and JM Cortes. Information flow between resting state networks **Brain connectivity** 5(9):554-64, 2015 (*Equal Contribution) **Publication selected for Special Collection on Alzheimer's Disease in 2017**

- **A Erramuzpe**, JM Encinas, A Sierra, M Maletic-Savatic, AL Brewster, AE Anderson, S Stramaglia and JM Cortes . Longitudinal variations of brain functional connectivity: A case report study based on a mouse model of epilepsy. **F1000Research** 4:144, 2015

## Other first author contributions

- V Kljajevic and **A Erramuzpe**. Proper name retrieval and structural integrity of cerebral cortex in midlife: A cross-sectional study **Brain and Cognition** 120, 26-33 , 2018

- **A Erramuzpe**, JM Cortes, JI Lopez. Multisite tumor sampling enhances detection of intratumor heterogeneity at all different temporal stages of tumor evolution **Virchows Archiv**, 1-8 ,2017

- **A Erramuzpe**, E Martinez, M Reisert, A Schulze-Bonhagen, P Bonifazi and JM Cortes. Combination of structural and functional data to unveil brain epileptic networks **Rev Neurol** 62: C92, 2016

## Other JCR articles

- T Lissek, (...) **A Erramuzpe** et al. . NeuroView: Building Bridges through Science **Neuron**, 96(4), 730-735, 2017.

- O Aurtenetxe, L Zaldumbide, **A Erramuzpe**, R Lopez, JI Lopez, JM Cortes, R Pulido and CE Nunes-Xavier. Neuroblastoma PTPome analysis unveils association of DUSP5 and PTPN1 expression with poor prognosis **Under review Cellullar Oncology**, 2017

- JI Lopez, **A Erramuzpe**, R Guarch, JM Cortes, R Llarena, JC Angulo. CD34 immunostaining enhances a distinct pattern of intratumor angiogenesis with prognostic implications in clear cell renal cell carcinoma. **APMIS** 125: 128133, 2017

- I Ortega-Martinez, J Gardeazabal, **A Erramuzpe**, A Sanchez-Diez, JM Cortes, MD Garcia-Vazquez, G Perez-Yarza, R Izu, JL Diaz-Ramon, IM de la Fuente, A Asumendi and MD Boyano. Vitronectin and Dermcidin serum levels predict the metastatic progression of AJCC I-II early stage melanoma. **International Journal of Cancer** 139(7):1598-607, 2016

- JI Lopez, P Errarte, **A Erramuzpe**, R Guarch, JM Cortes, JC Angulo, R Pulido, J Irazusta, R Llarena, G Larrinaga. Fibroblast activation protein predicts prognosis in clear cell renal cell carcinoma. **Human Pathology** 54, 100105, 2016

- J Mingo, **A Erramuzpe**, S Luna, I Diez, JM Cortes, R Pulido. One-Tube-Only Standardized Site-Directed Mutagenesis: An alternative approach to generate amino acid substitution collections **PLoS One** 11(8):e0160972, 2016

- L Zaldumbide, **A Erramuzpe**, R Guarch, R Pulido, JM Cortes and JI Lopez. Snail heterogeneity in clear cell renal cell carcinoma, **BMC Cancer** 16:194, 2016

- L Zaldumbide, **A Erramuzpe**, R Guarch, JM Cortes and JI Lopez. Large (3.8 cm) Clear Cell Renal Cell Carcinomas are Morphologically and Immunohistochemically Heterogeneous. **Virchows Archiv** 466.1: 61-66, 2015

## Software contributions

- O Esteban, (...) **A Erramuzpe** (...), KJ Gorgolewski, (2018, February 23). poldracklab/fmriprep: 1.0.8 . Zenodo. `http://doi.org/10.5281/zenodo.1183390`

- `https://github.com/erramuzpe`

- `https://github.com/compneurobilbao`

## Internships related to this Thesis

- **Google Summer of Code 2016**, "Neurovault: Image Search for Brain Maps"
  Mentor: Chris Gorgolewski

- **Google Summer of Code 2015**, "Building Non-Linear Analysis Tools For C-PAC"
  Mentors: Ivan J. Roijals-Miras & Cameron Craddock